



Nanostructured hybrid solar cells based on PECVD grown SiNWs and organic semiconducting polymers

Taewoo Jeon

► To cite this version:

Taewoo Jeon. Nanostructured hybrid solar cells based on PECVD grown SiNWs and organic semiconducting polymers. Electronics. Ecole Polytechnique X, 2013. English. NNT: . pastel-00917826

HAL Id: pastel-00917826

<https://pastel.hal.science/pastel-00917826>

Submitted on 12 Dec 2013

HAL is a multi-disciplinary open access archive for the deposit and dissemination of scientific research documents, whether they are published or not. The documents may come from teaching and research institutions in France or abroad, or from public or private research centers.

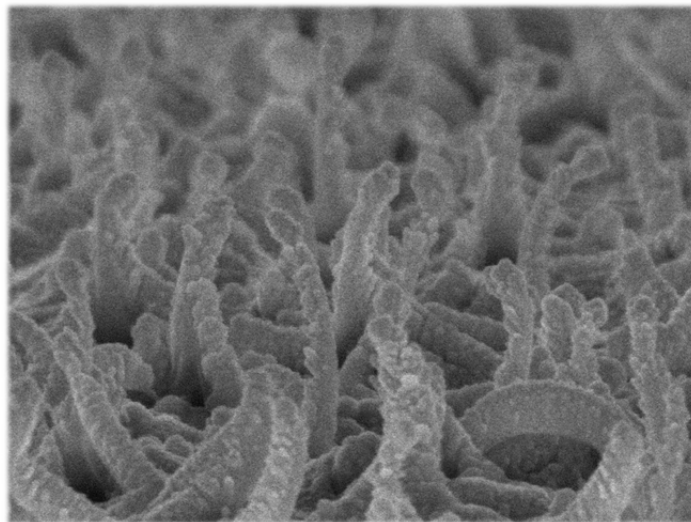
L'archive ouverte pluridisciplinaire **HAL**, est destinée au dépôt et à la diffusion de documents scientifiques de niveau recherche, publiés ou non, émanant des établissements d'enseignement et de recherche français ou étrangers, des laboratoires publics ou privés.



Doctoral Thesis in Physics and Materials Science

**Nanostructured hybrid solar cells based on PECVD grown
SiNWs and organic semiconducting polymers**

TAEWOO JEON





THÈSE

présentée en vue d'obtenir le grade de

Docteur de l'École Polytechnique

Spécialité : Physique et Science de Matériaux

par

TAEWOO JEON

Nanostructured hybrid solar cells based on PECVD grown SiNWs and organic semiconducting polymers

Thèse soutenue le 25 Novembre 2013 devant le jury composé de :

Prof.	Bernard Ratier	Rapporteur
Prof.	Joaquim Puigdollers	Rapporteur
Dr.	Daniel Lincot	Examineur
Dr.	Thomas Heiser	Examineur
Prof.	Yvan Bonnassieux	Directeur de Thèse
Dr.	Bernard Geffroy	Co-directeur de Thèse

ACKNOWLEDGEMENTS

I could complete my thesis, which is a subject quite challenging and multidisciplinary, by great helps of all colleagues at LPICM. First of all, I sincerely thanks to my thesis advisor, Prof. Yvan Bonnassieux, for his wholehearted support and a guidance that make me encourage and motivate. I express my gratitude to Dr. Bernard Geffroy, who was co-advisor of the thesis, for his kind discussion on the subjects with helpful comments. Also, I thank to Prof. Pere Roca I Cabarrocas for his passions and curiosity that let me very motivate.

I can't forget ORGATECH members who give me a technical support, discussion and a joyful laboratory life during my stay. I would like to thank to Denis Tondelier, Abderrahim Yassar, Gaël Zucchi, Jean-Charles Vanel, François Moreau, Chang-Hyun Kim, Hassina Derbal-Habak, Subimal Majee, Xiaoguang Huang, and Jinwoo Choi. I am grateful to members of SiNWs team; Linwei Yu, Benedict O'Donnell, Soumyadeep Misra and Alienor Togonal. They helped me a lot for the SiNWs growth. The discussion with them gave me insights on the SiNWs. And I thank to also Serge Palacin, Bruno Jousset, and Pascale Jegou, who are the members of CEA for their helps for scientific discussion.

I am especially grateful to Dmitri Daineka, Mark Chaigneau, Jinyoun Cho, Mun-Ho Song, Antoine Salmon, Romain Cariou, Igor Sobkowitz, Ka-Hyun Kim, Chang-Seok Lee, Ki-Hwan Kim, Poncho Torres Rios, Junzhuan Wang, Youn-Ho Heo, Joonwon LIM, Jongwoo Jin, Youngbin Jeong, Myungjin Lim, Tae-Ha Hwang, Ki-Hwan Seok, Hojoong Kwon, Sungyeop Jeong, Heejae Lee, Jongyoon Park, Gijun Seo, and Haena Won.

I express my love and gratitude to my wife, Eunjung PARK, and my son, Yesung JEON, and also to my family in Korea for their love and faith for me.

CONTENTS

<i>Acknowledgements</i>	
<i>Contents</i>	<i>i</i>
<i>List of Figures</i>	<i>v</i>
<i>List of Tables</i>	<i>xi</i>
<i>List of Acronyms</i>	<i>xiii</i>
CHAPTER 1 - BACKGROUND KNOWLEDGE	1
1.1 INTRODUCTION	2
1.2 SILICON MATERIALS	2
1.2.1 SILICON NANOWIRES	2
1.2.2 HYDROGENATED AMORPHOUS SILICON	6
1.3 ORGANIC SEMICONDUCTOR	7
1.3.1 π -CONJUGATED SYSTEM	7
1.3.2 P3HT AND PCBM	9
1.3.3 PEDOT:PSS	11
1.4 CHARACTERIZATION OF MATERIALS AND SOLAR CELLS	12
1.4.1 SCANNING ELECTRON MICROSCOPE	12
1.4.2 RAMAN SPECTROSCOPY	13
1.4.3 X-RAY PHOTOEMISSION SPECTROSCOPY	15
1.4.4 UV-VIS SPECTROSCOPY	15
1.4.5 CURRENT-VOLTAGE CHARACTERISTICS OF SOLAR CELLS	17
1.5 HYBRID SOLAR CELLS BASED ON SILICON AND ORGANIC MATERIALS	22
1.6 APPROACHES OF THESIS	27
<i>Reference</i>	<i>28</i>
CHAPTER 2 - PECVD GROWTH OF SINWS AND NANO-MORPHOLOGY	33
2.1 INTRODUCTION	34
2.2 PLASFIL SYSTEM (PECVD)	35
2.3 VLS GROWTH OF SINWS AND CATALYST CHOICE	37
2.4 SN-CATALYZED SINWS	41
2.4.1 GROWTH TIME DEPENDENCE	43
2.4.2 DENSITY CONTROL BY H ₂ PLASMA	46
2.5 BI-CATALYZED SINWS	49
2.5.1 N-TYPE CHARACTERISTIC OF BI-CATALYZED SINWS	50

2.5.2	TEMPERATURE DEPENDENCE	51
2.5.3	RF POWER DEPENDENCE	54
2.5.4	GAS FLOW RATIO DEPENDENCE	56
2.6	CONCLUSION: PROPER USE OF EACH SINWS	60
2.6.1	SN-CATALYZED SiNWs	60
2.6.2	Bi-CATALYZED SiNWs	61
	<i>Reference</i>	63
CHAPTER 3	- NANO-STRUCTURED HYBRID SOLAR CELLS	67
3.1	INTRODUCTION	68
3.2	DEVICE DESIGN, FABRICATION AND WORKING PRINCIPLE	70
3.3	PHOTOVOLTAIC EFFECT ESTABLISHMENT BY PEDOT:PSS	74
3.4	MORPHOLOGY OF SINWS & PHOTOVOLTAIC EFFECTS	86
3.5	CONCLUSION: REQUIREMENTS FOR PHOTOVOLTAIC ACTION	93
	<i>Reference</i>	95
CHAPTER 4	- OPTIMIZATION OF SINWS FOR EFFICIENT LIGHT TRAPPING	99
4.1	INTRODUCTION	100
4.2	ACID TREATMENTS FOR RESIDUAL CATALYST REMOVAL	102
4.2.1	HCL TREATMENT OF SiNWs AND ITS EFFECT ON SiNWs ARRAY	102
4.2.2	EFFECTS OF ACID TREATMENTS ON HYBRID SOLAR CELL PERFORMANCE	112
4.3	A-Si:H ETCHING BY HYDROGEN PLASMA	123
4.3.3	SELECTIVE ETCHING OF A-Si:H FROM SiNWs ARRAY	123
4.3.4	ENHANCED SOLAR CELL PERFORMANCE BY A-Si:H ETCHING	130
4.4	CONCLUSION: BENEFITS FROM SN-CATALYZED SINWS	137
	<i>Reference</i>	141
CHAPTER 5	- HYBRID HETEROJUNCTION BASED SOLAR CELL	143
5.1	INTRODUCTION	144
5.2	HYBRID INTERFACE: P3HT AND SILICON MATERIALS	144
5.3	REALIZATION OF HYBRID SOLAR CELLS	148

5.4 DEVICE PERFORMANCES	150
5.4.1 DARK CURRENT-VOLTAGE CHARACTERISTIC	150
5.4.2 SOLAR CELL PERFORMANCE	153
5.5 CONCLUSION: CHALLENGES AND PERSPECTIVES	161
<i>Reference</i>	163
 CONCLUSION	 167
 APPENDIX.....	 169
A.1 TCO DEPENDENCE OF HYBRID SOLAR CELL PERFORMANCE.....	170
A.2 SINWS GROWTH CONDITIONS	171
A.2.1 SN-CATALYZED SiNWS: GROWTH TIME DEPENDENCE (SECTION 2.4.1).....	171
A.2.2 SN-CATALYZED SiNWS: H ₂ DEPENDENCE (SECTION 2.4.2).....	171
A.2.3 BI-CATALYZED SiNWS: TEMPERATURE DEPENDENCE (SECTION 2.5.2).....	172
A.2.4 BI-CATALYZED SiNWS: RF POWER DEPENDENCE (SECTION 2.5.3)	172
A.2.5 BI-CATALYZED SiNWS: GAS FLOW RATIO DEPENDENCE (SECTION 2.5.4)	172
A.3 ORGANIC THIN-FILM FORMATION	173

LIST OF FIGURES

Figure 1.1 – Band diagram of crystalline silicon with characterized energy level based on vacuum levels.	3
Figure 1.2 – Absorptance of silicon thin film and silicon nanowires as a function of photon energy of incident light.	4
Figure 1.3 – Benefits of silicon nanowire fabricated by (a) etching of crystalline silicon and (b) plasma-enhanced chemical vapor deposition.	5
Figure 1.4 – Density of states of hydrogenated amorphous silicon. Exponential band tail states and deep states are illustrated.	6
Figure 1.5 – Graphical description of π -conjugated system: (a) the example of Benzene (b) bonding between 2 π -orbitals. According to the wave function overlap, bonding and anti-bonding states are generated.	7
Figure 1.6 – Energy band formation in organic materials with increased number of atoms. π and π^* band is described with HOMO and LUMO levels.	8
Figure 1.7 – Molecular structure of (a) P3HT and (b) PCBM	9
Figure 1.8 – Molecular structure of PEDOT:PSS	11
Figure 1.9 – Examples of SEM images: (a) Tin-catalyzed SiNWs (b) Bismuth-catalyzed SiNWs by PECVD	13
Figure 1.10 – Raman spectrum of Sn-catalyzed SiNWs. Crystal silicon peak is observed at 518 cm^{-1} with amorphous silicon peak (broad) at 480 cm^{-1}	14
Figure 1.11 – Absorbance measured by UV-Vis spectroscopy. SiNWs, P3HT:PCBM and SiNWs with P3HT:PCBM are measured based on the same base line	16
Figure 1.12 – Air mass; solar spectral irradiance as a function of wavelength Inset shows incident angle of sunlight relative to zenith (normal to the earth's surface).	18
Figure 1.13 – A typical solar cell J-V curve with solar cell parameters.	19
Figure 1.14 – Equivalent circuit model of solar cell consisted of constant current source, diode, series and shunt resistance.	20
Figure 1.15 – The example of type 1 hybrid solar cell based on n-type silicon nanocone and PEDOT:PSS. (a) solar cell structure and (b) solar cell performance	23
Figure 1.16 – The example of type 2 hybrid solar cells based on P3HT and silicon nanocrystals. (a) solar cell structure (b) absorbance and (c) solar cell performance	24
Figure 1.17 - The example of type 3 hybrid solar cell based on n-type silicon wafer and P3HT. (a) solar cell structure and (b) solar cell performance	25
Figure 2.1 – SEM images of SiNWs fabricated by top-down (TD) approaches and bottom-up (BU) approaches. By (a) reactive ion etching (TD) (b) metal-catalyzed electro-less etching (TD) (c) chemical vapor deposition (BU) (d) plasma-enhanced chemical vapor deposition (BU)	34
Figure 2.2 – PECVD system; (a) The photo of PLASFIL system used in this study, (b) Schematic diagram of PLASFIL	36
Figure 2.3 – Schematic diagrams of vapor-liquid-solid process. (a) Catalyst metal film deposition (b) catalyst droplet formation (c) dissociation of precursor gas (in this case silane) (d) diffusion of silicon atoms into catalyst droplets (e) continuous integration and diffusion of silicon atoms in catalyst droplets (f) crystalline phase of silicon is precipitated at the interface after the silicon concentration reaches saturation.	38
Figure 2.4 – Periodic table of transition metals and post-transition metals as potential catalyst metals for VLS process.	39

Figure 2.5 – Impurities energy level of catalyst metals as a function of eutectic point with silicon. Red triangles and blue squares correspond to post-transition and transition metals respectively.	40
Figure 2.6 – Sn-catalyzed SiNWs growth procedures by PECVD. (a) Hydrogen plasma of thin tin deposited ITO/glass substrate (b) Silane plasma with tri-methyl boron for SiNWs growth (c) VLS growth process and (d) Sn-catalyzed SiNWs array.	42
Figure 2.7 – SEM images of Sn-catalyzed SiNWs with the growth time (a) 5 min (b) 5 min, cross-sectional view (c) 10 min and (d) 15 min.....	43
Figure 2.8 – Length and diameter of SiNWs as a function of growth time. (Black symbol and line for length, Red symbol and line for diameter).....	44
Figure 2.9 – Absorbance of SiNWs for SiNWs arrays of different growth time.....	45
Figure 2.10 – SEM images of Sn-catalyzed SiNWs depending on hydrogen plasma duration during catalyst droplets formation. (a) 2 min (b) 4 min (c) 6 min and (d) 8 min.	46
Figure 2.11 – Dimensional characteristics of SiNWs depending on hydrogen plasma duration during catalyst formation. (a) Density (b) Diameter and (c) Length of Sn-catalyzed SiNWs.	47
Figure 2.12 – Schematic diagram of catalyst generation from thin Sn film and also from ITO. (a) Thin Sn metal deposited on ITO/glass, (b) Hydrogen plasma at 350 °C at the beginning (c) Long time hydrogen plasma at 350 °C. In catalyst starts to generate. (d) Presence of Sn and In catalyst droplets	48
Figure 2.13 – SEM images of Bi-catalyze SiNWs depending on growth temperature. Growth temperatures are (a,b) 450 °C (c,d) 500 °C (e,f) 550 °C and (g,h) 600 °C.....	52
Figure 2.14 – Density and residual catalyst diameters as a function of growth temperature. (Black symbol and line for density, Red symbol and line for residual catalyst diameter).....	53
Figure 2.15 – SEM images of Bi-catalyze SiNWs depending RF power (a,b) 20 W (c,d) 40 W and (e,f) 60 W.....	54
Figure 2.16 – Density, residual catalyst diameters and length as a function of RF power. (Black symbol and line for density, Red symbol and line for residual catalyst diameter, Blue symbol and line for SiNWs' length).....	55
Figure 2.17 – SEM images of Bi-catalyze SiNWs depending gas flow ratio (H_2/SiH_4). (a,b) 0 (c,d) 10 (e,f) 20 and (g,h) 50	57
Figure 2.18 – Density and length as a function H_2/SiH_4 ratio. (Black symbol and line for density, Red symbol and line for SiNWs' length)	58
Figure 2.19 – Etching of residual bismuth catalyst on tip of SiNWs by hydrogen plasma at 600 °C.....	59
Figure 2.20 – (a) SEM image of Sn-catalyzed SiNW and (b) spacing between SiNWs: Mean spacing is 180 nm.	60
Figure 2.21 – SEM image: Nano-morphology variation of Bi-catalyzed SiNWs	61
Figure 2.22 – (a) SEM image of Bi-catalyzed SiNW and (b) spacing between SiNWs: Mean spacing is 20 nm.....	62
 Figure 3.1 – Representatives of hybrid solar cells device structures (a) bi-layer type (b) blend type (c) nano-structure type	68
Figure 3.2 – Description of spin-coating method; (a) dispensation of prepared solution on substrate (b) spin-up stage (c) spin-off and film formation and (d) the photo of spin-coating process photo	70
Figure 3.3 – Film thickness of (a) P3HT dissolved in 1,2-Dichlorobenzene according to the solution concentration from 2 mg/mL to 30 mg/mL and (b) PEDOT:PSS according to the rotation speed from 3000 rpm to 4000 rpm.	71
Figure 3.4 – Nano-structured hybrid solar cell fabrication process (a) as grown Sn-catalyzed SiNWs, (b) deposition of PEDOT:PSS buffer layer by spin coating, (c) deposition of P3HT:PCBM layer on PEDOT:PSS and (d) final device with LiF/Al top electrode.	72

Figure 3.5 – Band diagram explaining general working principle of organic solar cells which is quite similar with the hybrid solar cell in this study.....	73
Figure 3.6 – Absorbance of P3HT:PCBM layer on glass (dashed line) and SiNWs (solid line).....	75
Figure 3.7 – Current density-voltage characteristics of hybrid solar cells under dark (black, left y-axis in semi-log scale) and AM 1.5 (red, right y-axis in linear scale). The inset figure describes device structure (Glass/ITO/SiNWs/P3HT:PCBM/LiF/Al)	76
Figure 3.8 – Hybrid solar cells performances according to the PEDOT:PSS existence and thickness (a) under AM 1.5 illumination (b) dark.....	77
Figure 3.9 – SEM images of (a) as grown SiNWs and (b) SiNWs covered by PEDOT:PSS and Schematic diagram of (e) as grown SiNWs and (f) SiNWs covered by PEDOT:PSS.....	79
Figure 3.10 – Schematic diagram of P3HT:PCBM layer on SiNWs (a) without, (b) with PEDOT:PSS and (c) energy band diagram of P3HT, PCBM, SiNWs	81
Figure 3.11 – Transmittance of PEDOT:PSS layer on ITO with thickness variation	83
Figure 3.12 – Experimental photo-current density – effective voltage plots: J_{ph} is extracted by the equation $J_{ph}=J_L-J_D$	84
Figure 3.13 – Model diagrams of hybrid solar cells according to length of SiNWs and organic active layer thickness. (a) length of SiNWs > thickness of P3HT:PCBM, (b) length of SiNWs ~ thickness of P3HT:PCBM and (c) length of SiNWs < thickness of P3HT:PCBM,.....	87
Figure 3.14 – SEM images of hybrid solar cells case by case. (a) Case 1 on P3HT:PCBM. (b) Case 1 on P3HT:PCBM/LiF/Al (c) Case 2 on P3HT:PCBM and (d) Case 3 on P3HT:PCBM	87
Figure 3.15 – Hybrid solar cell performance for three case of SiNWs length and organic layer thickness relations. Measured under AM 1.5 condition.	88
Figure 3.16 – Absorbance of P3HT:PCBM with different SiNWs density; SiNWs absorption is excluded.....	90
Figure 3.17 – Hybrid solar cell performance according to the density of SiNWs. Measured under AM 1.5 condition.....	91
Figure 3.18 – Series resistance dependence of (a) short-circuit current and (b) power conversion efficiency.....	92
Figure 3.19 – Normalized external quantum efficiency of conventional organic bulk-heterojunction solar cells and hybrid solar cells	93
Figure 4.1 – Schematic diagrams of hybrid solar cells. (a) entire device structure of the hybrid solar cells based on PECVD grown SiNWs and P3HT:PCBM. This device can be divided into two sub-devices (b) sub-device 1 containing SiNWs and (c) sub-device 2 without SiNWs.	100
Figure 4.2 – SEM image of PECVD grown Sn-catalyzed SiNWs on ITO/glass substrate; 1) Thickness of Sn: 2 nm 2) Catalyst droplets formation (H ₂ plasma): 350 °C, 100 sccm of H ₂ , 360 mTorr, 5 W, 2 min 3) SiNWs growth: 600 °C, 10 sccm of SiH ₄ , 1.5 sccm of TMB, 100 sccm of H ₂ , 1 Torr, 2 W, 3 min.....	102
Figure 4.3 – Solar cell performance of organic bulk-heterojunction solar cells based on P3HT:PCBM with and without 1 nm of Tin on ITO under A.M 1.5.....	103
Figure 4.4 – Dipping of SiNWs into 5 % HCl to remove residual Sn; the dipping time is optimized by 20 min with consideration of SiNWs' damage	105
Figure 4.5 – Sheet resistance of ITO with HCl dipping time	106
Figure 4.6 – SEM images of Sn-catalyzed SiNWs array after dipping into HCl with different time. All SiNWs array was grown with identical condition; 1) Thickness of Sn: 2 nm 2) Catalyst droplets formation (H ₂	

plasma): 350 °C, 100 sccm of H ₂ , 360 mTorr, 5 W, 2 min 3) SiNWs growth: 600 °C, 10 sccm of SiH ₄ , 1.5 sccm of TMB, 100 sccm of H ₂ , 1 Torr, 2 W, 3 min	107
Figure 4.7 – Results of X-ray photoelectron spectroscopy of SiNWs array with different HCl dipping time for detecting residual catalyst (here, Sn). The graph describes normalized counts of Sn metal and oxide part as a function of binding energy. Sn metal and oxide are detected at 484.9 and 487.2 eV respectively. The inset table summarizes ratio of Sn metal and oxide compared with silicon according to the HCl dipping time.	108
Figure 4.8 – Schematic of distributed catalyst on as grown SiNWs array (cross-sectional view). (1) residual catalyst after growth (2) ultra-thin diffused catalyst on SiNWs' surface (3) Diffused SiNWs during the growth in SiNWs and (4) catalyst droplets covered by a-Si:H before initiating SiNWs growth.	109
Figure 4.9 – Transmittances of (a) ITO/glass substrate and (b) SiNWs/ITO/glass substrate as a function of wavelength with various HCl dipping time.	110
Figure 4.10 – Current density – voltage characteristics under dark with various HCl treatments.	113
Figure 4.11 – Solar cell performance of hybrid solar cells under illumination intensity (a) 13 mW/cm ² and (b) 100 mW/cm ² with various HCl dipping time.	114
Figure 4.12 – Open-circuit voltage (V_{oc}) change as a function of HCl dipping time; V_{oc} is measured under AM 1.5 conditions.	117
Figure 4.13 – Light intensity dependence of open-circuit voltage with various HCl dipping time. Linear fits for the data are drawn in solid line. While dashed line is drawn as an eye guide line for the slope of kT/q	120
Figure 4.14 – Dark current density – voltage characteristics with and without HF treatment.	121
Figure 4.15 – Solar cell performance with and without HF treatment measured under AM 1.5 condition	122
Figure 4.16 – Solar cell performance with and without a-Si:H layer (10 nm) on ITO/glass substrate. Measured under AM 1.5 condition.	125
Figure 4.17 – Raman spectroscopy of Sn-catalyzed SiNWs array measured by 621 nm wavelength of red laser with 0.15 mW light intensity. (a) Mapping images over 7 x 7 μm^2 , (b) Raman shift of SiNWs dominant region and (c) Raman shift of a-Si:H dominant region; SiNWs have diameter, length and density of 20 nm, 240 nm and 4.0×10^9 SiNWs/cm ²	126
Figure 4.18 – Schematic diagram of amorphous silicon etching process by hydrogen plasma; Big dark circle, small yellow and red circles represent silicon atoms, hydrogen atoms bonded during SiNWs growth for hydrogenation and hydrogen atoms supplied by hydrogen plasma. Grey solid lines mean covalent bond between atoms. Dark solid line depicts etching process of a-Si:H and dark dashed line indicates less sensitivity of SiNWs. H ₂ plasma is performed at 100 °C with flow rate, pressure and RF power of 200 sccm, 1 Torr and 20 W respectively.	127
Figure 4.19 – Absorbance of SiNWs/ITO/Glass substrates according to the hydrogen plasma time	129
Figure 4.20 – Dimensional properties of SiNWs array according to the hydrogen plasma duration. (a) Diameter of SiNWs, (b) Length of SiNWs, (c) density of SiNWs, and SEM images (d) 0s, (e) 90 s (f) 180 s of duration of hydrogen plasma. The white scale bars indicate 500 nm	130
Figure 4.21 – Solar cells performance according to the a-Si:H etching duration by hydrogen plasma	132
Figure 4.22 – Absorbance of P3HT:PCBM film on SiNWs treated by hydrogen plasma.	133
Figure 4.23 – Schematic diagram of holes transport from P3HT:PCBM layer to a-Si:H layer. [a] electron transfer from P3HT to PCBM [b] hole transport through P3HT to PEDOT:PSS [c] Injection of holes from PEDOT:PSS to a-Si:H (energy barrier, ϕ , is 0.5 eV) and [d] hole transport through band-gap states	134
Figure 4.24 – Experimental photo-current as a function of effective voltage (V_0-V) according to the H ₂ plasma duration.	135

Figure 4.25 – Solar cells performance according to the optimization method which are measured under AM 1.5 condition.	138
Figure 4.26 – Normalized external quantum efficiency (EQE) of solar cells; comparison of organic bulk-heterojunction solar cells (BHJ SC) and hybrid solar cell (HSC) with different treatment conditions. Organic active layer is composed of P3HT and PCBM. The thickness of active layer is same for BHJ SC and HSC.	139
Figure 5.1 – Energy band diagrams of P3HT, crystalline silicon (c-Si) and hydrogenated amorphous silicon (a-Si:H)	145
Figure 5.2 – Solar cell based on c-Si/P3HT junction. (a) Solar cell structure: P3HT is spin-coated on n-Si wafer, and then semi-transparent palladium is evaporated. (b) Solar cell performance with various thickness of P3HT. (Reprinted from Ref.[3])	146
Figure 5.3 – Solar cell based on a-Si:H/P3HT junction. (a) Solar cell structure: n-type a-Si:H are deposited by conventional PECVD with 20 nm thick. P3HT is spin-coated on a-Si:H layer and then silver (Ag) electrode is deposited by thermal evaporation. (b) Solar cell performance.	147
Figure 5.4 – Characteristics of Bi-catalyzed SiNWs. (a) SEM image: dense SiNWs are chosen for exciton dissociation and (b) Raman spectroscopy: crystalline silicon peak is observed with broad amorphous silicon peak.	148
Figure 5.5 – Hybrid solar cell structures based on Bi-catalyzed SiNWs on aluminum doped zinc oxide and P3HT with grid silver electrode.	149
Figure 5.6 – Dark current density – voltage characteristics of the hybrid solar cell based on Bi-catalyzed SiNWs/P3HT interface. Diode parameters are summarized in the graph.	151
Figure 5.7 – Dark current density – voltage characteristics of the hybrid solar cell based on Bi-catalyzed SiNWs/P3HT interface. Diode parameters are summarized in the graph.	152
Figure 5.8 – Solar cell performance of the hybrid solar cell based on Bi-catalyzed SiNWs/P3HT interface. Solar cell parameters are summarized in the graph. Average length of Bi-catalyzed SiNWs and thickness of solar cell are 130 and 150 nm respectively.	153
Figure 5.9 – Band diagram of SiNWs P3HT to explain photo-generated carrier generation. 1) Exciton generation by absorption of incident light. 2) Diffusion of exciton toward interface of SiNWs/P3HT. 3) Exciton dissociation (electron transfer from LUMO of P3HT to conduction band of SiNWs) 4) electron recombination 5) Transport of photo-generated carriers	154
Figure 5.10 – Solar cell performance of the hybrid solar cell based on Bi-catalyzed SiNWs/P3HT interface; dependence of PCBM contents (%) in P3HT solution	155
Figure 5.11 – (a) J_{sc} and V_{oc} of hybrid solar cells as a function of PCBM content (%) (b) Experimental photocurrent extracted from the equation of $J_L - J_D = J_{ph}$ as a function of effective voltage, $V_0 - V$	156
Figure 5.12 – Solar cell performance of planar solar cell without SiNWs. Solar cell parameters are summarized in the graph.	159
Figure 5.13 – Summary of solar cell performance of hybrid heterojunction based on SiNWs/P3HT, SiNW/P3HT:PCBM and organic inverted solar cells based on P3HT:PCBM.	160

LIST OF TABLES

Table 1.1 – Summary of types of hybrid solar cells based on light absorbing materials.	22
Table 3.1 – Summary of solar cell parameters with various PEDOT:PSS thickness	78
Table 3.2 – Summary of hybrid solar cell parameters case by case	88
Table 3.3 – Summary of hybrid solar cell parameters with various SiNWs density.....	91
Table 4.1 – Summary of solar cell parameters with substrates.....	103
Table 4.2 – Series and shunt resistance of hybrid solar cells under dark with various HCl dipping time.	113
Table 4.3 - Hybrid solar cells parameters with various HCl dipping time.	115
Table 4.4 – Diode parameters of hybrid solar cells: dependence of HF treatment	120
Table 4.5 – Solar cell parameters of hybrid solar cells: dependence of HF treatment	121
Table 4.6 – Solar cell parameters of hybrid solar cells: dependence of a-Si:H layer existence.	125
Table 4.7 – Solar cells parameters of hybrid solar cells: dependence of a-Si:H layer existence.....	131

LIST OF ACRONYMS

Acronym	
a-Si:H	Hydrogenated amorphous silicon
AZO	Aluminum-doped zinc oxide
c-Si	Crystalline silicon
CVD	Chemical vapor deposition
E_{binding}	Binding energy (eV)
E_{gap}	Band-gap (eV)
EQE	External quantum efficiencies
FF	Fill factor (%)
HOMO	Highest Occupied Molecular Orbital
ITO	Indium tin oxide
J_0	Reverse saturation current (mA/cm ²)
J_D -V	Dark current density - voltage characteristic
J_L -V	Illumination current density - voltage characteristic
J_{ph}	Photo-current density (mA/cm ²)
J_{sc}	Short-circuit current (mA/cm ²)
LUMO	Lowest Unoccupied Molecular Orbital
n	Diode ideality factor
P3HT	Poly(3-hexylthiophene)
PCBM	Phenyl-C61-butyric acid methyl ester
PECVD	Plasma enhanced chemical vapor deposition
PEDOT:PSS	Poly(3,4-ethylenedioxythiophene) poly(styrenesulfonate)
P_{light}	Incident light intensity (mW/cm ²)
P_{max}	Maximum power (mW/cm ²)
rpm	Revolutions per minute
R_s	Series resistance ($\Omega \cdot \text{cm}^2$)
R_{sh}	Shunt resistance ($\Omega \cdot \text{cm}^2$)
sccm	Standard cubic centimeters per minute
SEM	Scanning electron microscope
SiNWs	Silicon nanowires
T	Absolute temperature (K)
V_0	Defined as voltage where $J_L=0$ (V)
VLS	Vapor-liquid-solid
V_{oc}	Open-circuit voltage (V)
XPS	X-ray photoemission spectroscopy (eV)
η	Power conversion efficiency of solar cell (%)
ϕ	Work function (eV)

Chapter 1

BACKGROUND KNOWLEDGE

1.1 INTRODUCTION	2
1.2 SILICON MATERIALS.....	2
1.2.1 SILICON NANOWIRES.....	2
1.2.2 HYDROGENATED AMORPHOUS SILICON	6
1.3 ORGANIC SEMICONDUCTOR.....	7
1.3.1 π -CONJUGATED SYSTEM	7
1.3.2 P3HT AND PCBM	9
1.3.3 PEDOT:PSS	11
1.4 CHARACTERIZATION OF MATERIALS AND SOLAR CELLS.....	12
1.4.1 SCANNING ELECTRON MICROSCOPE	12
1.4.2 RAMAN SPECTROSCOPY	13
1.4.3 X-RAY PHOTOEMISSION SPECTROSCOPY	15
1.4.4 UV-VIS SPECTROSCOPY	15
1.4.5 CURRENT-VOLTAGE CHARACTERISTICS OF SOLAR CELLS.....	17
1.5 HYBRID SOLAR CELLS BASED ON SILICON AND ORGANIC MATERIALS.....	22
1.6 APPROACHES OF THESIS.....	27
<i>REFERENCE</i>	28

1.1 Introduction

Here, backgrounds needed to figure out this thesis are briefly introduced. For materials, silicon and organic materials used such as amorphous silicon, silicon nanowires (crystalline silicon), poly-3(hexylthiophene), phenyl-C61-butyric methyl ester and poly(3,4-ethylenedioxythiophene) poly(styrenesulfonate), are presented. Methods to characterize these materials, for instance, scanning electron microscope, Raman spectroscopy and UV-visible spectroscopy will be briefly discussed. Furthermore, the basic of solar cells, solar cell parameters and measurement methods are covered. Various types of hybrid solar cells developed during the last decade will be explained according to the working principle for better understanding of hybrid solar cells. Finally, our approaches to organize silicon and organic materials for hybrid solar cell development will be discussed.

1.2 Silicon materials

1.2.1 Silicon nanowires

Silicon is the most popular semiconductor material for solid-state electronics. For examples, first silicon solar cell based on p-n junction was presented in 1954 by Chapin et al [1]. Despite of the rapid development of novel materials such as organic materials, carbon nanotube and graphene, the silicon based electronics are supported by the abundance of material and the technical maturity. In recent year, numerous nano-structures of silicon are drawing strong attentions as efficient energy conversion materials due to their unique characteristics compared to the bulk silicon wafer, for examples nanoparticles [2], nanowires [3-12], nanorods [13, 14] etc. The physical properties of the nanostructured silicon are adjustable by changing their dimensional characteristics and nano-morphologies. Among them, silicon nanowires (SiNWs) are one of most interesting configuration because the geometry of nanowires provides the smallest dimension for light trapping, photo-carrier generation, separation and transport [15].

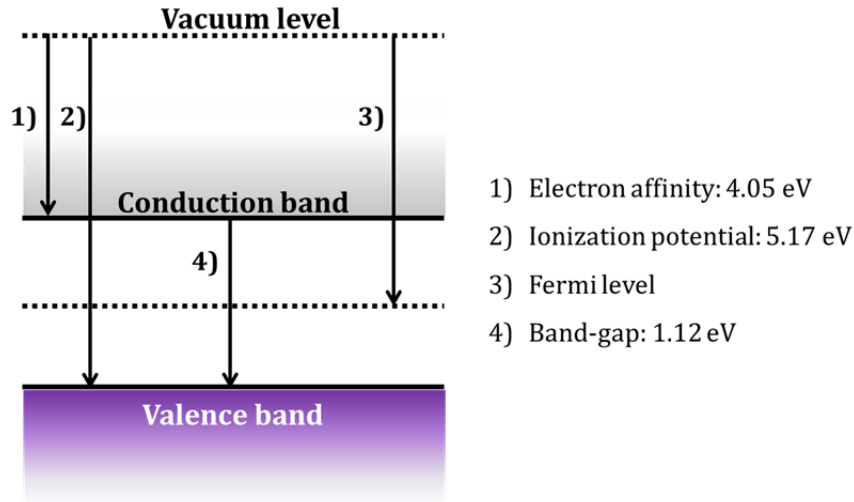


Figure 1.1 – Band diagram of crystalline silicon with characterized energy level based on vacuum levels.

SiNWs are rod-like crystalline silicon with diameter less than 100 nm. SiNWs stands on the basis of silicon whisker reported in 1957 by Treuting and Arnold where they presented $\langle 111 \rangle$ direction of silicon whiskers [16]. And Wagner and Ellis reported vapor-liquid-solid mechanism of SiNWs growth, which is still predominant mechanism of SiNWs growth, in 1964 [17]. A boom in research of SiNWs was started from 1998 in earnest with over 100 publications. Next, the dramatic increase in the number of publication was made in 2003-2007 with over 600 publications [18].

SiNWs fabrication methods can be largely classified into top-down and bottom-up approaches. Top-down method is generally used to crystalline silicon wafer as a source material. Reactive ion etching and metal-catalyzed electro-less etching of silicon are employed for physical and chemical etching of bulk silicon wafer [19, 20]. These nanowires have same electrical characteristics with mother silicon wafer. However, the cost of silicon wafer is an obstacle for wide uses of this technique. Bottom-up approaches are considered as an alternative for low cost SiNWs fabrication. Crystalline phase of SiNWs are synthesized by various methods. For examples, conventional chemical vapor deposition (CVD), plasma-enhanced CVD, laser ablation, molecular beam epitaxy and silicon dioxide evaporation, etc. SiNWs

growth can be catalyzed by numerous catalyst metals. The electrical characteristics of SiNWs can be tuned by the choice of catalyst and process parameters like the type of doping gas, doping gas flow ratio, etc. Bottom-up approaches commonly have higher degree of freedom in nano-morphology control than that of top-down approaches. As the SiNWs are crystalline, they have energetic band diagram of crystalline silicon illustrated in Figure 1.1. It describes electron affinity, ionization potential and band-gap, having 4.05 eV, 5.17 eV and 1.12 eV at 300 K, respectively. Fermi level depends on the doping profile [21].

Figure 1.2 illustrates the optical characteristic of silicon film and SiNWs which was reported by Hu and Chen in 2007 [22]. SiNWs have quite different absorption curves compared to that of silicon thin film of same thickness. The nanowires have lower absorptance in lower photon energy while they show higher absorptance in higher photon energy regime compared to the thin-film. For the SiNWs, low energy photons under 2 eV are just weakly absorbed in spite of higher energy than band-gap of silicon. This is mainly attributed to the indirect band gap structure of crystalline silicon. The photon with higher energy than 2 eV, and it shows plateau region over 3 eV.

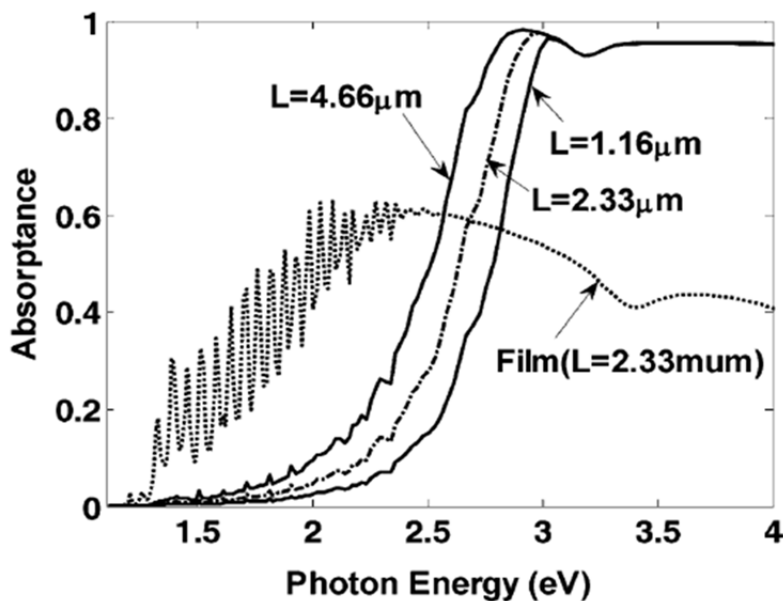


Figure 1.2 – Absorbance of silicon thin film and silicon nanowires as a function of photon energy of incident light [22].

Figure 1.3 shows examples of SiNWs fabricated by top-down and bottom-up approaches. SEM image and optical characteristic such as reflectance and absorption are reprinted from the references [23, 24]. Figure 1.3 (a) shows SiNWs by the etching of silicon wafer. It results in a considerable decrease of reflectance. In other words, incident light is well trapped in silicon wafer thanks to the nanowire structure which increases solar cell performance. On the other hands, PECVD grown SiNWs with a hydrogenated amorphous silicon covering are shown in Figure 1.3 (b). The nanowires enhance light-trapping in the hydrogenated amorphous silicon layer. The increase in absorption is observed with p-i-n structure. Optical characteristics of both types of SiNWs are modulated by changing their nano-morphology and dimensional properties such as length, diameter, density, etc.

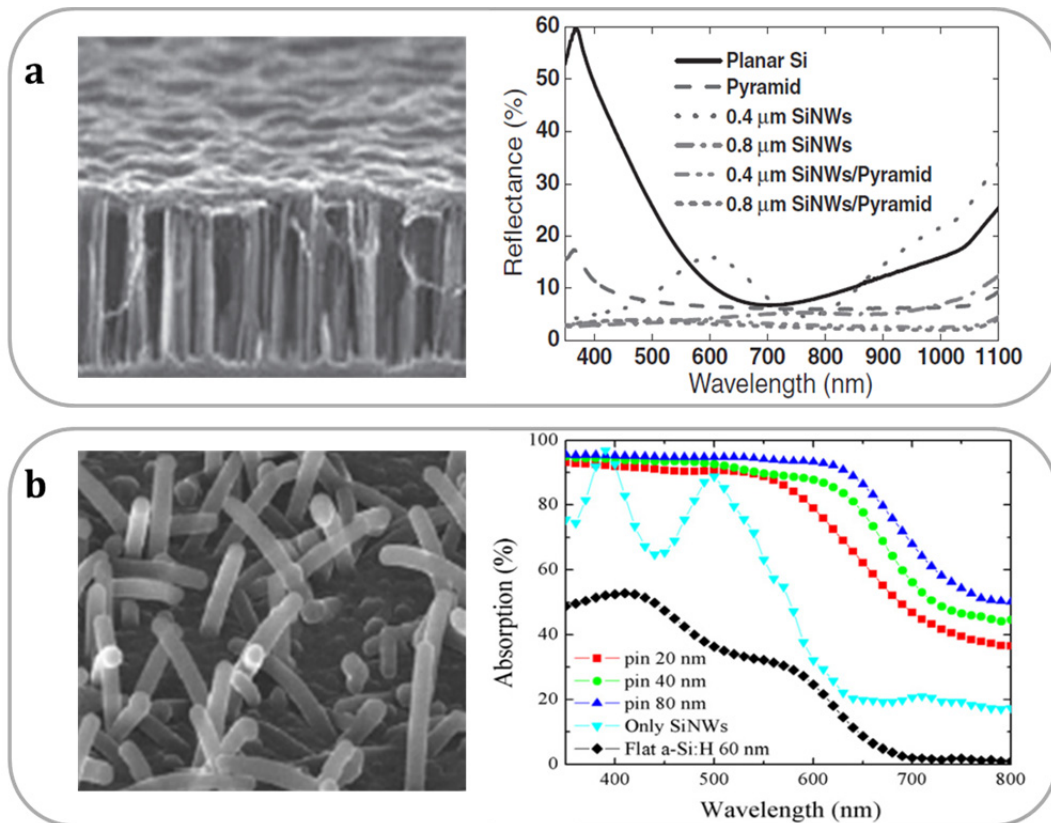


Figure 1.3 – Benefits of silicon nanowire fabricated by (a) etching of crystalline silicon [24] and (b) plasma-enhanced chemical vapor deposition [23].

1.2.2 Hydrogenated amorphous silicon

Hydrogenated amorphous silicon (a-Si:H) is a silicon material which has no periodic structure at all with hydrogen passivation of dangling bonds. It is still a fascinating light absorbing material for thin-film solar cells based on p-i-n or n-i-p structure due to its high absorption coefficient and easy fabrication on large and various substrates [23, 25, 26]. Since it has disordered structure, the optical and electrical characteristics quite differ from crystalline silicon. a-Si:H has 1.75 eV of band-gap and 1 μm thick of a-Si:H can absorb up to 90 % of incident light with the photon energy over band-gap energy. The band structure of a-Si:H is illustrated in Figure 1.4. The exponential band tails states on both conduction and valence bands and deep trap states are existed in the forbidden gap of a-Si:H unlike crystalline silicon. This band structure is originated from no periodic bonding structure of a-Si:H and dangle bonds. If intrinsic a-Si:H is doped by p- or n- type dopants, the defect density is more increased owing to the dopants. These mid-gap states could be liable for the degradation of device performance. For examples, it promotes the recombination of photo-generated carriers and increases resistive effects in solar cells.

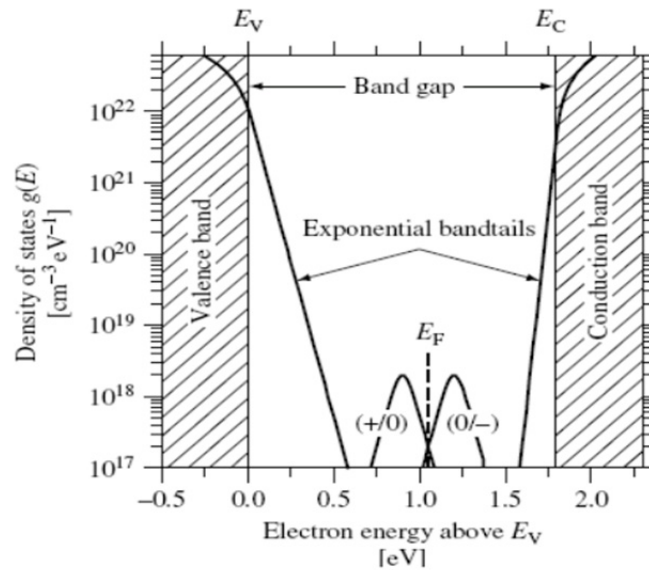


Figure 1.4 – Density of state of hydrogenated amorphous silicon. Exponential band tail states and deep states are illustrated [27].

It has to be taken into account that a-Si:H is co-deposited during the SiNWs growth by PECVD technique. a-Si:H could be preferentially deposited on the part of substrate without catalyst droplets by the physisorption (Chapter 2). Parasitic absorption and resistive effects are observed in our solar cells due to high absorption coefficient and high ionization potential (~ 5.7 eV) although it is good light absorbing material for p-i-n structure of a-Si:H (Chapter 4). These factors could veil benefits of SiNWs in our hybrid solar cell structure.

1.3 Organic semiconductor

1.3.1 π -conjugated system

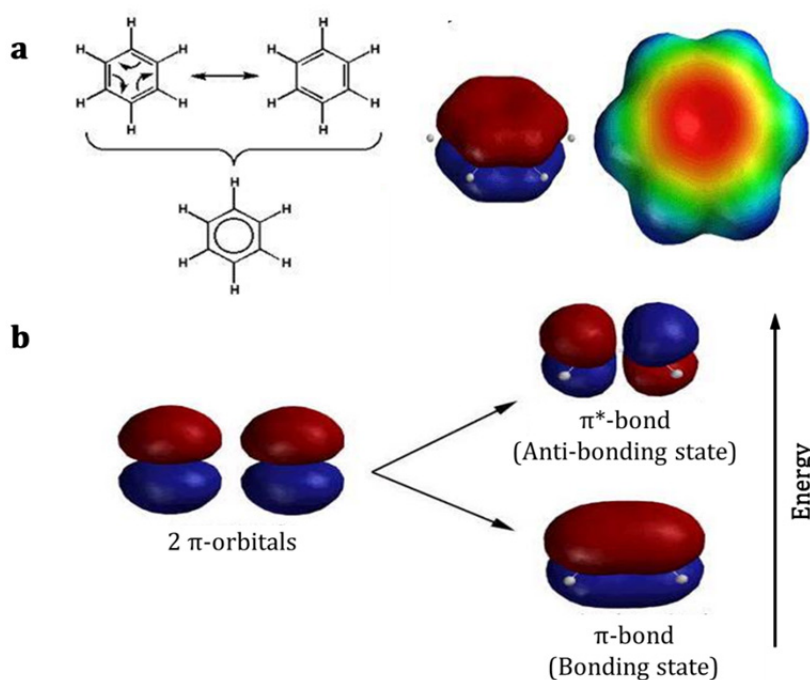


Figure 1.5 – Graphical description of π -conjugated system: (a) the example of Benzene (b) bonding between 2 π -orbitals. According to the wave function overlap, bonding and anti-bonding states are generated.

Most of organic materials are based on π -conjugation, namely, materials in which a single and a double or a single and a triplet bonds alternate

throughout a molecule or a polymer back bone. Figure 1.5 (a) shows a molecular structure and graphical configurations of the π -bonds of benzene as an example. The single bond represents a sigma bond and the double and triple bonds mean a sigma bond with one or two π -bond(s), respectively. Benzene has all p-orbitals within a ring. The overlapping between p-orbitals creates a delocalized electron cloud. In benzene ring, π -electrons are weakly nucleophilic as shown in the electrostatic potential surface by red color (on the right of Figure 1.5 (a)). According to the overlapping of wave functions, a bonding state and an anti-bonding state are generated in the energetic aspect illustrated in Figure 1.5 (b). They are called π - and π^* -bond, respectively. In case of the bonding state, the electrons move between two carbon atoms so that the state is stable. In contrast, the electrons move away from the center of two molecules in case of the anti-bonding state. Therefore, this state is unstable and has higher energy than that of the bonding-state. The bonding energy of π -bond is weaker than σ -bond. For the polymer, if the polymer back bone is existed along the x-axis, the π -bonds are formed by the overlapping of p_z or p_y orbitals. The electrons in the π -bond are free to roam on the molecule thanks to the π -conjugation. It is responsible for most of electronic and optical properties of the molecules and the polymers.

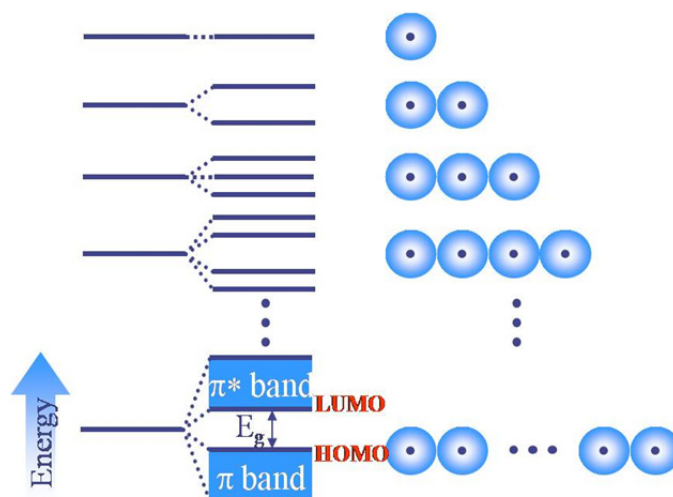


Figure 1.6 – Energy band formation in organic materials with increased number of atoms. π and π^* band is described with HOMO and LUMO levels.

In the device electronics, the concept of band is much practical. Figure 1.6 shows how the band structure is created. When the atoms or molecules are brought together, considerable overlap of atomic or molecular wave function is occurred. Thus, the energy levels are split as stated in the previous paragraph. As the number of atoms or molecules increases, namely, the number of added energy levels increases, the gap between the discrete energy levels becomes smaller. The gathering of discrete energy levels could be regarded as a continuous energy level, i.e., energy band. The continuous addition of p-orbitals forms the π - and π^* -band with a certain energy gap. Where the lowest state of the π^* -band is called LUMO (Lowest Unoccupied Molecular Orbital) and the highest state of π -band is called HOMO (Highest Occupied Molecular Orbital). The band gap (gap between LUMO and HOMO) decrease as the number of added molecules increase. A molecule or polymer has unique band gap according to the molecular configuration. The typical band gap ranges from 1.5 to 3 eV [28]. Energetically, favored electron excitation is from the HOMO to the LUMO. The larger the HOMO (LUMO) band-width generally results in the higher hole (electron) mobility.

1.3.2 P3HT and PCBM

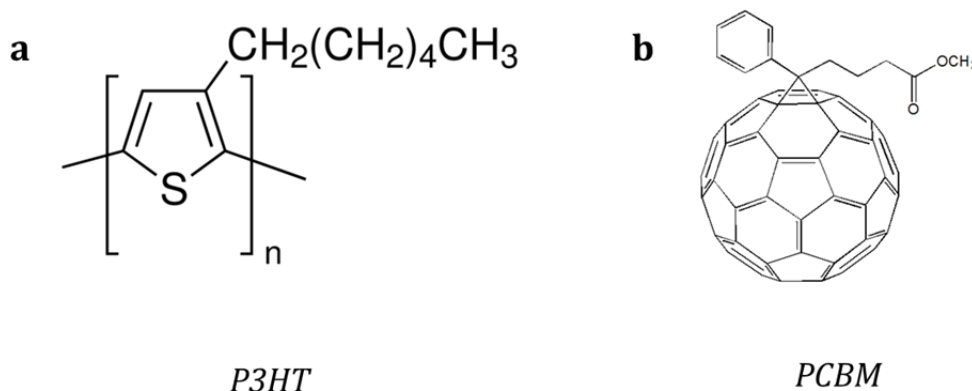


Figure 1.7 – Molecular structure of (a) P3HT and (b) PCBM

Poly(3-hexylthiophene), simply called P3HT, is the most popular conjugated polymer as a light absorbing material in organic solar cell. During

the last decade, it is mostly studied by more than 1,000 papers. Figure 1.7 (a) illustrates the molecular structure of P3HT. It is consisted of a thiophene ring backbone and a hexyl chain (C_6H_{13}). The regio-regularity of P3HT plays an important role for their crystallinity and solar cells performance. Generally, solar cells based on regio-regular P3HT exhibited better performance because high crystallinity enhances the optical absorption and the carrier transport [29]. In this study, the molecule with head-to-tail regio-regularity over 98 % is used for thin-film and solar cell fabrication. The number of conjugation 'n' in Figure 1.7 (a) has effects on molecular weight dependence of solar cell performance. P3HT shows high absorption coefficient of 10^5 cm^{-1} order which is comparable with a-Si:H [30]. It was reported that 95 % of the incident light could be absorbed in 240 nm thick P3HT [31]. Excitons, which are strongly bounded electron-hole pairs, are created by the light absorption of P3HT. The exciton diffuses toward interfaces and then it could be dissociated into a free electron and hole by the band-offset energy at the interface. The reported values of LUMO and HOMO of P3HT are differed from each other. The LUMO ranges from 2.6 eV to 3.5 eV, while the HOMO ranges from 4.7 eV to 5.2 eV [32-34]. Thus, the energy band-gap is 1.7 ~ 2.0 eV range. P3HT generally demonstrates hole mobility of $10^{-4} \text{ cm}^2/\text{V}\cdot\text{s}$ measured by the space-charge limited current [35].

Phenyl-C61-butyric acid methyl ester called PCBM is widely used as an electron acceptor in organic solar cells. PCBM is well known as the derivative of fullerene. It was first synthesized in 1995 by Hummelen et al [36]. Figure 1.7 (b) displays the molecular structure of PCBM. This is consisted of buckyball, which is fullerene, with an attached functional group. Due to the functional group, PCBM is soluble in various solvents such as chlorobenzene [37], dichlorobenzene [38], chloroform [39], toluene, etc [40]. PCBM has the absorption peak less than 400 nm of wavelength, thus it doesn't play a role of a main light absorbing material in solar cell. The LUMO level of PCBM ranges from 3.7 eV to 3.8 eV and the HOMO ranges from 5.5 eV to 5.9 eV. The energy levels of PCBM are preferred to dissociate excitons at the interface with P3HT or other organic semiconducting polymers [32-34].

The blend of both materials, P3HT:PCBM, is widely used for the active layer of organic bulk-heterojunction solar cells. As both materials are soluble, the thin-film is easily formed by solution process such as spin-coating, doctor blading from a prepared solution. Solar cell performance is strongly affected by the solvents, the blend ratio, the morphology, the thickness of active layer etc. Organic bulk-heterojunction solar cells based on the P3HT:PCBM blend system exhibits 3 % of solar cell efficiency in average [40].

1.3.3 PEDOT:PSS

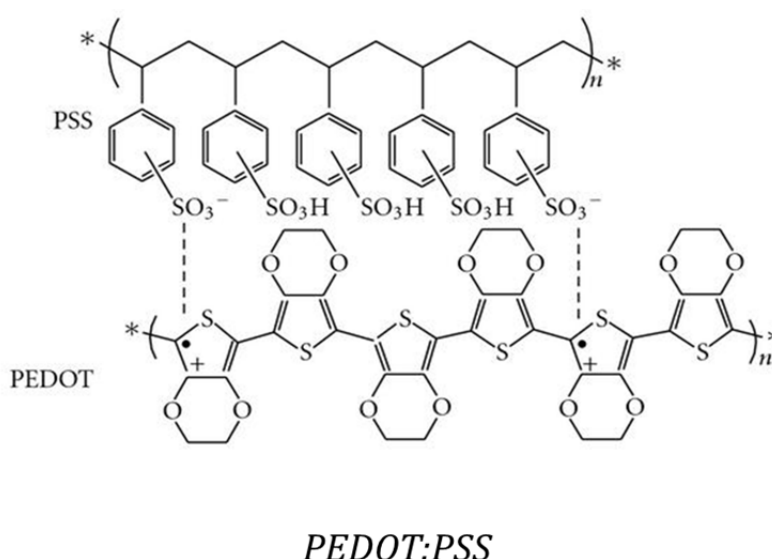


Figure 1.8 – Molecular structure of PEDOT:PSS

Poly(3,4-ethylenedioxythiophene) poly(styrenesulfonate) abbreviated to PEDOT:PSS is a transparent conducting polymer. For solar cell application, it is used as a buffer layer (hole injection layer) for the anode side [37, 41, 42]. Figure 1.8 illustrates the molecular structure of PEDOT:PSS. It is consisted of two parts, namely, PEDOT and PSS. PEDOT is a conjugated polymer based on polythiophene which transport positive charges. Meanwhile, PSS part is made by sulfonated polystyrene and sulfonyl groups conducting negative charges. The molecule is existed as the dispersion in water, thus, the films is formed by solution process like P3HT and PCBM.

The conductivity of PEDOT:PSS could be modified by adding solvents to pristine PEDOT:PSS solution [43, 44]. The added solvent leads to the conformational change of PEDOT:PSS. The bonding between PEDOT and PSS is broken and that is known as the prime reason of the increase in the conductivity. Pristine PEDOT:PSS demonstrates 0.1-10 S·cm⁻¹ range of the conductivity in literatures. But, it could be improved up to 10³ S·cm⁻¹ order of the conductivity by the solvent addition and post-treatment [44]. From results, PEDOT:PSS is also mentioned as a candidate for a solution processible anode in recent year.

1.4 Characterization of materials and solar cells

1.4.1 Scanning electron microscope

Scanning electron microscope (SEM) is an imaging technique used to characterize the surface of samples. Under the vacuum less than 10⁻⁵ Torr, the focused high energy electron beam scans the surface of samples. As the beam is negatively charged, it sensitively interacts with the specimen. Secondary electron, X-ray, Auger electron and back scattered electrons and cathodoluminescence (electron-induced luminescence from sample) are detected as signals by the interaction between sample and electron beam. In this study, secondary electron, which is the most common imaging mode for surface characterization, is used as the signal to image SiNWs and hybrid solar cells. By the inelastic scattering of electron beam with the sample, secondary electron is ejected from the k-shell of sample atoms. It could be generated within only a few nanometer depths from the sample's surface due to its low energy (under 50 eV).

The magnification of SEM ranges about 6 orders of magnitude, for examples, 10 to 500,000 times which is easily controlled by the modification of current of x, y scanning coils or voltage of x, y detector plate. In addition, SEM is able to produce high resolution images of sample's surface (1~5 nm). Therefore, SEM is useful for imaging numerous nanostructures. For example,

Figure 1.9 (a) and (b) show the SEM image of tin (Sn) and bismuth (Bi)-catalyzed SiNWs, respectively. Sn-catalyzed SiNWs exhibits straight and tapered shape. In contrast, Bi-catalyzed SiNWs shows winding shape. The difference in the appearance of SiNWs catalyzed by different metals is observable by taking SEM images.

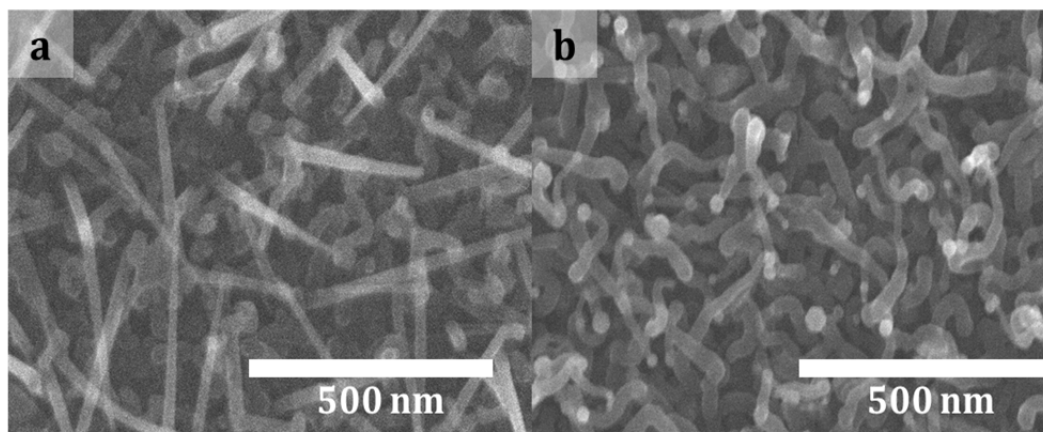


Figure 1.9 – Examples of SEM images: (a) Tin-catalyzed SiNWs (b) Bismuth-catalyzed SiNWs by PECVD

1.4.2 Raman spectroscopy

Raman spectroscopy is a spectroscopic method that is involved in vibrational spectroscopy domain, to reveal the molecular structure and characteristic by exploiting vibrational modes of the molecule. Raman spectroscopy is known as a simple nondestructive method suitable for nano-materials [45]. Monochromatic light, which is usually laser in visible region, is used as a probe to observe the vibrational modes. The incident monochromatic light into samples undergoes the inelastic scattering, namely, Raman scattering. On the pathway of the incident light through the sample, it can gain or lose the energy corresponding to the inherent vibrational energy of the samples. Also, it can be just passed the samples without energy change. The scattered light could possibly have energies; 1) higher (anti-stokes shift) 2) lower (stoke shift) than the incident light or 3) same (Rayleigh scattering) energy with it. By measuring the shifts, the molecule is characterized. In

general, stoke shift is mainly used due to higher intensity than others. Raman shifts are expressed using the equation given by

$$\Delta\nu = \left(\frac{1}{\lambda_0} - \frac{1}{\lambda} \right) \quad (1)$$

where $\Delta\nu$ is Raman shift which has unit of inverse length, λ_0 is the excitation wavelength and λ is Raman spectrum wavelength. In this study, Raman spectroscopy is employed to verify crystallinity of PECVD grown SiNWs and to characterize SiNWs array. Figure 1.10 shows Raman shift of Sn-catalyzed SiNWs as an example. It exhibits the peak of crystalline silicon at 518 cm^{-1} .

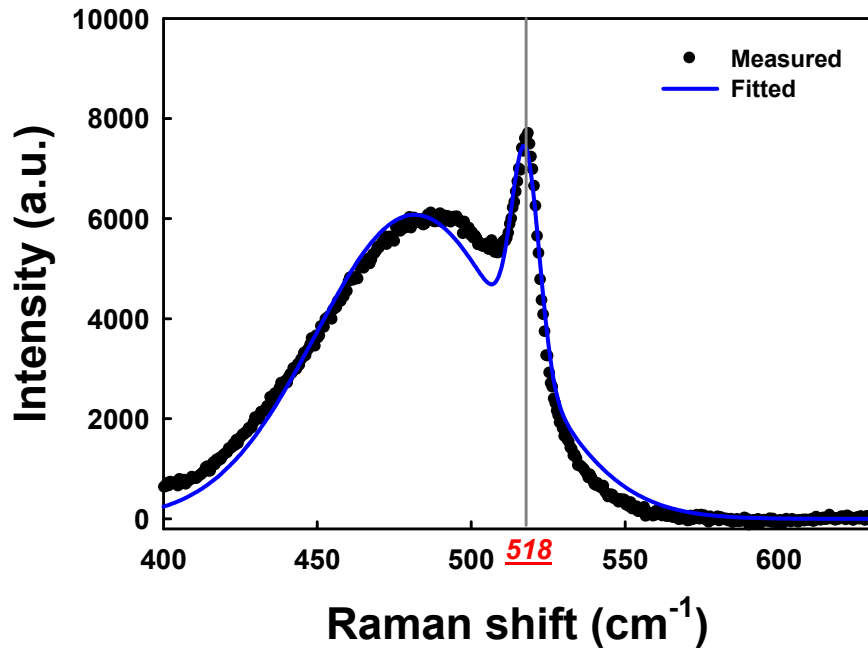


Figure 1.10 – Raman spectrum of Sn-catalyzed SiNWs. Crystal silicon peak is observed at 518 cm^{-1} with amorphous silicon peak (broad) at 480 cm^{-1} .

1.4.3 X-ray photoemission spectroscopy

X-ray photoemission spectroscopy called XPS is a spectroscopic approach to measure the elemental composition, the empirical formula and the electronic states of samples. XPS measures the kinetic energy and the number of electrons which are ejected (photoelectrons) from the samples by the X-ray irradiation. From 1 to 10 nm depth of samples could be analyzed under the ultra-high vacuum condition. The binding energy of the electron is extracted by the following equation.

$$E_{binding} = E_{photon} - (E_{kinetic} + \phi) \quad (2)$$

where E_{photon} is the energy of X-ray with particular wavelength, which is already known, $E_{kinetic}$ is the measured energy of electron and ϕ is work function of the spectrometer. The unique characteristic of electronic states is analyzed based on the electron binding energy. Here, XPS is employed to reveal the catalyst removal by hydrochloric acid treatment. The binding energy identifies metallic and oxidized catalysts. Besides, the count gives information for the catalyst removal in Chapter 4.

1.4.4 UV-Vis spectroscopy

The optical characteristics such as absorbance, transmittance and reflectance are closely related with the solar cell performance. UV-Vis spectroscopy measures the absorption or transmittance in UV-Vis region. Thin-films for solar cells such as P3HT and SiNWs can be characterized by measuring the absorbance of materials as a function of wavelength. The molecule undergoes an electrical transition from ground states to the one of discrete energy levels by absorbing the incident light. As a result, the received light at the detector differs from the incident light in terms of intensity after passing the sample. Absorbance is generally given by

$$A_{\lambda} = -\log \frac{I}{I_0} \quad (3)$$

where A_{λ} is the absorbance at a specific wavelength λ , I is the light intensity after passing a sample and I_0 is the intensity of incident light. From the absorbance equation, transmittance (I/I_0) could be extracted. Figure 1.11 shows the absorbance of SiNWs, P3HT:PCBM blend and SiNWs with P3HT:PCBM.

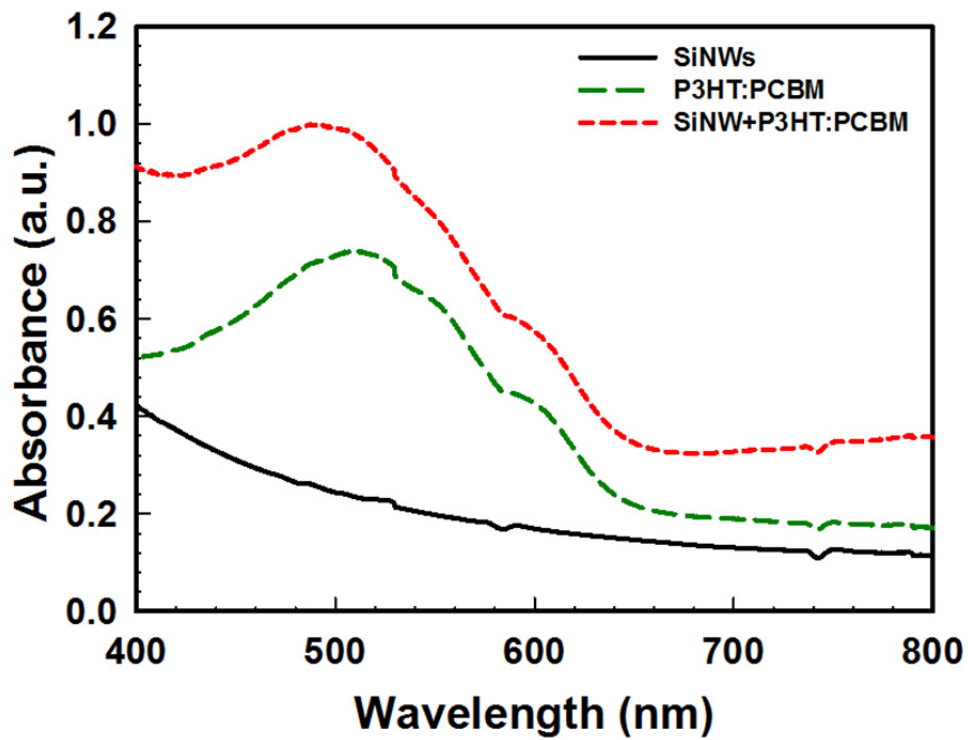


Figure 1.11 – Absorbance measured by UV-Vis spectroscopy. SiNWs, P3HT:PCBM and SiNWs with P3HT:PCBM are measured based on the same base line

1.4.5 Current-voltage characteristics of solar cells

The electrical characterization of solar cell gives the critical information for a diode, solar cell performance and various solar cell parameters. Typically, dark current density – voltage ($J_D - V$) and illumination current density – voltage ($J_L - V$) characteristics are measured. Because the solar cell is a diode, the diode characteristics can be explored by $J_D - V$ measurement. The ideal diode (zero resistance in forward bias regime and infinite resistance in reverse bias regime) equation is given by

$$J = J_0 \left[\exp \left(\frac{qV}{nk_B T} \right) - 1 \right] \quad (4)$$

where J_0 is the reverse saturation current, q is the electrical charge, V is an applied voltage, n is diode ideality factor, k_B is Boltzmann constant and T is the absolute temperature. By plotting the equation on natural logarithm plot, the linearity which could be extrapolated is normally found in the forward bias regime. From this linearity, slope (S) could be extracted for calculating the diode ideality factor and y-intercept giving the J_0 . Slope is extracted by the equation following

$$S = \frac{q}{nk_B T} \quad \text{thus, } n = \frac{q}{Sk_B T} \quad (5)$$

The larger slope results in the smaller diode ideality factor. As n is close to 1, the diode behavior is closer to that of the ideal diode.

To characterize the solar cell performance, $J_L - V$ characteristics are measured under the illumination of air mass (AM) 1.5 conditions which are universally employed like as a standard to characterize the solar cell performance. A solar simulator produces the similar illumination spectrum of AM 1.5. AM defines the optical path length through the atmosphere of Earth. As it travels, the sunlight undergoes the absorption and the scattering

by atoms and molecules in the atmosphere. As a result, the intensity of sunlight is attenuated. AM coefficient, which is a number following AM, characterizes the solar spectrum after the solar radiation has traveled through the atmosphere. Figure 1.12 illustrates the spectral irradiance of AM 0 and AM 1.5 as a function of wavelength. AM 0 is the spectrum of sunlight out of Earth's atmosphere. The AM 1.5G spectrum which is mostly used for the solar cell measurement is for the terrestrial applications. It includes the direct and diffuse light. And it integrates to 100 mW/cm^2 . The AM 1.5D spectrum is also for terrestrial applications but it includes direct light only. It integrates to 88.8 mW/cm^2 .

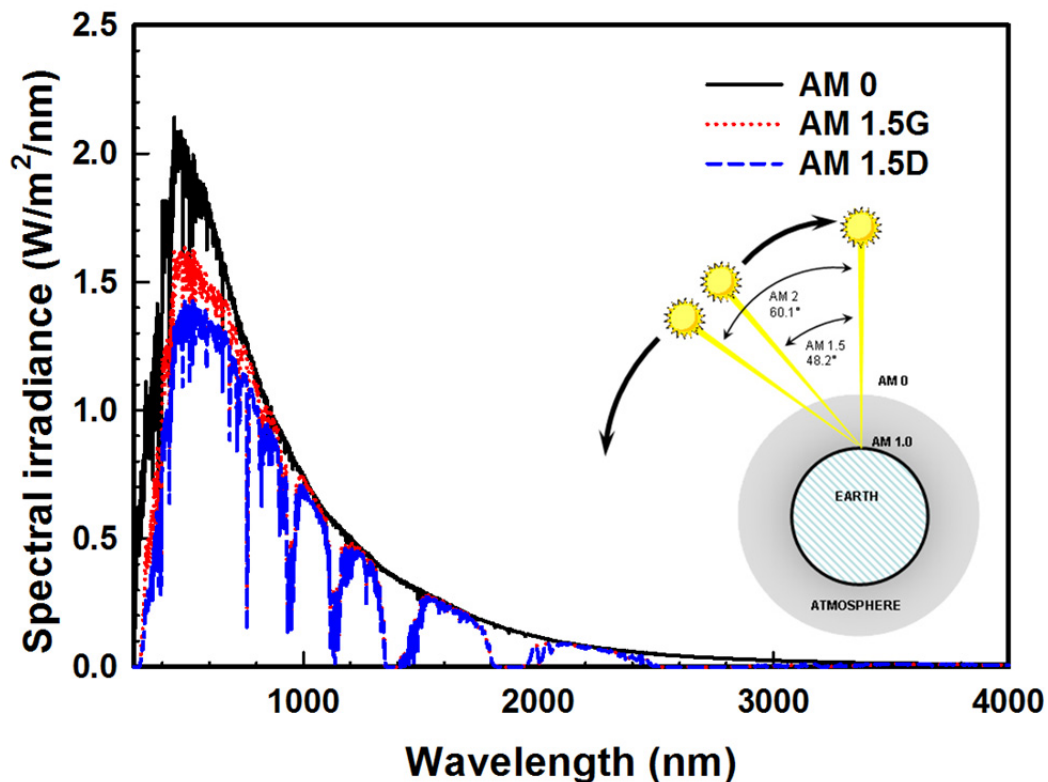


Figure 1.12 – Air mass; solar spectral irradiance as a function of wavelength Inset shows incident angle of sunlight relative to zenith (normal to the earth's surface).

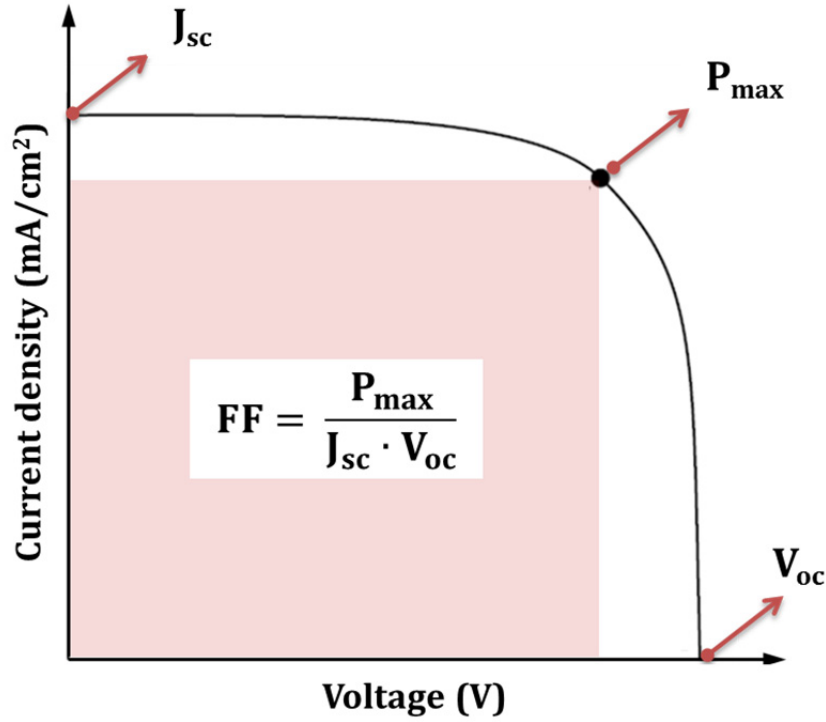


Figure 1.13 – A typical solar cell J-V curve with solar cell parameters.

Figure 1.13 illustrates a typical solar cell $J_L - V$ characteristic. Important solar cell parameters are noted in the figure. Short-circuit current density (J_{sc}) represents the generated current density under AM 1.5 illumination when applied voltage equals zero ($V=0$, short-circuited). J_L can be ideally expressed as the equation given by

$$J_L = J_{ph} + J_0 \left[\exp\left(\frac{qV}{nk_B T}\right) - 1 \right] \quad (6)$$

where J_{ph} is photo-current density which depends on the materials, device structures, the power of incident light, etc. However, the practical model of J_{sc} which contains series (R_s) and shunt (R_{sh}) resistance can be redefined based on the equivalent circuit model with resistance.

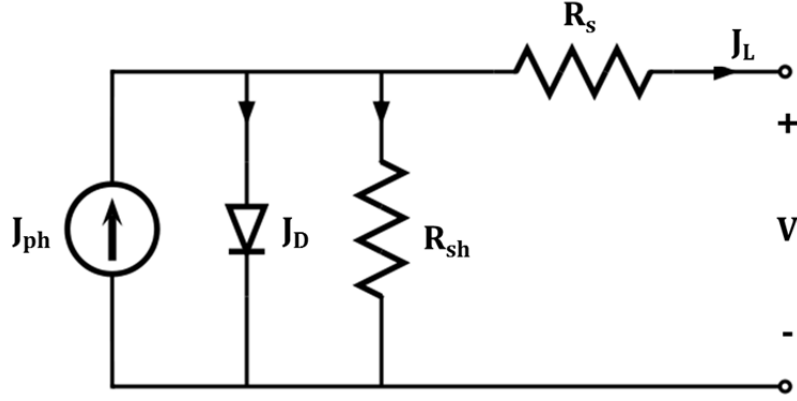


Figure 1.14 – Equivalent circuit model of solar cell consisted of constant current source, diode, series and shunt resistance.

Figure 1.14 illustrates an equivalent circuit model of the solar cell. A diode is connected in parallel with J_{ph} (a constant current source) and R_{sh} . Also it has series connection with R_s . From this equivalent circuit, J_L is expressed by

$$J_L = J_{ph} + J_0 \left[\exp \left(\frac{qV}{nk_B T} \right) - 1 \right] - \frac{V - J R_s}{R_{sh}} \quad (7)$$

Last term in this equation is called the shunt current which depends on both resistance values. If R_s and R_{sh} approach to zero and infinity respectively, the diode is the ideal diode. But in general, this shunt current can govern total J_L in the inverse case.

Open-circuit current (V_{oc}) is defined as the voltage without current flow in the solar cell ($J_L=0$, open-circuited). In other words, the same amounts of dark and photo currents flow in reverse direction each other. V_{oc} is given by

$$V_{oc} = \frac{k_B T}{q} \ln \left(\frac{J_{ph}}{J_0} + 1 \right) \quad (8)$$

Fill factor (FF) is defined as the ratio of the maximum power (P_{\max}) to the product of the J_{sc} and the V_{oc} which is given by the equation in Figure 1.13 inset. FF is always less than 1. FF is severely affected by resistive effects. It means that FF is improved with the increase in R_{sh} and the decrease in R_s .

The power conversion efficiency (η) is the most effective parameter describing solar cell performance. It is defined as the ratio of energy output from the solar cell to input energy from the sun. η is written as an equation based on the solar cell parameters introduced above.

$$\eta = \frac{J_{sc} \cdot V_{oc} \cdot FF}{P_{light}} \quad (9)$$

where P_{light} is the power of incident light. Typically, P_{light} of 100 mW/cm² is used as a standard.

1.5 Hybrid solar cells based on silicon and organic materials

Conventional silicon solar cells based on p-n junction showed high efficiency about 25 %. However, the high fabrication cost due to crystalline silicon wafer and high temperature process is a barrier for wide use. Organic materials are interesting in terms of fabrication costs because solution processes are possible at room temperature. However, the energy conversion efficiency of organic solar cells is evidently lower (11 %) than silicon based solar cells [46]. Hybrid solar cell is an approach which aims at the low cost and high efficiency solar cell. Basically, there are two kinds of approaches for hybrid solar cells. First, the organic materials are used to improve cost-efficiency of silicon based solar cells. PEDOT:PSS [20, 47, 48], P3HT [3] and Spiro-OMETAD [13] are generally deposited by the solution process. Second, many different types of silicon, such as crystalline silicon wafer [49], thin-films [50], nanocrystals [51], nanorods [13] and nanowires [4, 20, 52], are integrated with organic semiconducting polymers. The silicon materials could improve the efficiency by efficient exciton separation and rapid charge transport (compensation of low mobility of organic materials). The hybrid solar cells based on silicon and organic materials can be classed into three different types according to the main light absorbing material.

	Type 1	Type 2	Type 3
Light absorbing material(s)	Silicon	Organic semiconducting polymer	Both
Photo-carrier generation by	Electric field in silicon	Band energy offset at interface	Both
Efficiency	~ 10 %	0.1 ~ 1.5 %	2 ~ 6 %

Table 1.1 – Summary of types of hybrid solar cells based on light absorbing materials.

Table 1.1 summarizes the types of hybrid solar cells and related factors. Type 1 hybrid solar cell employs silicon as the main light absorbing material. Organic materials are used to create the built-in potential in silicon and to transport photo-generated carriers. Here, a key point is how many photo-generated carriers in silicon can be efficiently collected by the organic material. Therefore, the conductivity of organic material and surface states of silicon are significantly important. Figure 1.15 shows an example of Type 1 solar cells presented by Jeong et al [53]. It bases on silicon nanocone fabricated by the colloidal lithography of n-type silicon wafer to decrease reflectance of silicon surface. The p-n junction is formed by depositing PEDOT:PSS by a solution process (Figure 1.15 (a)). The incident light from top side is mainly absorbed by silicon through highly transparent 60 nm thick PEDOT:PSS. Silicon nanocone generates electron-hole pairs which are separated by the built-in potential created by PEDOT:PSS [49]. Photo-generated holes are transferred from silicon to PEDOT:PSS. It demonstrated high J_{sc} of 30 mA/cm². The efficiency reaches 11 % (Figure 1.15 (b)). This approach lowers the cost of fabrication compared to conventional silicon p-n junction solar cell owing to the solution process at room temperature. Type 1 hybrid solar cells normally show higher efficiency than that of other types due to the use of silicon wafer.

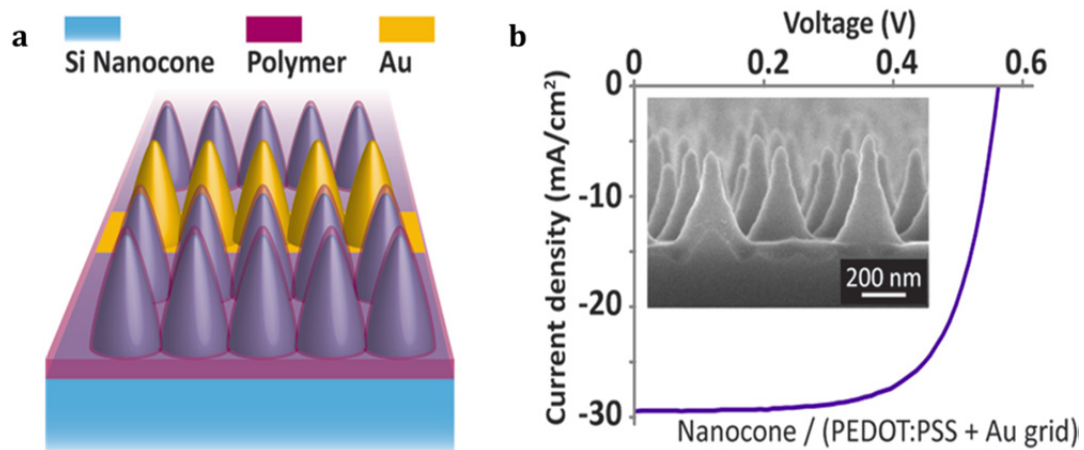


Figure 1.15 – The example of type 1 hybrid solar cell based on n-type silicon nanocone and PEDOT:PSS. (a) solar cell structure and (b) solar cell performance (reprinted from Ref. [53])

Type 2 hybrid solar cells are used organic semiconducting polymers, which create excitons by light absorption, as a main absorber. Silicon is employed as an electron acceptor. Thus, Type 2 solar cell is an excitonic solar cell [54]. For the high power conversion efficiency, the efficient exciton separation and the carrier transport are important. Figure 1.16 illustrates one of Type 2 solar cells based on P3HT absorber and silicon nanocrystals (SiNCs) reported by Liu et al [51]. The solar cell is constructed like organic bulk-heterojunction solar cells from the blend of P3HT and SiNCs (Figure 1.16 (a)). Figure 1.16 (b) clearly showed that the absorbance of the blend imitates the absorbance of P3HT. Surely, P3HT plays a role of the main light absorbing material. The excitons generated in P3HT are dissociated at the interface with SiNCs. The solar cell performance is altered by the concentration of SiNCs which is concerned with the interface area, the percolated pathway, the absorption of SiNCs, etc. Despite of low cost process and materials, the efficiency is seriously limited to 1 % (Figure 1.16 (c)). Among solar cell parameters, J_{sc} is quite lower compared to that of Type 1 hybrid solar cells.

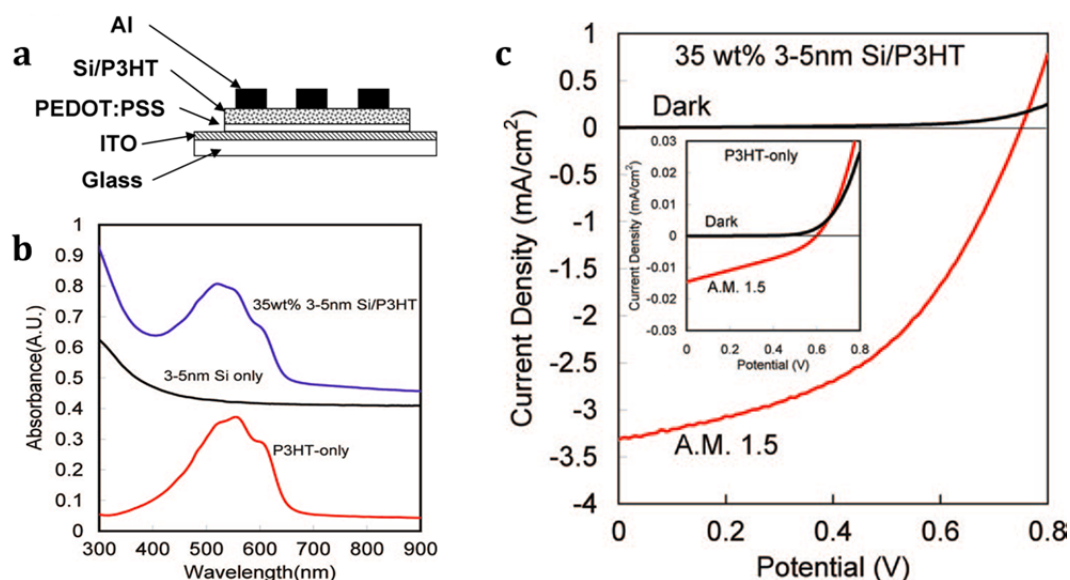


Figure 1.16 – The example of type 2 hybrid solar cells based on P3HT and silicon nanocrystals. (a) solar cell structure (b) absorbance and (c) solar cell performance. (reprinted from Ref. [51])

Type 3 hybrid solar cells are also available. Some solar cell devices are not easy to determine main absorber because they employed both silicon and organic material that show the efficient light absorption. In this case, both types' (Type 1 and 2) characteristics can be observable. It means that the incident light is absorbed in both materials and electron-holes pair and excitons are generated in silicon and organic semiconducting polymers, respectively. Figure 1.17 shows an example of type 3 hybrid solar cells reported by Zhang et al [3]. P3HT is deposited on nanostructured n-type silicon wafer by spin-coating of P3HT dissolved in chlorobenzene with 15 mg/mL concentration. P3HT and silicon wafer carry photo-generated holes and electrons, respectively. In this paper, P3HT plays a dominant role on the hydrogen terminated silicon surface. But, the efficiency is only 0.006 %. A surface modification of silicon strongly changed the trend of external quantum efficiency. Methyl-terminated silicon improves power conversion efficiency up to 5.9 % by the efficient collection of photo-generated holes from silicon. J_{sc} is considerably raised from 0.031 to 26.2 mA/cm². Another report on Type 3 hybrid solar cells based on a-Si:H and organic semiconducting polymers demonstrated lower efficiency (2~3 %) than that of crystalline silicon based solar cells [25, 26]. From this fact, the efficiency might be dominantly governed by silicon part.

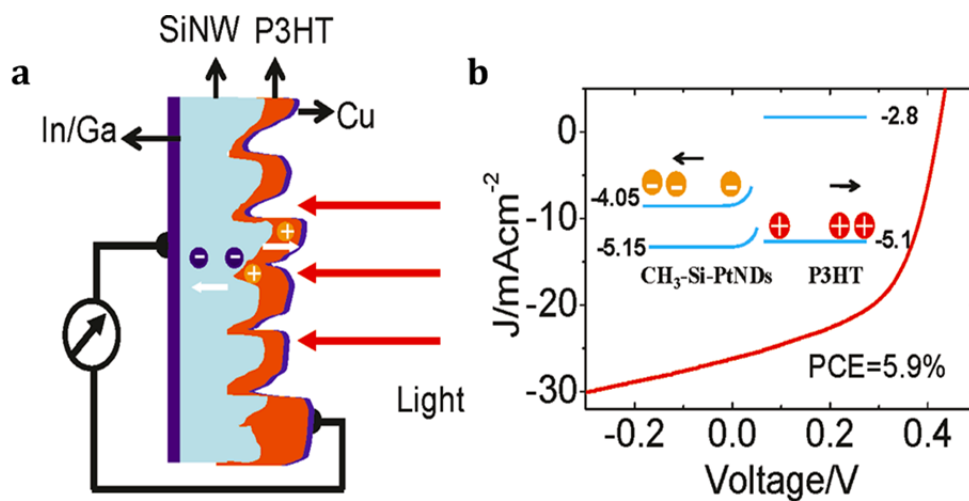


Figure 1.17 - The example of type 3 hybrid solar cell based on n-type silicon wafer and P3HT. (a) solar cell structure and (b) solar cell performance (reprinted from Ref. [3])

The three different types of hybrid solar cells using silicon and organic materials have been explored. The power conversion efficiency is mostly dependent on the main light absorbing material. The hybrid solar cells based on silicon absorber demonstrated the higher efficiency than that of the hybrid solar cells based on organic polymer absorber. However, the hybrid solar cell based on crystalline wafer should be avoided for the next-generation of solar cells due to the cost efficiency. The organic semiconducting polymers could be potential alternatives to silicon absorber. They have advantages of the tuning of molecule by synthesis, the high absorption coefficient and the easy fabrication process. Nevertheless, researches on the hybrid solar cell with organic semiconducting polymer as an absorber still have a long way to go regard to the efficiency improvement and the understanding of device physics.

1.6 Approaches of thesis

In this thesis, we investigated the integration of organic semiconducting polymer with PECVD grown SiNWs for a hybrid solar cell application. The hybrid solar cells based on P3HT absorber and SiNWs were fabricated. It is classed as Type 2 hybrid solar cell since P3HT showed dominant light absorption than SiNWs. PECVD grown SiNWs by Sn or Bi catalysts clearly showed the difference in their nano-morphology. According to their morphologies, hybrid solar cells are designed with the different role of SiNWs.

First, we explored the potential application of SiNWs as light trapping media. In this purpose, the blend of P3HT and PCBM was spin-coated on Sn-catalyzed SiNWs as an organic light absorbing material. The nanowires are not concerned in exciton dissociation because they are separated from the organic active layer by PEDOT:PSS. The SiNWs mainly concern with the light trapping and the extraction of photo-generated holes from the organic layer. Particularly, the correlation of the quality of SiNWs with solar cell performances in optical and electrical aspects is focused in Chapter 4.

Second, the investigations on hybrid heterojunction were performed based on P3HT and Bi-catalyzed and Bi-doped SiNWs. The ideal structure (large area of interface and electron/hole transport pathway) is available due to the nanostructure given by the SiNWs. Since Bi-catalyzed SiNWs exhibited the electrical n-type nature, they were employed as an electron acceptor to take electrons from P3HT. The exciton dissociation would be a key role of Bi-catalyzed SiNWs. The solar cell performance is discussed in Chapter 5.

REFERENCE

1. Chapin, D.M., C.S. Fuller, and G.L. Pearson, *A New Silicon p-n Junction Photocell for Converting Solar Radiation into Electrical Power*. Journal of Applied Physics, 1954. **25**(5): p. 676-677.
2. Liu, C.-Y., Z.C. Holman, and U.R. Kortshagen, *Optimization of Si NC/P3HT Hybrid Solar Cells*. Advanced Functional Materials, 2010. **20**(13): p. 2157-2164.
3. Zhang, F.T., et al., *Air Stable, Efficient Hybrid Photovoltaic Devices Based on Poly(3-hexylthiophene) and Silicon Nanostructures*. Chemistry of Materials, 2011. **23**(8): p. 2084-2090.
4. Kuo, C.Y. and C. Gau, *Arrangement of band structure for organic-inorganic photovoltaics embedded with silicon nanowire arrays grown on indium tin oxide glass*. Applied Physics Letters, 2009. **95**(5): p. 053302-3.
5. Golap, K. and et al., *Silicon nanowire array/polymer hybrid solar cell incorporating carbon nanotubes*. Journal of Physics D: Applied Physics, 2009. **42**(11): p. 115104.
6. Garnett, E.C., et al. *Silicon nanowire hybrid photovoltaics*. in *Photovoltaic Specialists Conference (PVSC), 2010 35th IEEE*. 2010.
7. Garnett, E.C. and P. Yang, *Silicon Nanowire Radial p-n Junction Solar Cells*. Journal of the American Chemical Society, 2008. **130**(29): p. 9224-9225.
8. Tsakalakos, L., et al., *Silicon nanowire solar cells*. Applied Physics Letters, 2007. **91**(23): p. 233117-3.
9. Syu, H.-J., S.-C. Shiu, and C.-F. Lin, *Silicon nanowire/organic hybrid solar cell with efficiency of 8.40%*. Solar Energy Materials and Solar Cells, 2012. **98**(0): p. 267-272.
10. Davenas, J., et al., *Silicon nanowire/poly(3-hexylthiophene) hybrids for thin film solar cells*. Journal of Non-Crystalline Solids, 2012. **358**(17): p. 2534-2536.
11. Th, S. and et al., *Silicon nanowire-based solar cells*. Nanotechnology, 2008. **19**(29): p. 295203.
12. Cho, J., et al., *Sn-catalyzed silicon nanowire solar cells with 4.9% efficiency grown on glass*. Progress in Photovoltaics: Research and Applications, 2012:
13. He, L., et al., *Highly efficient Si-nanorods/organic hybrid core-sheath heterojunction solar cells*. Applied Physics Letters, 2011. **99**(2): p. 021104-3.
14. Huynh, W.U., J.J. Dittmer, and A.P. Alivisatos, *Hybrid Nanorod-Polymer Solar Cells*. Science, 2002. **295**(5564): p. 2425-2427.
15. Qu, Y. and X. Duan, *One-dimensional homogeneous and heterogeneous nanowires for solar energy conversion*. Journal of Materials Chemistry, 2012. **22**(32): p. 16171-16181.

16. Treuting, R.G. and S.M. Arnold, *Orientation habits of metal whiskers*. Acta Metallurgica, 1957. **5**(10): p. 598.
17. Wagner, R.S. and W.C. Ellis, *Vapor-Liquid-Solid Mechanism of Single Crystal Growth*. Applied Physics Letters, 1964. **4**(5): p. 89-90.
18. Schmidt, V., et al., *Silicon Nanowires: A Review on Aspects of their Growth and their Electrical Properties*. Advanced Materials, 2009. **21**(25-26): p. 2681-2702.
19. Garnett, E. and P. Yang, *Light Trapping in Silicon Nanowire Solar Cells*. Nano Letters, 2010. **10**(3): p. 1082-1087.
20. Syed Abdul, M., et al., *A stamped PEDOT:PSS-silicon nanowire hybrid solar cell*. Nanotechnology, 2012. **23**(14): p. 145401.
21. Sze, S.M. and M.K. Lee, *Semiconductor Devices: Physics and Technology* 2012: Wiley.
22. Hu, L. and G. Chen, *Analysis of Optical Absorption in Silicon Nanowire Arrays for Photovoltaic Applications*. Nano Letters, 2007. **7**(11): p. 3249-3252.
23. Linwei, Y., et al., *Radial junction amorphous silicon solar cells on PECVD-grown silicon nanowires*. Nanotechnology, 2012. **23**(19): p. 194011.
24. He, L., et al., *High-Efficiency Si/Polymer Hybrid Solar Cells Based on Synergistic Surface Texturing of Si Nanowires on Pyramids*. Small, 2012. **8**(11): p. 1664-1668.
25. Pei, Z., et al., *An amorphous silicon random nanocone/polymer hybrid solar cell*. Solar Energy Materials and Solar Cells. 2011. **95**(8): p. 2431-2436.
26. Chao, C.-H., et al., *Efficient hybrid organic/inorganic photovoltaic cells utilizing n-type pentacene and intrinsic/p-type hydrogenated amorphous silicon*. Solar Energy Materials and Solar Cells, 2011. **95**(8): p. 2407-2411.
27. Chopra, K.L., P.D. Paulson, and V. Dutta, *Thin-film solar cells: an overview*. Progress in Photovoltaics: Research and Applications, 2004. **12**(2-3): p. 69-92.
28. Pope, M. and C.E. Swenberg, *Electronic processes in organic crystals and polymers* 1999: Oxford University Press.
29. Kim, Y., et al., *A strong regioregularity effect in self-organizing conjugated polymer films and high-efficiency polythiophene:fullerene solar cells*. Nat Mater, 2006. **5**(3): p. 197.
30. Kim, Y. and D.D.C. Bradley, *Bright red emission from single layer polymer light-emitting devices based on blends of regioregular P3HT and F8BT*. Current Applied Physics, 2005. **5**(3): p. 222-226.
31. Coakley, K.M. and M.D. McGehee, *Conjugated Polymer Photovoltaic Cells*. Chemistry of Materials, 2004. **16**(23): p. 4533-4542.
32. Dietmueller, R., et al., *Light-induced charge transfer in hybrid composites of organic semiconductors and silicon nanocrystals*. Applied Physics Letters, 2009. **94**(11): p. 113301-3.

-
33. Al-Ibrahim, M., et al., *The influence of the optoelectronic properties of poly(3-alkylthiophenes) on the device parameters in flexible polymer solar cells*. Organic Electronics, 2005. **6**(2): p. 65-77.
34. Chirvase, D., et al., *Electrical and optical design and characterisation of regioregular poly(3-hexylthiophene-2,5-diyl)/fullerene-based heterojunction polymer solar cells*. Synthetic Metals, 2003. **138**(1-2): p. 299-304.
35. Mihailetchi, V.D., et al., *sCharge Transport and Photocurrent Generation in Poly(3-hexylthiophene): Methanofullerene Bulk-Heterojunction Solar Cells*. Advanced Functional Materials, 2006. **16**(5): p. 699-708.
36. Hummelen, J.C., et al., *Preparation and Characterization of Fulleroid and Methanofullerene Derivatives*. The Journal of Organic Chemistry, 1995. **60**(3): p. 532-538.
37. Kim, Y., et al., *Effects of thickness and thermal annealing of the PEDOT:PSS layer on the performance of polymer solar cells*. Organic Electronics, 2009. **10**(1): p. 205-209.
38. Jeon, T., et al., *Effects of acid-treated silicon nanowires on hybrid solar cells performance*. Solar Energy Materials and Solar Cells, 2013. **117**: p. 632-637.
39. Wienk, M.M., et al., *Narrow-Bandgap Diketo-Pyrrolo-Pyrrole Polymer Solar Cells: The Effect of Processing on the Performance*. Advanced Materials, 2008. **20**(13): p. 2556-2560.
40. Dang, M.T., L. Hirsch, and G. Wantz, *P3HT:PCBM, Best Seller in Polymer Photovoltaic Research*. Advanced Materials, 2011. **23**(11): p. 3579-3602.
41. Ikenoue, T., H. Nishinaka, and S. Fujita, *Fabrication of conducting poly(3,4-ethylenedioxythiophene): poly(styrenesulfonate) thin films by ultrasonic spray-assisted mist deposition method*. Thin Solid Films, 2012. **520**(6): p. 1978-1981.
42. Hammond, S.R., et al., *Low-temperature, solution-processed molybdenum oxide hole-collection layer for organic photovoltaics*. Journal of Materials Chemistry, 2012. **22**(7): p. 3249-3254.
43. Kim, J.Y., et al., *Enhancement of electrical conductivity of poly(3,4-ethylenedioxythiophene)/poly(4-styrenesulfonate) by a change of solvents*. Synthetic Metals, 2002. **126**(2-3): p. 311-316.
44. Kim, Y.H., et al., *Highly Conductive PEDOT:PSS Electrode with Optimized Solvent and Thermal Post-Treatment for ITO-Free Organic Solar Cells*. Advanced Functional Materials, 2011. **21**(6): p. 1076-1081.
45. Kawashima, T., et al., *Raman Scattering Studies of Electrically Active Impurities in in Situ B-Doped Silicon Nanowires: Effects of Annealing and Oxidation*. The Journal of Physical Chemistry C, 2007. **111**(42): p. 15160-15165.
46. NREL, *Research Cell Efficiency Records*. 2013.

47. Avasthi, S., et al., *Role of Majority and Minority Carrier Barriers Silicon/Organic Hybrid Heterojunction Solar Cells*. Advanced Materials, 2011. **23**(48): p. 5762-5766.
48. He, L., et al., *Si Nanowires Organic Semiconductor Hybrid Heterojunction Solar Cells Toward 10% Efficiency*. ACS Applied Materials & Interfaces, 2012. **4**(3): p. 1704-1708.
49. He, L., et al., *High efficiency planar Si/organic heterojunction hybrid solar cells*. Applied Physics Letters, 2012. **100**(7): p. 073503-3.
50. Gowrishankar, V., et al., *Exciton harvesting, charge transfer, and charge-carrier transport in amorphous-silicon nanopillar/polymer hybrid solar cells*. Journal of Applied Physics, 2008. **103**(6): p. 064511-8.
51. Liu, C.-Y., Z.C. Holman, and U.R. Kortshagen, *Hybrid Solar Cells from P3HT and Silicon Nanocrystals*. Nano Letters, 2008. **9**(1): p. 449-452.
52. Huang, J.-S., et al., *Well-aligned single-crystalline silicon nanowire hybrid solar cells on glass*. Solar Energy Materials and Solar Cells, 2009. **93**(5): p. 621-624.
53. Jeong, S., et al., *Hybrid Silicon Nanocone–Polymer Solar Cells*. Nano Letters, 2012. **12**(6): p. 2971-2976.
54. Gregg, B.A., *Excitonic Solar Cells*. The Journal of Physical Chemistry B, 2003. **107**(20): p. 4688-4698.

Chapter 2

PECVD GROWTH OF SiNWs AND NANO-MORPHOLOGY

2.1 INTRODUCTION	34
2.2 PLASFIL SYSTEM (PECVD).....	35
2.3 VLS GROWTH OF SiNWS AND CATALYST CHOICE.....	37
2.4 SN-CATALYZED SiNWS	41
2.4.1. GROWTH TIME DEPENDENCE.....	43
2.4.2. DENSITY CONTROL BY H ₂ PLASMA	46
2.5 BI-CATALYZED SiNWS.....	49
2.5.1. N-TYPE CHARACTERISTIC OF BI-CATALYZED SiNWS	50
2.5.2. TEMPERATURE DEPENDENCE	51
2.5.3. RF POWER DEPENDENCE.....	54
2.5.4. GAS FLOW RATIO DEPENDENCE	56
2.6 CONCLUSION: PROPER USE OF EACH SiNWS.....	60
2.6.1. SN-CATALYZED SiNWS	60
2.6.2. BI-CATALYZED SiNWS	61
<i>REFERENCE</i>	<i>63</i>

2.1 Introduction

Silicon nanowires (SiNWs) are drawing substantial attentions as a promising nano-material for next-generation solar cells. The fabrication techniques of the SiNWs are classified into two categories, namely, top-down and bottom-up approaches. Figure 2.1 shows SEM images of the SiNWs fabricated by various methods. The nanowires depicted in Figure 2.1 (a) and (b) are fabricated by reactive ion etching and metal-catalyzed electro-less etching of silicon, respectively [1, 2]. These top-down methods have the advantages in SiNWs' quality. In other words, they conserve electrical characteristics of mother silicon wafer like doping profile. Moreover, the morphology of SiNWs is much uniform than bottom-up grown SiNWs in terms of crystal orientation, density, shape, etc. In spite of these merits, the cost of silicon wafer is still expensive and the benefits of these types of SiNWs in hybrid solar cell are still in question with regard to power conversion efficiency [3-7].

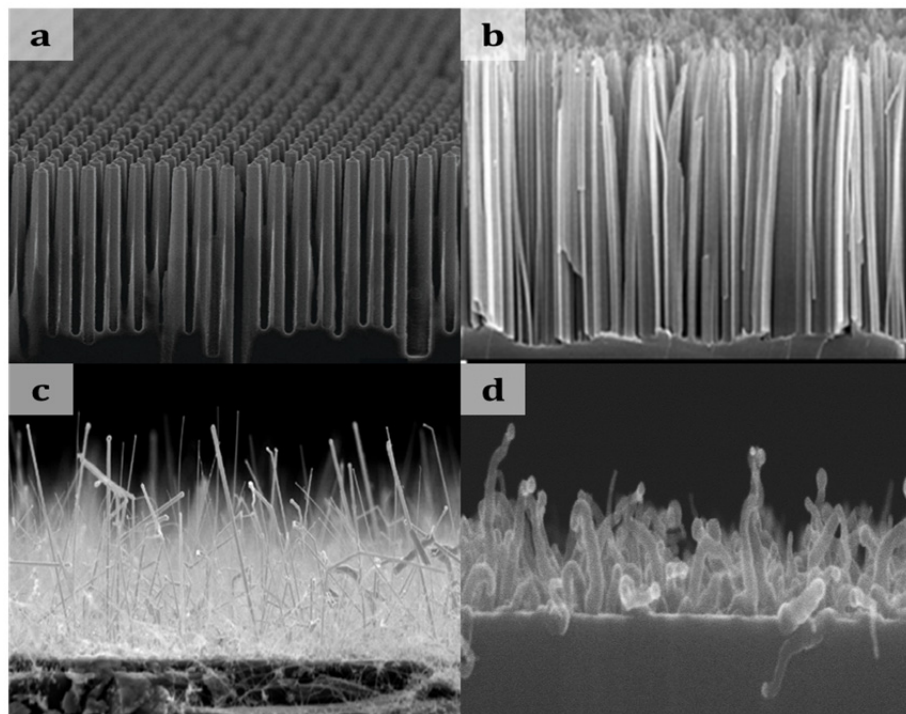


Figure 2.1 – SEM images of SiNWs fabricated by top-down (TD) approaches and bottom-up (BU) approaches. (a) reactive ion etching [1] (TD) (b) metal-catalyzed electro-less etching [2] (TD) (c) chemical vapor deposition (BU) [8] (d) plasma-enhanced chemical vapor deposition (BU) (this work)

Meanwhile, the nanowires shown in Figure 2.1 (c) and (d) are synthesized by chemical vapor deposition (CVD) and plasma-enhanced chemical vapor deposition (PECVD), respectively. The bottom-up approaches are considered as low-cost alternatives even though the low quality of SiNWs is pointed out as a shortage for the chemical growth [9]. These approaches have the higher degree of freedom to tune SiNWs by changing catalyst, doping concentration, density, length and diameter which are closely related with the electrical and optical characteristics of the nanowires. Thus, the growth of SiNWs by bottom-approaches is attractive for next generation solar cells.

This chapter mainly discusses the PECVD growth of SiNWs by post-transition metal catalysts and the control of their nano-morphology for hybrid solar cell application. Generally, the post-transition metal catalysts don't studied widely and it is recognized unusual choice. Despite of these facts, our laboratory constructs know-how for the growth and the control of post-transition catalyzed SiNWs based on Indium (In) , Tin (Sn) and Bismuth (Bi) [10-17]. Here, Sn and Bi are chosen for PECVD growth of SiNWs. The nanowires could be used as light trapping media and/or an electron acceptor in our solar cells depending on their electrical characteristics and nano-morphologies. The effect of growth time and the density control by hydrogen plasma are discussed for Sn-catalyzed SiNWs. Then, the effects of PECVD parameters on Bi-catalyzed SiNWs are studied by changing growth temperature, RF power and gas flow ratio between hydrogen and silane. Lastly, proper uses of these SiNWs will be suggested according to their characteristics.

2.2 PLASFIL system (PECVD)

PECVD is one of technologies to deposit thin-films and nanowires. Precursor gases are dissociated into ionized species by electron impact in electrical discharge. Radio frequency (RF, 13.56 MHz) that enable the deposition on insulating substrate is generally used to generate the discharge. Thanks to

the plasma, the reaction can be carried out at lower temperature than conventional CVD using only thermal energy. Thus, plasma plays an important role for the reaction of gas species with substrates. The plasma environments such as the energy of ionic particles, the voltage drop in sheath, etc. are controllable by various parameters. The sheath is described as the electron-free region that induces potential drop near the electrode named as plasma potential. The sheath is formed between each electrode and plasma owing to the weight difference between electron and ions (electron is much lighter than ions).

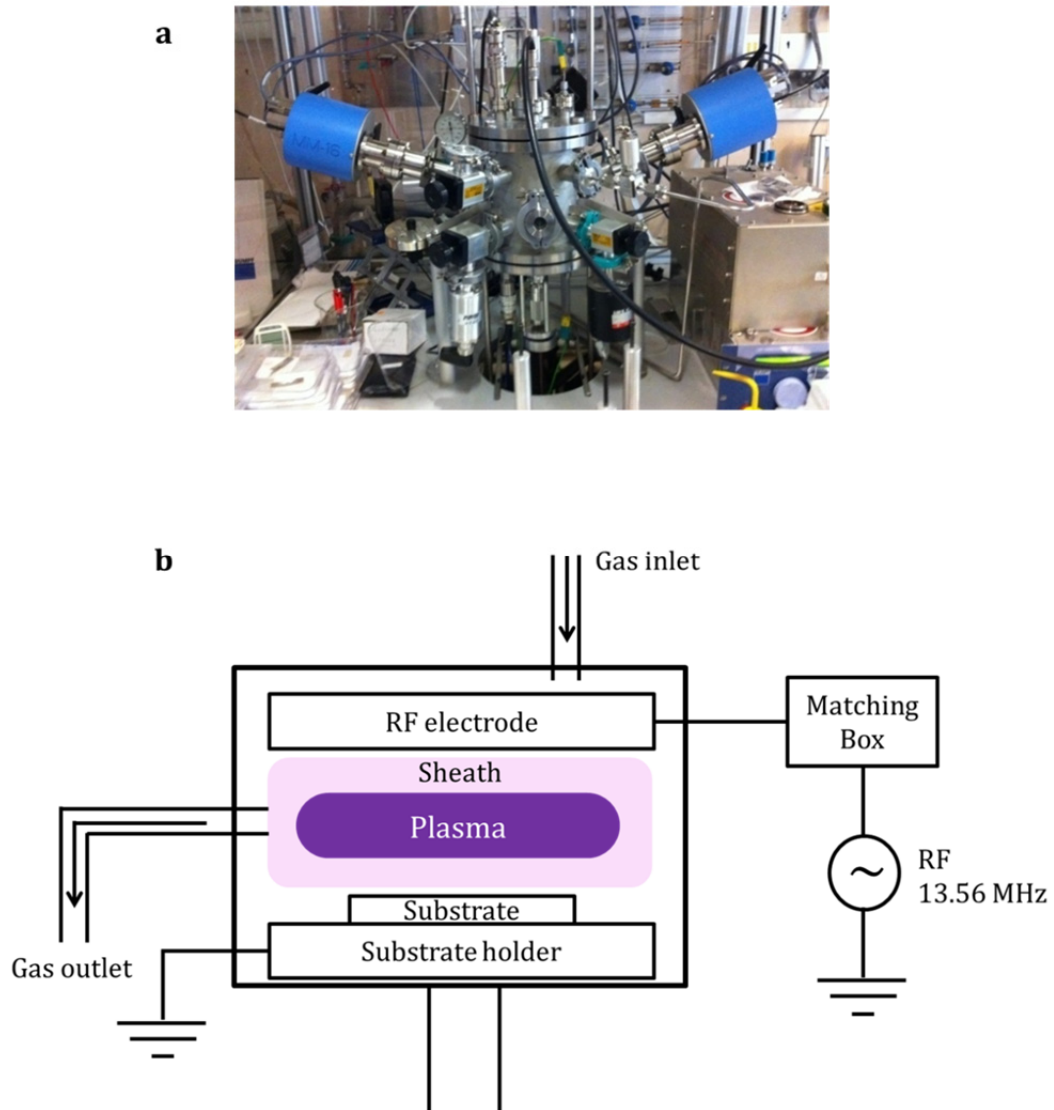


Figure 2.2 – PECVD system; (a) The photo of PLASFIL system used in this study, (b) Schematic diagram of PLASFIL

In this study, the SiNWs are grown in PLASFIL reactor shown in Figure 2.2 (a). The reactor has a RF electrode upside and a substrate holder downside. The chamber is opened and closed by moving the substrate holder up and down. The substrate holder and the RF electrode could be heated up to 650 °C and 450 °C of nominal temperature, respectively. Hydrogen (H₂), silane (SiH₄) for silicon deposition and tri-methyl boron (B(CH₃)₃) for p-type doping are available. Unfortunately, none of n-type doping gas line is installed. The growth is typically performed under vacuum less 5 x 10⁻⁶ mbar made by a turbo pump.

2.3 VLS growth of SiNWs and catalyst choice

Vapor-Liquid-Solid (VLS) growth mechanism was first proposed by Wagner and Ellis in 1964 [18]. This is still the dominant mechanism to synthesize not only silicon nanowires but also other semiconductor nanowires [19]. The name of VLS literally well describes the growth process of SiNWs. It means that silicon atoms undergo a phase transition from vapor to solid. Figure 2.3 illustrates the schematic diagram of VLS process. Since catalyst metal must be needed for VLS growth of SiNWs, thin metal films is deposited on a substrate (Figure 2.3 (a)). Then, catalyst droplets are formed by heating the substrate with temperature higher than the eutectic point between silicon and catalyst metal (Figure 2.3 (b)). Precursor gas containing silicon is inserted to synthesize the nanowires. In this study, SiH₄ is used for feeding silicon ions. Then it is dissociated at the interface with catalyst in case of CVD or in plasma in case of PECVD (Figure 2.3 (c)). Silicon atoms dissolve into catalyst droplets and the solubility of the ions depends on the catalyst and the substrate temperature (Figure 2.3 (d)). The integration of silicon atoms into catalyst droplets is continued until the saturation of silicon concentration (Figure 2.3 (e)). The solid phase of silicon begins to precipitate at the interface between catalyst droplets and substrates (Figure 2.3 (e)). Catalyst is continuing to catalyze dissociation, diffusion and nucleation of silicon atoms.

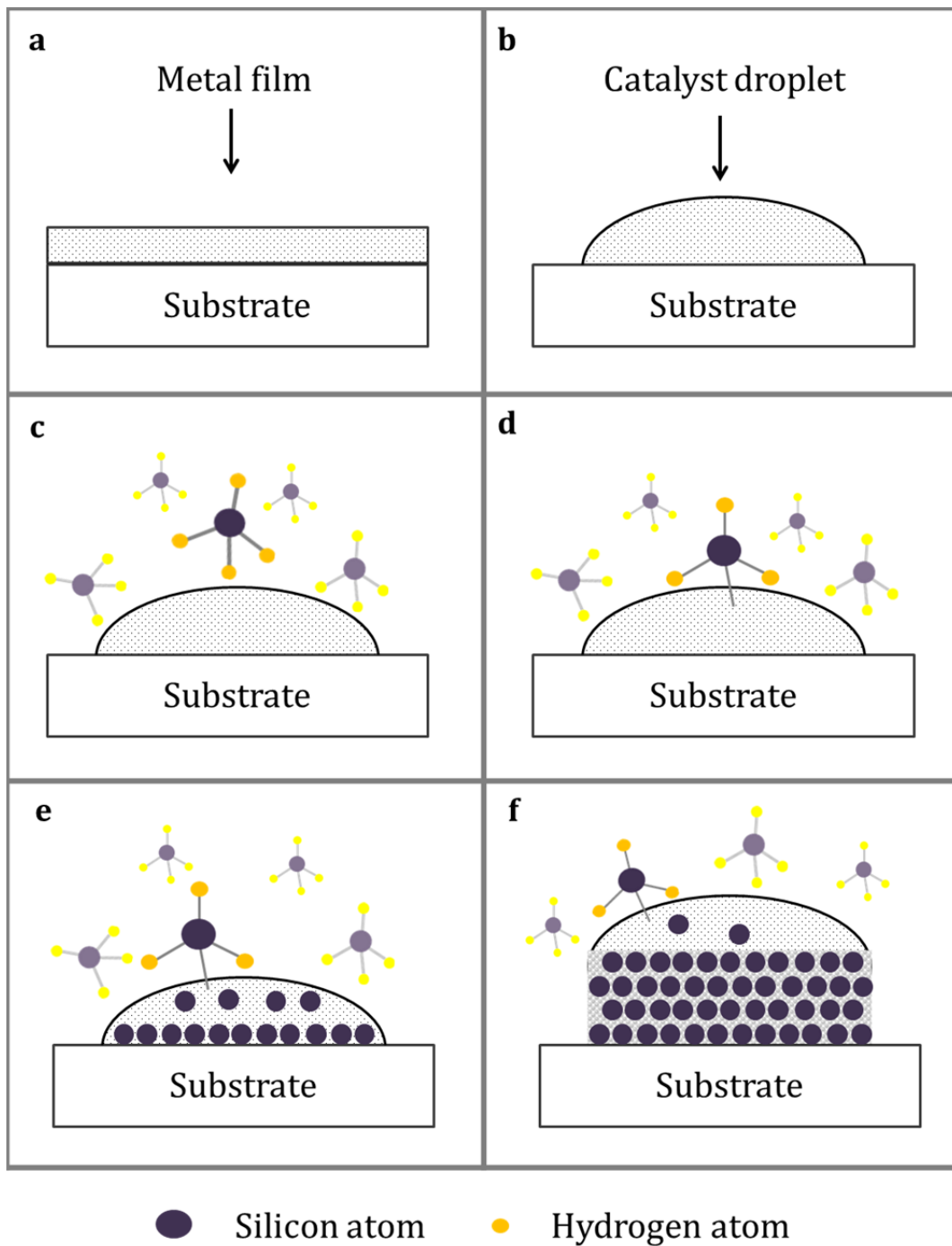




Figure 2.3 – Schematic diagrams of vapor-liquid-solid process. (a) Catalyst metal film deposition (b) Catalyst droplet formation (c) Dissociation of precursor gas (in this case silane) (d) Dissolution of silicon atom into catalyst droplets (e) Continuous integration and diffusion of silicon atoms in catalyst droplets (f) Crystalline phase of silicon is precipitated at the interface after the silicon concentration reaches saturation.

A wise choice of catalysts is important for target applications since the characteristics of SiNWs grown via VLS process strongly depends on the catalysts. Figure 2.5 shows a part of periodic table which describes the potential metal catalysts for VLS growth of SiNWs. Numerous metals are classed into transition metal (marked as the blue box) and post-transition metal (marked as the red box). A number of researches have been conducted based on transition metals because they are generally much convenient for the SiNWs growth via VLS mechanism than post-transition metals. Wagner and Ellis already reported VLS growth of SiNWs by Au, Pt, Pd, Ni, Ag and Cu in 1964 [18]. Among them, Au is still the most favored catalyst metal due to the non-toxicity, the low vapor pressure even at high temperature and the high solubility of silicon atoms [20-25]. In addition, researches on the catalytic reaction of Cd [26], Os [26], Co [27], Fe [28, 29] and Ti [30] for the SiNWs growth have been carried out. However, the SiNWs catalyzed by the post-transition metals are uncommon. Al [31], Ga [32], In [16], Sn [10, 12] and Bi [17] catalyzed SiNWs have been reported since 2001. This trend comes from the low silicon solubility and the low surface tension of post-transition metals in general.

									Al	Si	P
Ti	V	Cr	Mn	Fe	Co	Ni	Cu	Zn	Ga	Ge	As
Zr	Nb	Mo	Te	Ru	Rh	Pd	Ag	Cd	In	Sn	Sb
Hf	Ta	W	Re	Os	Ir	Pt	Au	Hg	Tl	Pb	Bi



Transition metals



Post-transition metals

Figure 2.4 – Periodic table of transition metals and post-transition metals as potential catalyst metals for VLS process.

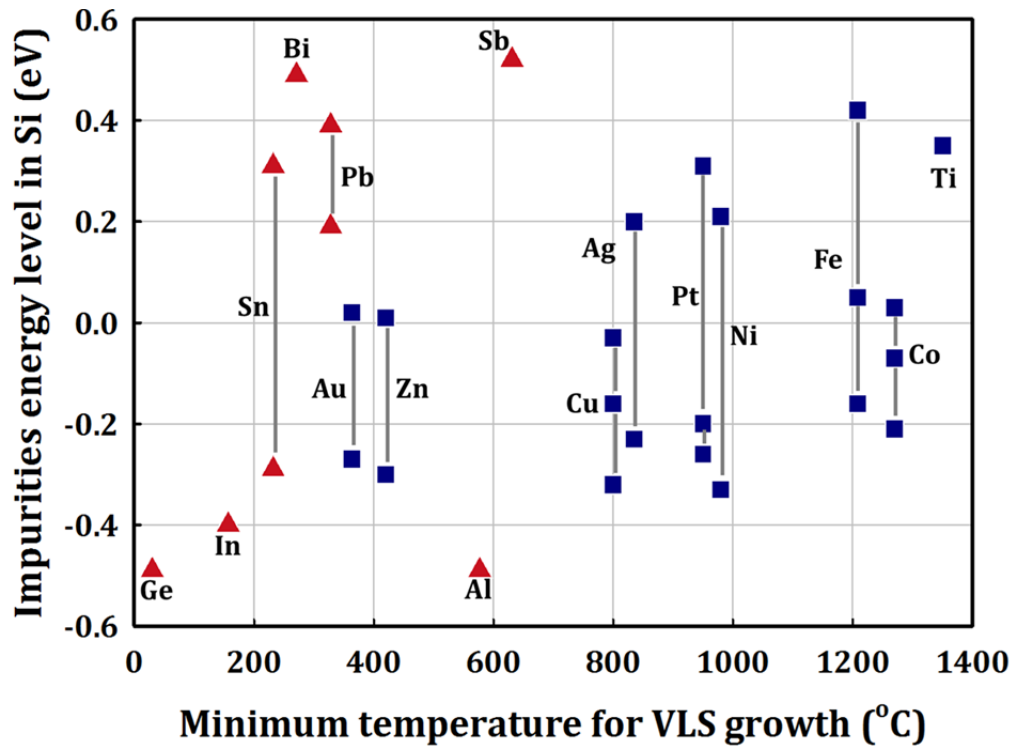


Figure 2.5 – Impurities energy level of catalyst metals as a function of eutectic point with silicon. Red triangles and blue squares correspond to post-transition and transition metals respectively.

For the moment, the transition metal catalyzed SiNWs are main stream in academia, however, the trend could be moved to post-transition metals. Figure 2.5 shows impurities energy level in silicon band-gap as a function of minimum temperature necessary for the VLS growth. The SiNWs growth using such transition metals requires a high process temperature ranged from 363 °C (Au) to 1350 °C (Ti). Besides, the most transition metals introduce deep traps within a silicon band-gap according to their impurity energy levels (Figure 2.5). The contamination of the SiNWs by the diffusion of catalyst causes the degradation of electrical performance of SiNWs based devices [33]. On the other hand, post-transition metals show minimum process temperature ranged from 30 °C (Ge) to 600 °C (Al). It means that process cost can be lowered compared to the high temperature process. Also, it implies that SiNWs can be grown even on flexible substrates thanks to the low process temperature. This is an attractive property for the next-generation solar cell. Another advantage of post-transition metals is that

they introduce electrically neutral or shallow levels in the silicon band-gap. The electrical recombination could be reduced as contrasted with the transition metal catalyzed SiNWs. The process temperatures and the energy levels correspond to 232 °C and +0.3 eV and -0.29 eV for Sn, 271.4 °C and +0.49 eV for Bi, respectively (Figure 2.5) [34]. Especially, Bi can be used to grow the n-type SiNWs by the metal doping without doping gases. Notwithstanding theoretical advantages, the synthesis of SiNWs by post-transition metals is still challenging due to their low silicon solubility, low surface tension and oxidation of metal [35]. Fortunately, PECVD suggests a possible solution to overcome those huddles. The oxidized post-transition metals require the higher thermal energy to form catalyst droplets. But, H₂ plasma application with temperature higher than eutectic point helps to organize the catalyst droplets since the hydrogen radical reduces oxidized metal layer. Plasma also plays a critical role to break the precursor gas and to facilitate the reaction of atomic silicon with the catalyst droplets. Namely, plasma lowers the activation energy required to catalyze the nanowires. Thus, the SiNWs growth by post-transition metal could be conducted despite of the obstacles mentioned above.

2.4 Sn-catalyzed SiNWs

A number of studies on the Sn-catalyzed SiNWs are already carried out by our group from the catalyst formation, the SiNWs growth to radial-junction a-Si:H solar cells [10-13, 36]. As stated above, Sn is interesting catalyst metal due to their process temperature and neutral energy levels in silicon band-gap. The Sn-catalyzed SiNWs generally shows straight and tapered appearance with the growth temperature above 450 °C from previous works. SnO₂/glass [10], aluminum doped zinc oxide (AZO)/glass [12] or c-Si wafer are used as substrates for the a-Si:H radial junction solar cells. However, ITO is chosen in this study for the hybrid solar cell applications due to its high work function [37]. The hybrid solar cells based on ITO shows better solar cell performance than that with AZO (Appendix

A.1). Figure 2.6 illustrates a process flow for the Sn-catalyzed SiNWs growth on ITO. A few nanometers thick Sn layer is deposited on ITO by the thermal evaporation, then, the substrates covered by Sn layer are exposed to H_2 plasma with heating of substrates for catalyst droplets formation in a PECVD chamber, Figure 2.6 (a). The SiNWs are grown under SiH_4 plasma with TMB (Tri-Methyl Boron, $B(CH_3)_3$) for p-type doping, Figure 2.6 (b). The VLS mechanism is briefly summarized in Figure 2.6 (c). As grown SiNWs is shown in Figure 2.6 (d) that describes the Sn-catalyzed SiNWs and a-Si:H deposited around the nanowires by the physisorption of silicon atoms on ITO/glass. In this study, only H_2 plasma duration was altered to control the density of SiNWs. The etching of the a-Si:H layer and its effects on our hybrid solar cell will be discussed in Chapter 4. Detailed experimental conditions are available in Appendix A.2.

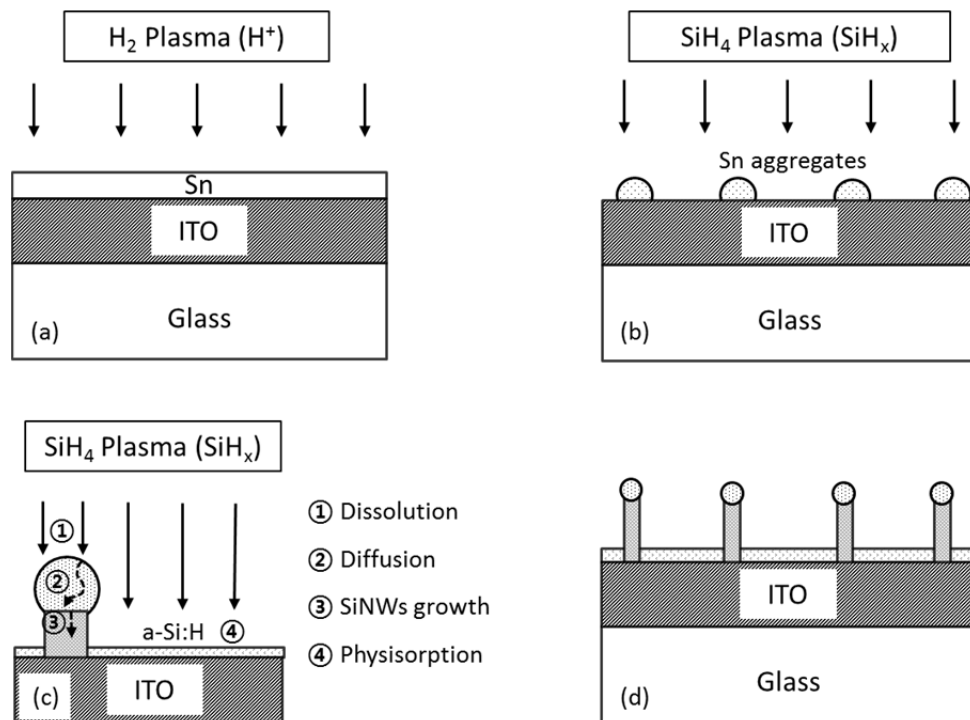


Figure 2.6 – Sn-catalyzed SiNWs growth procedures by PECVD. (a) Hydrogen plasma of thin tin deposited ITO/glass substrate (b) Silane plasma with tri-methyl boron for SiNWs growth (c) VLS growth process and (d) Sn-catalyzed SiNWs array.

2.4.1 Growth time dependence

Figure 2.7 shows SEM images of SiNWs with different growth time altered from 5 min to 15 min with 5 min interval. Other conditions, like catalyst thickness, H_2 plasma and SiH_4 plasma condition are unchanged. The Sn-catalyzed SiNWs show a straight and tapered shape. The SiNWs are randomly oriented with respect to the substrate, namely, they are not perfectly vertical to the substrate (Figure 2.7 (b)). As the growth time increases, the SiNWs becomes longer and slightly thicker in terms of diameter (Figure 2.7 (a), (c) and (d)). The configurations of SiNWs are characterized by an image threating software called ImageJ for quantitative analysis. The software helps to measure the dimensional properties of the SiNWs from the taken SEM images.

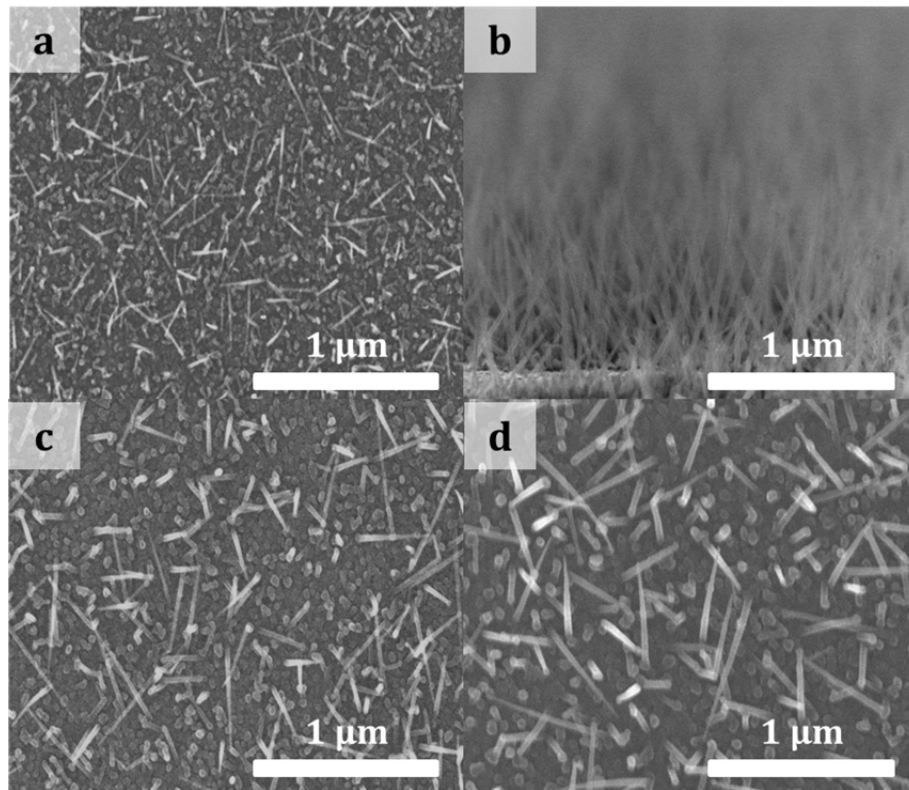


Figure 2.7 – SEM images of Sn-catalyzed SiNWs with the growth time (a) 5 min (b) 5 min, cross-sectional view (c) 10 min and (d) 15 min

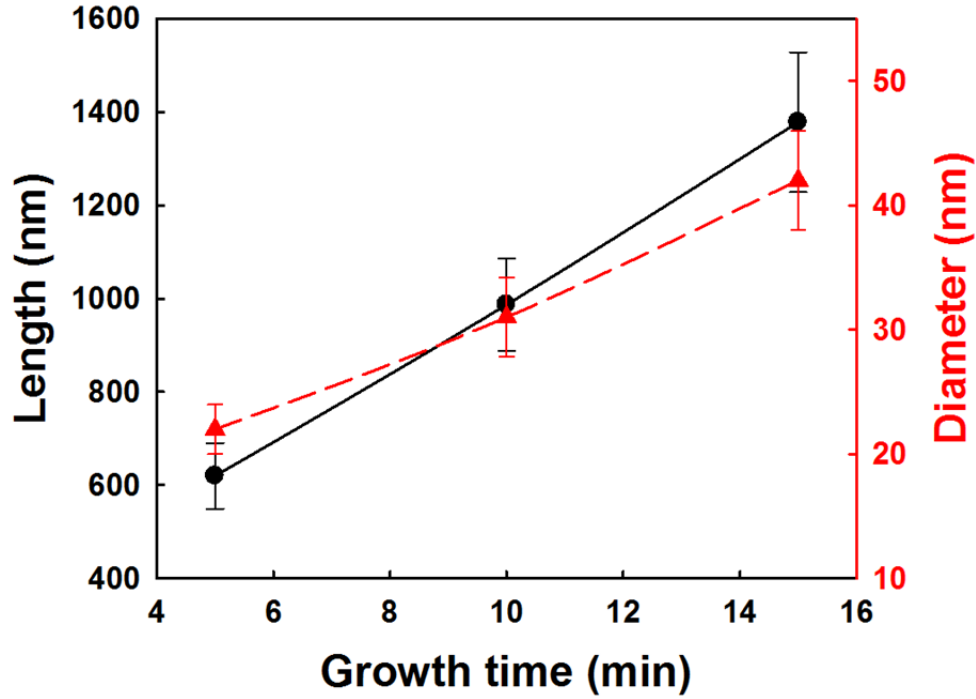


Figure 2.8 – Length and diameter of SiNWs as a function of Growth time. (Black symbol and line for length, Red symbol and line for diameter)

Figure 2.8 describes the length and diameter of SiNWs as a function of the growth time. SiNWs' lengths are 620 nm, 980 nm and 1380 nm for 5 min, 10 min and 15min, respectively. The longer nanowires are observed with longer SiH_4 plasma duration due to the continuous reaction of catalyst with the gas species of silicon. The diameter measured at the middle of SiNWs scales linearly with the growth times. It is attributed to the tapering effect during the growth. For the PECVD growth of SiNWs, the longitudinal growth is observed with the radial growth of silicon on the side wall of SiNWs. The longer growth duration results in the continuous radial growth, therefore, the diameter linearly increases with the growth time [38, 39]. Such dimensional changes modulate the optical characteristics of a SiNWs array. Figure 2.9 shows the optical absorbance of the SiNWs array depending on the growth time. The SiNWs generally show higher absorbance in a shorter wavelength region while the absorbance in a longer wavelength region is limited due to the indirect band gap of crystalline silicon. The longer growth time of SiNWs normally leads to the higher absorbance. The absorption

characteristics of SiNWs depend on the length and the diameter of SiNWs. Longer and wider SiNWs show higher absorption but it saturated with wavelength less than 350 nm [40]. The experimental results correspond to the general trend of absorption variation according to the dimensional properties.

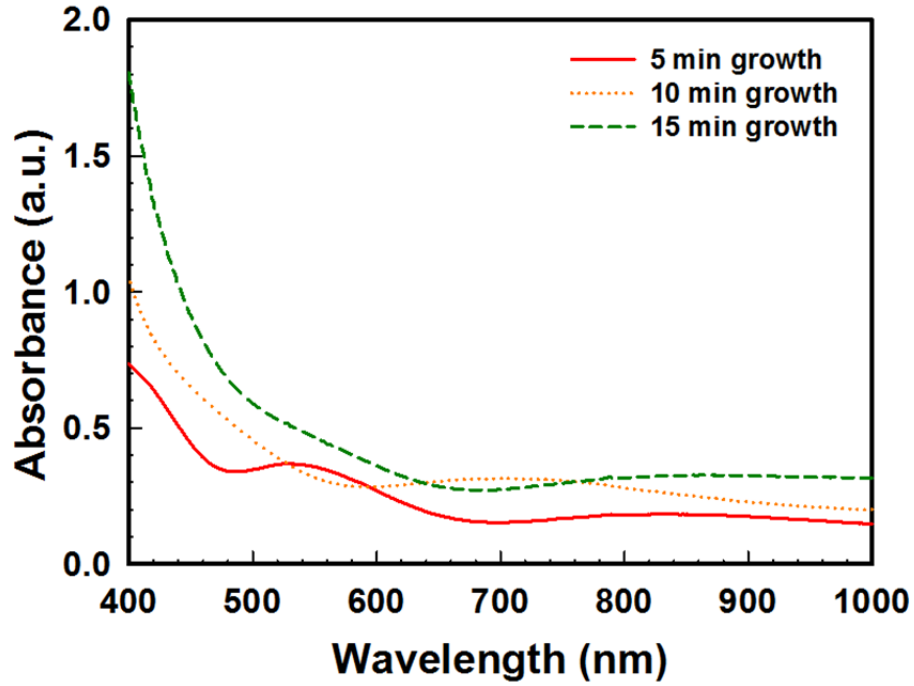


Figure 2.9 – Absorbance of SiNWs for SiNWs arrays of different growth time

2.4.2 Density control by H₂ plasma

Figure 2.10 shows SEM images of the Sn-catalyzed SiNWs with different density controlled by the H₂ plasma duration. As the H₂ plasma duration increases (from Figure 2.10 (a) to (d)), the density of SiNWs tends to increase. The SiNWs commonly show the straight appearance with remained catalyst metals on their tip due to the short growth time of 3 min. This phenomenon could be avoided with longer SiNWs growth time with same thickness of Sn layer [13, 36]. But, the long SiNWs like 1 μm lead the creation of shunting paths in our solar cell structure. Thus, it becomes one of obstacles for the efficient hybrid solar cell (Section 3.4). The residual catalyst removal will be discussed in Chapter 4.

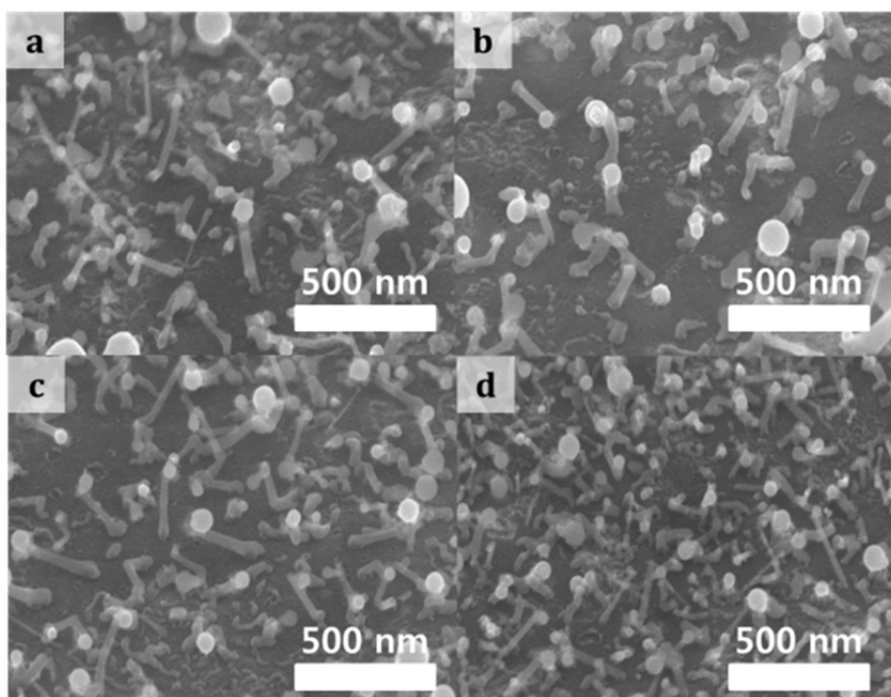


Figure 2.10 – SEM images of Sn-catalyzed SiNWs depending on hydrogen plasma duration during catalyst droplets formation. (a) 2 min (b) 4 min (c) 6 min and (d) 8 min.

Figure 2.11 summarizes dimensional properties of SiNWs as a function of the H₂ plasma duration. The length is kept around 300 nm, suggesting that H₂ plasma isn't strongly related to the SiNWs' length change (Figure 2.11 (a)).

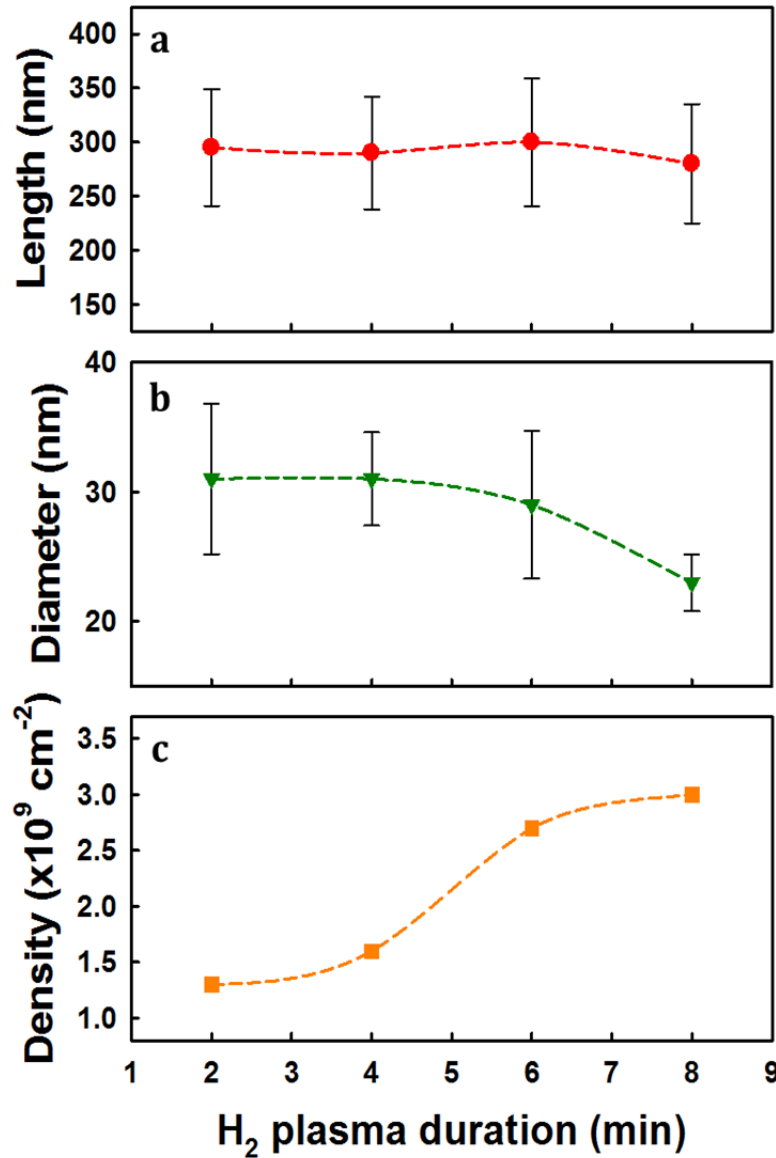


Figure 2.11 – Dimensional characteristics of SiNWs depending on hydrogen plasma duration during catalyst formation. (a) Density (b) Diameter and (c) Length of Sn-catalyzed SiNWs.

It is believed that the growth time strongly effects on SiNWs' length. Meanwhile, the decrease in diameter is observed. 31 nm of diameter with 2 min of H₂ plasma is reduced to 23 nm after 8 min of H₂ plasma. The density roughly tends to increase with long H₂ plasma time. It is slightly increased between 2 min and 4 min. It dramatically increases with 6 min of H₂ plasma and then it increases more in 8 min with a reduced slope. The similar tendency of diameter and density was already observed for the SiNWs grown on a silicon wafer. It might be related to the decrease of Sn catalyst droplet size with longer H₂ plasma time [41]. Despite of these similar tendencies, the

effect of H₂ plasma on ITO/glass substrate should be considered once over. In 2008, Pierre-Jean Alet reported In-catalyzed SiNWs from ITO [16]. In this paper, In catalyst droplets are generated by the reduction of ITO by H₂ plasma. They could contribute to the density increase by H₂ plasma in this study. Figure 2.12 illustrates schematic diagrams of the catalyst droplet formation process on Sn/ITO/glass. When H₂ plasma applied on Sn deposited ITO/glass substrate, Sn metal drops are formed at the beginning of H₂ plasma (Figure 2.12 (a) and (b)). As a few nanometers thick Sn layer is transformed to Sn droplets, one part of ITO is gradually exposed to atomic hydrogen with a substrate temperature higher than the eutectic point of In-Si system (157 °C) [42]. The conditions are met for a catalyst generation by the superficial reduction of ITO. Therefore, Indium catalyst droplets are probably located around Sn catalyst droplets with continuous H₂ plasma (Figure 2.12 (c) and (d)). As a result, the density of SiNWs can be increased with longer H₂ plasma time because they can be catalyzed by In as well as Sn.

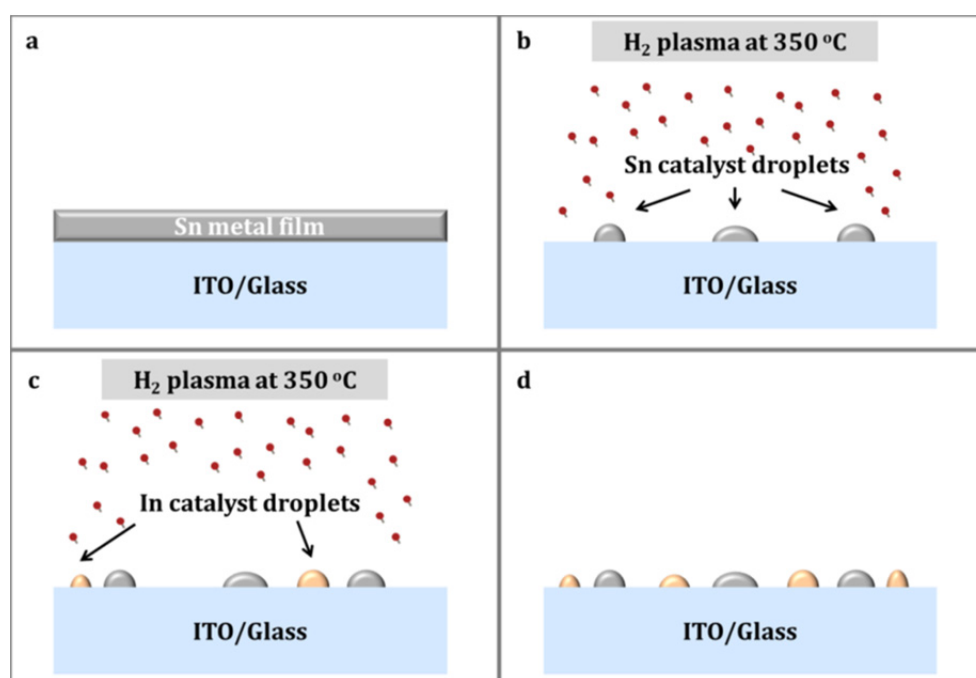


Figure 2.12 – Schematic diagram of catalyst generation from thin Sn film and also from ITO. (a) Thin Sn metal deposited on ITO/glass, (b) Hydrogen plasma at 350 °C at the beginning (c) Long time hydrogen plasma at 350 °C. In catalyst starts to be generate. (d) Presence of Sn and In catalyst droplets

2.5 Bi-catalyzed SiNWs

Among the post-transition metals, Bi is a promising catalyst with regard to electrical characteristic and the process temperature. The energy level of Bi is slightly lower from the conduction band of crystalline silicon, thus, SiNWs can be doped as n-type by Bi doping during the VLS process without doping gases. Furthermore, these SiNWs can be catalyzed with the eutectic temperature of 271.4 °C (Figure 2.5). The temperature is lower than Au catalyst (363 °C). In spite of these advantages, it is difficult to manipulate Bi as a catalyst for the SiNWs growth. First, Bi has the higher vapor pressure, namely, Bi is easily evaporated during the growth. At 1165 K, Bi shows 100 Pa which is higher compared to the Au (100 Pa at 2021 K). Thus, it brings a narrow growth condition with regard to the growth temperature. Second, Bi shows the low surface tension of 0.37 N/m like most of post-transition metals (for example, Sn=0.56 N/m, In=0.55 N/m, Ga=0.71 N/m) [43]. In contrast Au has 1.14 N/m of surface tension. It was known that the unidirectional growth of silicon is difficult when the SiNWs growth is catalyzed by a low surface tension catalyst [44]. This is why the Bi-catalyzed SiNWs are rare despite of its potential. Bi-catalyzed SiNWs are reported in recent year. Our group first reported Bi-catalyzed SiNWs by PECVD technique in 2012 [17]. Bi is used not only to catalyze SiNWs growth but also to dope the SiNWs as n-type. Based on these SiNWs, radial junction a-Si:H solar cells were investigated. n-type characteristic of Bi-catalyzed SiNWs are proven by solar cell characteristics. Another report was published in 2012 by Rakesh Kumar et al. They synthesized Bi-catalyzed SiNWs by electron beam evaporation technique [45]. The nanowires were grown by conventional VLS process and the diffusion of Bi metal into them was observed. As a barrier for using Bi to catalyzed SiNWs has just been overcome, further investigations are necessary. In this section, PECVD parameters influencing on the SiNWs nano-morphology are studied for the hybrid solar cells and the radial junction solar cells.

2.5.1 n-type characteristic of Bi-catalyzed SiNWs

The doping of the silicon is crucial to determine electrical characteristic of silicon. The verification of doping profile and electrical characteristic of Bi-catalyzed SiNWs is starting point to properly take advantages of the SiNWs. Secondary ion mass spectroscopy (SIMS) is generally used to determine impurities density in silicon. Doping concentration is extracted by counting the number of all impurities. However, this conventional method shows limitations for characterizing SiNWs unlike crystalline silicon wafer; 1) all of impurities are counted even though they are entirely not activated, 2) some amount of impurities could not substitutionally incorporated with silicon. In other words, impurities can be on the surface of SiNWs or remained on the tip of SiNWs after deposition [11, 46]. Dopant concentration of SiNWs could be overestimated [34]. Thin-film transistor geometry could be used to decide electrical type of SiNWs [47, 48]. However, there is a practical difficulty to grow the Bi-catalyzed SiNWs with a sufficient long and straight shape for a thin-film transistor. Generally, catalyst metal is incorporated in the SiNWs during VLS growth, thus, n-type doping is caused as grown SiNWs. The SiNWs were employed for n-i-p structure of a-Si:H solar cells. Our previous works determined the electrical type of Bi-catalyzed SiNWs by the a-Si:H solar cell configuration with and without Bi layer [17]. Compare to i-i-p structure, n-i-p structure of a-Si:H solar cell with Bi thin layer as n layer instead of n-type a-Si:H layer increases open-circuit voltage of the solar cells. In addition, the Bi-catalyzed SiNWs contribute to form open-circuit voltage in a nano-structured radial junction a-Si:H solar cell. Results prove n-type characteristic of Bi-catalyzed SiNWs. Consequently, the fact is interesting that n-type SiNWs can be obtained by the incorporation of catalyst metal without doping gas which overcomes the limitation of the PLASFIL system which has none of n-type gases installed (Section 2.2). The SiNWs can be incorporated with organic materials, which are mostly p-type, for the hybrid solar cell application.

2.5.2 Temperature dependence

The growth temperature of SiNWs is one of decisive parameters to control the appearance of SiNWs. The temperature should be higher than a eutectic point of catalyst-silicon system to initiate the incubation of silicon gas species in catalyst droplets and to begin the growth process. The growth temperature of Bi-catalyzed SiNWs by PECVD ranged from 450 °C to 600 °C with keeping other parameters unchanged. Figure 2.13 shows SEM image of Bi-catalyzed SiNWs, depending on the growth temperature. Significant changes in SiNWs' appearance and morphology are observed. At 450 °C, none of SiNWs is synthesized. Instead, catalyst droplets are observed in Figure 2.13 (a) and (b). This might be due to the low concentration of silicon in catalyst droplets, thus, they could not activate the SiNWs growth. The SiNWs are observed at 500 °C. The nanowires seem like winding and residual Bi is observed on the tip of the nanowires. Remained catalyst confirms again VLS growth of the SiNWs [45]. At 550 °C, the SiNWs with more straight appearance than those of 500 °C are observed. Some of the SiNWs show kink, which could be explained as the change of growth direction. Lastly at 600 °C, the SiNWs is grown and they have tapered morphology and the amount of residual catalyst seems to be reduced compared to that of lower temperature. Resultingly, increase in the growth temperature was observed to influence the appearance of SiNWs array. The straight SiNWs at higher temperature, more than 400 °C, is a generally observation [10, 39, 49-51]. The increase in the growth temperature tends to reduce time to need for the incubation, thus, the growth of SiNWs can be promoted [52]. This is attributed to the activation energy decrease for the reaction between catalyst droplets and silicon gas species [53, 54]. From these facts, no SiNWs growth at 450 °C might be attributed to the longer incubation time and the higher activation energy than those of higher temperature. Winding and kink effects are reduced with the high growth temperature. Probability of kink generation tends to be reduced with high temperature and low pressure although it is not totally resolve kink problem

[55]. This probably related with straight appearance at high temperature like SiNWs grown at 600 °C.

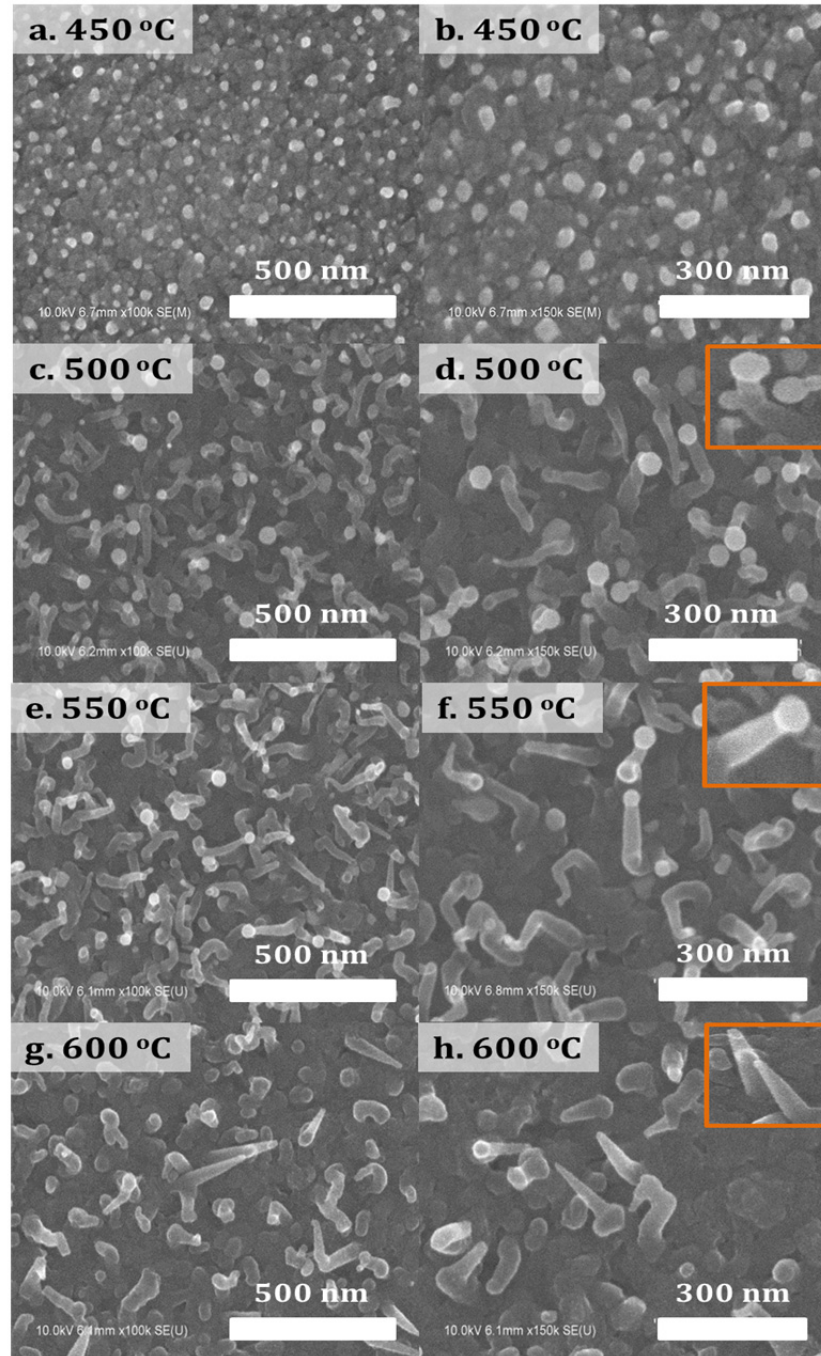


Figure 2.13 – SEM images of Bi-catalyzed SiNWs depending on growth temperature. Growth temperatures are (a,b) 450 °C (c,d) 500 °C (e,f) 550 °C and (g,h) 600 °C.

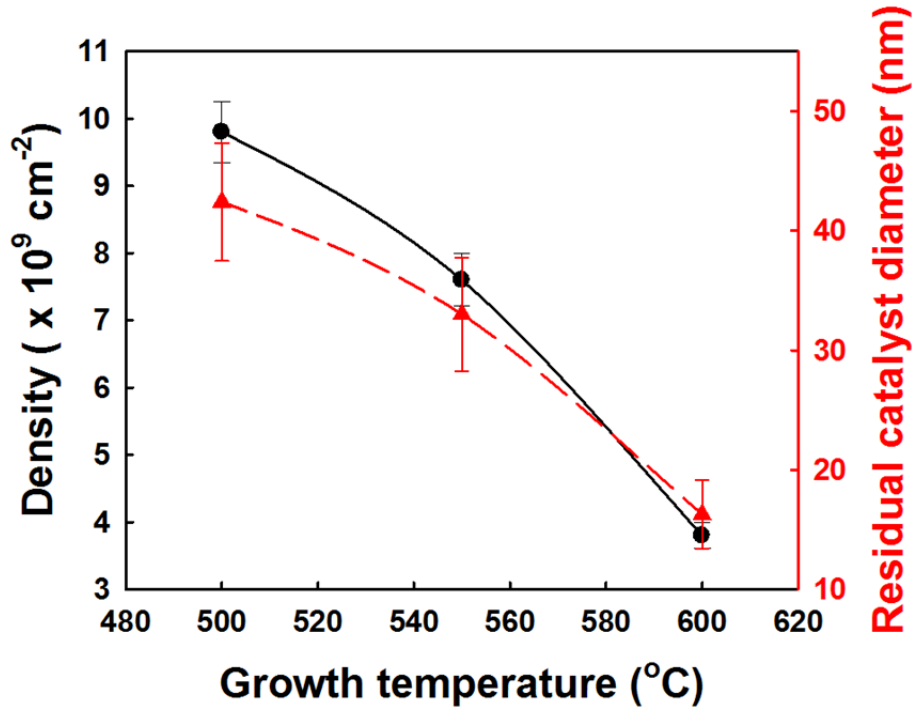


Figure 2.14 – Density and residual catalyst diameters as a function of growth temperature. (Black symbol and line for density, Red symbol and line for residual catalyst diameter)

Figure 2.14 presents the density and the residual catalyst diameter as a function of the growth temperature. As the temperature increases, both parameters are decreased. The density ranges from $9.8 \times 10^9 / \text{cm}^2$ to $3.5 \times 10^9 / \text{cm}^2$ and the residual catalyst diameter is reduced from 40 nm to 16 nm with higher temperature. These are probably due to the high vapor pressure of Bi. After catalyst droplet formation (H_2 plasma at 350 °C), temperature is raised to 450 – 600 °C range for the SiNWs growth and it is maintained during 10 min for a stabilization of substrate temperature under H_2 flow (no plasma). Bi catalyst droplets are much easily evaporated at higher temperature by thermal energy. The loss of catalyst droplets might be the main reason of density decrease. The trend of the residual catalyst diameter also proves the evaporation of Bi catalyst droplets. The growth temperature has effects on SiNWs' appearances, density and the evaporation of catalyst droplets. For the better quality of the SiNWs, straight SiNWs without any kink and remnant of catalyst are sought. However, it seems that the control

of straight shape with a desired density is limited due to the Bi catalyst droplets are very sensitive to the temperature.

2.5.3 RF power dependence

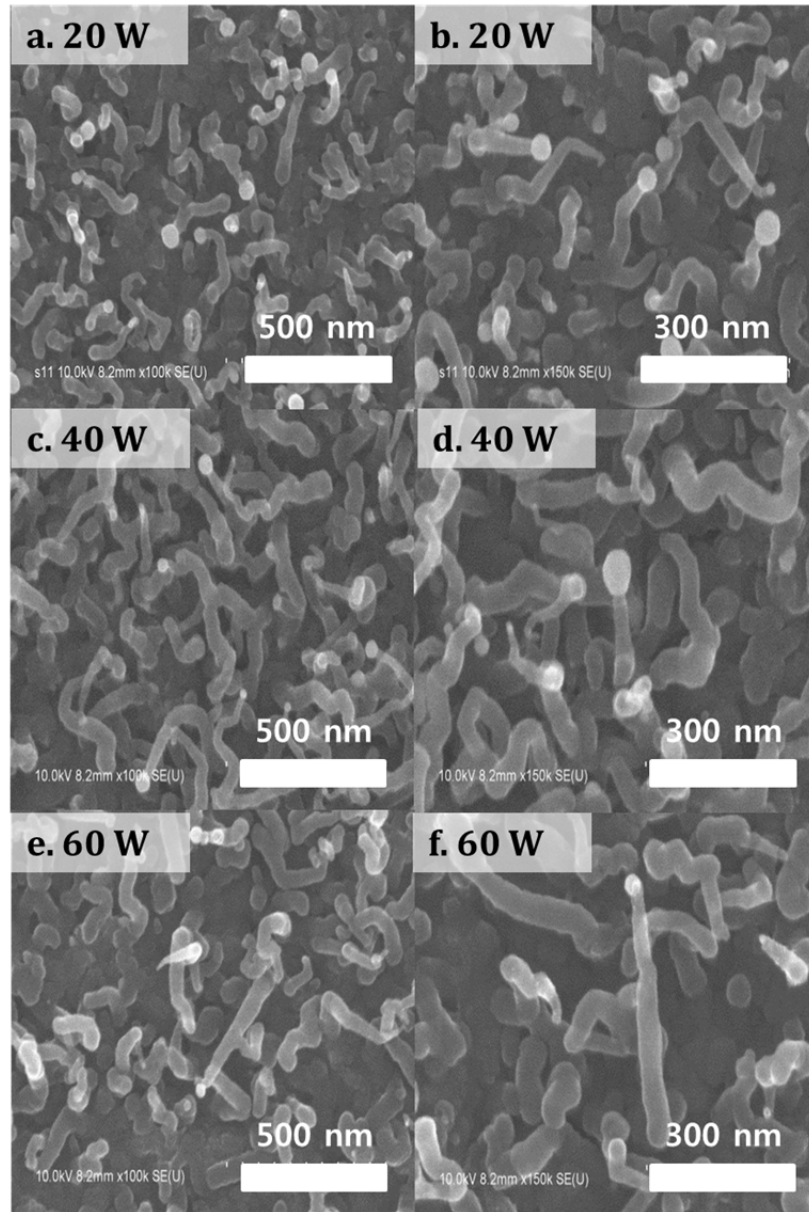


Figure 2.15 – SEM images of Bi-catalyze SiNWs depending RF power (a,b) 20 W (c,d) 40 W and (e,f) 60 W

Fast and active reaction for SiNWs is expected as a number of gas species exist in plasma. Since Bi is evaporated easily during the SiNWs growth, it is

important to feed sufficient silicon gas species for a limited time. Note that RF power influences the change of plasma environment. Namely, the higher RF power cracks the higher fraction of precursor gases. Thereby the density and energy of ions is increased in plasma. The reactivity is improved and growth rate is increased with the higher RF power [20, 36]. RF power density is controlled with 20 – 60 W range with 20 W intervals while the growth temperature was fixed at 550 °C. Figure 2.15 shows SEM images of SiNWs, depending on the RF power. The longer SiNWs are observed with higher RF power. But, there is an impression of winding shape of SiNWs even with 60 W. And remnant catalyst size is decreases with respect to the RF power.

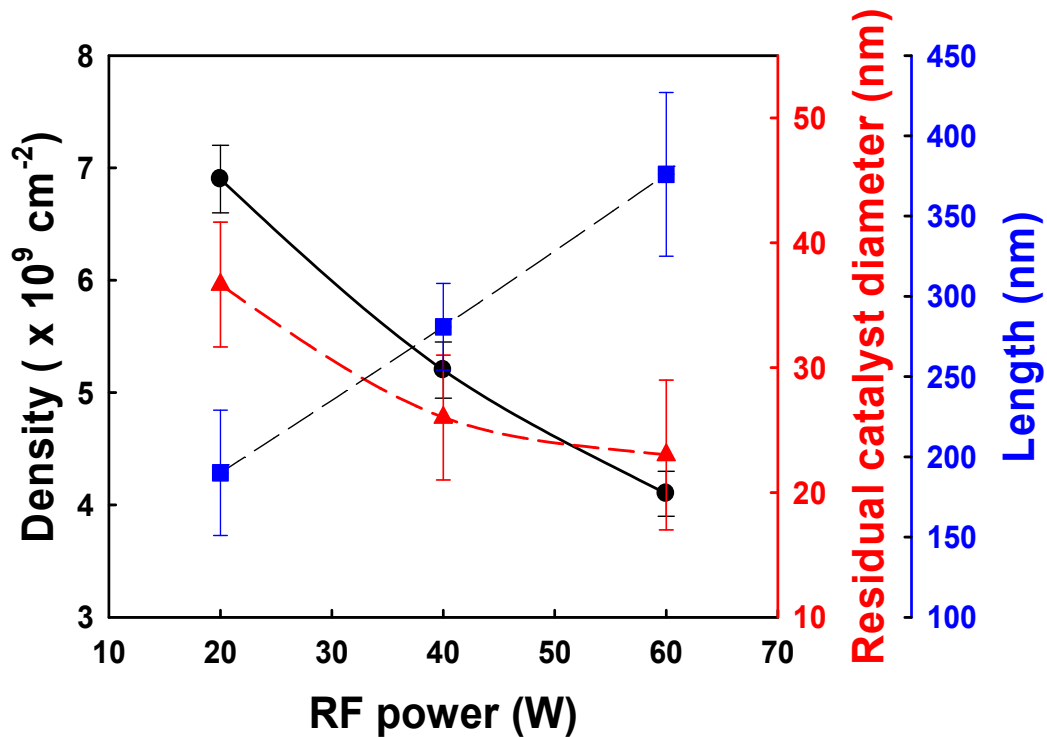


Figure 2.16 – Density, residual catalyst diameters and length as a function of RF power. (Black symbol and line for density, Red symbol and line for residual catalyst diameter, Blue symbol and line for SiNWs' length)

Figure 2.16 summarizes the length, the residual catalyst and density of SiNWs as a function of the RF power. As expected, the nanowires become longer with the higher RF power. It scales almost linearly from 190 nm to 370 nm within the RF power range used in this experiment. Thus, the growth rate corresponds to 0.8 nm/s, 1.2 nm/s and 1.6 nm/s for 20 W, 40 W and 60 W, respectively. This is due to the larger amount of reactive silicon gas species for the higher RF power. Meanwhile, decreases in density and residual catalyst diameter are observed. If we assume that the same amount of a catalyst droplet is used for catalyzing the SiNWs growth, less amount of catalyst is remained with the higher RF power due to the abundance of reactive silicon ions in plasma. The residual catalyst diameter is smaller for 60 W compared to those of 20 W and 40 W. In addition, the higher RF power also improves deposition rate of a-Si:H during VLS growth of SiNWs [56]. Some fraction of Bi catalyst droplets can be buried by the deposited a-Si:H before the growth of SiNWs. These catalyst droplets cannot contribute to catalyze SiNWs growth, for that reason, the density of SiNWs is decreased with the RF power increases.

From the results, the RF power variation does not cause significant change of SiNWs' appearance except the length. In this context, the advantage of high RF power is ambiguous since dusts or aggregates can be generated in plasma environment. This situation has no choice but the contamination of SiNWs array because PLASFIL system has a substrate holder bottom side. Furthermore, the fast deposition of intrinsic a-Si:H silicon with high RF power would cause resistive effects in the hybrid solar cells although it increases the SiNWs growth rate. Consequently, 20 W of RF power is kept going to be used during the study.

2.5.4 Gas flow ratio dependence

Plasma chemistry is closely related with the SiNWs growth. Precursor gas composition is one of methods to control the plasma chemistry. Atomic hydrogen is diluted into silicon ions atmosphere to control dimensional

properties of SiNWs [38, 57]. The influences of H_2/SiH_4 ratio are investigated. The ratio ranges from 0 to 50 while keeping the pressure and the temperature at 1 Torr (except pure SiH_4) and 600 °C, respectively.

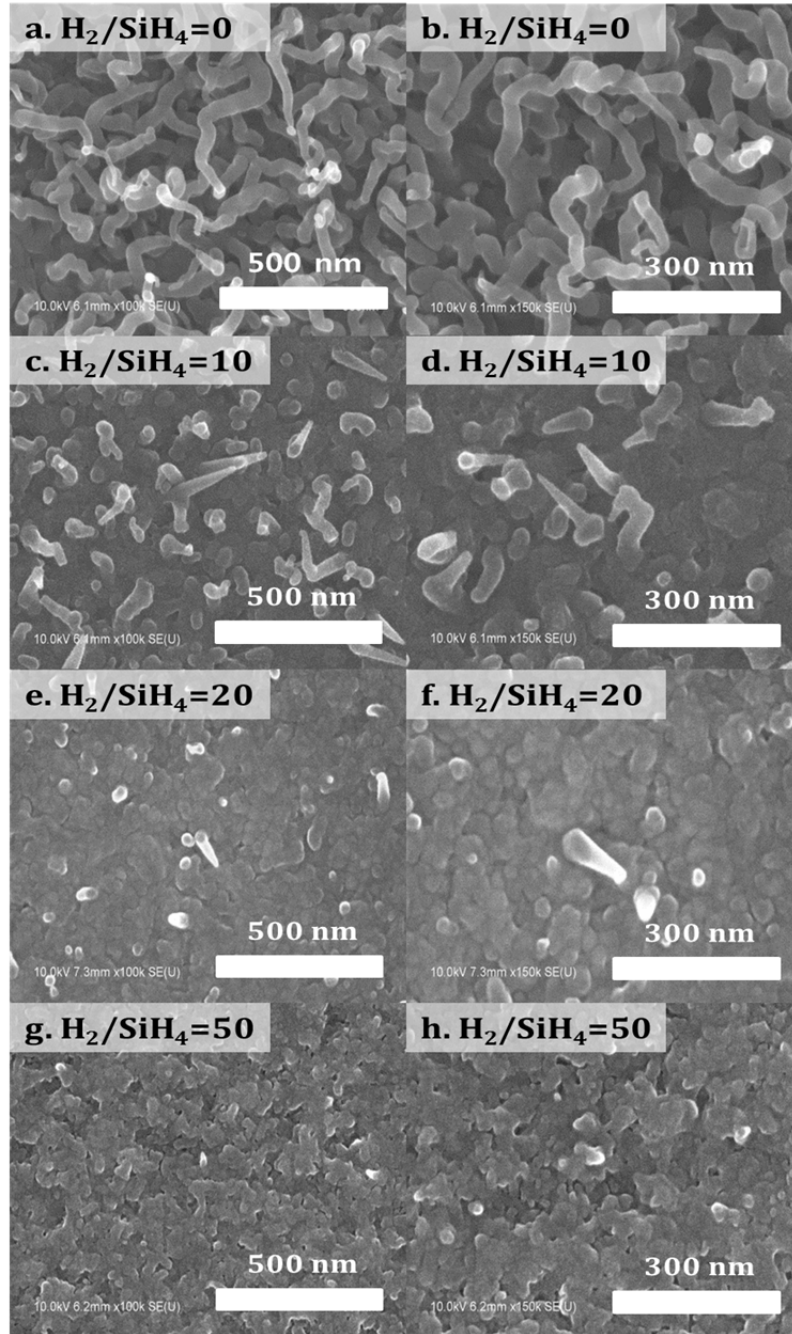


Figure 2.17 – SEM images of Bi-catalyzed SiNWs depending gas flow ratio (H_2/SiH_4). (a,b) 0 (c,d) 10 (e,f) 20 and (g,h) 50

Figure 2.17 shows SEM images of the SiNWs depending on the gas flow ratio (H_2/SiH_4). Without H_2 dilution, the SiNWs seem to be longer, denser and more winding than other ratios. When the atomic hydrogen is diluted, the substantial change is observed. The SiNWs are straight and tapered with $H_2/SiH_4=10$. The density is considerably decreased compared to that without the H_2 dilution while keeping the nanowires appearance. Further increase in H_2 dilution results in the continuous decrease in density with the straight and tapered shape. Finally, when H_2/SiH_4 reaches 50, the SiNWs are not observed. Figure 2.18 summarizes the variations of the length and the density according to the H_2/SiH_4 ratio. As the ratio increases, the density is decreased almost one order of magnitude. And the length becomes one-third compared to that of pure SiH_4 atmosphere. Hydrogen fraction increase in plasma results in 1) the suppression of lateral growth of silicon and 2) the etching of a-Si:H at a low temperature. Therefore, SiNWs has straight and tapered appearance as atomic hydrogen is diluted.

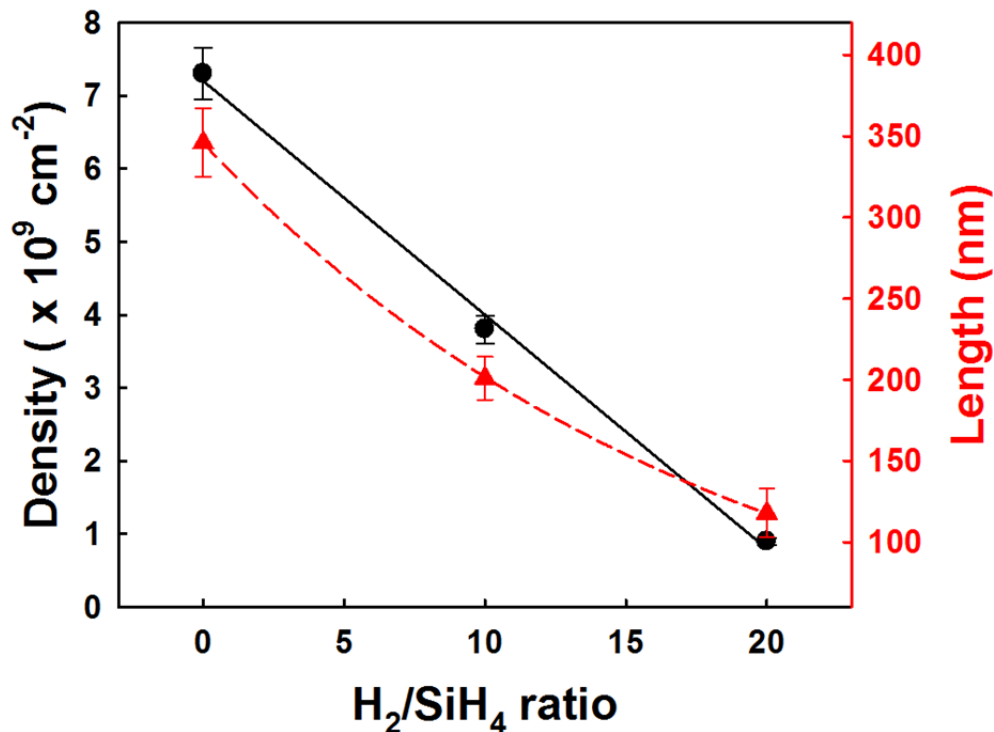


Figure 2.18 – Density and length as a function H_2/SiH_4 ratio. (Black symbol and line for density, Red symbol and line for SiNWs' length)

In addition, hydrogen has other effects on Bi-catalyzed SiNWs growth; 1) it can etch out catalyst droplets at a high temperature. Etching depth of a-Si:H is lower at the high temperature compared to the low temperature. Instead, Bi catalyst droplet is etched out. Figure 2.19 shows residual catalyst etching by H₂ plasma at 600 °C. They are evidently removed by atomic hydrogen. This H₂ plasma effect on SiNWs is negligible. 2) High fraction of atomic hydrogen lowers partial pressure of silicon which would decrease the growth rate and the density. As results, the density and length of SiNWs demonstrates considerable changes by the gas flow ratio.

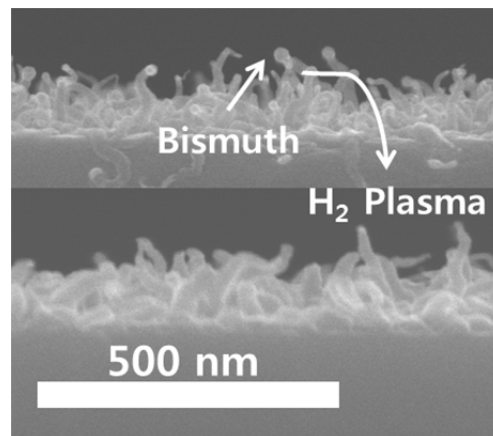


Figure 2.19 – Etching of residual bismuth catalyst on tip of SiNWs by hydrogen plasma at 600 °C.

2.6 Conclusion: proper use of each SiNWs

For the hybrid solar cell application based on the combination with an organic semiconducting polymer, the nano-morphology of SiNWs is crucial. Through this chapter the Sn-catalyzed SiNWs and the Bi-catalyzed SiNWs showed quite different electrical and geometrical characteristics. Here, the proper application of each SiNWs is discussed according to their characteristics.

2.6.1 Sn-catalyzed SiNWs

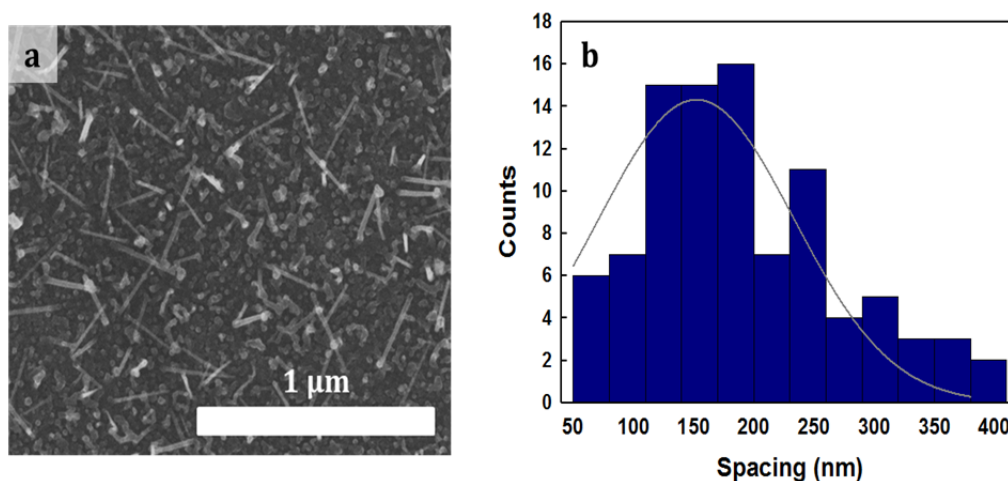


Figure 2.20 – (a) SEM image of Sn-catalyzed SiNW and (b) spacing between SiNWs: Mean spacing is 180 nm.

Figure 2.20 shows a SEM image of the Sn-catalyzed SiNWs and the spacing between the SiNWs. The Sn-catalyzed SiNWs are doped by TMB as p-type, thus, it could be used at anode side. They exhibited the average spacing around 180 nm. 50 nm and 400 nm are recorded as minimum and maximum, respectively. Since the diffusion length of organic semiconductor as 10 nm [58, 59], Sn-catalyzed SiNWs are not proper as an electron acceptor for P3HT. Despite of PECVD parameters changes, the spacing is not approached to the proper distance less than 20 nm. Instead of the electron acceptor, the SiNWs probably used as the light-trapping media in the hybrid solar cell structure based on its straight and tapered morphology. Thus, the hybrid solar cell is

designed based on organic bulk-heterojunction solar cells with the embedded Sn-catalyzed SiNWs. The solar cells are largely discussed through chapter 3 and 4.

2.6.2 Bi-catalyzed SiNWs

Bi-catalyzed SiNWs by PECVD technique have naturally n-type characteristic, thus, they might form a p-n junction with numerous organic semiconducting polymers. Cathode side of solar cell is proper as it is the n-type SiNWs. Nano-morphology is greatly changed depending on PECVD process condition as shown in previous section. Figure 2.21 shows the various nano-morphologies of the Bi-catalyzed SiNWs. According to the target application, the most proper one should be chosen. Unfortunately, the control of the density and the appearance is not compatible. In other words, the winding SiNWs generally has the high density and straight SiNWs has the slow density. The investigation on the precise control of density should be considered, for example, catalyst thickness change. The Bi-catalyzed SiNWs are capable to be applied to the hybrid solar cell as well as the radial junction a-Si:H solar cell applications.

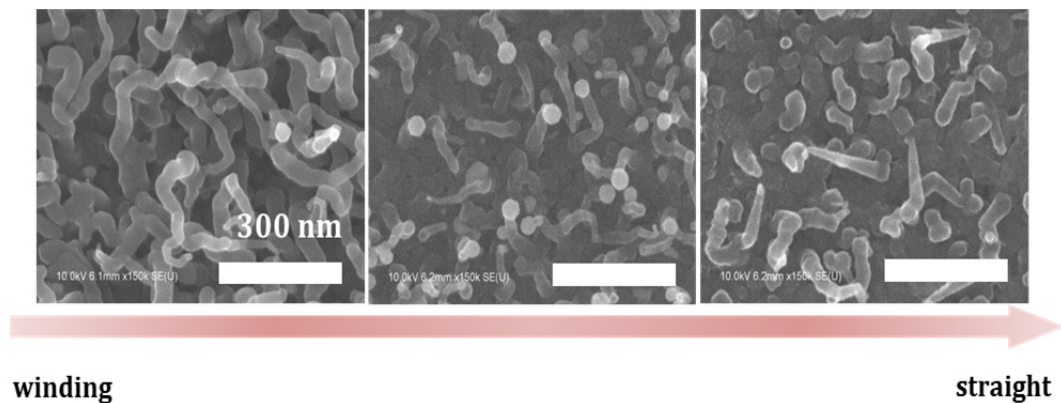


Figure 2.21 – SEM image: Nano-morphology variation of Bi-catalyzed SiNWs

Figure 2.22 shows a SEM image of Bi-catalyzed SiNWs and the spacing between the nanowires. As shown in the SEM image, the Bi-catalyzed SiNWs are winding and highly dense. Thus, the average spacing between SiNWs exhibited around 20 nm. The nanowires can be employed as an electron acceptor to dissociate excitons, which are generated in organic semiconducting polymer, in the hybrid solar cells based on hybrid interface. The hybrid solar cells based on Bi-catalyzed SiNWs/poly(3-hexylthiophene) hybrid junction is discussed in Chapter 5.

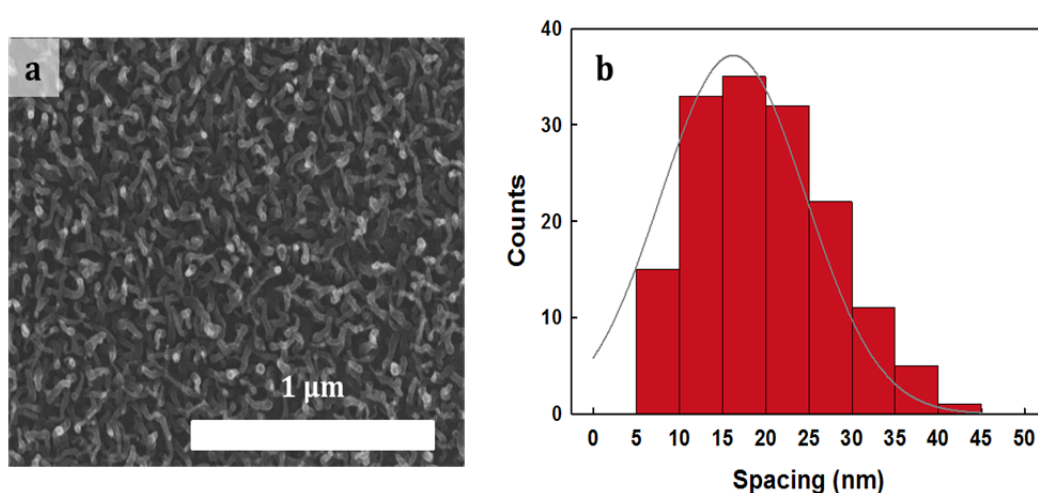


Figure 2.22 – (a) SEM image of Bi-catalyzed SiNW and (b) spacing between SiNWs: Mean spacing is 20 nm.

REFERENCE

1. Garnett, E. and P. Yang, *Light Trapping in Silicon Nanowire Solar Cells*. Nano Letters, 2010. **10**(3): p. 1082-1087.
2. Syed Abdul, M., et al., *A stamped PEDOT:PSS–silicon nanowire hybrid solar cell*. Nanotechnology, 2012. **23**(14): p. 145401.
3. He, L., et al., *Si Nanowires Organic Semiconductor Hybrid Heterojunction Solar Cells Toward 10% Efficiency*. ACS Applied Materials & Interfaces, 2012. **4**(3): p. 1704-1708.
4. He, L., et al., *Highly efficient Si-nanorods/organic hybrid core-sheath heterojunction solar cells*. Applied Physics Letters, 2011. **99**(2): p. 021104-3.
5. He, L., et al., *High-Efficiency Si/Polymer Hybrid Solar Cells Based on Synergistic Surface Texturing of Si Nanowires on Pyramids*. Small, 2012. **8**(11): p. 1664-1668.
6. He, L., et al., *High efficiency planar Si/organic heterojunction hybrid solar cells*. Applied Physics Letters, 2012. **100**(7): p. 073503-3.
7. Avasthi, S., et al., *Role of Majority and Minority Carrier Barriers Silicon/Organic Hybrid Heterojunction Solar Cells*. Advanced Materials, 2011. **23**(48): p. 5762-5766.
8. Th, S. and et al., *Silicon nanowire-based solar cells*. Nanotechnology, 2008. **19**(29): p. 295203.
9. Peng, K.-Q. and S.-T. Lee, *Silicon Nanowires for Photovoltaic Solar Energy Conversion*. Advanced Materials, 2010. **23**(2): p. 198-215.
10. Linwei, Y. and et al., *Synthesis, morphology and compositional evolution of silicon nanowires directly grown on SnO₂ substrates*. Nanotechnology, 2008. **19**(48): p. 485605.
11. Yu, L., et al., *Stability and evolution of low-surface-tension metal catalyzed growth of silicon nanowires*. Applied Physics Letters, 2011. **98**(12): p. 123113-3.
12. Cho, J., et al., *Sn-catalyzed silicon nanowire solar cells with 4.9% efficiency grown on glass*. Progress in Photovoltaics: Research and Applications, 2012. **21**(1): p. 77-81.
13. Linwei, Y., et al., *Radial junction amorphous silicon solar cells on PECVD-grown silicon nanowires*. Nanotechnology, 2012. **23**(19): p. 194011.
14. Linwei, Y. and et al., *Plasma-enhanced low temperature growth of silicon nanowires and hierarchical structures by using tin and indium catalysts*. Nanotechnology, 2009. **20**(22): p. 225604.
15. Yu, L., et al., *An In-Plane Solid-Liquid-Solid Growth Mode for Self-Avoiding Lateral Silicon Nanowires*. Physical Review Letters, 2009. **102**(12): p. 125501.

-
16. Alet, P.-J., et al., *In situ generation of indium catalysts to grow crystalline silicon nanowires at low temperature on ITO*. Journal of Materials Chemistry, 2008. **18**(43): p. 5187-5189.
 17. Yu, L., et al., *Bismuth-Catalyzed and Doped Silicon Nanowires for One-Pump-Down Fabrication of Radial Junction Solar Cells*. Nano Letters, 2012. **12**(8): p. 4153-4158.
 18. Wagner, R.S. and W.C. Ellis, *VAPOR-LIQUID-SOLID MECHANISM OF SINGLE CRYSTAL GROWTH*. Applied Physics Letters, 1964. **4**(5): p. 89-90.
 19. Oh, S.H., et al., *Oscillatory Mass Transport in Vapor-Liquid-Solid Growth of Sapphire Nanowires*. Science, 2010. **330**(6003): p. 489-493.
 20. Hofmann, S., et al., *Gold catalyzed growth of silicon nanowires by plasma enhanced chemical vapor deposition*. Journal of Applied Physics, 2003. **94**(9): p. 6005-6012.
 21. Alet, P.-J., et al., *Transition from thin gold layers to nano-islands on TCO for catalyzing the growth of one-dimensional nanostructures*. physica status solidi (a), 2008. **205**(6): p. 1429-1434.
 22. Sharma, S., T.I. Kamins, and R.S. Williams, *Synthesis of thin silicon nanowires using gold-catalyzed chemical vapor deposition*. Applied Physics A, 2005. **80**(6): p. 1225-1229.
 23. Hertog, M., et al., *Gold Catalyzed Silicon Nanowires: Defects in the Wires and Gold on the Wires*, in *Microscopy of Semiconducting Materials 2007*, A.G. Cullis and P.A. Midgley, Editors. 2008, Springer Netherlands. p. 217-220.
 24. Demichel, O., et al., *Surface Recombination Velocity Measurements of Efficiently Passivated Gold-Catalyzed Silicon Nanowires by a New Optical Method*. Nano Letters, 2010. **10**(7): p. 2323-2329.
 25. Koto, M., et al., *Gold-Catalyzed Vapor-Liquid-Solid Germanium-Nanowire Nucleation on Porous Silicon*. Small, 2010. **6**(9): p. 1032-1037.
 26. Wagner, R.S., et al., *Study of the Filamentary Growth of Silicon Crystals from the Vapor*. Journal of Applied Physics, 1964. **35**(10): p. 2993-3000.
 27. Tuan, H.-Y., D.C. Lee, and B.A. Korgel, *Nanocrystal-Mediated Crystallization of Silicon and Germanium Nanowires in Organic Solvents: The Role of Catalysis and Solid-Phase Seeding*. Angewandte Chemie International Edition, 2006. **45**(31): p. 5184-5187.
 28. Morales, A.M. and C.M. Lieber, *A Laser Ablation Method for the Synthesis of Crystalline Semiconductor Nanowires*. Science, 1998. **279**(5348): p. 208-211.
 29. Zhang, Y.F., et al., *Silicon nanowires prepared by laser ablation at high temperature*. Applied Physics Letters, 1998. **72**(15): p. 1835-1837.
 30. Kamins, T.I., et al., *Chemical vapor deposition of Si nanowires nucleated by TiSi_2 islands on Si*. Applied Physics Letters, 2000. **76**(5): p. 562-564.
 31. Y. Wang, et al., *Epitaxial growth of silicon nanowires using an aluminium catalyst*. Nat Nano, 2006. **1**: p. 186-189.

32. Sunkara, M.K., et al., *Bulk synthesis of silicon nanowires using a low-temperature vapor-liquid-solid method*. Applied Physics Letters, 2001. **79**(10): p. 1546-1548.
33. Holmberg, V.C., K.A. Collier, and B.A. Korgel, *Real-Time Observation of Impurity Diffusion in Silicon Nanowires*. Nano Letters, 2011. **11**(9): p. 3803-3808.
34. Schmidt, V., J.V. Wittemann, and U. Gösele, *Growth, Thermodynamics, and Electrical Properties of Silicon Nanowires†*. Chemical Reviews, 2010. **110**(1): p. 361-388.
35. Schmidt, V., et al., *Silicon Nanowires: A Review on Aspects of their Growth and their Electrical Properties*. Advanced Materials, 2009. **21**(25-26): p. 2681-2702.
36. O'Donnell, B., *Plasma Growth Silicon Nanowires Catalyzed By Post-Transition Metals & Applications in Radial Junction Solar Cells*. Ph.D. Thesis, 2012.
37. Klein, A., et al., *Transparent Conducting Oxides for Photovoltaics: Manipulation of Fermi Level, Work Function and Energy Band Alignment*. Materials, 2010. **3**(11): p. 4892-4914.
38. Colli, A., et al., *Thermal and chemical vapor deposition of Si nanowires: Shape control, dispersion, and electrical properties*. Journal of Applied Physics, 2007. **102**(3): p. 034302-13.
39. Zardo, I., et al., *Growth study of indium-catalyzed silicon nanowires by plasma enhanced chemical vapor deposition*. Applied Physics A: Materials Science & Processing, 2010. **100**(1): p. 287-296.
40. Hu, L. and G. Chen, *Analysis of Optical Absorption in Silicon Nanowire Arrays for Photovoltaic Applications*. Nano Letters, 2007. **7**(11): p. 3249-3252.
41. Song, M.H., *Tin catalyzed vertical epitaxial silicon nanowire on crystalline silicon (1 1 1) and radial junction silicon nanowire solar cell* Master Thesis, 2011.
42. Olesinski, R.W., N. Kanani, and G.J. Abbaschian, *The In-Si (Indium-Silicon) system*. Bulletin of Alloy Phase Diagrams, 1985. **6**(2): p. 128-130.
43. Keene, B.J., *Review of data for the surface tension of pure metals*. International Materials Reviews, 1993. **38**(4): p. 157-192.
44. Nebol'sin, V.A. and A.A. Shchetinin, *Role of Surface Energy in the Vapor-Liquid-Solid Growth of Silicon*. Inorganic Materials, 2003. **39**(9): p. 899-903.
45. Kumar, R.R., K.N. Rao, and A.R. Phani, *Bismuth catalyzed growth of silicon nanowires by electron beam evaporation*. Materials Letters, 2012. **82**(0): p. 163-166.
46. Jeon, T., et al., *Effects of acid-treated silicon nanowires on hybrid solar cells performance*. Solar Energy Materials and Solar Cells, 2013. **117**: p 632-637.
47. Goldberger, J., et al., *Silicon Vertically Integrated Nanowire Field Effect Transistors*. Nano Letters, 2006. **6**(5): p. 973-977.

-
48. Cui, Y., et al., *High Performance Silicon Nanowire Field Effect Transistors*. Nano Letters, 2003. **3**(2): p. 149-152.
49. Zardo, I. and et al., *Gallium assisted plasma enhanced chemical vapor deposition of silicon nanowires*. Nanotechnology, 2009. **20**(15): p. 155602.
50. Griffiths, H., et al., *Plasma assisted growth of nanotubes and nanowires*. Surface and Coatings Technology, 2007. **201**(22-23): p. 9215-9220.
51. Kumar, R.R., K.N. Rao, and A.R. Phani, *Growth of silicon nanowires by electron beam evaporation using indium catalyst*. Materials Letters, 2012. **66**(1): p. 110-112.
52. Kalache, B., P.R.i. Cabarrocas, and A.F.i. Morral, *Observation of Incubation Times in the Nucleation of Silicon Nanowires Obtained by the Vapor-Liquid-Solid Method*. Japan. J. Appl. Phys., 2006. **45**: p. 190.
53. Schmid, H., et al., *Patterned epitaxial vapor-liquid-solid growth of silicon nanowires on Si(111) using silane*. Journal of Applied Physics, 2008. **103**(2): p. 024304-7.
54. Lew, K.-K. and J.M. Redwing, *Growth characteristics of silicon nanowires synthesized by vapor-liquid-solid growth in nanoporous alumina templates*. Journal of Crystal Growth, 2003. **254**(1-2): p. 14-22.
55. Westwater, J., et al., *Growth of silicon nanowires via gold/silane vapor--liquid-solid reaction*. Journal of Vacuum Science & Technology B: Microelectronics and Nanometer Structures, 1997. **15**(3): p. 554-557.
56. Kroll, U., et al., *Origins of atmospheric contamination in amorphous silicon prepared by very high frequency (70 MHz) glow discharge*. Journal of Vacuum Science & Technology A: Vacuum, Surfaces, and Films, 1995. **13**(6): p. 2742-2746.
57. Masanori Otobe, M.K.a.S.O., *Selective Etching of Hydrogenated Amorphous Silicon by Hydrogen Plasma*. Japanese Journal of Applied Physics, 1994. **33**: p. 4442-4445.
58. Scully, S.R. and M.D. McGehee, *Effects of optical interference and energy transfer on exciton diffusion length measurements in organic semiconductors*. Journal of Applied Physics, 2006. **100**(3): p. 034907-5.
59. Mikhnenko, O.V., et al., *Exciton diffusion length in narrow bandgap polymers*. Energy & Environmental Science, 2012. **5**(5): p. 6960-6965.

Chapter 3

NANO-STRUCTURED HYBRID SOLAR CELLS

3.1	INTRODUCTION.....	68
3.2	DEVICE DESIGN, FABRICATION AND WORKING PRINCIPLE.....	70
3.3	PHOTOVOLTAIC EFFECT ESTABLISHMENT BY PEDOT:PSS.....	74
3.4	MORPHOLOGY OF SiNWs & PHOTOVOLTAIC EFFECTS.....	86
3.5	CONCLUSION: REQUIREMENTS FOR PHOTOVOLTAIC ACTION	93
	<i>REFERENCE</i>	94

3.1 Introduction

Research and development for solar cells generally aim at high solar energy conversion efficiency with a low cost. Organic semiconducting materials and nano-structured materials are potential for the third generation of solar cells which represent the high efficiency and the low fabrication cost. In this context, hybrid solar cells based on silicon and an organic semiconducting polymer are worthy to be considered as an alternative. Recently, solar cells employing both inorganic and organic materials are drawing attentions as efficient solar cells by taking advantages of the materials, for examples, the high mobility and the light-trapping property of inorganic materials and the absorption and the process simplicity of organic materials.

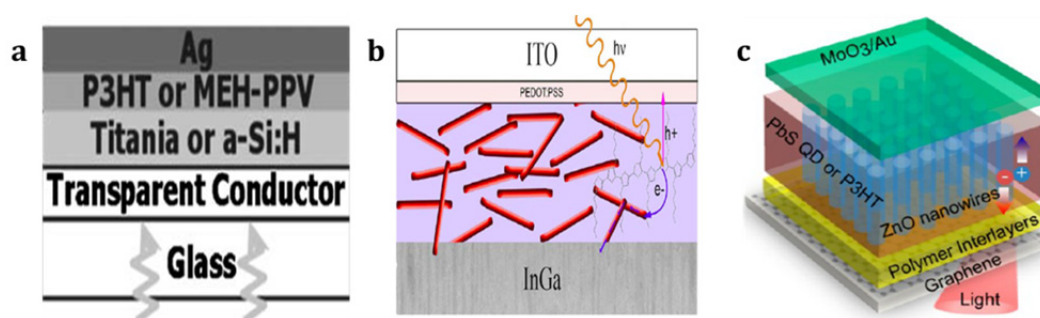


Figure 3.1 – Representatives of hybrid solar cells device structures (a) bi-layer type [1] (b) blend type [2] (c) Nano-structure type [3].

The structure design of solar cells is one of important factors to make a best use of both organic and inorganic materials for the solar cell application. The structural approaches of solar cells are classified into three different types. Figure 3.1 represents solar cell structures according to the junction area and the carrier transport methods. Figure 3.1 (a) is a bi-layer structure which is made of sequential deposition of the planar films of an inorganic material (titania or a-Si:H) and an organic semiconducting polymer (poly(3-hexylthiophene-2,5-diyl) (P3HT) and poly[2-methoxy-5-(2'-ethylhexyloxy)-p-phenylene vinylene] (MEH-PPV)). The junctions between organic and

inorganic materials where excitons are dissociated are formed by the planar interface with same surface area as top electrode. The limited junction area restricts efficient exciton dissociation although it guarantees independent carrier transport pathways. Also, the general exciton diffusion length of organic semiconductors is around 1-10 nm [4-7]. It means that the exciton within 10 nm from the interface could only contribute to the photo-generated carrier creation. Thus, 0.3 % of power conversion efficiency was reported [1]. Solar cells based on the blend of donor and acceptor materials are designed for large interface area. Semiconductor nanowires, nano-rods and nano-particles are used as an acceptor material [8-11]. Figure 3.1 (b) describes one example of blend type hybrid solar cells which employs P3HT donor and gallium nanowires electron acceptor. This structure promotes exciton dissociation due to the larger surface area. However, the carrier transport is pointed out as the shortage of this structure since the formation of independent carrier pathways is restricted. A nano-structured hybrid solar cell suggests an alternative depicted in Figure 3.1 (c). It shows the hybrid solar cell based on P3HT donor and zinc oxide nanowires as an electron acceptor. Both the large interface area and the carrier transport pathways are achieved. Therefore, it is regarded as an ideal structure for an effective photovoltaic action. In this context, the SiNWs are the interesting inorganic material for realizing the nano-structured hybrid solar cell with their light trapping property and adjustable nano-morphology [12-15].

In this chapter, the realization of the hybrid solar cells based on the Sn-catalyzed SiNWs and organic materials is mainly dealt with, aiming to propose an alternative solar cell structure. To fully benefit from the Sn-catalyzed SiNWs studied in Chapter 2, the hybrid solar cell is designed to profit by the light-trapping through the nanowires for an organic active layer. Despite of theoretical advantages of hybrid solar cells, there are practical hurdles to overcome for the establishment of the photovoltaic action. The key points are ‘interface’ and ‘geometry’ precisely. For the better interface, PEDOT:PSS buffer layer plays an important role to overcome the hurdles by smoothening nano-structured surface and by simplifying complex interfaces

causing the loss of photo-generated carriers. The thickness effect of PEDOT:PSS is also discussed for further insights into the influences on the solar cells. On the other hand, the relation between the SiNWs length and the thickness of organic materials is critical for the device performance in terms of geometry. Based on the experimental results, we will discuss the optimum configuration of our solar cells. Then, the correlation of solar cell performance with the SiNWs density is studied to fully discuss geometric effects.

3.2 Device design, fabrication and working principle

Hybrid solar cells in this study are consisted of PECVD grown SiNWs and organic materials formed by solution process. During the study, the spin-coating method used widely in organic solar cell research due to the simplicity of process is employed.

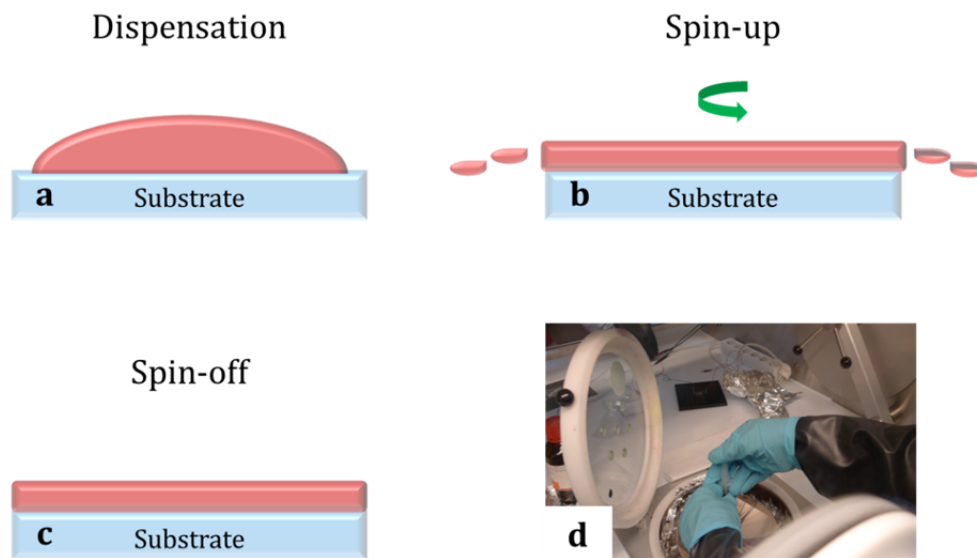


Figure 3.2 – Description of spin-coating method; (a) Dispensation of prepared solution on substrate (b) Spin-up stage (c) Spin-off and film formation and (d) The photo of spin-coating process.

Figure 3.2 describes a spin-coating process. This is a method to form a thin-film from a solution. At first, the solution is dropped on a substrate fixed

by vacuum (Figure 3.2 (a)). In this study, 1,2-Dichlorobenzene is used as the solvent for P3HT and Phenyl-C61-butyric acid methyl ester (PCBM). The concentration of the solution is 15 mg/mL or 30 mg/mL. Then the substrate is rotated according to the programmed conditions such as a rotation speed in rpm, acceleration, duration, etc. (Figure 3.2 (b)). Here, A two steps process is employed. 3000 rpm, 30s and 4000 rpm, 30s is mostly used for PEDOT:PSS, and 500 rpm, 30s and 1000 rpm, 45s are chosen for the organic active layer. Most of solution is lost to the outside of substrate due to the rotation. After spin-off, the thin-film is obtained on the substrate (Figure 3.2 (c)). The final film thickness is affected by many parameters such as the rotation speed, the duration, the concentration of solutions, the volume of solution, etc. Figure 3.3 shows the film thickness of P3HT and PEDOT:PSS with the solution concentration and the rotation speed, respectively. As the concentration of solution increases, the thickness of the P3HT film naturally increases. The thickness is controllable from 20 nm to 230 nm and it tends to increase linearly with the concentration in our experimental conditions (Figure 3.3 (a)). On the other hand, the thickness of the PEDOT:PSS film is decreased by increasing the rotation speed as shown in Figure 3.3 (b). The thickness of PEDOT:PSS film is dropped from 90 nm to 60 nm with 1000 rpm increment.

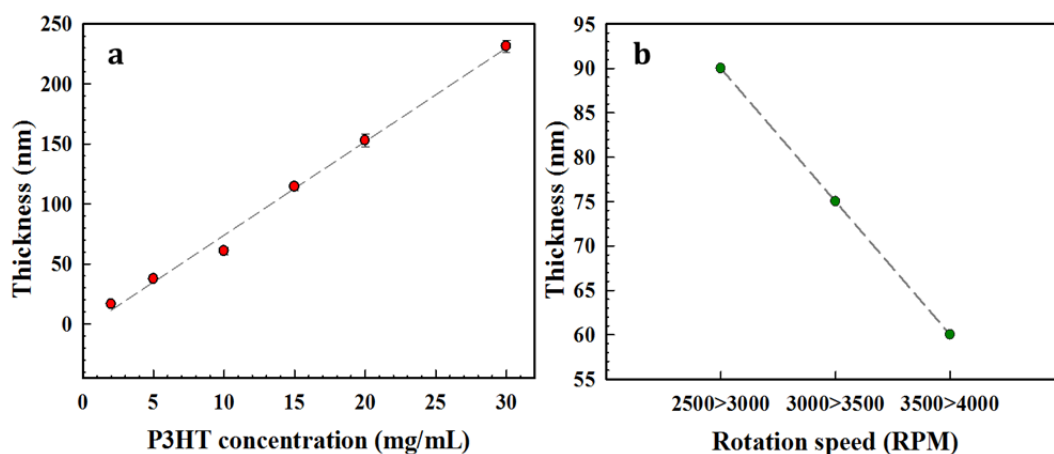


Figure 3.3 – Film thickness of (a) P3HT dissolved in 1,2-Dichlorobenzene according to the solution concentration from 2 mg/mL to 30 mg/mL and (b) PEDOT:PSS according to the rotation speed from 3000 rpm to 4000 rpm.

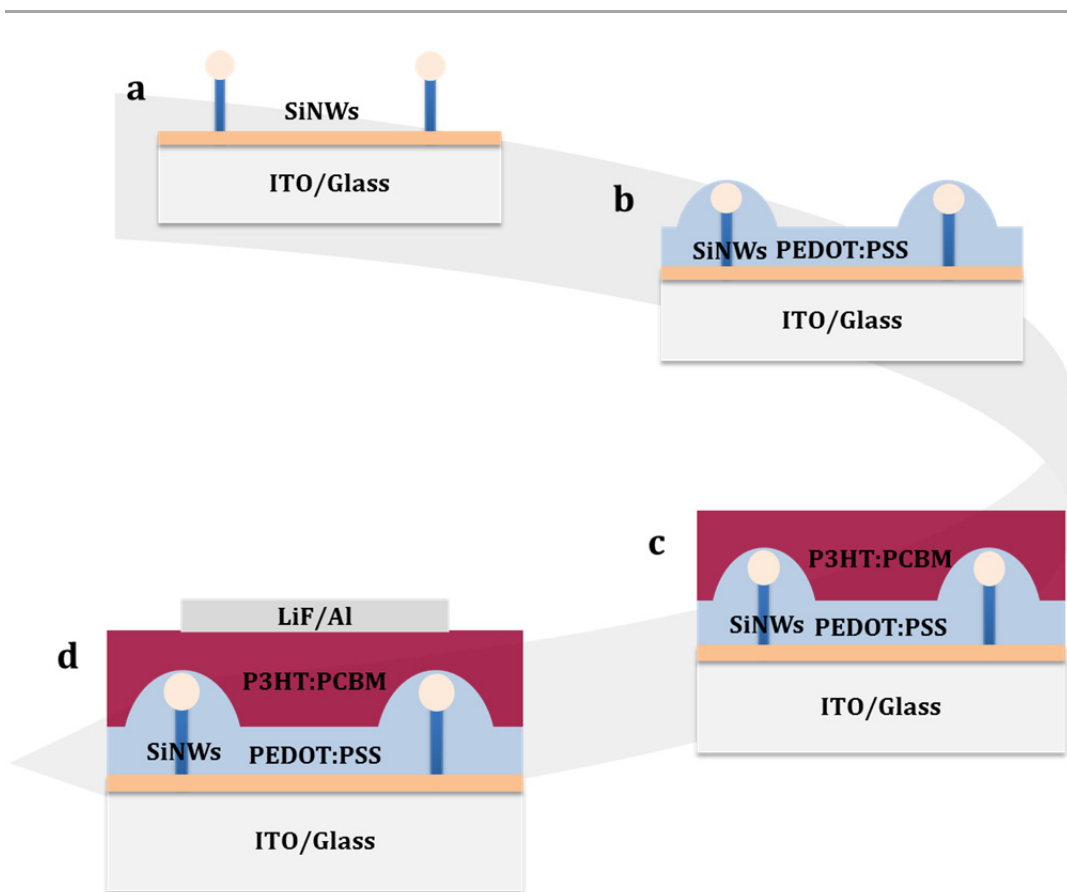


Figure 3.4 – Nano-structured hybrid solar cell fabrication process (a) as grown Sn-catalyzed SiNWs, (b) deposition of PEDOT:PSS buffer layer by spin coating, (c) deposition of P3HT:PCBM layer on PEDOT:PSS and (d) final device with LiF/Al top electrode.

The nano-structured hybrid solar cells based on the Sn-catalyzed SiNWs is the focus of the chapter. The appropriate application is necessary, depending on their nano-morphology. SiNWs generally showed interspacing between SiNWs over 100 nm as mentioned in Chapter 2. Meanwhile, The exciton diffusion length of P3HT is about 10 nm. The SiNWs would be unfavorable for efficient exciton dissociation, that is, it is not good choice as an electron acceptor material. Alternatively, it seems to be intelligent to use the SiNWs as light-trapping media in our solar cell structure. Based on this idea, one structure was proposed to enhance the light-trapping property. Figure 3.4 illustrates the process flow and the proposed solar cell design. On the as grown SiNWs on ITO (Figure 3.4 (a)), PEDOT:PSS which is a solution based on the water is spin-coated on the SiNWs (Figure 3.4 (b)). Then, the solution of P3HT:PCBM dissolved in 1,2-Dichlorobenzene is spin-coated on

PEDOT:PSS layer as main light absorbing layer (Figure 3.4 (c)). Finally, lithium fluoride and aluminum (LiF/Al) is deposited by thermal evaporation as a cathode (Figure 3.4 (d)). The structure is similar to the conventional organic bulk-heterojunction solar cell except the SiNWs array. Accordingly, the basic working principle is analogous with the organic bulk-heterojunction solar cell.

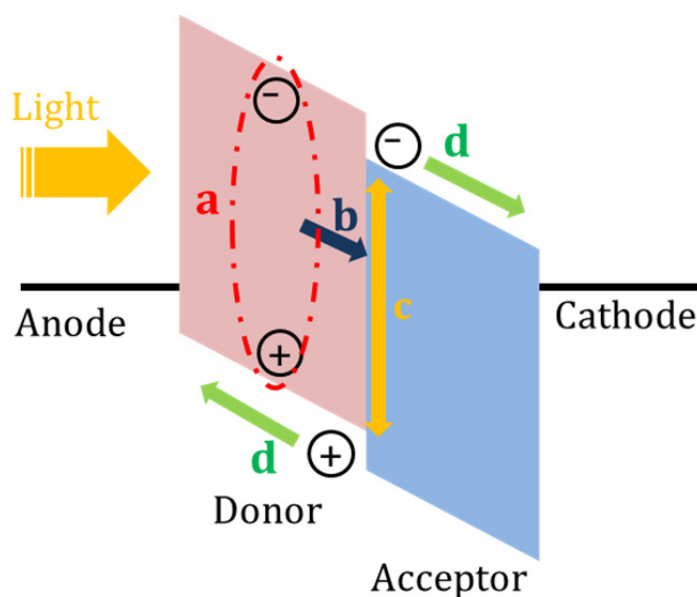


Figure 3.5 – Band diagram explaining general working principle of organic solar cells which is quite similar with the hybrid solar cell in this study.

Figure 3.5 describes the basic working principle of organic solar cells. The incident light is mainly absorbed in an organic donor material, which is P3HT here, then, the exciton is formed in the donor material (a). After exciton creation, it diffuses toward the interface formed by the donor and acceptor materials (b). The exciton is dissociated into a free electron and hole by the band offset energy at the interface (c). Electron is transferred to the LUMO level of the acceptor and hole is on the HOMO level of the donor. Then, they are transported toward corresponding electrodes by the internal electric field (d). This principle can be equally applied to our hybrid solar cells because it uses P3HT:PCBM blend for the light absorption and the generation of photo-generated carriers is like the conventional organic solar

cell based on P3HT:PCBM. The process (d) should be different for holes in the hybrid solar cells. The holes pass through not only PEDOT:PSS layer like organic bulk-heterojunction solar cells but also the SiNWs array during a journey to ITO. The details will be discussed in Chapter 4.

3.3 Photovoltaic effect establishment by PEDOT:PSS

Attempts to use SiNWs with the blend of P3HT and PCBM [16, 17] were made in few groups. In the work of Kuo et al [16], they used Au-catalyzed SiNWs by VLS process for the enhancement of organic active layer's absorption and the charge transport. They demonstrated a photovoltaic action but they showed poor solar cell performance; especially, open-circuit voltage (V_{oc}) is only 0.26 V although they optimized top electrode to assign an optimal role to SiNWs. This value is lower compared to the conventional P3HT:PCBM bulk-heterojunction solar cells which are reported elsewhere ($V_{oc} \sim 0.6$ V) [18]. This is probably due to an energy band mismatch between the nanowires and organic active layer, weak electrode selectivity [19] and surface states of the gold-catalyzed SiNWs [20]. Another example is the work of Huang et al [17]. They choose SiNWs which is fabricated by the etching of a crystalline silicon wafer to obtain the high quality SiNWs compared to chemically synthesized SiNWs [21]. Although short-circuit current (J_{sc}) and power conversion efficiency (η) are improved by introducing the SiNWs but V_{oc} of the solar cell was 0.4 V that is also lower than conventional P3HT:PCBM organic bulk-heterojunction solar cells. V_{oc} could mainly be determined by the P3HT:PCBM for the hybrid solar cell in this study because of the blend is the main light absorbing layer. The diminution in V_{oc} from the theoretical maximum is occurred when there are non-radiative decay pathways which promote the leakage current flow and the recombination [22]. From both references [16, 17], it is in doubt that the SiNWs in blend are correlated with the decrease in V_{oc} . Here, the investigation on the photovoltaic effect of nano-structured hybrid solar cells is carried out. The photovoltaic effect has been well established by inserting organic conducting

polymer PEDOT:PSS between the SiNWs array and the P3HT:PCBM layer . The V_{oc} was 0.59 V at maximum which is higher than that of similar hybrid systems [16, 17]. The influence and the role of the PEDOT:PSS in our solar cell will be discussed with the thickness change.

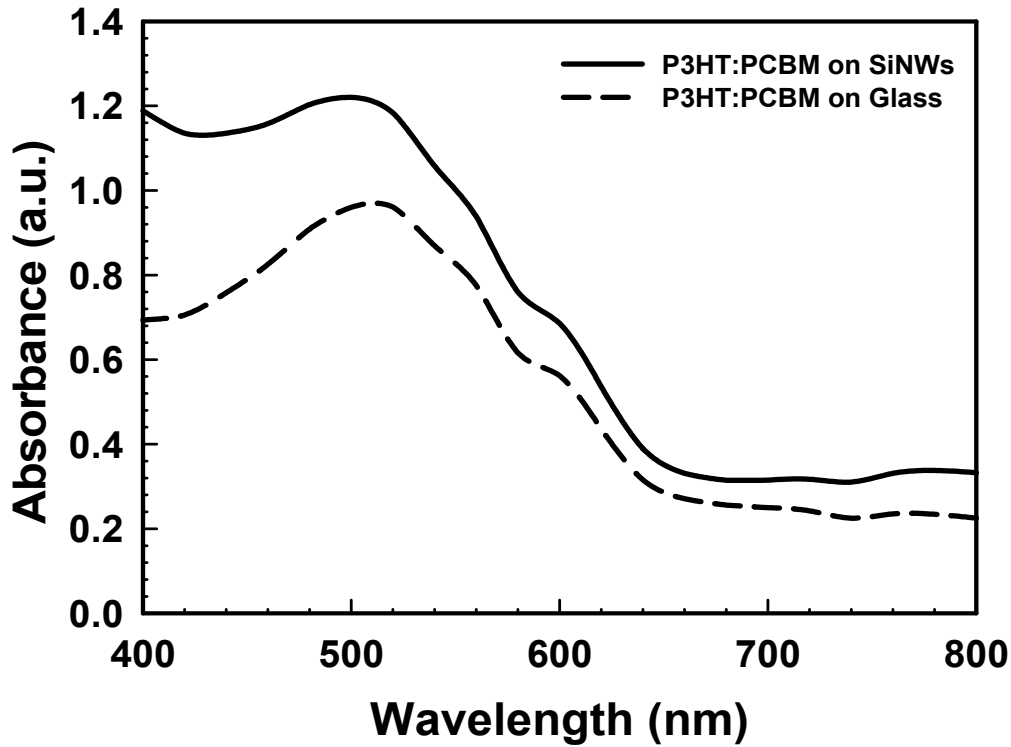


Figure 3.6 – Absorbance of P3HT:PCBM layer on glass (dashed line) and SiNWs (solid line)

Figure 3.6 shows the absorbance of P3HT:PCBM layer on glass or the SiNWs which are characterized with 400 nm to 800 nm range of wavelength region by UV-Vis spectroscopy. Both spectra exhibit a maximum absorbance around 510 nm and a shoulder around 600 nm. This coincides with a general P3HT absorption spectrum. P3HT:PCBM on the SiNWs has higher absorbance than the layer on glass. As depicted, P3HT:PCBM layer is in charge of main absorber in our hybrid solar cells. The solar cells could take advantages from the SiNWs in terms of optical aspect, that is, absorption enhancement in P3HT:PCBM layer. It is well known that the absorbance of the SiNWs can be changed, depending on dimensional properties such as

length, diameter and density [23]. To minimizing the absorption of the SiNWs for enhancing the absorption of P3HT, we have grown SiNWs with length, diameter and density around 280 nm, 30 nm and $1.0 \times 10^9/\text{cm}^2$, respectively. The SiNWs are relatively shorter and smaller than other SiNWs for solar cells applications [12, 14, 24]. This fact contributes to increase the absorption of P3HT, thus, the higher J_{sc} is expected. As mentioned above, the spacing between the nanowires is insufficient to dissociate exciton of P3HT efficiently. This is the reason why we employed P3HT:PCBM blend.

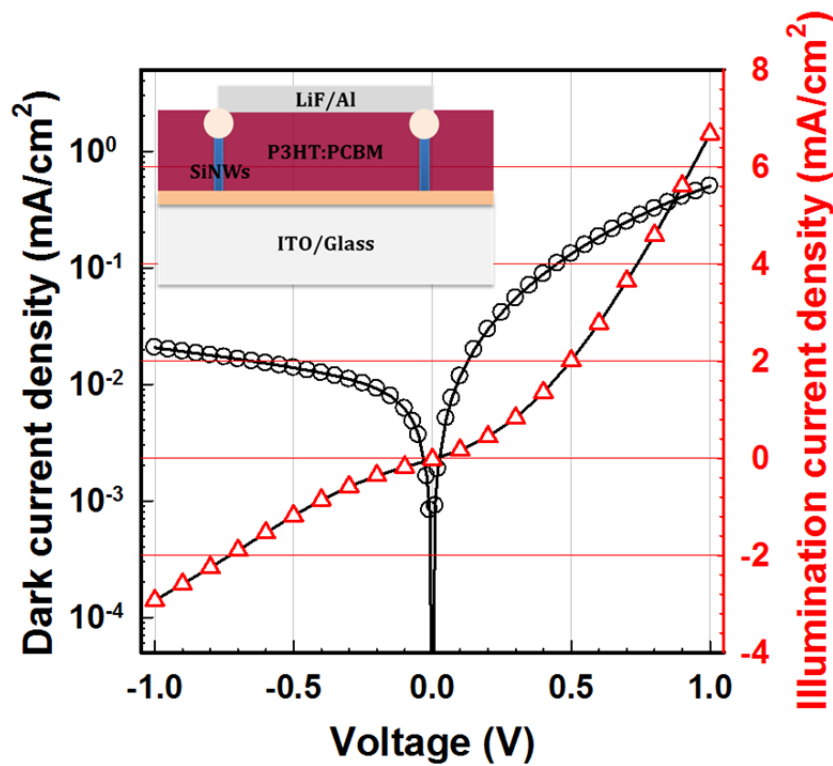


Figure 3.7 – Current density-voltage characteristics of hybrid solar cells under dark (black, left y-axis in semi-log scale) and AM 1.5 (red, right y-axis in linear scale). The inset figure describes device structure (Glass/ITO/SiNWs/P3HT:PCBM/LiF/Al)

Figure 3.7 shows current density - voltage characteristics of the hybrid solar cells with structure of ITO/SiNWs/P3HT:PCBM/LiF/Al as shown in the inset of Figure 3.7. Despite of the expectation by nanostructure and optical benefit, this solar cell exhibits very poor electrical performance. Dark current density is limited over measured voltage range due to the resistive effects.

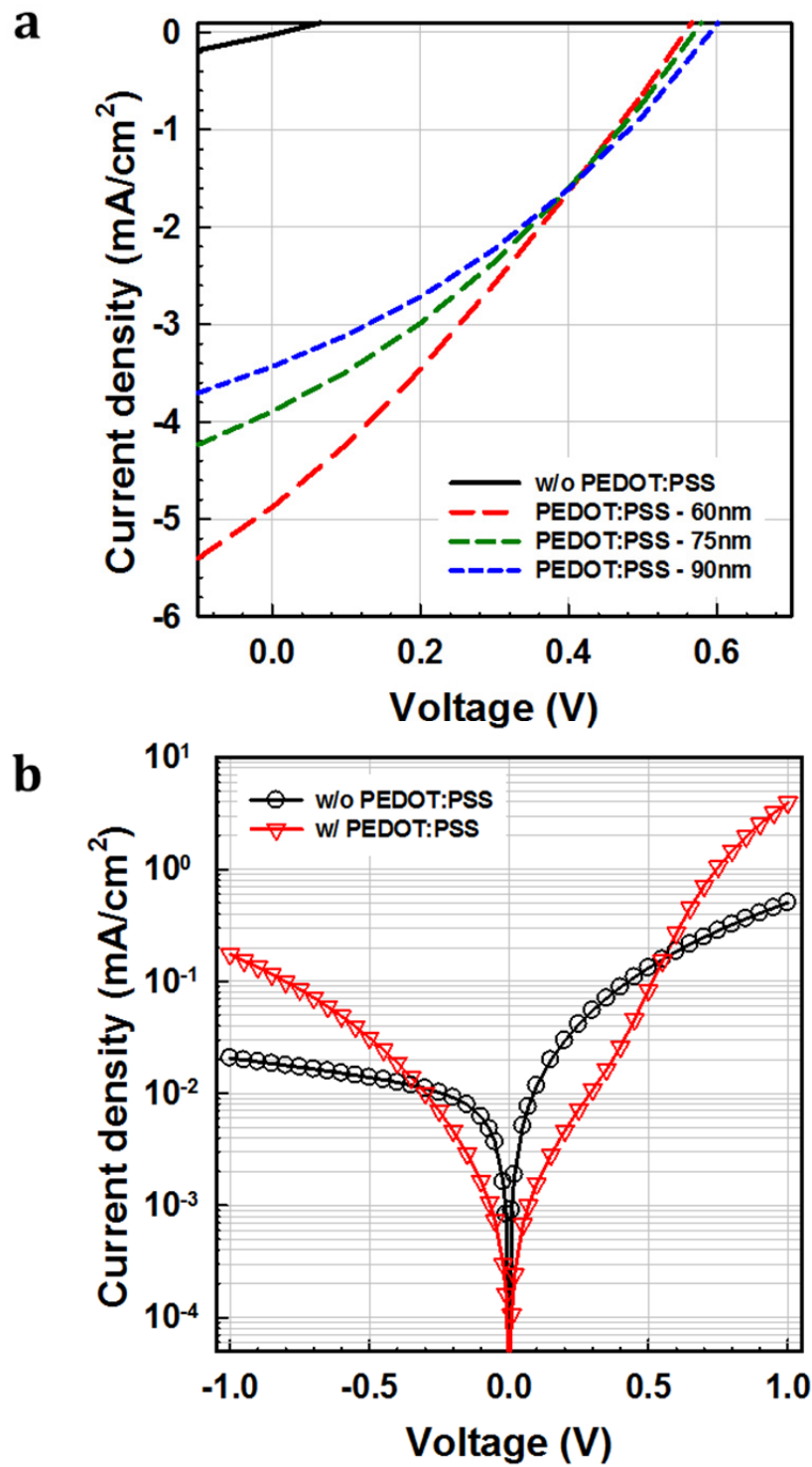


Figure 3.8 – Hybrid solar cells performance according to the PEDOT:PSS existence and thickness (a) under AM 1.5 illumination and (b) dark.

PEDOT:PSS thickness	J_{sc} mA/cm²	V_{oc} V	FF %	η %	R_s Ω·cm²	R_{sh} Ω·cm²
without	0.02	0.01	-	-	-	-
60 nm	4.9	0.55	29	0.78	90	171
75 nm	3.9	0.57	32	0.71	92	268
90 nm	3.4	0.59	34	0.68	95	343

Table 3.1 – Summary of solar cell parameters with various PEDOT:PSS thickness

On current density has 10^{-1} mA/cm² order and off current is 10^{-2} mA/cm² order. This limits diode performance, thus, the diode is not observed in a forward bias region [25]. The current density is improved by the illumination, namely, current density jumps up to 10^0 mA/cm² orders. It means that our solar cell demonstrates the increase in a photoconductivity under AM 1.5 condition. Photovoltaic effects are severely limited with $J_{sc}=0.02$ mA/cm² and $V_{oc}=0.01$ V. It is believed that photo-generated holes have difficulties to reach ITO because they have to cross the SiNWs array. It will discuss further in the next section.

PEDOT:PSS is introduced between the SiNWs array and P3HT:PCBM layer to overcome the obstacles which hinder the photovoltaic effect establishment. PEDOT:PSS is considered as a good candidate since it has high transparency, good hole selecting property with 5.2 eV of work function [19, 26]. Figure 3.8 shows solar cell performance with and without PEDOT:PSS layer under dark and AM 1.5 condition. Solar cell parameters are summarized in Table 3.1. Figure 3.8 (a) clearly shows that a PEDOT:PSS insertion brings dramatic improvement in the solar cell performance. First, V_{oc} is well established and it ranges from 0.55 V to 0.59 V, depending on the thickness of PEDOT:PSS. This is comparable to the theoretical maximum of P3HT:PCBM based solar cells. And strikingly, it is higher than that of the hybrid solar cells discussed above. J_{sc} is also significantly improved. It reaches 3.4 mA/cm² and 4.9 mA/cm² according to the thickness of

PEDOT:PSS. The thinner PEDOT:PSS results in the higher J_{sc} . As a result, the power conversion efficiency is reached 0.79 % with 60 nm of PEDOT:PSS. Meanwhile, the dark current density-voltage characteristic in Figure 3.8 (b) also proves the effects of PEDOT:PSS. Diode characteristic is established in forward bias regime with PEDOT:PSS interlayer. This is might be attributed to improved anode selectivity by high work function of PEDOT:PSS (5.2 eV).

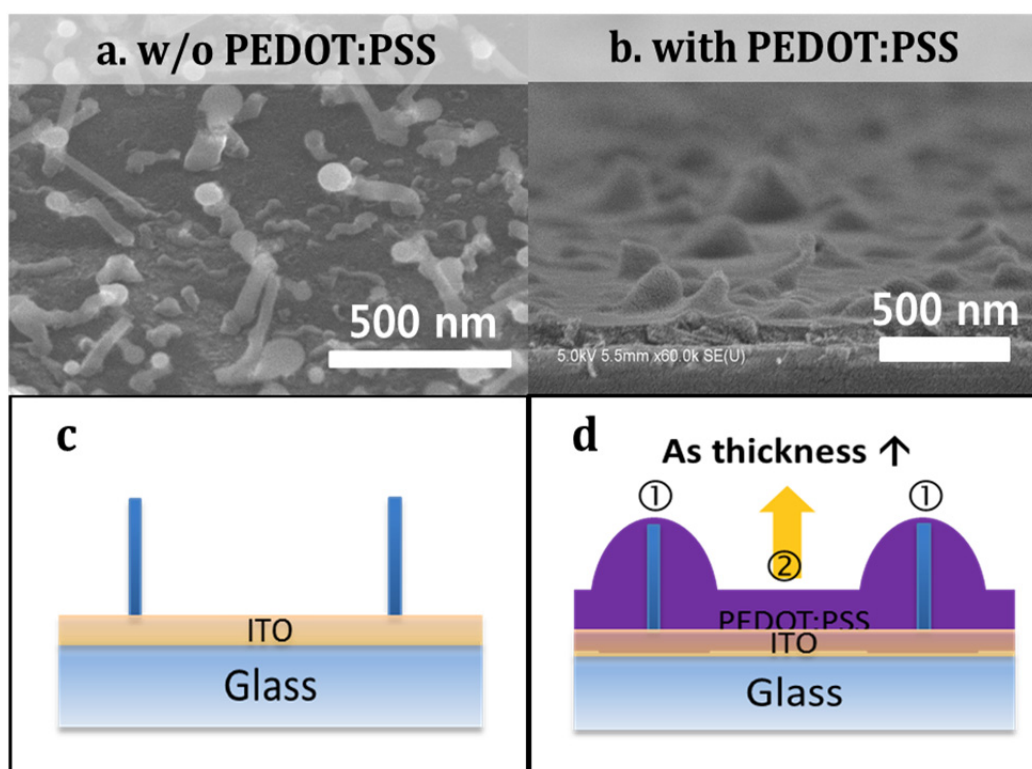


Figure 3.9 – SEM images of (a) as grown SiNWs and (b) SiNWs covered by PEDOT:PSS and Schematic diagram of (c) as grown SiNWs and (d) SiNWs covered by PEDOT:PSS

A tentative explanation of these results could start from a consideration in optical and electrical aspects. The unique difference between the above experiments is the presence of PEDOT:PSS. The SiNWs arrays grown by same conditions at same time are used for the hybrid solar cells fabrication. And P3TH:PCBM films are deposited from a same bottle with identical spin-coating conditions. Naturally, P3HT:PCBM film deposited on SiNWs without PEDOT:PSS could absorb more incident light since there is no loss of the incident light by PEDOT:PSS. Thus, it might not be the optical problem but

electrical problem. The device structure of the hybrid solar cell in Figure 3.4 (d) gives an idea to find the origin of problems. The cathode side, that is P3HT:PCBM/LiF/Al, is already demonstrated and verified in plenty number of literatures [27-31]. Therefore, it is in doubt that the SiNWs at anode side probably causes drawbacks. We supposed that rough surface by the SiNWs, complex interfaces and anode selectivity at anode side without PEDOT:PSS could mainly limit solar cell performance in this hybrid system. Figure 3.9 shows SEM images and schematic diagrams of as grown SiNWs and the SiNWs covered by PEDOT:PSS. As grown SiNWs naturally provide the highly rough surface to P3HT:PCBM due to the inherently high aspect ratio (length/diameter) around 9 here. The needle-like SiNWs could result in the large leakage current of solar cells in combination with organic materials. It is well known that organic materials are sensitive to rough surface and large peak-to-valley roughness causes the large leakage current [32]. PEDOT:PSS is spin-coated over this rough surface to make it smooth (Figure 3.9 (b), (d)). It means that the morphology of the needle-like nanostructure becomes a hill-like shape with PEDOT:PSS coating. This smoothening effect might reduce the leakage current at low voltage regime in Figure 3.7 (b). Furthermore, the anode selectivity could be improved by PEDOT:PSS. The SiNWs have a conduction band at 4.0 eV and a valence band at 5.12 eV because of its crystallinity. By introducing PEDOT:PSS, which have an energy level of 5.2 eV, the energetic mismatch between the SiNWs and P3HT/PCBM is reduced.

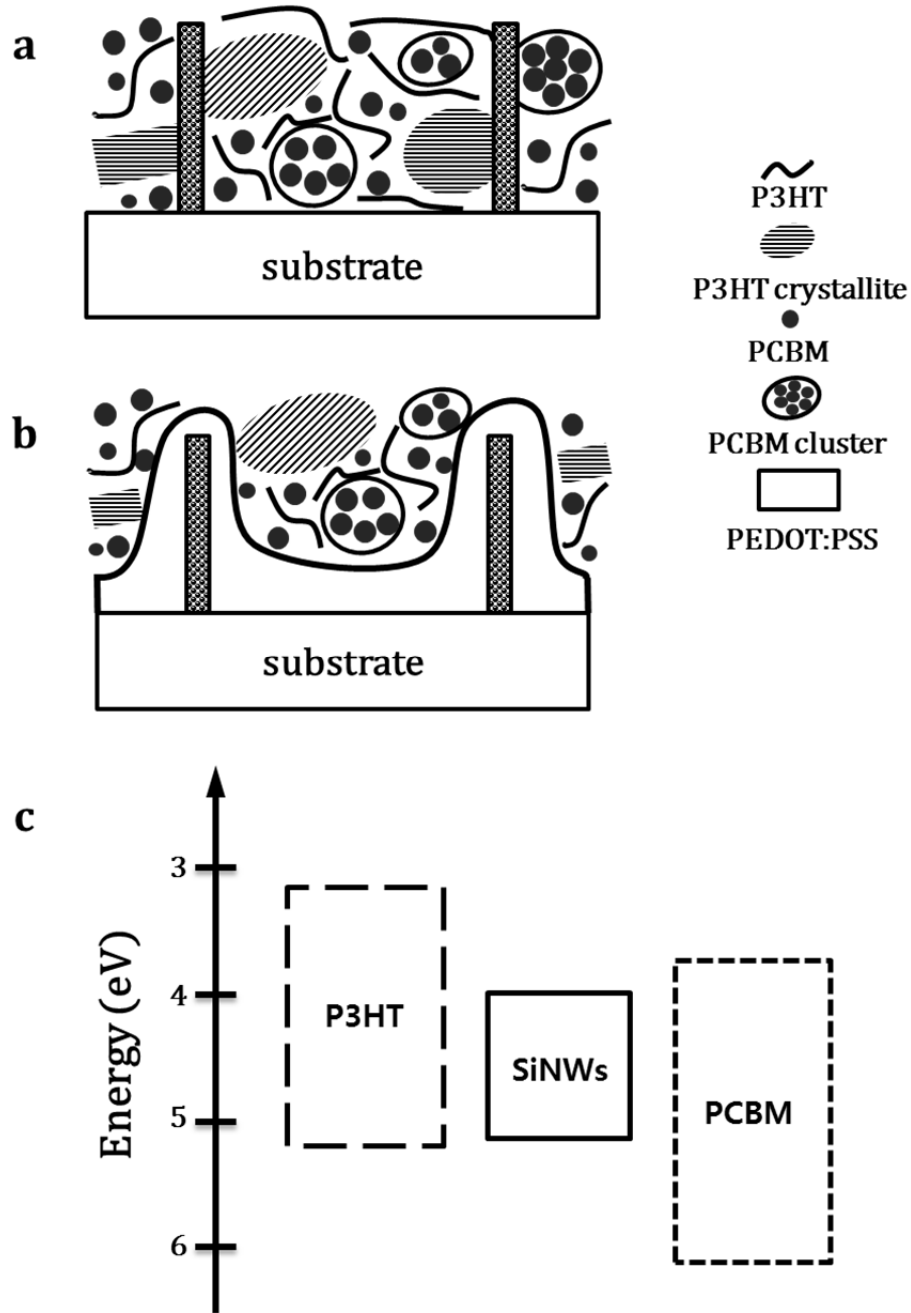


Figure 3.10 – Schematic diagram of P3HT:PCBM layer on SiNWs (a) without, (b) with PEDOT:PSS and (c) energy band diagram of P3HT, PCBM, and SiNWs

A noticeable role of PEDOT:PSS is the interface simplification. The solar cells without PEDOT:PSS have many interfaces which make solar cell functions complex. It means that the P3HT:PCBM interface studied by many research groups [33-37] is seriously affected by the SiNWs. Figure 3.10 shows the schematic diagram of hybrid solar cells without and with PEDOT:PSS layer and the energy band diagram of P3HT, PCBM and SiNWs.

For the hybrid solar cell without PEDOT:PSS, there exist interfaces of P3HT/PCBM, SiNWs/P3HT and SiNWs/PCBM. This is highly difficult to understand clearly. Note again that P3HT is principal light absorbing material, namely, excitons are generated in P3HT and dissociated at interfaces. Electron is transferred from LUMO of P3HT to LUMO of PCBM through charge transfer state at P3HT/PCBM interface [33, 34] and hole stays HOMO of P3HT. Meanwhile, the exciton of P3HT can be also dissociated by electron transfer from LUMO of P3HT to the conduction band (CB) of SiNWs at the SiNWs/P3HT interface. Next, the contrary could be occurred at the SiNWs/PCBM interface. the SiNWs and PCBM tend to have hole and electron respectively [38]. Thus, a single nanowire could have the electron from P3HT and the hole from PCBM. This situation is described in Figure 3.10 (a). In that case, the photo-generated electron and hole recombine in the nanowire. These complex interfaces would not ensure the photovoltaic action when it is measured under AM 1.5 conditions (Figure 3.7 (a)).

These complex interfaces can be simplified by PEDOT:PSS. Figure 3.10 (b) describes the schematic diagram of hybrid solar cells with PEDOT:PSS. PEDOT:PSS on the SiNWs shows a particular role which is different from planar solar cells. Here, PEDOT:PSS isolates the SiNWs array from the P3HT:PCBM layer. It prevents the SiNWs/P3HT and the SiNWs/PCBM interfaces formation, namely, single SiNW could not have electron and hole from P3HT and PCBM, respectively. And it guarantees the photovoltaic action of the P3HT:PCBM layer just like a typical organic bulk-heterojunction solar cells. Consequently, created excitons in P3HT are dissociated at P3HT:PCBM interfaces. Then, electrons move toward LiF/Al electrode through percolated pathways of PCBM and holes move toward ITO through percolated pathways of P3HT, PEDOT:PSS and SiNWs array. The SiNWs mainly plays the role of light-trapping media.

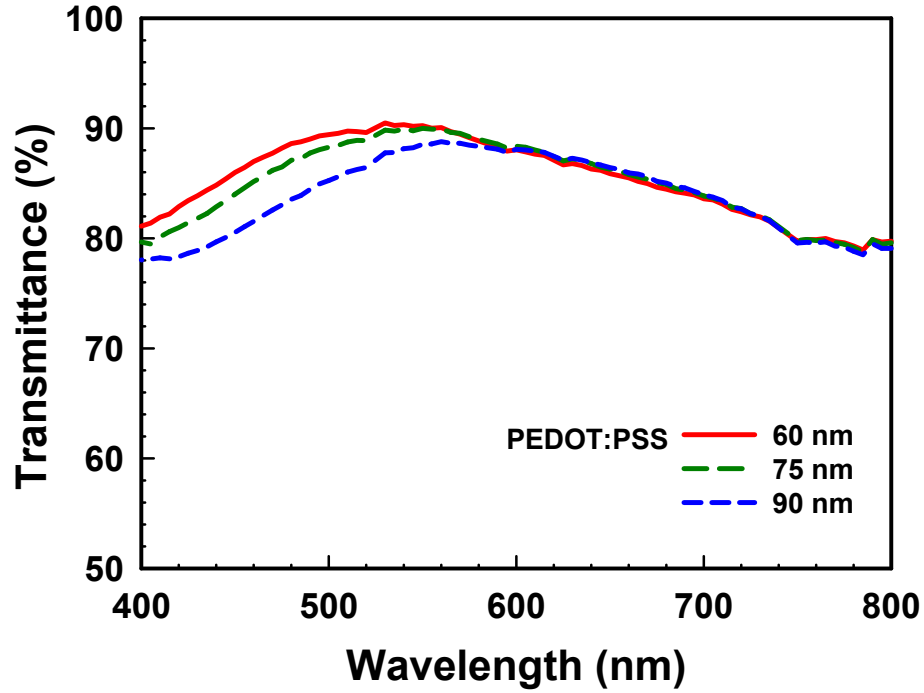


Figure 3.11 – Transmittance of PEDOT:PSS layer on ITO with thickness variation

Influence of PEDOT:PSS thickness was investigated. The thickness of PEDOT:PSS was modified with different rotation speed of spin-coater. Solar cells performance is affected by a thickness change. Results are summarized in Figure 3.7 (a) and Table 3.1. As thickness increases, V_{oc} and FF tend to increase whereas J_{sc} tends to decrease. The η is written as the following equation,

$$\eta = \frac{J_{sc} \cdot V_{oc} \cdot FF}{P_{light}} \quad (1)$$

η is decreased as the thickness increases despite of V_{oc} and FF increases because J_{sc} is more seriously influenced by the thickness variation. As the thickness increases, the decrease in transmittance near 400 nm to 600 nm wavelength ranges in Figure 3.11 and a little increase in R_s are observed (Table 3.1). The decrease in transmittance of PEDOT:PSS means the decrease in absorption of P3HT. It results in the J_{sc} diminution. In the work of Y. Kim et

al, J_{sc} of P3HT:PCBM bulk-heterojunction solar cells is changed only 10 % with PEDOT:PSS thickness range from 50 nm to 160 nm [19]. The thickness of PEDOT:PSS didn't demonstrate significant effects in the planar structure. However, our results showed a large variation in J_{sc} although the thickness of PEDOT:PSS is only altered 30 nm. J_{sc} is 4.9 mA/cm² with 60 nm thick PEDOT:PSS. In contrast, it is 3.4 mA/cm² with 90 nm thick PEDOT:PSS. The 30 % of J_{sc} change is observed.

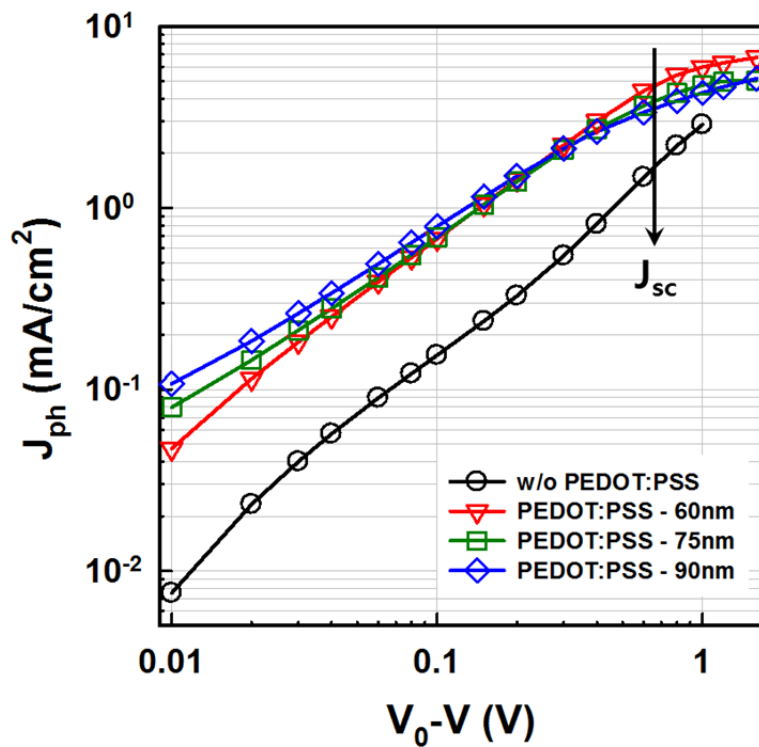


Figure 3.12 – Experimental photo-current density (J_{ph}) – effective voltage plots: J_{ph} is extracted by the equation $J_{ph} = J_L - J_D$.

The reason why the thickness of PEDOT:PSS is sensitive to J_{sc} is found in experimental photo-current density (defined by J_{ph}) characteristics. The experimental J_{ph} could be easily extracted by using dark (J_D) and illumination (J_L) current density with the equation given by

$$J_L = J_D + J_{ph}, \text{ thus, } J_{ph} = J_L - J_D \quad (2)$$

Then, extracted J_{ph} is plotted as a function of effective voltage ($V_0 - V$) in double logarithm scale. V_0 is defined as the voltage where $J_L - J_D = 0$ and V is the applied voltage. Note that the thickness variation of PEDOT:PSS has effects on the effective voltage dependency of J_{ph} shown in Figure 3.12. At the lower effective voltage regime ($V_0 - V < 0.1$ V) where diffusion has important role, J_{ph} scales linearly with the effective voltage regardless of the thickness of PEDOT:PSS that implies the competition of diffusion and drift of photo-carriers. The thicker PEDOT:PSS shows the higher J_{ph} in this regime. It implies that the thicker layer leads to higher diffusion of photo-carriers at lower effective voltage regime. But, the tendency of J_{ph} is advantageous to the thinner PEDOT:PSS as the effective voltage increases. At the higher effective voltage regime ($V_0 - V > 0.1$ V) where the drift is gradually increased by higher applied voltage, the J_{ph} enters the saturation regime. The recombination limited [39] or space-charge limited photo-current [40] characteristics of J_{ph} are not observed in this experiment. The tendencies of J_{ph} are turn over in this regime where J_{sc} is determined. The thinner PEDOT:PSS results in higher J_{ph} over 0.2 V of effective voltage, therefore the solar cell with 60 nm of PEDOT:PSS produces the higher J_{sc} than others. The solar cells with thinner PEDOT:PSS show stronger effective voltage dependence of J_{ph} than that with the thicker one.

3.4 Morphology of SiNWs & Photovoltaic effects

In general, nano-morphology of SiNWs, such as length, density and diameter, has critical effects on hybrid solar cells performances [41-43]. PECVD has possibilities to control process parameters, for example, growth time, temperature, pressure, gas flow, radio frequency power, etc. This implies that PECVD growth of SiNWs has certain flexibility of nano-morphology control. This section deals with the correlations between the nano-morphology of SiNWs with the hybrid solar cells performance, especially on the length and the density of SiNWs. Figure 3.13 depicts model diagrams of hybrid solar cells according to the configuration of the hybrid solar cells. Representatives are classed into three different cases. Case 1 shows that the length of SiNWs is longer than the total thickness of organic layers. It is observed that SiNWs penetrate organic active layer. In case 2, the length of SiNWs is similar with the thickness of organic layers. Lastly, case 3 shows shorter SiNWs' length than total thickness of organic layers. The length of SiNWs are modified by the growth time while P3HT:PCBM layer is formed with same experimental conditions. The thickness of PEDOT:PSS is 60 nm and P3HT:PCBM is 230 nm. The length of SiNWs are 700 nm, 280 nm and 140 nm for Case 1,2, and 3, respectively. The other parameters of PECVD except the growth time were kept unchanged to modify only the length of SiNWs. Figure 3.14 shows SEM images of the P3HT:PCBM layer on the SiNWs with different length. Figure 3.14 (a) and (b) for case 1 show longer SiNWs than organic layers' thickness. Most of SiNWs penetrate all organic layers. This induces the direct contact between LiF/Al and the SiNWs. In contrast, Figure 3.14 (c) and (d) for case 2 and 3 show that SiNWs are well covered by P3HT:PCBM, thus, LiF/Al contact only with P3HT:PCBM layer. These morphological differences are closely related with photovoltaic effect.

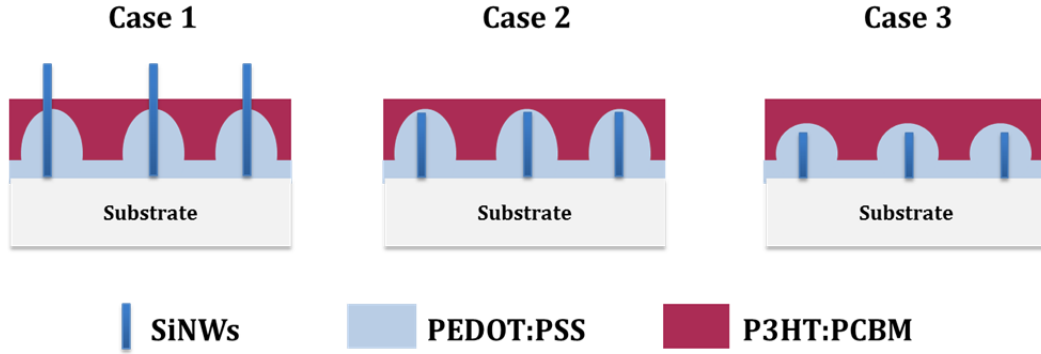


Figure 3.13 – Model diagrams of hybrid solar cells according to length of SiNWs and organic active layer thickness. (a) length of SiNWs > thickness of P3HT:PCBM, (b) length of SiNWs ~ thickness of P3HT:PCBM and (c) length of SiNWs < thickness of P3HT:PCBM,

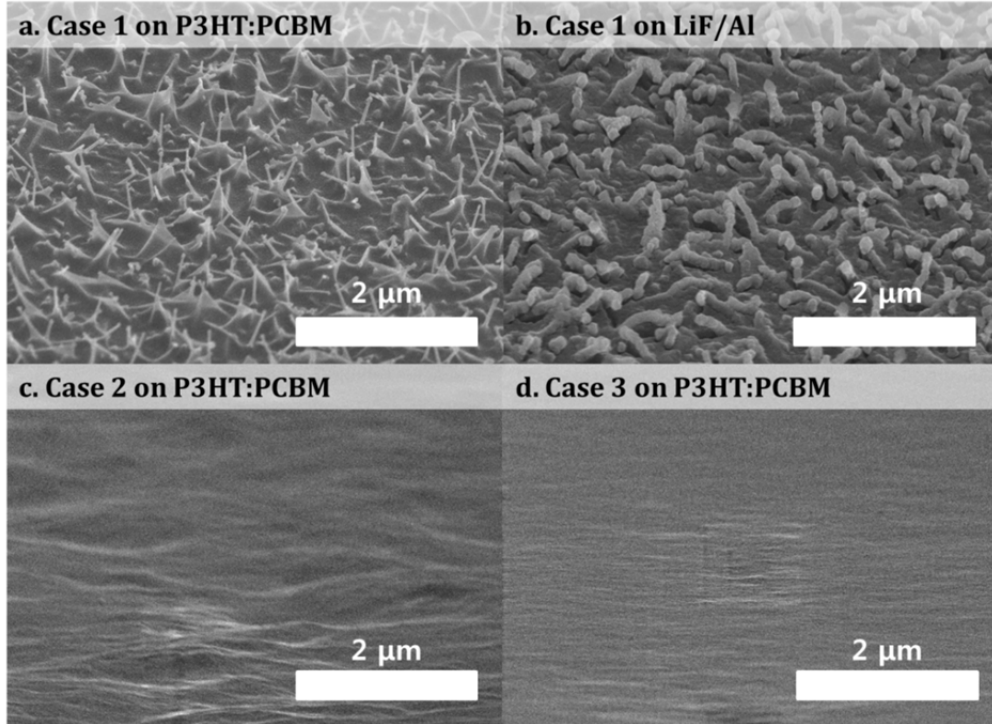


Figure 3.14 – SEM images of hybrid solar cells case by case. (a) Case 1 on P3HT:PCBM. (b) Case 1 on P3HT:PCBM/LiF/Al (c) Case 2 on P3HT:PCBM and (d) Case 3 on P3HT:PCBM

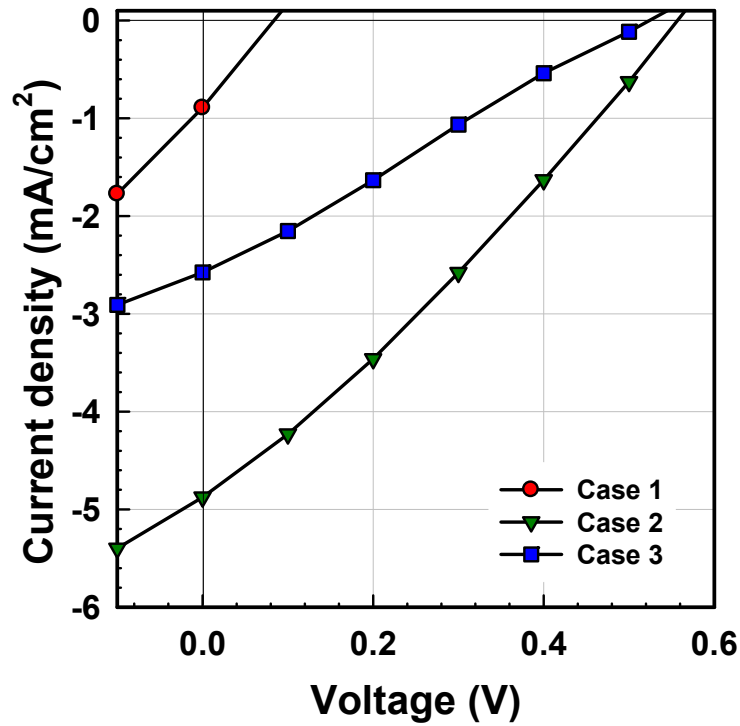


Figure 3.15 – Hybrid solar cell performance for three cases of SiNWs length and organic layer thickness relations. Measured under AM 1.5 condition.

	J_{sc} mA/cm^2	V_{oc} V	FF %	η %	R_s $\Omega \cdot cm^2$	R_{sh} $\Omega \cdot cm^2$
Case 1	0.9	0.09	26	0.02	0.09	0.07
Case 2	4.9	0.55	29	0.80	87	182
Case 3	2.6	0.52	25	0.34	233	266

Table 3.2 – Summary of hybrid solar cell parameters case by case

Figure 3.15 shows solar cell performance case by case and solar cell parameters are summarized in Table 3.2. Case 1 (SiNWs length > organic layers' thickness) has worse performance than other cases. There is a problem on V_{oc} establishment that is only 0.09 V. J_{sc} also shows a very limited value of 0.9 mA/cm² compared to best case. Penetrated SiNWs through organic layers create the shunting pathway due to the direct contact between LiF/Al and SiNWs [44]. Therefore, low resistance value is observed in Table 3.2. Even PEDOT:PSS buffer layer is useless if SiNWs too long to

cover. It implies that there are complex interfaces explained in previous section. Besides, SiNWs make cathode (LiF/Al) non-continuous. It means that photo-generated electrons could not be effectively collected to cathode which might be related with low J_{sc} . The solar energy conversion efficiency is too poor to call it as the solar cell. Meanwhile, Case 2 (SiNWs length \sim organic layers' thickness) demonstrates better solar cell performances than others. V_{oc} is 0.55 V that is comparable with that of organic bulk-heterojunction solar cells and higher than similar hybrid solar cells [16, 17]. 4.9 mA/cm² of J_{sc} is observed for Case 2 which is the highest value among three cases. By reducing the length of SiNWs, problems observed in Case 1 are resolved. Namely, a continuous cathode formation, a simple interface and no direct contact of SiNWs with cathode were achieved. Case 2 shows 0.8 % of power conversion efficiency. Case 3 (SiNWs length < organic layers' thickness) demonstrates solar cell curve between Case 1 and 2 (Figure 3.15). It keeps 0.52 V of V_{oc} which is slightly lower than Case 2. A great difference in J_{sc} between Case 2 and 3 is observed. One of reasons is high R_s for Case 3 that is two times higher than Case 2. This resistance governs overall curve of hybrid solar cells. It is believed that photo-generated holes near the cathode side travel longer way to come in PEDOT:PSS, but the distance is much shorter for Case 2. Long pathway might cause recombination during the transport. Accordingly, the optimum combination of the length of SiNWs with the thickness of organic layers is necessary to guarantee photovoltaic action and fully benefit from the SiNWs array. Consequentially, the length of SiNWs should be comparable to the thickness of organic layers for the performance establishment like Case 2.

Until now, the effects of correlation between the SiNWs' length and organic layers' thickness on photovoltaic action have been discussed. From now, the relation between the density of SiNWs and solar cell performance will be dealt with. The density control of the SiNW by H₂ plasma was studied in Section 2.4.2. As the SiNWs density increases, the absorption of SiNWs array is improved [45]. Real absorption of P3HT:PCBM layer (exclusion of SiNWs absorption) could be changed by the density of SiNWs.

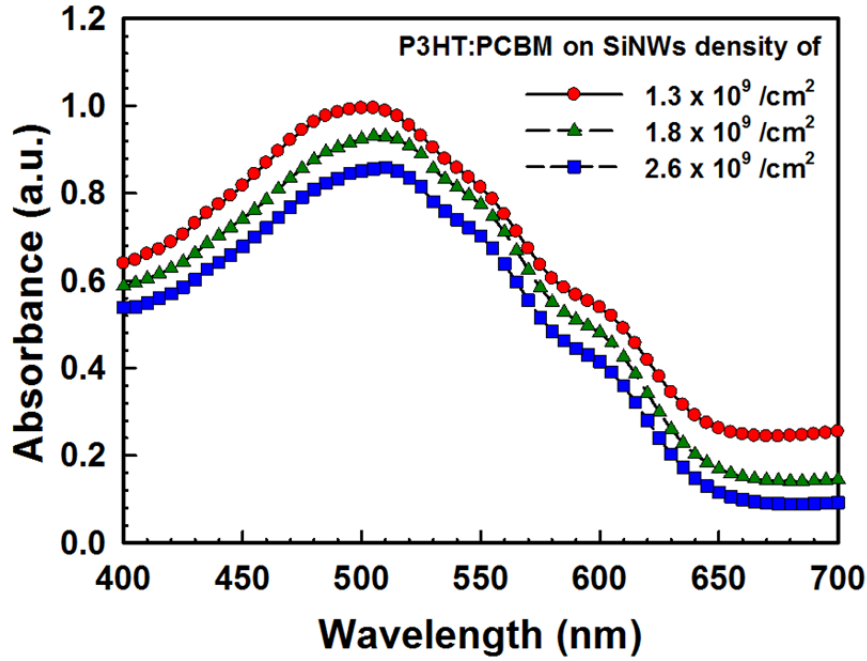


Figure 3.16 – Absorbance of P3HT:PCBM with different SiNWs density; SiNWs absorption is excluded.

Figure 3.16 shows the absorbance of P3HT:PCBM with excluding the absorption of the nanowires depending on the density of SiNWs. The length and the diameter of SiNWs are kept with 280 nm and 30 nm in average, respectively. P3HT is the dominant light absorbing material in these hybrid films. As stated above, they exhibited typical absorption property of P3HT. The absorbance of P3HT:PCBM is higher over the wavelength region as the density of SiNWs is lower. Especially, over 600 nm wavelength, there is absorption benefits in P3HT:PCBM layer due to the nanowires. Hybrid solar cells characteristics depending on the density of SiNWs are depicted in Figure 3.17 and the parameters are summarized in Table 3.3. As SiNWs' density decreases the better photovoltaic effect is observed. Lower density of SiNWs results in high J_{sc} and V_{oc} . The power conversion efficiency varied from 0.21 % to 0.77 % according to the density. J_{sc} could be increased due to P3HT:PCBM absorption improvement in Figure 3.16. High absorbance would result in higher photo-generated carriers in P3HT:PCBM layers if we assume same exciton separation probability, temperature and electric field [40, 46].

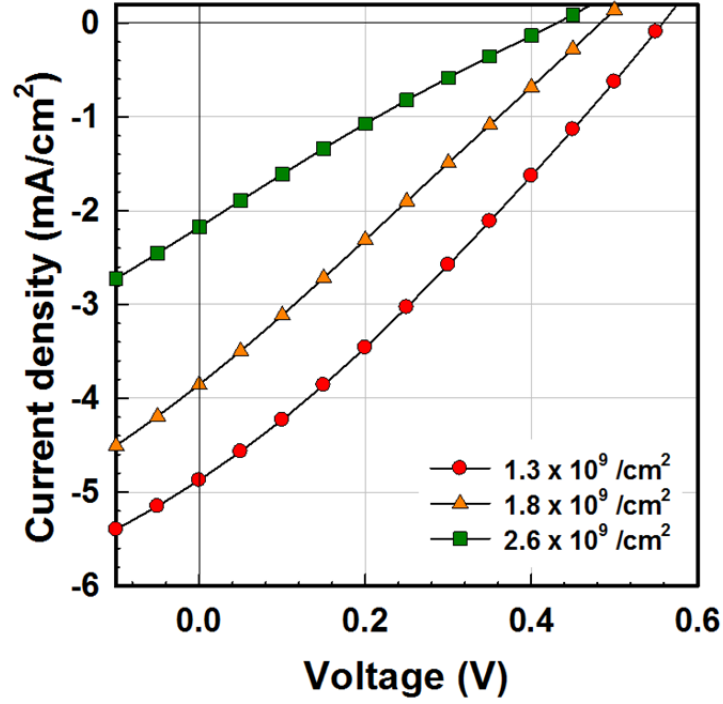


Figure 3.17 – Hybrid solar cell performance according to the density of SiNWs. Measured under AM 1.5 condition.

SiNWs density ($\times 10^9 / \text{cm}^2$)	J_{sc} mA/cm^2	V_{oc} V	FF %	η %	R_s $\Omega \cdot \text{cm}^2$	R_{sh} $\Omega \cdot \text{cm}^2$
1.3	4.8	0.55	29	0.77	90	171
1.8	3.8	0.48	26	0.48	119	144
2.6	2.2	0.43	23	0.21	221	178

Table 3.3 – Summary of hybrid solar cell parameters with various SiNWs density

The trend in V_{oc} could also be explained by the absorbance improvement. Koster et al. introduced a formula concerning V_{oc} with light-intensity dependence. The equation is given by [47]

$$V_{oc} = \frac{E_{gap}}{q} - \frac{kT}{q} \ln \left(\frac{(1-P)\gamma N_c^2}{PG} \right) \quad (3)$$

where E_{gap} is band-gap of active material, q is electric charge, k is Boltzmann's constant, T is absolute temperature, γ is Langevin recombination constant, N_c is the effective density of states, P is exciton dissociation probability, G is generation rate of bound electron-hole pair. PG is generation rate of free photo-generated carriers. Among parameters, the generation rate of bound electron-hole pairs are varied according to the absorbance of P3HT:PCBM. P is constant regardless of the density of SiNWs. Thus, the generation rate of free photo-generated carrier increases as P3HT:PCBM absorption increases. This trend makes V_{oc} higher according to the equation (3). Thus, V_{oc} has higher value with lower SiNWs' density than others. In addition, R_s has significant effects on the solar cell performance. As the density of SiNWs becomes denser, R_s is increased from $90 \Omega \cdot \text{cm}^2$ to $220 \Omega \cdot \text{cm}^2$. Figure 3.18 demonstrates J_{sc} and η as a function of R_s . Both parameters strongly depend on R_s and scale linearly with it. This observation suggests that the denser SiNWs brings the higher R_s and it is predominate to determine solar cells performance. Reasons of high R_s with dense SiNWs might be due to native oxide shell on SiNWs, and residual catalyst after finishing the growth process.

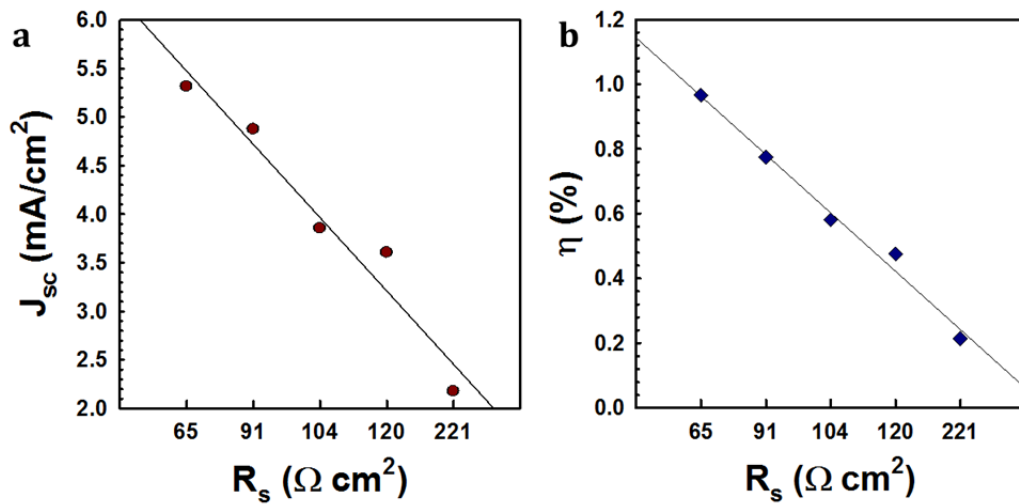


Figure 3.18 – Series resistance dependence of (a) short-circuit current and (b) power conversion efficiency.

3.5 Conclusion: requirements for photovoltaic action

For the best use of the Sn-catalyzed SiNWs, a nano-structured hybrid solar cell was proposed. P3HT:PCBM layer is deposited on the Sn-catalyzed SiNWs array by spin-coating method. P3HT plays a role of main light absorbing material. Despite of the advantages of this combination, there were difficulties to establish the photovoltaic action due to the rough surface of SiNWs, the anode selectivity and the complex interfaces. By inserting PEDOT:PSS between the SiNWs array and P3HT:PCBM layer, such problems are improved. PEDOT:PSS has effects of; 1) smoothening SiNWs surface, 2) improving anode selectivity and 3) simplifying of complex interface by isolating SiNWs with P3HT:PCBM. As results, the photovoltaic effect is established. Although PEDOT:PSS helps the photovoltaic action of our hybrid solar cells, the performance is also limited by geometric factors of the nanowires. The length of SiNWs should be similar with the total thickness of organic layers used (PEDOT:PSS and P3HT:PCBM). The solar cell performance tends to improve with decreased density of SiNWs.

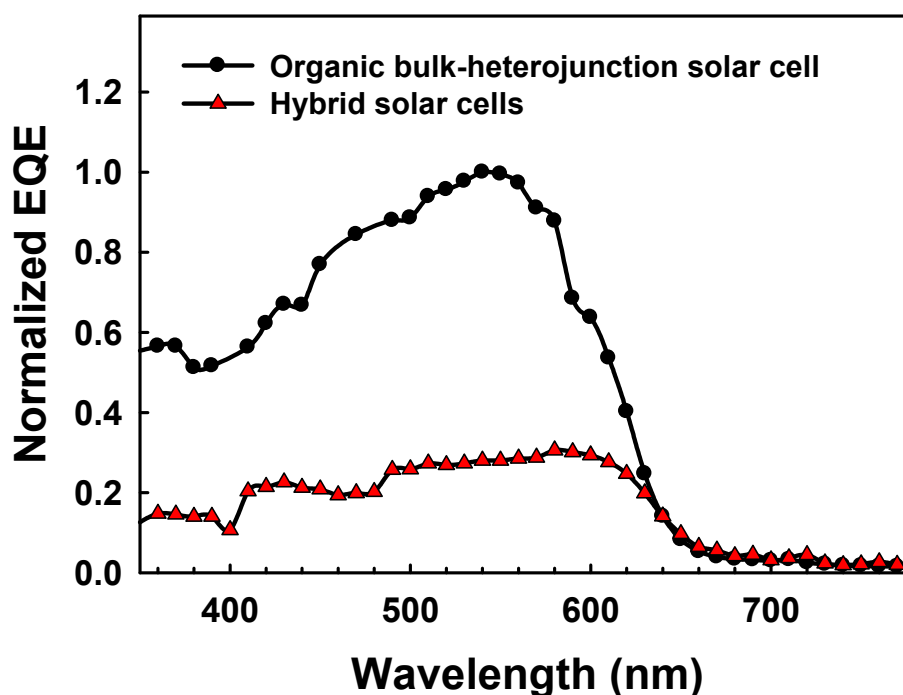


Figure 3.19 – Normalized external quantum efficiency of conventional organic bulk-heterojunction solar cells and hybrid solar cells

Observations through this chapter state that the ‘interface’ and the ‘morphology’ should be seriously considered for efficient photovoltaic action in our hybrid solar cell structure. Figure 3.19 shows normalized external quantum efficiencies (EQE) of an organic bulk-heterojunction and a hybrid solar cells based on P3HT as main absorber. The EQE of organic solar cell resembles the absorbance curve of P3HT. It has a maximum around 540 nm and a shoulder peak around 600 nm. The EQE of hybrid solar cell is severely limited compared to that of the organic solar cells except long wavelength region over 620 nm. It is assumed that there are problems of photo-generated carrier collection because P3HT:PCBM layer is isolated from SiNWs, that is, it works independently. Free electrons and holes are generated in P3HT:PCBM layer by illumination, then, they are transported to corresponding electrodes. It is believed that this low EQE of the hybrid solar cell is related with the quality of SiNWs array such as residual catalyst, native oxide and parasitic a-Si:H deposition during the growth process. Further investigations on the improvement of SiNWs’ quality and its correlation with the device performance for the best use of Sn-catalyzed SiNWs are necessary.

REFERENCE

1. Gowrishankar, V., et al., *Exciton harvesting, charge transfer, and charge-carrier transport in amorphous-silicon nanopillar/polymer hybrid solar cells*. Journal of Applied Physics, 2008. **103**(6): p. 064511-8.
2. Pasquier, A.D., et al., *Photoinduced charge transfer between poly(3-hexylthiophene) and germanium nanowires*. Applied Physics Letters, 2007. **91**(18): p. 183501-3.
3. Park, H., et al., *Graphene Cathode-Based ZnO Nanowire Hybrid Solar Cells*. Nano Letters, 2012. **13**(1): p. 233-239.
4. Blom, P.W.M., et al., *Device Physics of Polymer:Fullerene Bulk Heterojunction Solar Cells*. Advanced Materials, 2007. **19**(12): p. 1551-1566.
5. Scully, S.R. and M.D. McGehee, *Effects of optical interference and energy transfer on exciton diffusion length measurements in organic semiconductors*. Journal of Applied Physics, 2006. **100**(3): p. 034907-5.
6. Shaw, P.E., A. Ruseckas, and I.D.W. Samuel, *Exciton Diffusion Measurements in Poly(3-hexylthiophene)*. Advanced Materials, 2008. **20**(18): p. 3516-3520.
7. Gregg, B.A., *Excitonic Solar Cells*. The Journal of Physical Chemistry B, 2003. **107**(20): p. 4688-4698.
8. He, L., et al., *Highly efficient Si-nanorods/organic hybrid core-sheath heterojunction solar cells*. Applied Physics Letters, 2011. **99**(2): p. 021104-3.
9. Sun, B., et al., *Hybrid Photovoltaics Based on Semiconductor Nanocrystals and Amorphous Silicon*. Nano Letters, 2009. **9**(3): p. 1235-1241.
10. Jeong, S., et al., *Hybrid Silicon Nanocone-Polymer Solar Cells*. Nano Letters, 2012. **12**(6): p. 2971-2976.
11. Liu, C.-Y., Z.C. Holman, and U.R. Kortshagen, *Hybrid Solar Cells from P3HT and Silicon Nanocrystals*. Nano Letters, 2008. **9**(1): p. 449-452.
12. Garnett, E. and P. Yang, *Light Trapping in Silicon Nanowire Solar Cells*. Nano Letters, 2010. **10**(3): p. 1082-1087.
13. Linwei, Y. and et al., *Synthesis, morphology and compositional evolution of silicon nanowires directly grown on SnO₂ substrates*. Nanotechnology, 2008. **19**(48): p. 485605.
14. Linwei, Y., et al., *Radial junction amorphous silicon solar cells on PECVD-grown silicon nanowires*. Nanotechnology, 2012. **23**(19): p. 194011.
15. Yu, L., et al., *Bismuth-Catalyzed and Doped Silicon Nanowires for One-Pump-Down Fabrication of Radial Junction Solar Cells*. Nano Letters, 2012. **12**(8): p. 4153-4158.

-
16. Kuo, C.Y. and C. Gau, *Arrangement of band structure for organic-inorganic photovoltaics embedded with silicon nanowire arrays grown on indium tin oxide glass*. Applied Physics Letters, 2009. **95**(5): p. 053302-3.
 17. Huang, J.-S., et al., *Well-aligned single-crystalline silicon nanowire hybrid solar cells on glass*. Solar Energy Materials and Solar Cells, 2009. **93**(5): p. 621-624.
 18. Dennler, G., M.C. Scharber, and C.J. Brabec, *Polymer-Fullerene Bulk-Heterojunction Solar Cells*. Advanced Materials, 2009. **21**(13): p. 1323-1338.
 19. Kim, Y., et al., *Effects of thickness and thermal annealing of the PEDOT:PSS layer on the performance of polymer solar cells*. Organic Electronics, 2009. **10**(1): p. 205-209.
 20. Schmidt, V., J.V. Wittemann, and U. Gösele, *Growth, Thermodynamics, and Electrical Properties of Silicon Nanowires†*. Chemical Reviews, 2010. **110**(1): p. 361-388.
 21. Yuan, G., et al., *Understanding the Origin of the Low Performance of Chemically Grown Silicon Nanowires for Solar Energy Conversion*. Angewandte Chemie International Edition, 2011. **50**(10): p. 2334-2338.
 22. Vandewal, K., et al., *On the origin of the open-circuit voltage of polymer-fullerene solar cells*. Nat Mater, 2009. **8**(11): p. 904-909.
 23. Hu, L. and G. Chen, *Analysis of Optical Absorption in Silicon Nanowire Arrays for Photovoltaic Applications*. Nano Letters, 2007. **7**(11): p. 3249-3252.
 24. Gunawan, O. and S. Guha, *Characteristics of vapor-liquid-solid grown silicon nanowire solar cells*. Solar Energy Materials and Solar Cells, 2009. **93**(8): p. 1388-1393.
 25. Dongaonkar, S., et al., *Universality of non-Ohmic shunt leakage in thin-film solar cells*. Journal of Applied Physics, 2010. **108**(12): p. 124509-10.
 26. Nagata, T., et al., *Effect of UV-ozone treatment on electrical properties of PEDOT:PSS film*. Organic Electronics, 2011. **12**(2): p. 279-284.
 27. Padinger, F., R.S. Rittberger, and N.S. Sariciftci, *Effects of Postproduction Treatment on Plastic Solar Cells*. Advanced Functional Materials, 2003. **13**(1): p. 85-88.
 28. Hauch, J.A., et al., *Flexible organic P3HT:PCBM bulk-heterojunction modules with more than 1 year outdoor lifetime*. Solar Energy Materials and Solar Cells, 2008. **92**(7): p. 727-731.
 29. Waldauf, C., et al., *Highly efficient inverted organic photovoltaics using solution based titanium oxide as electron selective contact*. Applied Physics Letters, 2006. **89**(23): p. 233517-3.
 30. De Bettignies, R., et al., *Accelerated lifetime measurements of P3HT:PCBM solar cells*. Synthetic Metals, 2006. **156**(7-8): p. 510-513.

31. Reyes-Reyes, M., K. Kim, and D.L. Carroll, *High-efficiency photovoltaic devices based on annealed poly(3-hexylthiophene) and 1-(3-methoxycarbonyl)-propyl-1-phenyl-(6,6)C61 blends*. Applied Physics Letters, 2005. **87**(8): p. 083506-083506-3.
32. Ki-Beom KIM, Y.-H.T., Yoon-Soo HAN, Kwang-Heum BAIK, Myung-Hee YOO, Moon-Ho LEE, *Relation between Surface Roughness of Indium Tin Oxide and Leakage Current of Organic Light-Emitting Diode*. Japanese Journal of Applied Physics, 2004. **42**: p. 438-440 .
33. Hallermann, M., et al., *Charge Transfer Excitons in Polymer/Fullerene Blends: The Role of Morphology and Polymer Chain Conformation*. Advanced Functional Materials, 2009. **19**(22): p. 3662-3668.
34. Deibel, C., T. Strobel, and V. Dyakonov, *Role of the Charge Transfer State in Organic Donor-Acceptor Solar Cells*. Advanced Materials, 2010. **22**(37): p. 4097-4111.
35. Zhokhavets, U., et al., *Relation between absorption and crystallinity of poly(3-hexylthiophene)/fullerene films for plastic solar cells*. Chemical Physics Letters, 2006. **418**(4-6): p. 347-350.
36. Grzegorzczak, W.J., et al., *Temperature-Independent Charge Carrier Photogeneration in P3HT-PCBM Blends with Different Morphology*. The Journal of Physical Chemistry C, 2010. **114**(11): p. 5182-5186.
37. Ma, W., et al., *Effect of the Molecular Weight of Poly(3-hexylthiophene) on the Morphology and Performance of Polymer Bulk Heterojunction Solar Cells*. Macromolecular Rapid Communications, 2007. **28**(17): p. 1776-1780.
38. Dietmueller, R., et al., *Light-induced charge transfer in hybrid composites of organic semiconductors and silicon nanocrystals*. Applied Physics Letters, 2009. **94**(11): p. 113301-3.
39. Lenes, M., et al., *Recombination-Limited Photocurrents in Low Bandgap Polymer/Fullerene Solar Cells*. Advanced Functional Materials, 2009. **19**(7): p. 1106-1111.
40. Mihailetchi, V.D., J. Wildeman, and P.W.M. Blom, *Space-Charge Limited Photocurrent*. Physical Review Letters, 2005. **94**(12): p. 126602.
41. He, L., et al., *Si Nanowires Organic Semiconductor Hybrid Heterojunction Solar Cells Toward 10% Efficiency*. ACS Applied Materials & Interfaces, 2012. **4**(3): p. 1704-1708.
42. Ozdemir, B., *Silicon nanowire - poly(3,4-ethylenedioxythiophene)-poly(styrenesulfonate) heterojunction solar cells*. Appl. Phys. Lett., 2011. **99**(11): p. 113510.
43. Shiu, S.-C., et al., *Morphology Dependence of Silicon Nanowire/Poly(3,4-ethylenedioxythiophene):Poly(styrenesulfonate) Heterojunction Solar Cells*. Chemistry of Materials, 2010. **22**(10): p. 3108-3113.

-
44. Park, S., et al., *Effects of intrinsic ZnO buffer layer based on P3HT/PCBM organic solar cells with Al-doped ZnO electrode*. Solar Energy Materials and Solar Cells, 2009. **93**(6-7): p. 1020-1023.
45. Yoon, W.-J., et al., *Plasmon-enhanced optical absorption and photocurrent in organic bulk heterojunction photovoltaic devices using self-assembled layer of silver nanoparticles*. Solar Energy Materials and Solar Cells, 2010. **94**(2): p. 128-132.
46. Koster, L.J.A., et al., *Origin of the light intensity dependence of the short-circuit current of polymer/fullerene solar cells*. Applied Physics Letters, 2005. **87**(20): p. 203502-3.
47. Koster, L.J., *Light intensity dependence of open-circuit voltage of polymer:fullerene solar cells*. Appl. Phys. Lett., 2005. **86**(12): p. 123509.

Chapter 4

OPTIMIZATION OF SiNWs FOR EFFICIENT LIGHT TRAPPING

4.1	INTRODUCTION	100
4.2	ACID TREATMENTS FOR RESIDUAL CATALYST REMOVAL.....	102
4.2.1.	HCL TREATMENT OF SiNWs AND ITS EFFECT ON SiNWs ARRAY.....	102
4.2.2.	EFFECTS OF ACID TREATMENTS ON HYBRID SOLAR CELL PERFORMANCE.....	112
4.3	A-Si:H ETCHING BY HYDROGEN PLASMA	123
4.3.1.	SELECTIVE ETCHING OF A-Si:H FROM SiNWs ARRAY	123
4.3.2.	ENHANCED SOLAR CELL PERFORMANCE BY A-Si:H ETCHING.....	131
4.4	CONCLUSION: BENEFITS FROM SN-CATALYZED SiNWs.....	137
	<i>REFERENCE</i>	<i>141</i>

4.1 Introduction

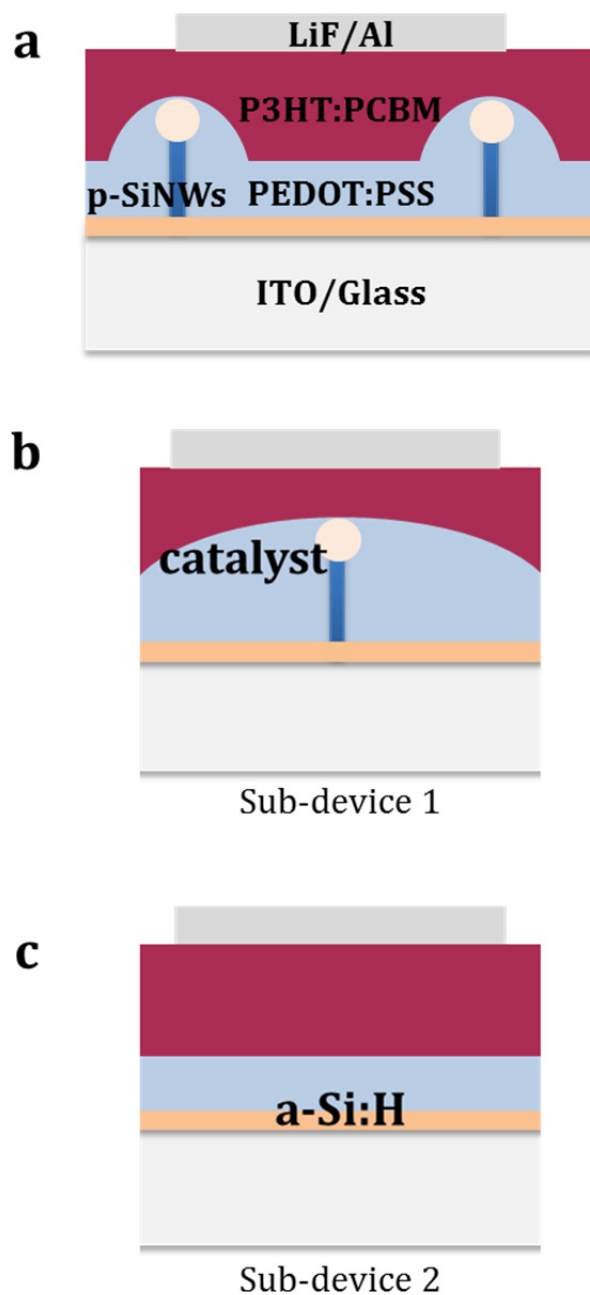


Figure 4.1 – Schematic diagrams of hybrid solar cells. (a) Entire device structure of the hybrid solar cells based on PECVD grown SiNWs and P3HT:PCBM. This device can be divided in two sub-devices (b) sub-device 1 containing SiNWs and (c) sub-device 2 without SiNWs.

In the previous chapter, we dealt with the hybrid solar cells based on the Sn-catalyzed SiNWs. Their solar cells performance is severely limited by SiNWs array compared to the conventional organic bulk-heterojunction solar cells. To discover real advantages of the SiNWs in this hybrid solar cell structure, the methods to improve the quality SiNWs array should be considered. Figure 4.1 (a) shows a device structure of the hybrid solar cells based on Sn-catalyzed and P3HT:PCBM layers investigated in Chapter 3. The device design is similar with an organic bulk-heterojunction solar cell but the SiNWs are used as a nanostructure aimed to enhance the light trapping in the organic active layer. Our hybrid solar cells could be considered with two sub-devices. Figure 4.1 (b) depicts sub-device 1 that contains SiNWs. There are Sn catalysts remaining after the SiNWs growth and native oxide could be formed on the surface of the SiNWs when the sample comes out from PECVD chamber for the hybrid solar cell fabrication. The residual catalyst could cause a parasitic optical absorption and electrical defects and native oxide could bring resistive effect. Sub-device 2 is described in Figure 4.1 (c). This describes the planar structure without the SiNWs. The incident light from bottom is mainly passing through this sub-device 2 before meet P3HT:PCBM layer. It resembles organic bulk-heterojunction solar cells but the hydrogenated amorphous silicon (a-Si:H) layer is between PEDOT:PSS and ITO. This thin layer could seriously effects on the device behaviors not only solar cell performance but also dark current density-voltage characteristic. Moreover, the parasitic absorption of a-Si:H could limit the light absorption of P3HT:PCBM layer. To achieve higher power conversion efficiency, those issues must be resolved.

In this chapter, we study the optimization of Sn-catalyzed SiNWs array for better hybrid solar cell performance by chemical and physical methods. According to the inherent characteristics of SiNWs growth by VLS mode [1-4], the catalyst metal must be needed to initiate the growth and a-Si:H is deposited around SiNWs during the growth. From these facts, we can point out the performance limiting factors; 1) residual catalyst after the SiNWs growth, 2) co-deposition of a-Si:H during the growth and 3) native oxide

formation when the samples step out of the chamber. Acids treatments are carried out to address the limiting factor 1) and 3) by using hydrochloric and hydrofluoric acid, respectively. Hydrogen plasma is applied just after the SiNWs growth to selectively etch a-Si:H layer. We explore the correlation between the optimization of SiNWs array and the hybrid solar cell performance.

4.2 Acid treatments for residual catalyst removal

4.2.1 HCl treatment of SiNWs and its effect on SiNWs array

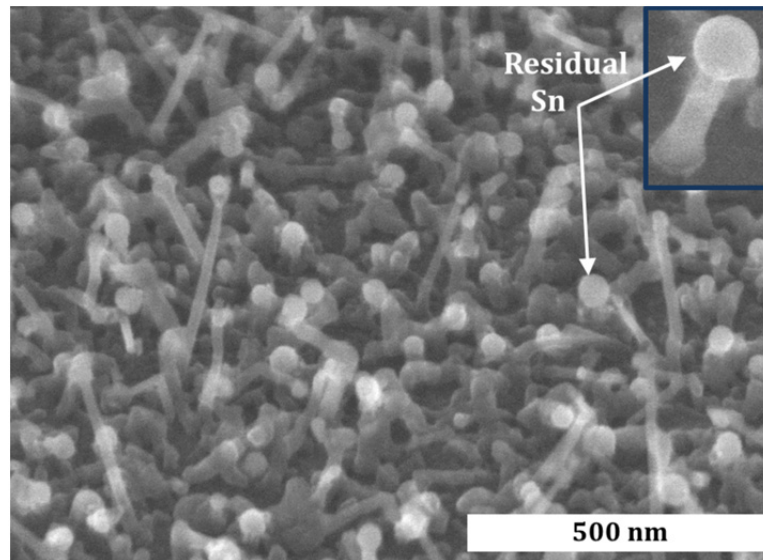


Figure 4.2 – SEM image of PECVD grown Sn-catalyzed SiNWs on ITO/glass substrate; 1) Thickness of Sn: 2 nm 2) Catalyst droplets formation (H₂ plasma): 350 °C, 100 sccm of H₂, 360 mTorr, 5 W, 2 min 3) SiNWs growth: 600 °C, 10 sccm of SiH₄, 1.5 sccm of TMB, 100 sccm of H₂, 1 Torr, 2 W, 3 min

Figure 4.2 shows a SEM image of Sn-catalyzed SiNWs array. Note that the considerable amount of residual catalysts presented in white spheres in the image is observed on the tip of SiNWs. As mentioned in Chapter 2, the catalyst metal could be totally left if the SiNWs are grown with sufficient growth time like 10 min to consume all the catalyst. However, the SiNWs of few hundreds nanometer length is preferred for the hybrid solar cells

because such long ($> 1 \mu\text{m}$) SiNWs easily create shunting paths (Chapter 3). The residual catalyst removal is considered more important in hybrid solar cells application than radial junction solar cells which are based on the SiNWs of micron length order [5-7].

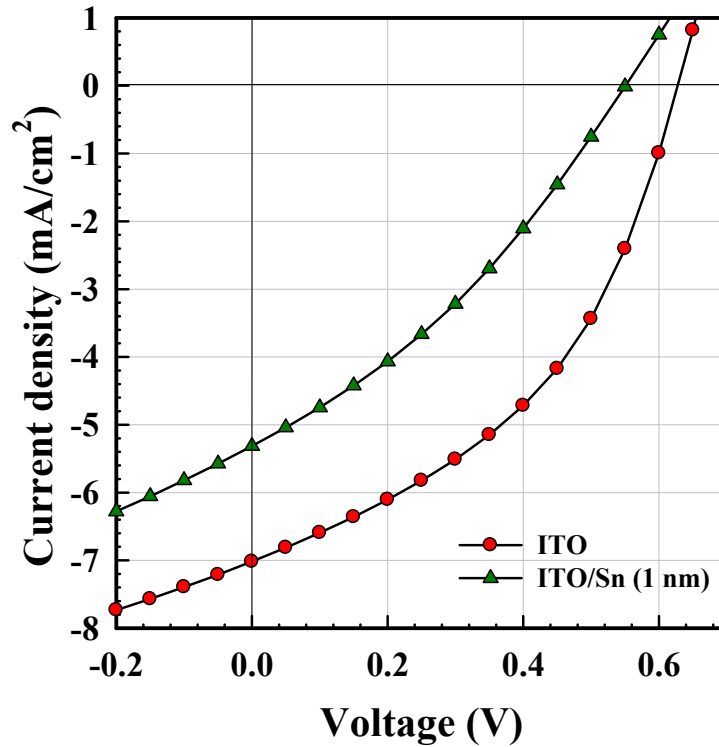


Figure 4.3 – Solar cell performance of organic bulk-heterojunction solar cells based on P3HT:PCBM with and without 1 nm of Tin on ITO under A.M 1.5

Substrate	Jsc mA/cm^2	Voc V	FF %	$\eta\%$	Rs $\Omega \cdot \text{cm}^2$	Rsh $\Omega \cdot \text{cm}^2$
ITO	7.0	0.62	43.58	1.9	28	250
ITO/Sn (1 nm)	5.3	0.55	33.05	1.0	66	187

Table 4.1- Summary solar cell parameters with substrates

Before going further, conventional organic bulk-heterojunction solar cells are fabricated with the structure of ITO/(1 nm of Sn or nothing)/PEDOT:PSS (50 nm)/P3HT:PCBM (230 nm)/LiF (1.2 nm)/Al (100

nm) to have brief insight on the effects of thin Sn layer on solar cells performance. Figure 4.3 shows solar cell performance under AM 1.5 condition. The reference cell demonstrates a usual characteristic with 230 nm thickness of P3HT:PCBM layer and it shows 1.9 % of power conversion efficiency. Whereas, the solar cell with 1 nm thick Sn layer on ITO shows poorer performance. The resistive effects due to Sn layer are observed. It means that 1 nm of Sn interlayer strongly affects the resistances of the solar cell compared to the reference cell (Table 4.1). Furthermore, it may promote the recombination of photo-generated holes. Thus, the V_{oc} is lower than the reference cell. Accordingly, all solar cell parameters are worse than reference despite of just 1 nm thick Sn layer on ITO.

Since the residual catalysts are considered as defects in the solar cells, they raise problems affecting hybrid solar cell performances, for example, parasitic absorption of incident light by the metal, low shunt resistance (R_{sh}), recombination, etc [8, 9]. For these reasons, the removal of residual catalysts is correlated with the improvement of hybrid solar cell efficiency. There are few reports discussing the catalyst thickness effects on solar cell performance by inorganic core-shell solar cells and also hybrid solar cells based on the nanowires [2, 10, 11]. The results stated that thick catalyst is related with large leakage current in solar cells. However, the analysis on the catalyst effects was carried out with limited scope. Since the thickness change of catalysts for the SiNWs growth accompanies the changes of nanowires morphology and the quantity of residual catalyst at same time. To observe the effect of catalyst removal, the analyses of hybrid solar cells have to be conducted with the SiNWs grown by same thickness of catalyst to exclude the effects of morphology changes (Chapter 3).

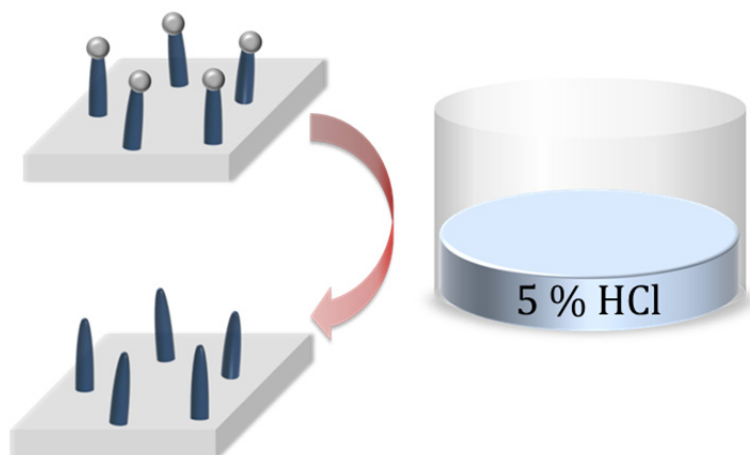
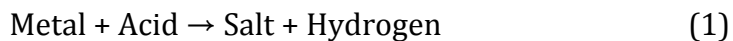
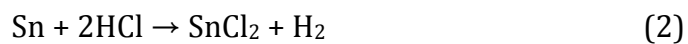


Figure 4.4 – Dipping of SiNWs into 5 % HCl to remove residual Sn; the dipping time is optimized by 20 min with consideration of SiNWs' damage

Residual Sn is removed by simple chemical method; that is the dipping of SiNWs array into 5 % hydrochloric acid (HCl) depicted in Figure 4.4. The reaction between Sn and HCl could potentially produce two kinds of tin chloride, SnCl_2 and SnCl_4 . HCl is not a strong oxidizing agent, therefore, the catalyst removal by HCl follows usual reaction like below.



According to this characteristic, SnCl_2 formation is predominant. Hence, the residual Sn removal using HCl follows equation below,



This method is quite simple but it is only available when the transparent conducting oxide (TCO) is resistive to HCl. For example, ZnO:Al is easily etched out by HCl even by the low concentration like 5 %.

Here we employed commercially available ITO as a TCO. As well known, HCl can etch ITO according to the concentration and temperature [12]. We checked the degradation of ITO against 5 % HCl at room temperature by measuring the sheet resistance with four point probe. Figure 4.5 describes the sheet resistance of ITO as a function of HCl dipping time from 0 min to 120 min. ITO shows 31.5 Ω/sq of sheet resistance as received. It remains constant with HCl dipping time up to 30 min which means there are no significant effects of HCl on ITO. However, ITO is affected after 30 min dipping and the sheet resistance is 37 Ω/sq after 120 min of dipping. HCl treatment has to be performed less than 30 min to keep the sheet resistance low.

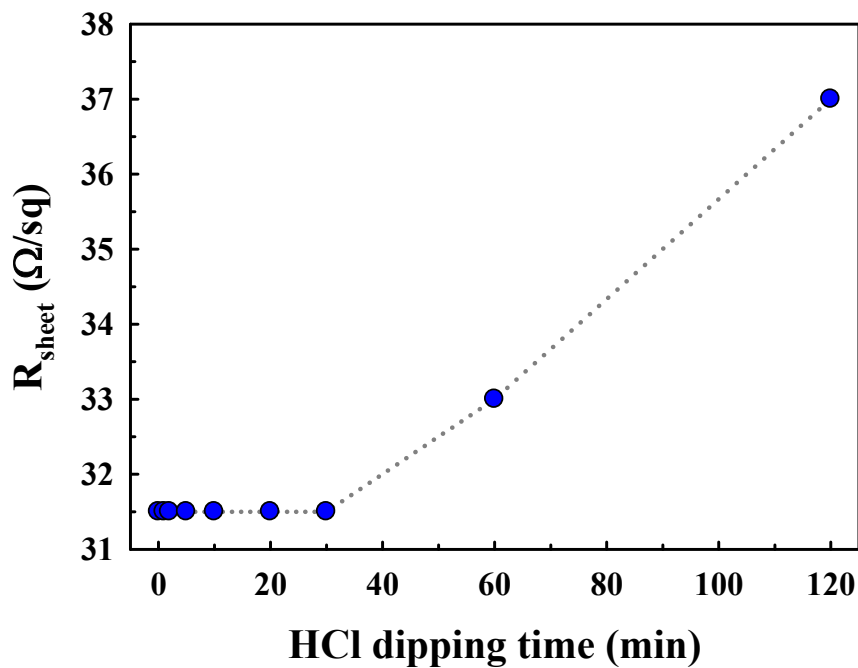


Figure 4.5 – Sheet resistance of ITO substrate with HCl dipping time

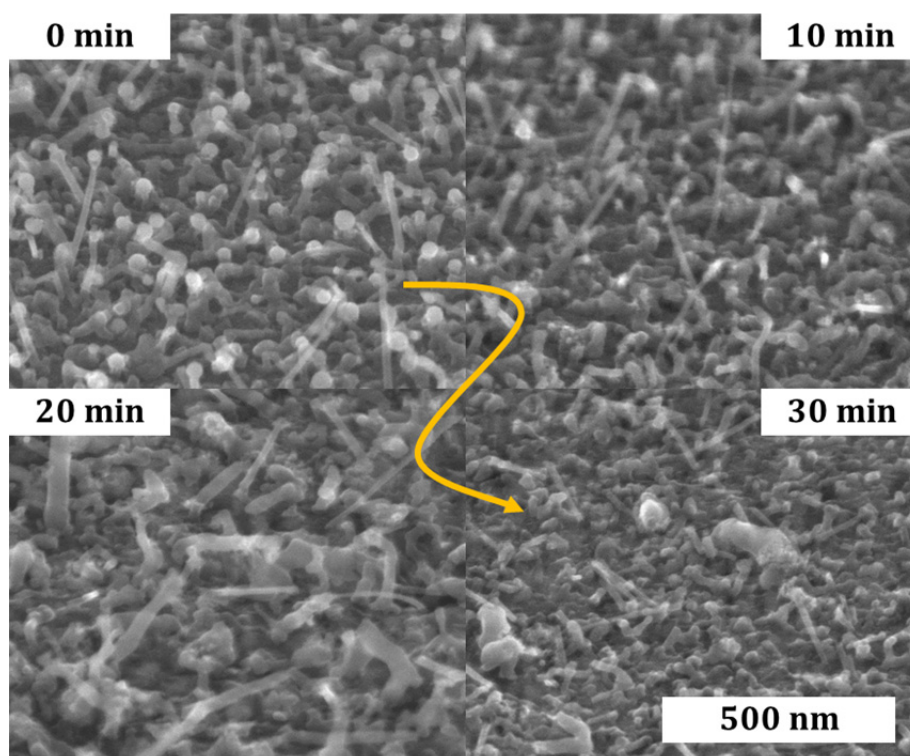


Figure 4.6 – SEM images of Sn-catalyzed SiNWs array after dipping into HCl with different time. All SiNWs array was grown with identical condition; 1) Thickness of Sn: 2 nm 2) Catalyst droplets formation (H₂ plasma): 350 °C, 100 sccm of H₂, 360 mTorr, 5 W, 2 min 3) SiNWs growth: 600 °C, 10 sccm of SiH₄, 1.5 sccm of TMB, 100 sccm of H₂, 1 Torr, 2 W, 3 min

Figure 4.6 shows SEM images of SiNWs array which intuitively reveal the effects of HCl according to the dipping time. Residual catalysts are described in these images with white spheres for as grown SiNWs array. The dramatic reduction in amount of catalyst is observed after 10 min of HCl dipping without the destruction of SiNWs. After longer dipping time, additional catalyst removal is no longer observable by SEM images of the SiNWs array. However, it seems that SiNWs are gradually damaged by HCl. Such effects have been regarded in literature due to the reaction of diffused Sn catalyst on the surface of SiNWs with HCl [13].

X-ray photoelectron spectroscopy (XPS) measurement was carried out for the quantitative analysis of residual catalyst removal. Here, SiNWs are grown on p-type silicon wafers by identical growth conditions with the SiNWs grown on ITO because ITO already contains a lot of Sn which can affect the XPS result. The SiNWs/Si substrates are dipped into 5 % HCl during 1 min and 20 min to measure initial and stabilized states. XPS was

performed with a Kratos Axis Ultra DLD using a high-resolution monochromatic Al-K α line X-ray source at 1486.6 eV. Fixed analyzer pass energy of 20 eV was used for core level scans. The photoelectron take-off angle was always normal to the surface.

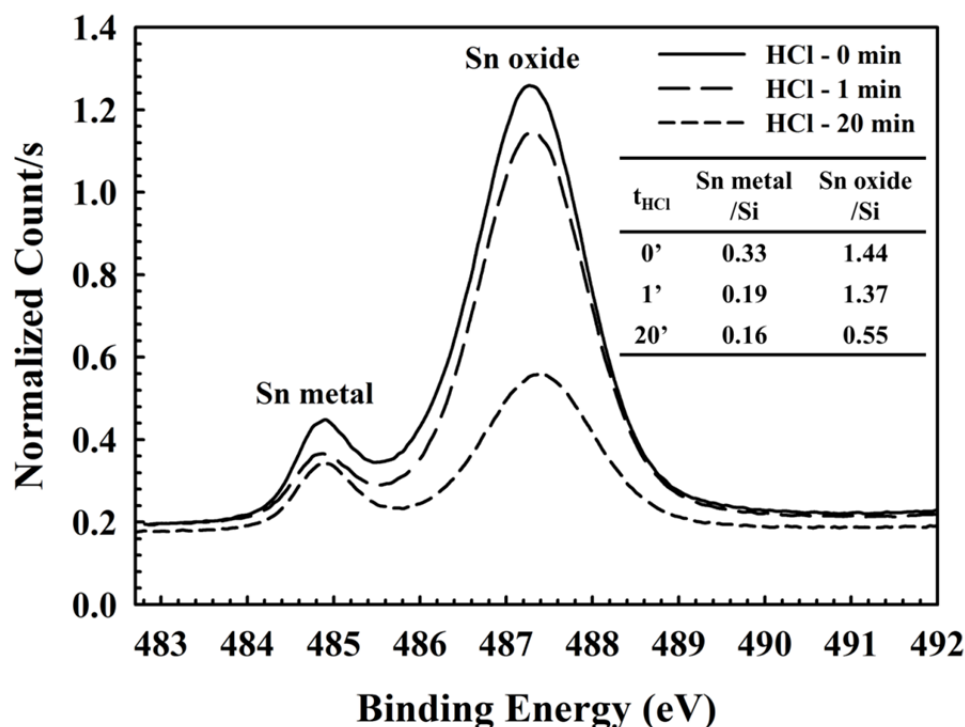


Figure 4.7 – Results of X-ray photoelectron spectroscopy of SiNWs array with different HCl dipping time for detecting residual catalyst (here, Sn). The graph describes normalized counts of Sn metal and oxide part as a function of binding energy. Sn metal and oxide are detected at 484.9 and 487.2 eV respectively. The inset table summarizes ratio of Sn metal and oxide compared with silicon according to the HCl dipping time.

Figure 4.7 shows the results of XPS of SiNWs with regard to HCl treatment. Sn metal and Sn oxide are observed at 484.9 eV and 487.2 eV of binding energy respectively. Note that Sn is a metal easily oxidized at room temperature. This is the reason why Sn oxide shows the higher counts than Sn metal. Generally, as HCl dipping time increases, Sn metal and Sn oxide counts are decreased with producing SnCl_2 and H_2 . 50 % of residual Sn metal is removed by 1 min of the HCl dipping. Then, there is no significant reaction between HCl and metallic Sn. The peak area ratio of Sn and Sn oxide to silicon is summarized in an inset table of Figure 4.7. Without HCl treatment, Sn metal occupies 0.33 but it decreased

to 0.16 after 20 min of HCl dipping. In contrast, the amount of Sn oxides is decreased about 5 % compared with the HCl untreated sample after 1 min dipping. The continuing reaction between HCl and Sn oxide results in further decrease of Sn oxide till 62 % of the initial amount in 20 min. From the value of the inset table, Sn oxide maintains higher counts than silicon without HCl treatment and with 1 min of HCl dipping. Then, Sn oxide part becomes one-third of its initial value after 20 min of HCl dipping.

Despite of the HCl treatment for residual catalyst removal, Sn metal and oxide still remain on the nanowires array. Figure 4.8 illustrates a schematic diagram of cross-sectional view of the catalyst distribution on the as grown SiNWs array. There are four different positions of catalyst although the residual catalyst on the tip of SiNWs is only observable by SEM measurement; (1) is the residual catalysts which are not completely consumed during the growth process, (2) is an ultra-thin sidewall-spreading catalyst layer on the surface of SiNWs which is reported by L. Yu for post-transition metal catalyst in 2011 [14]. It is known that this catalyst sidewall helps to stabilize the catalyst drop during the growth, especially, for low surface tension catalysts like Sn, In and Bi. Next, (3) is the catalyst metal diffused into the SiNWs during the growth. This phenomenon was already observed by real-time in situ transmission electron microscopy by V. C. Holmberg et al [13]. Lastly, (4) is catalyst droplets covered by a-Si:H before the SiNWs growth.

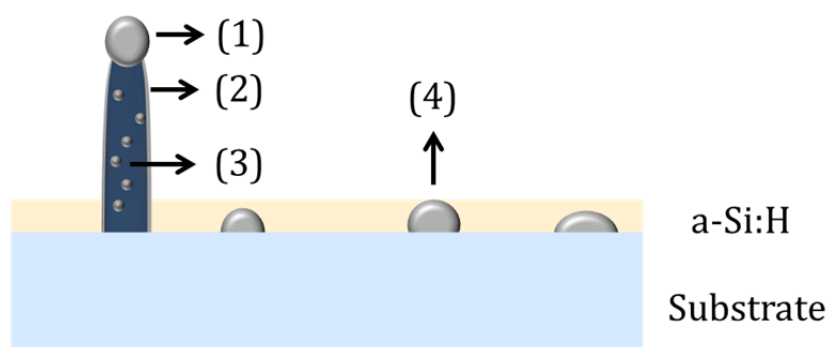


Figure 4.8 – Schematic of distributed catalyst on as grown SiNWs array (cross-sectional view). (1) residual catalyst after growth (2) ultra-thin diffused catalyst on SiNWs' surface (3) Diffused SiNWs during the growth in SiNWs and (4) catalyst droplets covered by a-Si:H before initiating SiNWs growth.

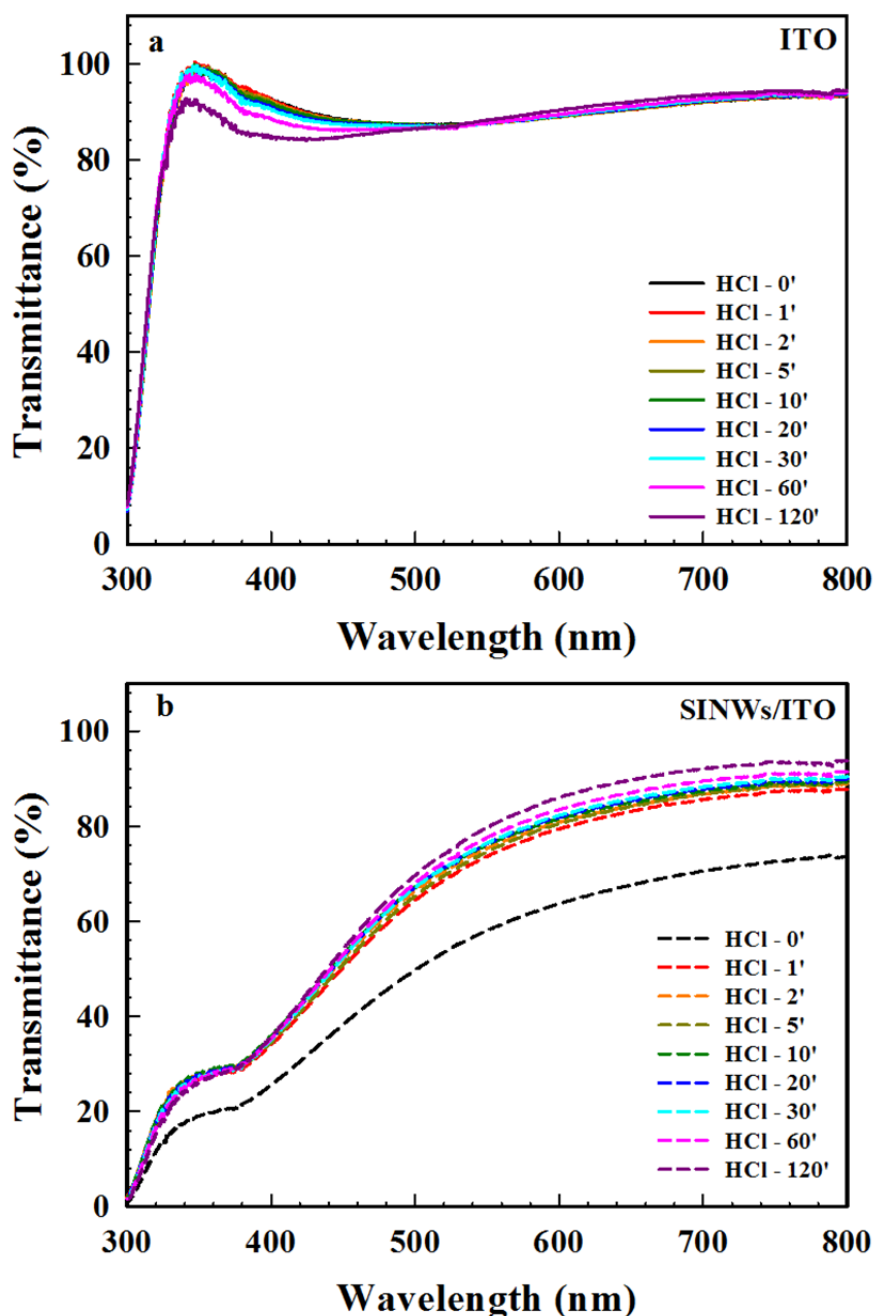


Figure 4.9 – Transmittances of (a) ITO/glass substrate and (b) SiNWs/ITO/glass substrate as a function of wavelength with various HCl dipping times.

Naturally, catalyst type (1) is easier to react with HCl than others since it is directly exposed to HCl. The ultra-thin sidewall of catalyst (2) is also easy to be etched. Then the catalyst near the SiNWs surface could be affected by HCl. On the other hand, the catalyst diffused into SiNWs (3) is not easy to be removed due to surrounding silicon atoms. Moreover, the catalyst droplets could be covered by a-Si:H (4) before the super-saturation of silicon atoms in

catalyst droplets. These catalyst droplets are protected from the attack of HCl, then, detected by XPS measurement. For this reason, distributed residual catalysts on the SiNWs array are not perfectly removed by HCl, however, 20 min of HCl dipping leads to the hybrid solar cell performance improvement that will be discussed in Section 4.2.2.

The optical characteristic of SiNWs plays an important role in our device structure because the solar cells are illuminated from the bottom of substrate. The residual catalyst removal has a favorable influence on the transmittance of SiNWs array. Figure 4.9 shows the transmittance of ITO and SiNWs/ITO with the different dipping time. The transmittance of ITO is not severely affected by HCl. Only, the transmittance with wavelength less than 540 nm is decreased as dipping time increases up to 120 min. However, the change is negligible up to 20 min of dipping. The transmittance of SiNWs/ITO exhibits a different tendency. Generally, the transmittance of SiNWs is lower in short wavelength region, then, it becomes higher at longer wavelength region. As reported [8, 15, 16], the SiNWs strongly absorb the incident light with short wavelength (high photon energy), whereas they do not strongly absorb the incident light of long wavelength near the band-gap energy (low photon energy) due to the indirect band-gap of silicon. The transmittance is greatly increased in the wavelength range from 300 nm to 800 nm by 1 min of HCl dipping. Further dipping than 1 min brings just a slight increase in the transmittance. Note that 1 min of HCl dipping removes 50 % of Sn metal in Figure 4.7, suggesting that Sn metal removal is responsible for the strong increase in the transmittance of SiNWs/ITO. Metallic Sn increases the parasitic absorption of SiNWs array. It reduces the number of photons entering P3HT:PCBM layer. It gives rise to the decrease in short-circuit current density (J_{sc}). Consequently, the removal of residual Sn is potentially helpful for solar cell application in optical aspect.

4.2.2 Effects of acid treatments on hybrid solar cell performance

Acid treatments on the SiNWs array have shown the advantage in terms of optical property of SiNWs/ITO/glass substrate. This result leads us expect the better solar cell performance. In this section, the investigations on the correlation between acid treatments by HCl and hydrofluoric acid (HF) and solar cell performance are conducted in the interest of efficient hybrid solar cells.

Figure 4.10 shows dark current density – voltage (J_D -V) characteristics of the hybrid solar cells for various HCl dipping times. The hybrid solar cell without HCl treatment shows symmetric behavior in current density. A diode is not observed in a forward bias region. Conventional diode equation based on the diode and resistance model is given by [17],

$$J_D = J_0 \left[e^{\left(\frac{q(V-JR_s)}{nk_B T} \right)} - 1 \right] - \frac{V-JR_s}{R_{sh}} \quad (3)$$

where J_0 is reverse saturation current density of diode, q is electric charge, R_s is series resistance, R_{sh} is shunt resistance, n is diode ideality factor, k_B is Boltzmann constant, T is absolute temperature and A is surface area of diode. First term and second term describe the diode current and the shunt (leakage) current, respectively. The low R_{sh} causes the influential shunt current that restricts the diode current. R_s and R_{sh} of solar cells for various HCl dipping times are shown in Table 4.2. The current density is severely governed by the shunt current related to the low R_{sh} without HCl treatment [17, 18]. This device exhibits $3,000 \Omega \cdot \text{cm}^2$ of R_{sh} which is sufficient to hinder the diode current. The device with 1 min of HCl dipping has a little bit better J_D -V characteristic. But, despite the removal of Sn metal, the hybrid solar cell is still suffered from the leakage current with R_{sh} about $4,000 \Omega \cdot \text{cm}^2$. As stated in previous section, metallic Sn is removed rapidly during 1 min of HCl treatment. Therefore, large amount of Sn oxide would be responsible for low R_{sh} .

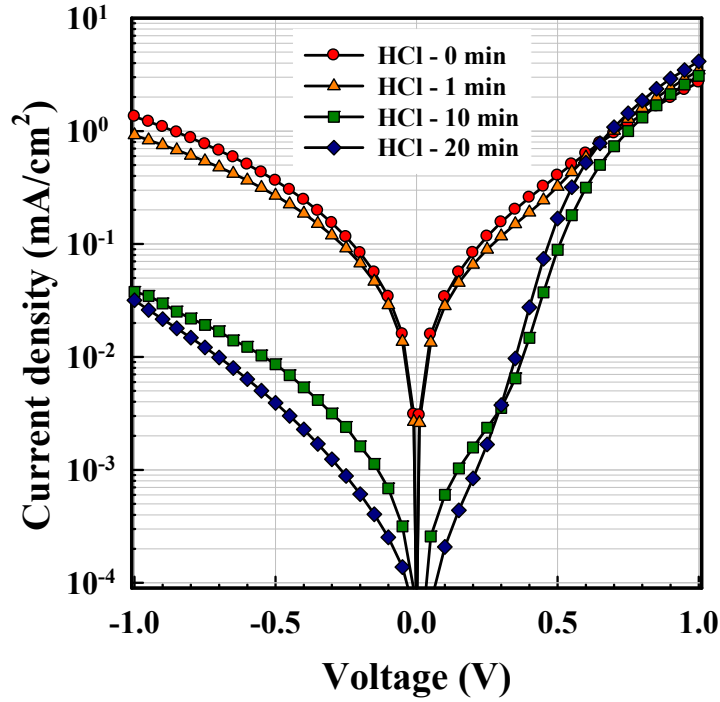


Figure 4.10 – Current density – voltage characteristics under dark with various HCl treatments.

t_{HCl} min	R_s $\Omega \cdot \text{cm}^2$	R_{sh} $\Omega \cdot \text{cm}^2$
0	150	3,000
1	113	4,000
10	110	155,000
20	90	434,000

Table 4.2 – Series and shunt resistance of hybrid solar cells under dark with various HCl dipping time.

Further HCl dipping clearly demonstrates the diode with increases in R_{sh} . The R_{sh} is dramatically increased hundred times with 20 min of HCl treatment. These results make sure that Sn oxide predominantly increases the shunt current (decreases R_{sh}) because it is like defects creating leakage current paths. In contrast, Sn metal seems to have a weak effect on it. The residual catalyst removal results in decreases in contaminations and leakage paths, thus, the better diode performance are achieved.

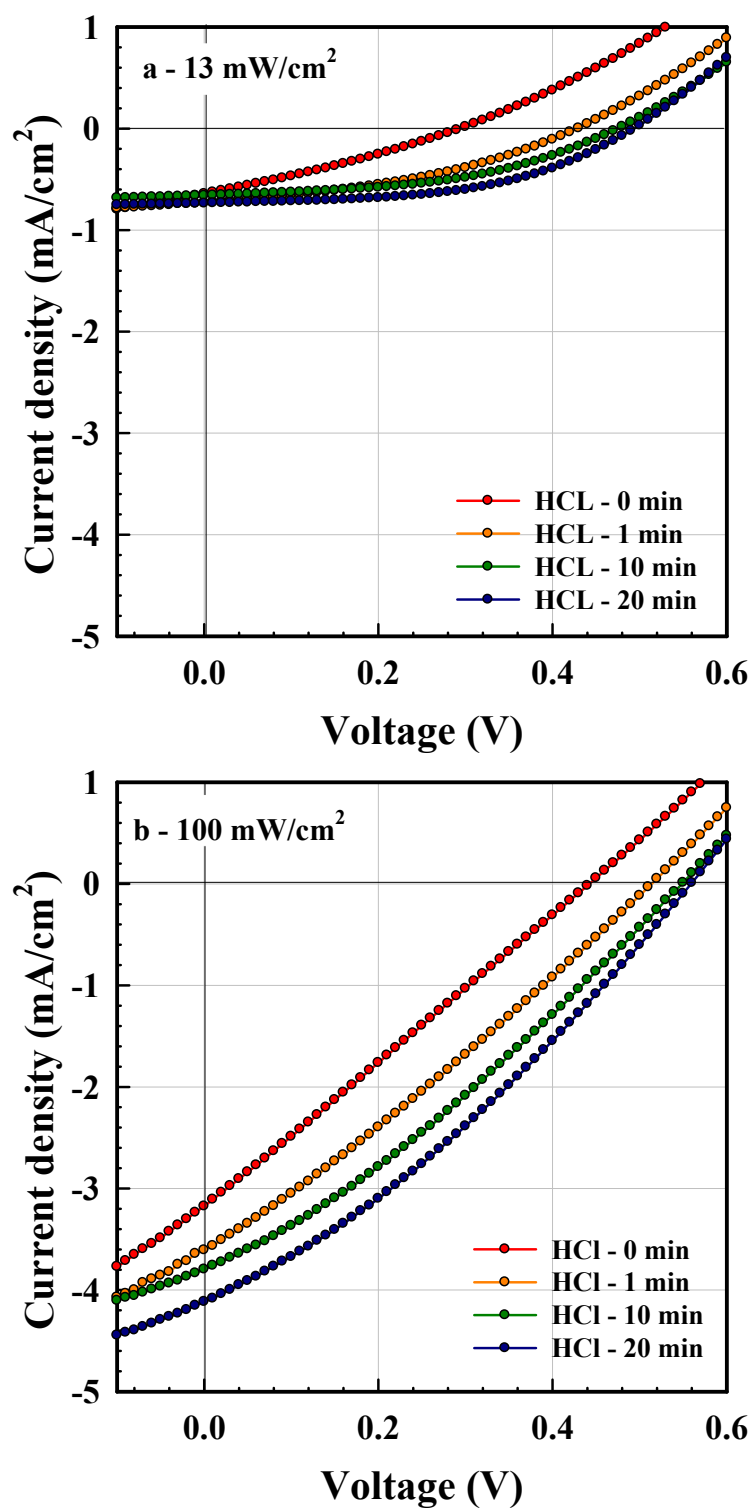


Figure 4.11 – Solar cell performance of hybrid solar cells under illumination intensity (a) 13 mW/cm² and (b) 100 mW/cm² with various HCl dipping time.

Table 4.3 - Hybrid solar cells parameters with various HCl dipping time.

t_{HCl} <i>min</i>	13 mW/cm ²						100 mW/cm ²					
	J_{sc} <i>mA/cm²</i>	V_{oc} <i>V</i>	FF %	η %	R_s <i>$\Omega \cdot \text{cm}^2$</i>	R_{sh} <i>$\Omega \cdot \text{cm}^2$</i>	J_{sc} <i>mA/cm²</i>	V_{oc} <i>V</i>	FF %	η %	R_s <i>$\Omega \cdot \text{cm}^2$</i>	R_{sh} <i>$\Omega \cdot \text{cm}^2$</i>
0	0.64	0.29	29.8	0.42	330	620	3.2	0.44	25.4	0.35	140	160
1	0.67	0.41	40.3	0.86	270	1630	3.6	0.51	27.9	0.51	120	200
10	0.73	0.47	46.7	1.21	250	3610	3.8	0.54	30.6	0.62	110	280
20	0.74	0.49	50.8	1.41	200	2500	4.1	0.55	31.6	0.72	100	260

Figure 4.11 shows the solar cell performance characterized by two different light intensities with various HCl dipping times. Solar cells parameters are summarized in Table 4.3. The R_{sh} increase is pointed out as an important effect of the residual catalyst removal in J_D -V characteristics. However, it is well-known that the R_s is more dominant than R_{sh} at 100 mW/cm² of light intensity that is conventional solar cells measurement condition. The current-voltage measurement is reasonable to be carried out under low light intensity where R_{sh} has dominant effect to verify the increases in R_{sh} by the HCl treatment. The light intensity is modulated with neutral density filter which reduced light intensity from 100 mW/cm² to 13 mW/cm². The solar cell performance under this intensity is shown in Figure 4.11 (a). A large difference in curve shapes is observed with the HCl dipping time. The remarkable phenomenon is a dramatic improvement in FF. Initial 30 % of FF is increased to 50 % by 20 min of HCl dipping of SiNWs. Reduced amount of Sn and Sn oxide by HCl dipping largely increases R_{sh} especially at low light intensity. It clearly supports our hypothesis on reduced shunt current on account of the Sn and Sn oxide removal. As a result, the efficiency can reach 1.4 % under 13 mW/cm² of light intensity.

Solar cell performance measured with usual condition, 100 mW/cm² of light intensity, is shown in Figure 4.11 (b). The solar cell performance is better with increased HCl dipping time in general. The critical reasons of η improvement with the HCl dipping time are notable improvement of J_{sc} and V_{oc} . There is also an increase in fill factor (FF), however, it is still limited by low R_{sh} and high R_s . The increase in transmittance of SiNWs/ITO by etching residual metallic Sn leads the higher absorption in P3HT:PCBM layer. It means that P3HT:PCBM layer can generate more photo-generated carriers. As a result, the J_{sc} is increased around 13 % from initial value with 1 min of HCl treatment. In addition, we observed further increases in J_{sc} although the transmittance increase of SiNWs/ITO is negligible over 1 min of HCl treatment in Figure 4.9 (b). It is attributed to the reduced shunt current (increased R_{sh}) by the Sn oxide removal because it lessens the loss of photocurrent. Therefore, the solar cells shows 28 % increase in J_{sc} (4.1

mA/cm²) after 20 min of HCl dipping compared to that without HCl treatment. The combination of those improvements leads to increased η from 0.35 % to 0.75 %.

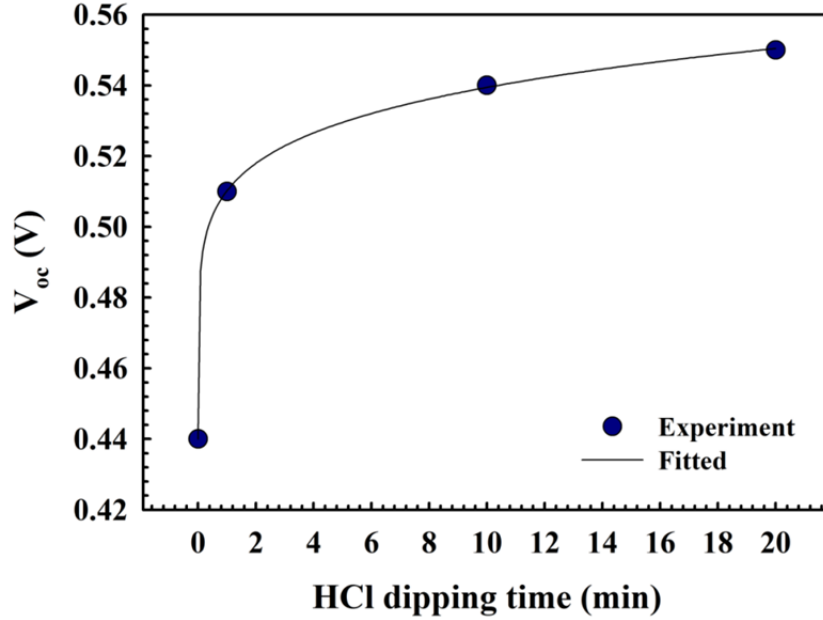


Figure 4.12 – Open-circuit voltage (V_{oc}) change as a function of HCl dipping time; V_{oc} is measured under AM 1.5 condition.

In Table 4.3, the impressive increase in V_{oc} by residual catalyst removal is noted. V_{oc} is the voltage point where there is no current extraction ($J=0$) and it means that photo-generated carriers are totally recombined. Hence, V_{oc} is particularly sensitive to the recombination processes [19, 20]. Figure 4.12 plots V_{oc} variation as a function of the HCl dipping time. As the dipping time increases, V_{oc} tends to increase from initial value. The solid line of Figure 4.12 represents a fitting result. The overall V_{oc} variation follows equation which is extracted from the fitted curve written below,

$$V_{oc}(t_{HCl}) = V_{oci} + A \cdot t_{HCl}^B \quad (4)$$

where V_{oci} is V_{oc} without HCl treatment, t_{HCl} is HCl dipping time, A is proportional factor and B is an exponent. $V_{oci}=0.44$, $A=0.07$ and $B=0.15$ are extracted for this experimental results. 1 min of HCl dipping shows remarkable increase in V_{oc} . Although V_{oc} is continuously improved after 1 min, but it has smaller increment compared to $t_{HCl}=1$. It is believed that 1 min HCl dipping is enough to considerably raise the V_{oc} thanks to the combination of two effects; 1) considerable transmittance increase of SiNWs/ITO (increased in the number of photo-generated carriers) and 2) reduced recombination through Sn. If we assume that the recombination current is constant, the higher V_{oc} is observable with higher absorption in P3HT:PCBM. In addition, the reduced recombination through Sn contributes to V_{oc} increase.

We measured V_{oc} under various light intensities to have further insight into the recombination issue related to the HCl treatment. The photovoltaic action of our hybrid solar cells is mostly governed by P3HT:PCBM. The SiNWs array is used as light trapping media and the hole transport materials. The holes transported through the SiNWs would recombine if there are trap-like Sn and Sn oxide. For this reason, it is reasonable to employ a model used for organic polymer solar cells to explain the recombination in the hybrid solar cells. The response of V_{oc} on the light intensity is given by [21, 22].

$$V_{oc} = \frac{E_{gap}}{q} - \frac{kT}{q} \frac{\ln((1-P)BN_{cv}^2)}{PG} \quad (5)$$

where E_{gap} is the effective energy gap, P is the dissociation probability of bound electron hole pairs, N_{cv} is the effective density of states, G is the generation rate of electron-hole pair and B is the recombination strength. B is equal to the Langevin recombination strength when there is trap-free recombination and the slope of V_{oc} versus natural logarithm of the light intensity plot yields kT/q . On the other hand, if trap-assisted recombination exists, B includes trap-assisted recombination strength and Langevin

recombination strength, thereby enhancing light intensity dependence of V_{oc} . That is, the slope yields bigger value than kT/q . Therefore, the slope is the measure indicating the occurrence of trap-assisted recombination. The higher trap-assisted recombination strength leads to the steeper slope [21, 23].

Figure 4.13 shows V_{oc} as a function of light intensity for various HCl dipping times. The results reveal the evidence of trap-assisted recombination of the hybrid solar cells as discussed above. The residual catalyst removal by the HCl dipping is closely related to the relative decreases in the trap-assisted recombination strength. The slopes are 2.9, 1.7, 1.3 and 1.1 times of kT/q for 0, 1, 10 and 20 min of HCl treated solar cells, respectively. As the HCl dipping time increases, the slope tends to approach kT/q (dashed line in Figure 4.13) which indicates the trap-free recombination although the residual catalysts are not totally eliminated.

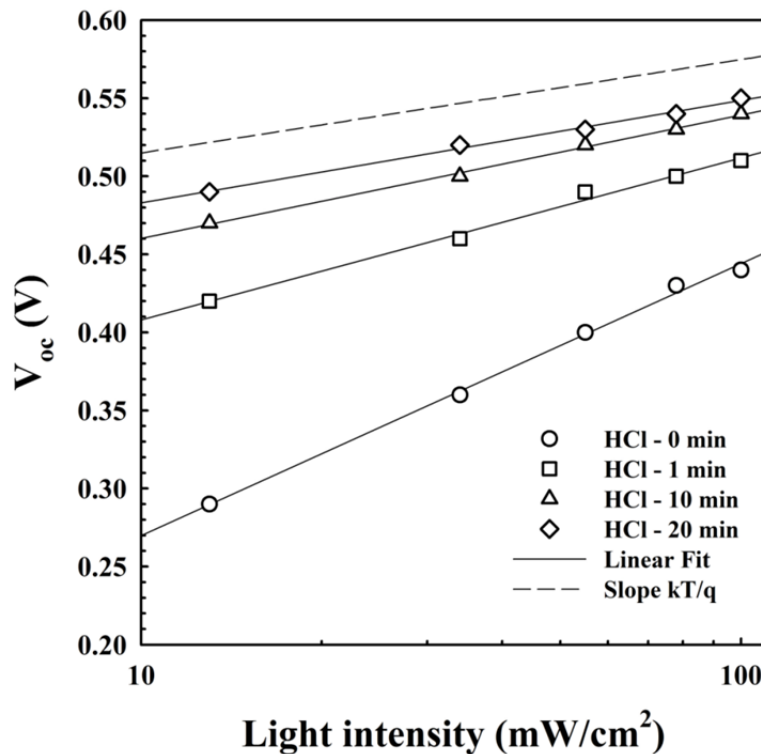


Figure 4.13 – Light intensity dependence of open-circuit voltage with various HCl dipping time. Linear fits for the data are drawn in solid line. Dashed line is drawn as an eye guide line for the slope of kT/q .

By the residual catalyst removal, we obtained better solar cells performance due to the improved transmittance and the reduced trap-assisted recombination. Nevertheless, the solar cell performance showed limitations in terms of resistances and FF. We assumed that native oxide (SiO_x) on the silicon surface is concerned with these limitations. PECVD grown SiNWs come out from the chamber to fabricate hybrid solar cells. Thus, they are immediately exposed to ambient air. The formation of native oxide on SiNWs surface had been already reported in literatures [3, 24, 25].

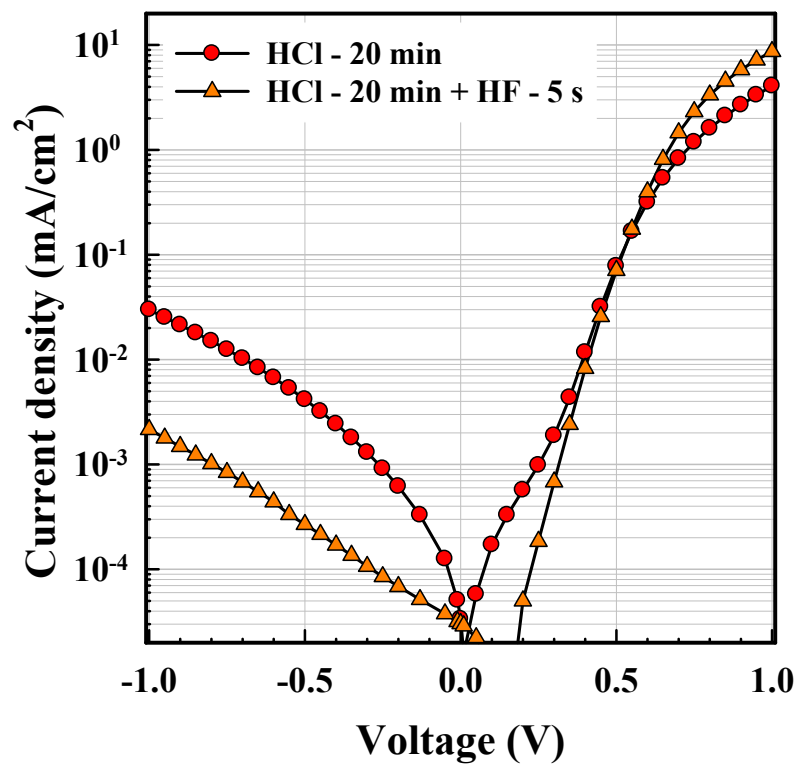


Figure 4.14 – Dark current density – voltage characteristics with and without HF treatment.

HF	n	J_0 mA/cm^2	R_s $\Omega \cdot \text{cm}^2$	R_{sh} $\Omega \cdot \text{cm}^2$
without	1.9	1.4×10^{-5}	88	1.4×10^3
with	1.6	2.4×10^{-6}	13	3.5×10^4

Table 4.4 – Diode parameters of hybrid solar cells: dependence of HF treatment

The oxide could hinder photo-generated carrier extraction in our device because the native oxide is considered as poor charge transport material and only negligible carrier tunneling through oxide occurs [26]. Therefore, 5 % of HF, which is a popular silicon oxide etchant, was employed to remove the thickness of native oxide sheath. The SiNWs are dipped into HF during few seconds after HCl treatment. The dipping time have to be kept short because HF can damage to TCO underlying the SiNWs.

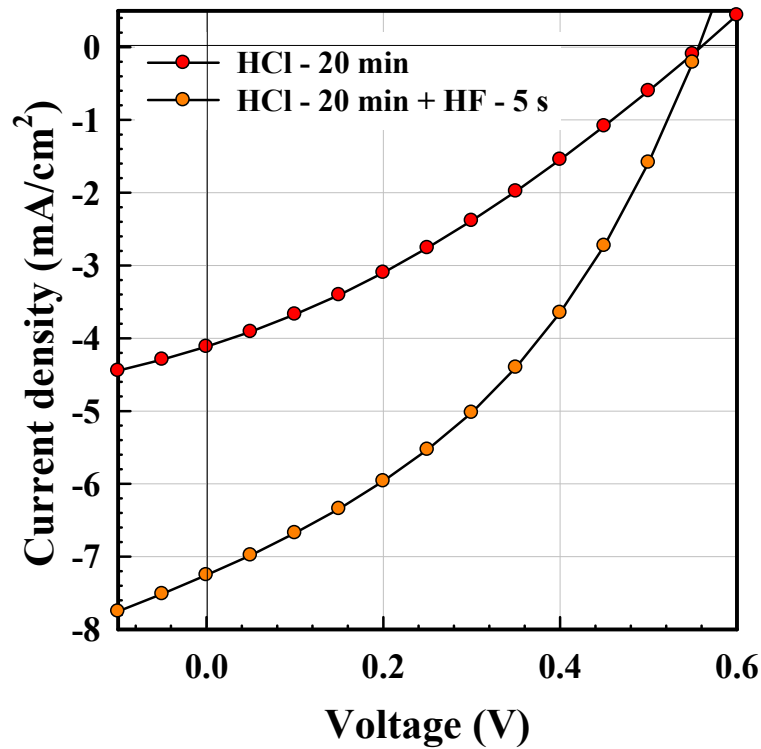


Figure 4.15 – Solar cell performance with and without HF treatment measured under AM 1.5 condition

HF	J_{sc} mA/cm^2	V_{oc} V	FF %	η %	R_s $\Omega \cdot cm^2$	R_{sh} $\Omega \cdot cm^2$
without	4.1	0.55	31.62	0.72	100	261
with	7.3	0.55	38.63	1.54	33	188

Table 4.5 – Solar cell parameters of hybrid solar cells: dependence of HF treatment

Figure 4.14 shows the J_D -V characteristics of hybrid solar cells with and without HF treatment. The first positive effect of HF treatment is the improvement of the diode characteristics. In this figure, lower shunt current in reverse bias regime and higher current in forward bias regime are observed. The diode parameters were extracted from experimental data for quantitative comparison of devices by using diode equation (3) in this chapter. The results are summarized in Table 4.4. HF treatment delivers improved diode parameters. The ideality factor (n) and R_s are improved from 1.9 to 1.6 and from $88 \Omega \cdot \text{cm}^2$ to $13 \Omega \cdot \text{cm}^2$ respectively. In addition, J_0 and R_{sh} are also improved from $1.4 \times 10^{-5} \text{ mA/cm}^2$ to $2.4 \times 10^{-6} \text{ mA/cm}^2$, and from $1 \times 10^3 \Omega \cdot \text{cm}^2$ to $3 \times 10^3 \Omega \cdot \text{cm}^2$ respectively. Better diode characteristics will result in solar cell performance improvement regarding FF and J_{sc} .

The positive effects of HF treatment are also observed in illumination current density. Figure 4.15 shows illumination current density - voltage (J_L -V) characteristics of hybrid solar cells with and without HF treatment and Table 4.5 summarizes solar cell parameters. Note that the η becomes double compared to the device treated by only HCl from 0.72 % to 1.54 %. V_{oc} is not considered as a contributor since it is not affected by HF treatment. Dramatic J_{sc} improvement largely contributes to the increase in the efficiency. This is mainly attributed to the decrease in R_s after HF treatment. The solar cells show about $100 \Omega \cdot \text{cm}^2$ of R_s which governs current flow in fourth quadrant, but it decreases to $33 \Omega \cdot \text{cm}^2$ with HF treatment which eases burden for current flow. Due to the reduced R_s , FF is also little bit increased. The combination of HCl and HF treatments of SiNWs strongly enhances the photo-generated carrier generation and extraction. Consequently, solar energy conversion efficiency of the hybrid solar cells is remarkably improved.

4.3 a-Si:H etching by hydrogen plasma

4.3.1 Selective etching of a-Si:H from SiNWs array

As discussed in Chapter 2, which dealt with growth of SiNWs by PECVD using post-transition metals, a-Si:H is deposited around the SiNWs during the growth process wherever there is no catalyst droplets. This reaction is unavoidable for PECVD grown SiNWs array. The a-Si:H layer could be useful or not according to applications. The a-Si:H layer is considered harmful in the hybrid structure for efficient carrier collection. Note that the doped a-Si:H has deep states and tail states in forbidden gap and high absorption coefficient [24]. The doped a-Si:H could cause problems in hybrid solar cells; 1) photo-generated carriers, especially holes in our devices, could be severely lost by recombination when the holes are extracted 2) the absorption of the organic active layer could be reduced due to the absorption of a-Si:H and 3) the light trapping effect could be limited. Addressing those problems is essential to obtain a better performance of hybrid solar cells and understand the practical advantages of SiNWs.

Before the exploration of SiNWs array and nano-structured hybrid solar cell, the experiments were conducted for planar organic bulk-heterojunction solar cells. For the comparison, a-Si:H was deposited on ITO/glass substrates under the SiNWs growth conditions; at 600 °C, 10 sccm of SiH₄, 1.5 sccm of TMB, 100 sccm of H₂, 1 Torr, 2 W, 3 min without catalyst formation process. Then, conventional organic bulk-heterojunction solar cells were deposited by solution process. Final device structures are ITO/(a-Si:H 10 nm or nothing)/PEDOT:PSS (50 nm)/P3HT:PCBM (230 nm)/LiF (1.2 nm)/Al (100 nm).

Figure 4.16 and Table 4.6 show solar cell performances with and without 10 nm thick a-Si:H on ITO. Without the a-Si:H layer, the solar cell demonstrates a usual characteristic of the organic bulk-heterojunction solar cell based on P3HT:PCBM. J_{sc} reaches about 8 mA/cm² and V_{oc} is 0.63 V, then, power conversion efficiency records 2.4 % under AM 1.5 condition. On the other hand, the performance of solar cells with a-Si:H layer is seriously

limited even for 10 nm thickness of a-Si:H. The power conversion efficiency is only 0.36 %. Among parameters, J_{sc} and FF are mostly affected. J_{sc} and FF are 2.5 mA/cm^2 and 26 % respectively. As extracted, the solar cell with a-Si:H shows 10 times higher R_s than that of the solar cell without a-Si:H. Such high R_s governs overall current density curve shape, thus, J_{sc} and FF are low. From this results, the maleficence of a-Si:H layer, specially resistive effects, is clearly revealed for this solar cell which collect holes through a-Si:H layer. This impact of a-Si:H layer should be equally discussed for hybrid solar cells.

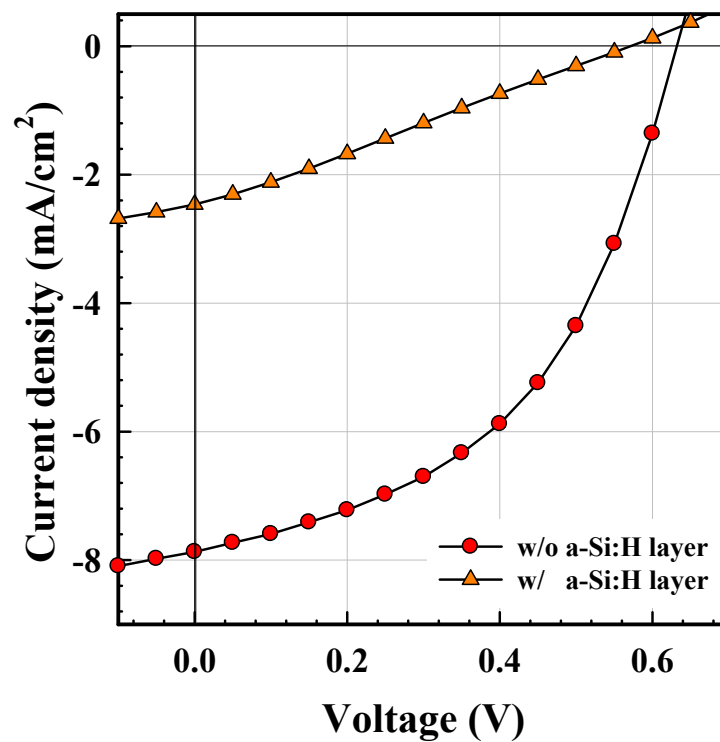


Figure 4.16 – Solar cell performance with and without a-Si:H layer (10 nm) on ITO/glass substrate. Measured under AM 1.5 condition.

a-Si:H [p]	J_{sc} mA/cm^2	V_{oc} V	FF %	η %	R_s $\Omega \cdot \text{cm}^2$	R_{sh} $\Omega \cdot \text{cm}^2$
without	7.87	0.63	48	2.4	23	402
with	2.46	0.57	26	0.36	226	361

Table 4.6 – Solar cell parameters of hybrid solar cells: dependence of a-Si:H layer existence.

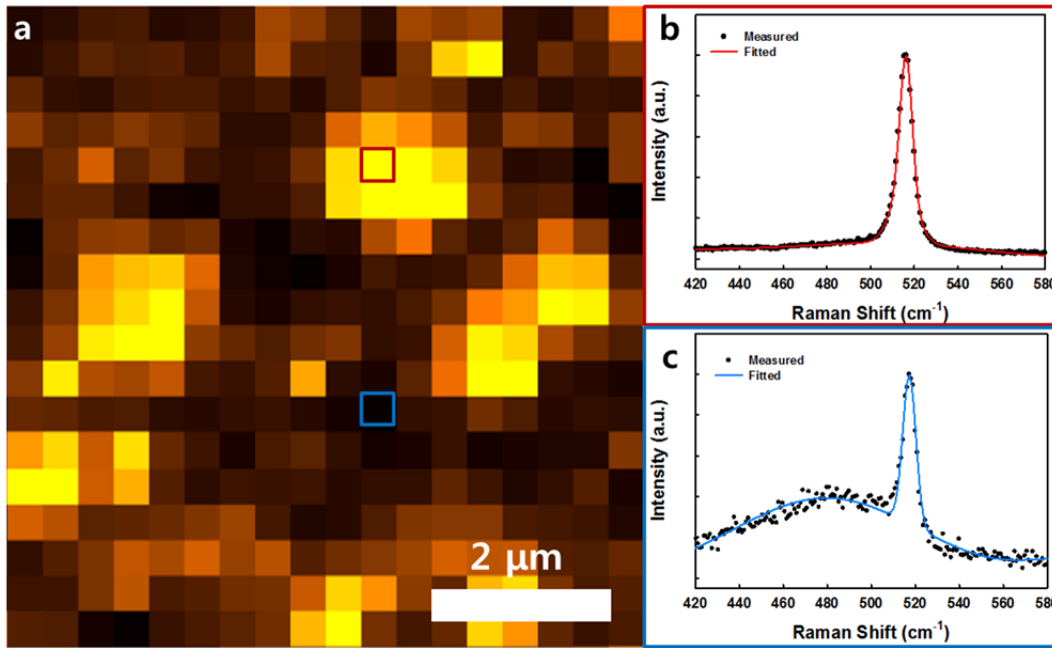


Figure 4.17 – Raman spectroscopy of Sn-catalyzed SiNWs array measured by 621 nm wavelength of red laser with 0.15 mW light intensity. (a) Mapping images over $7 \times 7 \mu\text{m}^2$, (b) Raman shift of SiNWs dominant region and (c) Raman shift of a-Si:H dominant region; SiNWs have diameter, length and density of 20 nm, 240 nm and $4.0 \times 10^9 \text{ SiNWs}/\text{cm}^2$

The presence of a-Si:H on the SiNWs array is estimated by Raman mapping through the as grown SiNWs array. To minimize crystallization of amorphous phase silicon by laser, the red light of 621 nm wavelength with low light intensity around 0.15 mW was employed. The result is shown in Figure 4.17 which is measured over $7 \mu\text{m} \times 7 \mu\text{m}$ region of SiNWs array. The mapping image (Figure 4.17 (a)) is divided into small squares of $0.4 \mu\text{m} \times 0.4 \mu\text{m}$. The squares have different brightness according to Raman signal intensity. While bright region means intense signal, dark region indicates less intense signal. Some part shows intense silicon signal but the other shows weak silicon signal according to the SiNWs distribution, since the resolution of Raman spectroscopy is similar with SiNWs spacing. Despite of this fact, its portion of the crystalline SiNWs determines the signal intensity, thus, the result could well describe the SiNWs array. When the laser focuses on the SiNWs, which is highlighted by a small red box (bright square), these kinds of squares indicate strong crystalline silicon peak at 518 cm^{-1} like

Figure 4.17 (b). It means that the Sn-catalyzed SiNWs by PECVD definitively have good crystallinity. Whereas, when the layer focuses around SiNWs, which is highlighted by a small blue box (dusky square). These kinds of squares show not only broad amorphous peak at 480 cm^{-1} but also weak crystalline silicon peak (Figure 4.17 (c)). This result reveals the a-Si:H deposition around SiNWs. The silicon atoms are physically adsorbed with amorphous phase on the substrate where there are no catalyst droplets preferentially during the growth. From the measurement, we confirm that two different phases of silicon are obtained after the SiNWs growth by PECVD on ITO. The deposition rate were estimated by ellipsometry using a-Si:H layer deposited on glass substrate. 10.2 nm of a-Si:H is deposited during 3 min, thus, deposition rate is 0.057 nm/s.

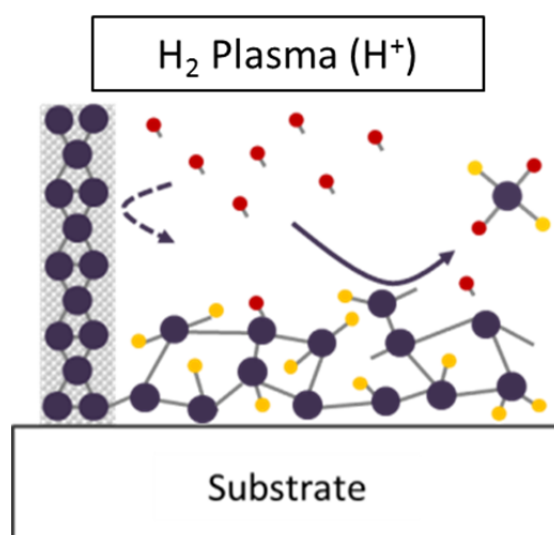


Figure 4.18 – Schematic diagram of amorphous silicon etching process by hydrogen plasma; Big dark circle, small yellow and red circles represent silicon atoms, hydrogen atoms bonded during SiNWs growth for hydrogenation and hydrogen atoms supplied by hydrogen plasma, respectively. Grey solid lines mean covalent bond between atoms. Dark solid line depicts etching process of a-Si:H and dark dashed line indicates less sensitivity of SiNWs. H_2 plasma is performed at $100\text{ }^\circ\text{C}$ with flow rate, pressure and RF power of 200 sccm, 1 Torr and 20 W respectively.

By using the bonding force difference between amorphous and crystalline phases of silicon, the a-Si:H layer could be selectively etched from the SiNWs array. The selective etching method of a-Si:H by H_2 plasma is

already reported by M. Otobe et al in 1994 [27]. The paper studied etching depth difference between amorphous and crystalline phase of silicon depending on temperature, pressure and time. Among these parameters, we benefit from the temperature for selective etching of a-Si:H from the SiNWs array. It is mentioned that the etching depth difference between two different silicon atom phases is bigger at low temperature (at 100 °C). By using this condition we could etch a-Si:H from the SiNWs array. Figure 4.18 shows schematic diagram of selective etching of a-Si:H. The SiNWs array consists of SiNWs which have periodically well bonded silicon and a-Si:H which are irregularly bonded with silicon and hydrogen. When the H₂ plasma is applied just after the growth process, the atomic hydrogen depicted as red circles preferentially react with a-Si:H due to their weaker bonding energy than crystalline silicon. Finally, silicon atoms bonded with neighbor silicon in a-Si:H layer become silane gas (SiH₄) while silicon atoms in SiNWs are almost unaffected by hydrogen radical at 100 °C. Note that we mostly focus on the effects of a-Si:H selective etching on SiNWs array's properties and the correlation with hybrid solar cells performance in this study. The etching rate of a-Si:H is estimated around 0.045 nm/s at 100 °C. The H₂ plasma was applied during 0, 90 and 180 s for comparison.

The evidence of a-Si:H etching is observed by measuring optical absorption of the SiNWs array after H₂ plasma treatment. The absorption of SiNWs/ITO/Glass samples is shown in Figure 4.19. In general, these samples have low absorption at lower photo energy, and then it tends to increase as photon energy increases. The absorption of a photon with energy just above 1.1 eV (~ 1000 nm) is very limited because of silicon has indirect band gap. As the photon energy increases, absorption is increased due to the phonon assisted absorption of SiNWs [15]. As the H₂ plasma duration increases, the absorption is decreased over whole photon energy region. This would lead the enhancement of absorption of organic active layer on SiNWs array.

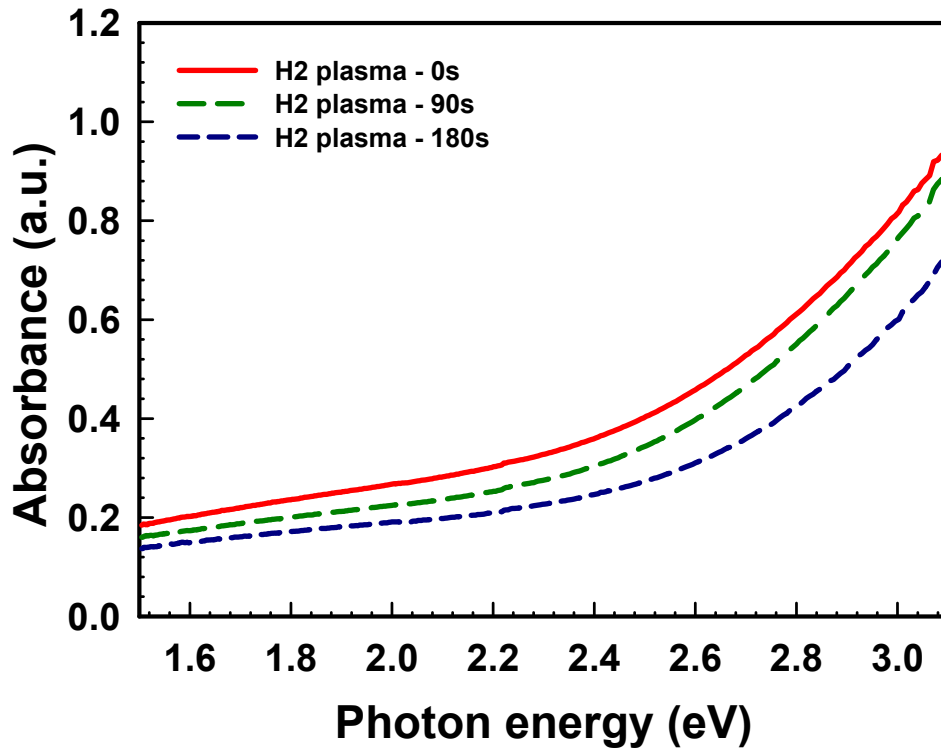


Figure 4.19 – Absorbance of SiNWs/ITO/Glass substrates according to the hydrogen plasma time

However, we have to consider that the absorption of the SiNWs array can be changed by geometrical properties (diameter, length and density) of the nanowires. This is important for accurate analysis of a-Si:H etching effects. Generally, the absorbance is improved as diameter, length and density increase [15]. Thus, if the SiNWs' nano-morphology is affected by H₂ plasma, the absorption property can be modified not only by a-Si:H etching but also by the change in the nano-morphology of SiNWs. Figure 4.20 shows the SEM images and dimensional properties (such as diameter, length and density) of the SiNWs with the H₂ plasma duration. The SEM images with H₂ plasma duration are very similar each other from Figure 4.20 (d) to (f). The SiNWs are straight and tapered regardless of H₂ plasma time due to the strong bonding strength of crystalline silicon as mentioned above. The synthesized SiNWs has diameter, length and density around 20 nm, 240 nm and 4.2 x 10⁹/cm² respectively. These values don't depend on the H₂ plasma duration.

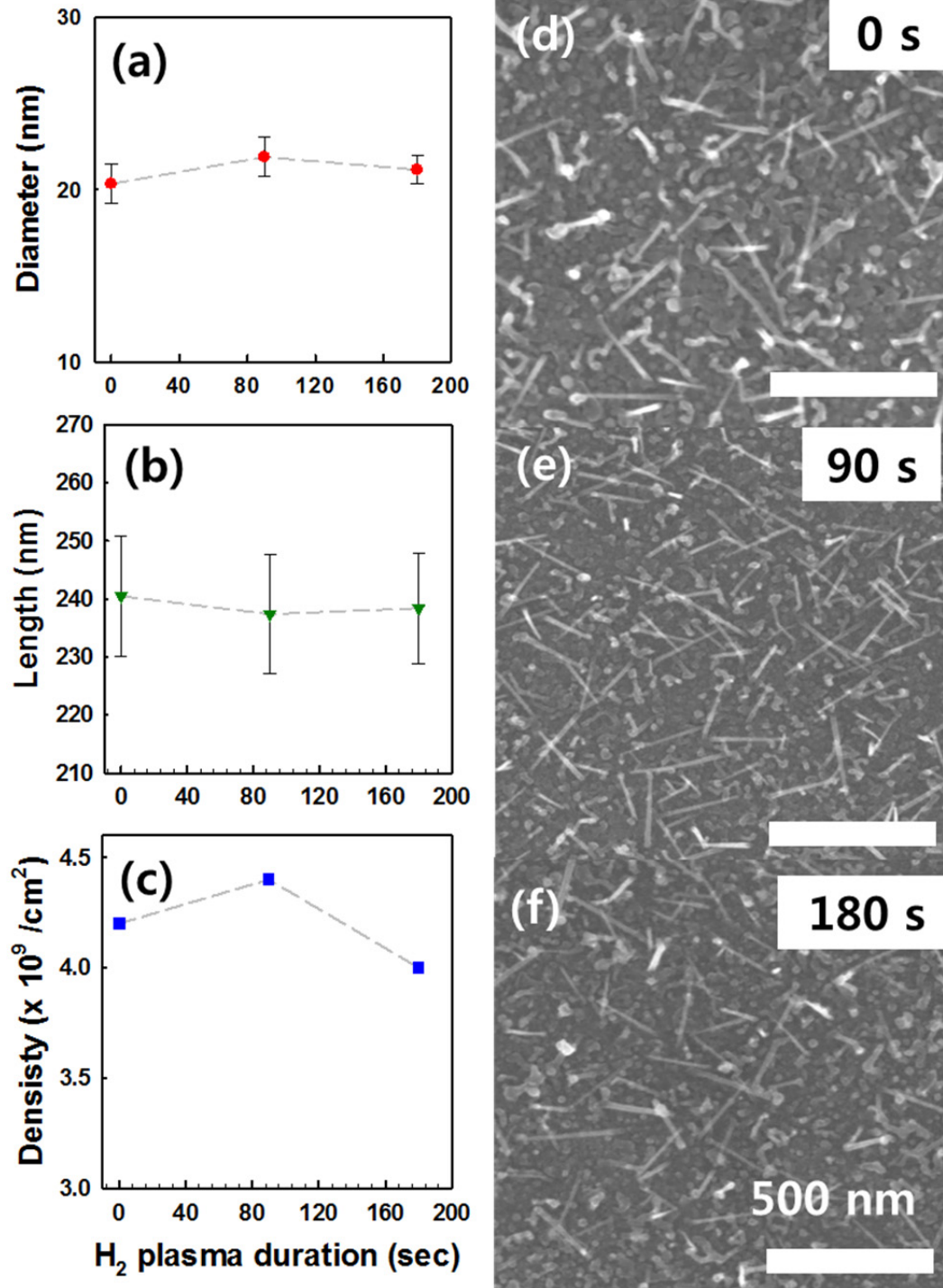


Figure 4.20 – Dimensional properties of SiNWs array according to the hydrogen plasma duration. (a) Diameter of SiNWs, (b) Length of SiNWs, (c) density of SiNWs, and SEM images (d) 0s, (e) 90 s (f) 180 s of duration of hydrogen plasma. The white scale bars indicate 500 nm

The dimensional properties of SiNWs clearly demonstrate that there is no critical influence of hydrogen radicals on the nano-morphology of SiNWs. Accordingly, we can exclude the variation in absorption characteristics by the nano-morphology changes of SiNWs. In other word, the absorption change with different H₂ plasma duration is dominantly related to the a-Si:H etching instead of SiNWs' morphology change. It is well known that a-Si:H is a material with high absorption coefficient about 10⁵ cm⁻¹ at 2.4 eV where P3HT has its maximum absorption. Therefore, it is expected that the etching of a-Si:H will increase the amount of light absorbed by the polymer through the SiNWs array. Namely, more photons will be absorbed in P3HT:PCBM layer that results in high J_{sc} and it could encourage the light trapping through SiNWs array by rule out parasitic absorption by a-Si:H.

4.3.2 Enhanced solar cell performance by a-Si:H etching

The etching of a-Si:H from the SiNWs array is considerably correlated to hybrid solar cell performances although it does not change any SiNWs' morphology. Figure 4.21 and the Table 4.7 describe the current density-voltage characteristics measured under AM 1.5 condition and solar cell parameters with different a-Si:H etching time. The current density curve tends to have better form with the longer etching time. It means that J_{sc} and FF become higher with a-Si:H etching. J_{sc} is the parameter which is more affected than other parameters. It increases more than 50 % by 180 s of H₂ plasma. Another remarkable solar cell parameter is FF. The a-Si:H etching improves FF from 32 % to 44 % which is strongly related with R_s and R_{sh} of solar cells. R_s is gradually reduced, thus, the current density curve is steeper near V_{oc} as H₂ plasma time increases. Also, R_{sh} is improved, hence, the lower slope near 0 V is observed with the longer etching time. As the final outcome, power conversion efficiency show dramatic improvement from 1.2 % to 2.6 % due to the two reasons mentioned above.

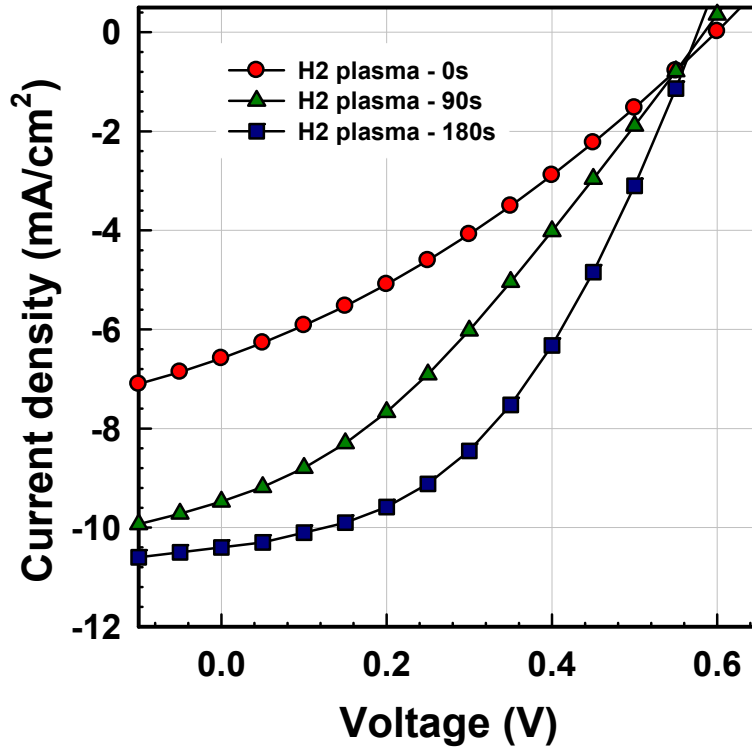


Figure 4.21 – Solar cells performance according to the a-Si:H etching duration by hydrogen plasma

H ₂ plasma	J _{sc} mA/cm ²	V _{oc} V	FF %	η %	R _s Ω·cm ²	R _{sh} Ω·cm ²
0 s	6.6	0.59	32	1.2	61	169
90 s	9.5	0.58	33	1.8	43	186
180 s	10.4	0.57	44	2.6	23	403

Table 4.7 – Solar cells parameters of hybrid solar cells: dependence of a-Si:H layer existence

The improvement in J_{sc} is connected to the increased absorption of P3HT:PCBM layer. As shown in Figure 4.19, the decreased absorbance of SiNWs array by a-Si:H etching results in the absorption of the organic active layer and the light trapping effect by SiNWs. Figure 4.22 shows the absorbance of P3HT:PCBM films with excluding the absorbance of SiNWs. The curve shape of absorbance corresponds to the P3HT absorption [28, 29]. PCBM absorption is not observable due to the strong absorption of SiNWs at

high photon energy region. The absorbance of P3HT:PCBM on SiNWs without H₂ plasma treatment shows similar optical absorption with P3HT:PCBM on glass. But even for this case we can observe the stronger absorption of P3HT:PCBM on SiNWs around 2.2 eV to 2.5 eV region than the film on glass. It means the light trapping effect caused by SiNWs array even though the effects is limited since a-Si:H absorbs incident light before it enters the organic active layer.

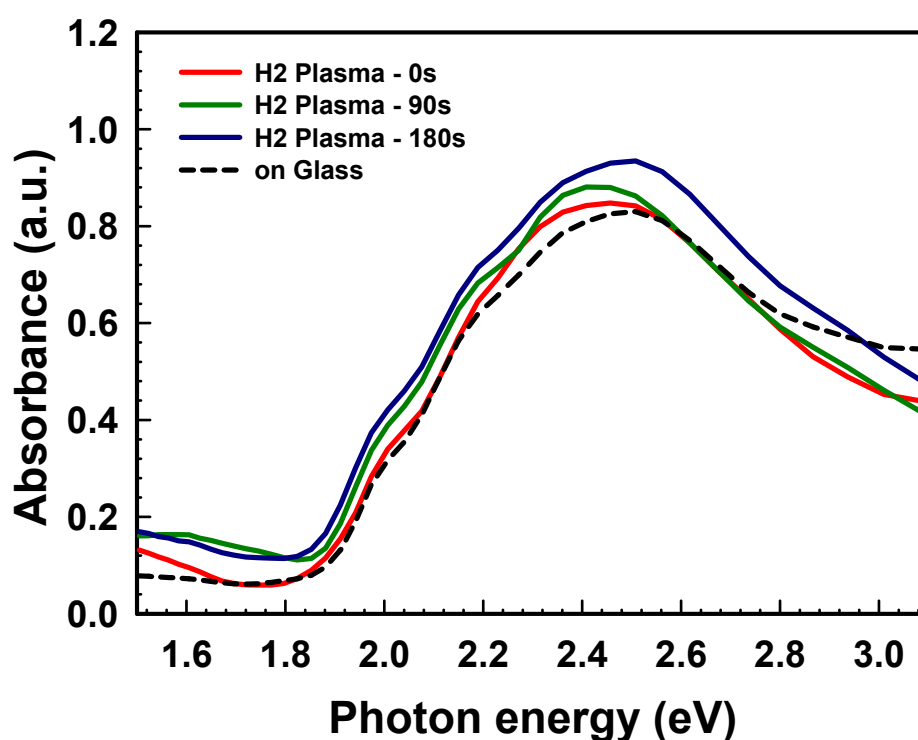


Figure 4.22 – Absorbance of P3HT:PCBM film on SiNWs treated by hydrogen plasma.

The absorbance is increased with 90 s of H₂ plasma for the photon energy under 2.6 eV. P3HT absorption is much more improved after a-Si:H etching. The absorbance is greatly improved over large photon energy range after 180 s of H₂ plasma. This is attributed to the substantial decrease in parasitic absorption of a-Si:H. The parasitic absorption could restrict the absorption of P3HT since the optimal absorption wavelength is similar for both materials. Furthermore, a-Si:H also limit light trapping effects of SiNWs.

These are harmful optical effects of parasitic a-Si:H deposition when we remind the working principle of this hybrid solar cell in Chapter 3.

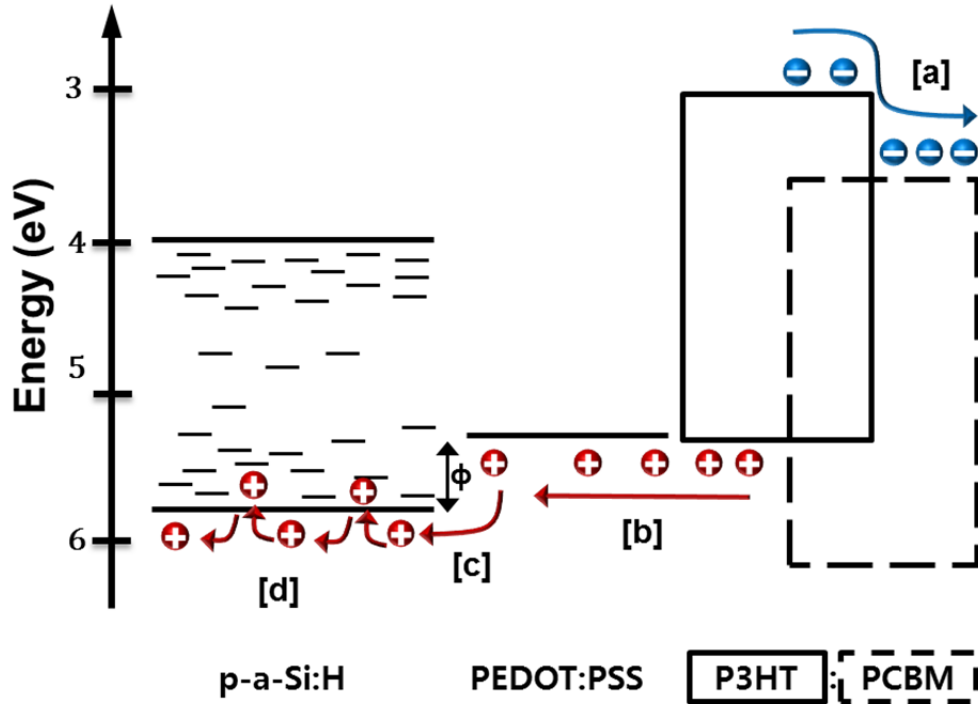


Figure 4.23 – Schematic diagram of holes transport from P3HT:PCBM layer to a-Si:H layer. [a] electron transfer from P3HT to PCBM [b] hole transport through P3HT to PEDOT:PSS [c] Injection of holes from PEDOT:PSS to a-Si:H (energy barrier, ϕ , is 0.5 eV) and [d] hole transport by multi-trapping and release through p-type a-Si:H.

As mentioned, the a-Si:H etching brings a decrease in R_s and an increase in R_{sh} of hybrid solar cells. Electrically, a-Si:H is resistive material because the bonding between silicon atoms are disordered and its band configuration shows band-gap states due to the dangling bond and the aperiodicity. Figure 4.23 describes energy band diagram of the hybrid solar cells. P3HT creates exciton by light absorption then the exciton is dissociated at the P3HT/PCBM interface into free electron and hole. The electron is transferred to LUMO of PCBM by electron transfer [a] and the hole travels through HOMO of P3HT and it goes to PEDOT:PSS [b]. Up to this process, it is general steps for organic bulk-heterojunction solar cells [30, 31], but the difficulty of hole transport is occurred at PEDOT:PSS/a-Si:H interface. Process [c] in Figure

4.23 shows the hole injection from PEDOT:PSS to valence band of a-Si:H. It is predicted that this process is not preferable due to the large injection barrier of $\phi=0.5$ eV. If holes are injected to the a-Si:H over the barrier, they are transported toward the anode by the multi-trapping and release mechanism through the p-type a-Si:H. This isn't an effective way to transport holes because it lowers the mobility of holes and induces the recombination of holes due to trap levels. These are origins of the resistive effects of a-Si:H in our solar cells [32]. Addressing those negative effects of a-Si:H by the selective etching using H₂ plasma is concerned with the improvement of hybrid solar cell performance.

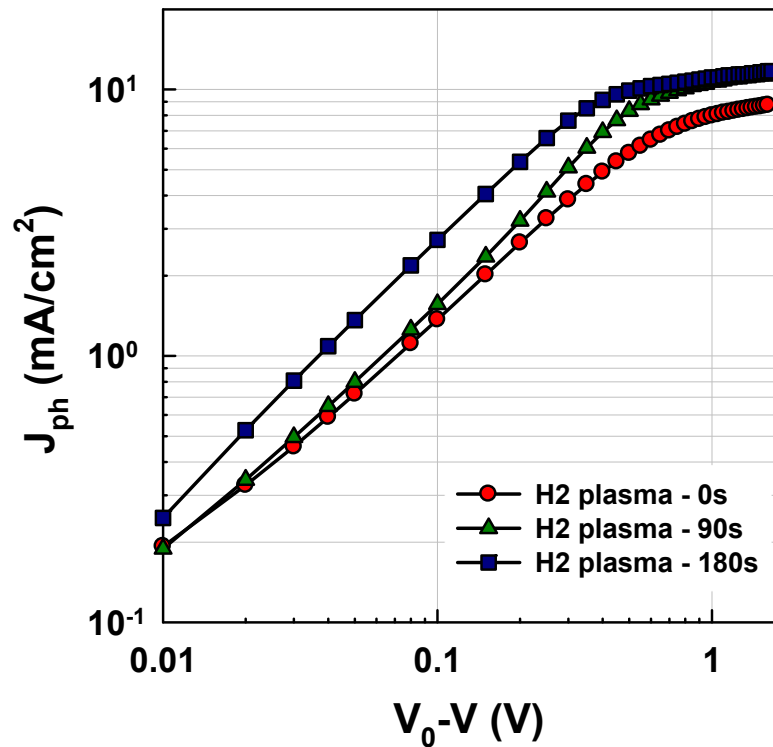


Figure 4.24 – Experimental photo-current as a function of effective voltage ($V_0 - V$) according to the H₂ plasma duration.

Note that the curve shape in Figure 4.21 is conspicuously influenced by a-Si:H etching time. It means that the a-Si:H etching has a decisive effect on the overall photo-generated charge collection efficiency of the hybrid solar cells [27]. The observation of the experimental photo-current density (J_{ph})

are conducted to take into account the influence of the a-Si:H etching on the photo-generated carriers. Figure 4.24 shows experimental J_{ph} as a function of effective voltage discussed in Chapter 3. The J_{ph} scales linearly with low effective voltage under 0.2-0.3 V where the diffusion of photo-generated carriers is considered as important. Then, the J_{ph} enters the saturation regime where the drift of photo-generated carriers plays a critical role with large effective voltage [19, 21, 33-35]. With increased H_2 plasma duration, the enhancement of J_{ph} is observed within the measured effective voltage range. In low effective voltage region, all of J_{ph} starts at similar current level, however, the bigger slope of $\log(J_{ph})/\log(V_0-V)$ is observed as the H_2 plasma duration increases. In other words, J_{ph} is more sensitively scales with the effective voltage. In saturation regime, the J_{ph} shows higher value with 180 s of H_2 plasma than others which is a driving force to produce higher J_{sc} . Moreover, J_{ph} tends to enter the saturation regime with relatively lower effective voltage as the H_2 plasma duration increases. These are attributed to increased organic layer's absorption, enhancement of light trapping by reducing parasitic absorption and efficient photo-generated carrier collection by the etching a-Si:H layer.

4.4 Conclusion: benefits from Sn-catalyzed SiNWs

“Are the PECVD grown SiNWs beneficial for hybrid solar cell application?”

This question is not clearly answered yet in academia. In 2009, Kuo et al. reported a hybrid solar cells based on Au-catalyzed SiNWs array and P3HT:PCBM film [10]. They demonstrated 0.42 % of power conversion efficiency with proper arrangement of band structure by changing top electrode of the device. The efficiency is quite low compared to the hybrid solar cells based on the SiNWs fabricated by top-down approaches [16, 36-39]. This is related to the inherent quality difference according to the fabrication methods; namely, bottom-up and top-down approaches. Yuan et al. reported that chemically synthesized SiNWs have low quality compared to the etched SiNWs from a silicon wafer [40]. Thus, further understanding of the growth chemistry is necessary for efficient solar energy conversion. For this reason, few research results concerning hybrid solar cells using SiNWs grown by bottom-up methods are reported globally. The roles and benefits of SiNWs in hybrid solar cells are still questionable.

Here we investigated hybrid solar cells based on PECVD grown SiNWs and P3HT:PCBM layer. The optimization of SiNWs array in terms of optical and electrical aspects is mostly important for enhancing hybrid solar cell performance. We unveiled the benefits of the SiNWs by optimizing the SiNWs array. In hybrid solar cells with as grown SiNWs, the roles and benefits are undiscoverable due to the residual catalyst, the native oxide of SiNWs and a-Si:H around SiNWs. Those parameters cause great parasitic absorption and electrical resistivity that can degrade electrical performance of the hybrid solar cells. Therefore, we studied the chemical and physical methods to improve the quality of SiNWs array. First, we considered residual catalysts and native oxide removal. Then, we etched out a-Si:H around SiNWs. Furthermore, we revealed the correlation between those optimization methods and the hybrid solar cells performance.

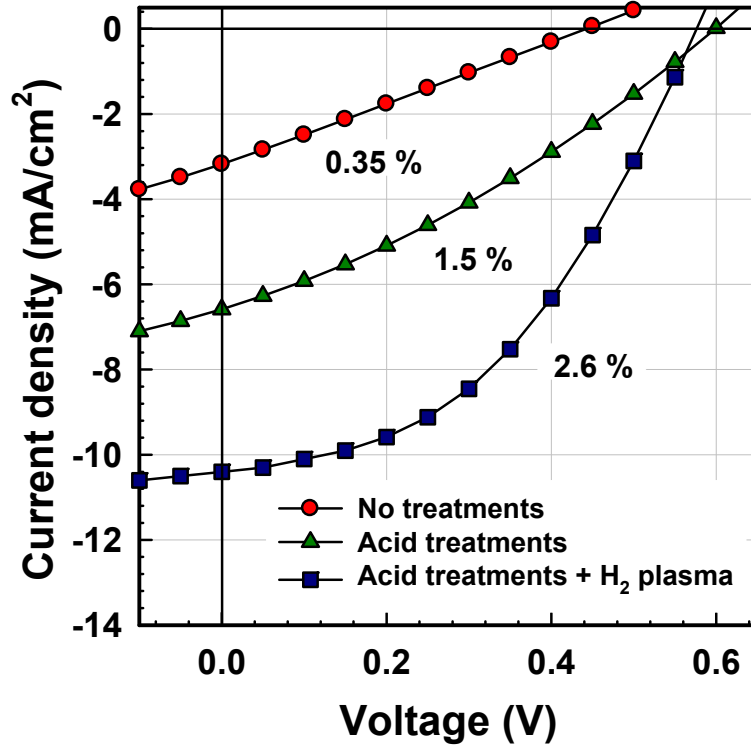


Figure 4.25 – Solar cells performance according to the optimization method which are measured under AM 1.5 condition.

Figure 4.25 clearly summarizes the performance of the hybrid solar cells, which is the main subject of this chapter, depending on the SiNWs array optimization processes. At the initial state without any treatment, solar energy conversion efficiency is lower than others. The curve shape is very limited by resistive effects near 0 V and at V_{oc} . Acid treatments (HCl & HF) brought substantial improvement of solar cell performance. Evidently, J_{sc} and V_{oc} are better with acid treatments. Despite of this considerable advance, the current density-voltage characteristic is still affected by resistances of the devices. The power conversion efficiency is much more improved by the combination of acid treatment and H_2 plasma for a-Si:H etching. Resistive effects, which always cause trouble, are surely improved compared to two other hybrid solar cells. This graph definitely discloses the strong correlation of solar cell performance with the SiNWs array's quality.

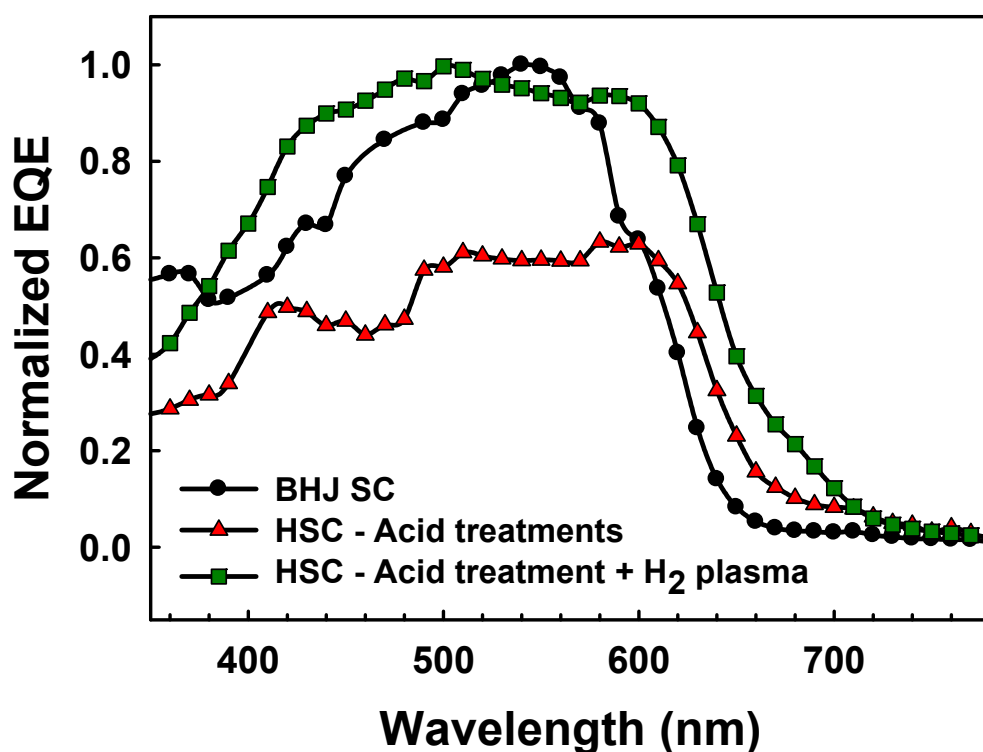


Figure 4.26 – Normalized external quantum efficiency (EQE) of solar cells; comparison of organic bulk-heterojunction solar cells (BHJ SC) and hybrid solar cell (HSC) with different treatment conditions. Organic active layer is composed of P3HT and PCBM. The thickness of active layer is same for BHJ SC and HSC.

Benefits of SiNWs are obviously emerged through external quantum efficiency (EQE) measurement of the hybrid solar cells. Figure 4.26 shows normalized EQE of an organic bulk-heterojunction solar cell and hybrid solar cells. All solar cells have P3HT:PCBM layer deposited from same bottle by same spin-coating conditions. The EQE of the solar cell with only acid treatment is limited although it shows similar level of EQE with P3HT:PCBM bulk-heterojunction reference at longer wavelength region over 620 nm. For the maximum absorption of P3HT, around 500 nm, EQE is 40 % lower compared to that of planar organic bulk-heterojunction solar cell. In addition to acid treatment, a-Si:H etching was carried out. For this solar cell, we could observe significant increase in EQE. The EQE has matchable level to the planar organic bulk-heterojunction solar cell with increases in EQE of shorter and longer wavelength regions. The optimization of SiNWs brings

substantial advancement in hybrid solar cell using SiNWs in terms of optical and electrical aspects.

Now, it is time to answer the question written in first sentence of this section. From various results, the SiNWs are advantageous for hybrid solar cell application. They shows impressive enhancement of 1) the absorption of the organic active layer in our structure and 2) the EQE of hybrid solar cell compared to the organic bulk-heterojunction solar cell. The hybrid solar cell with optimized SiNWs array has power conversion efficiency (2.6 %) which stacks up to that of organic solar cells (2.4 %) for the same active layer. This is remarkable progress although absolute power conversion efficiency of our hybrid solar cell still has long way to go compared to the recent advance of organic solar cell.

REFERENCE

1. Wagner, R.S. and W.C. Ellis, *VAPOR-LIQUID-SOLID MECHANISM OF SINGLE CRYSTAL GROWTH*. Applied Physics Letters, 1964. **4**(5): p. 89-90.
2. Gunawan, O. and S. Guha, *Characteristics of vapor-liquid-solid grown silicon nanowire solar cells*. Solar Energy Materials and Solar Cells, 2009. **93**(8): p. 1388-1393.
3. Hofmann, S., et al., *Gold catalyzed growth of silicon nanowires by plasma enhanced chemical vapor deposition*. Journal of Applied Physics, 2003. **94**(9): p. 6005-6012.
4. Nebol'sin, V.A. and A.A. Shchetinin, *Role of Surface Energy in the Vapor-Liquid-Solid Growth of Silicon*. Inorganic Materials, 2003. **39**(9): p. 899-903.
5. Yu, L., et al., *Bismuth-Catalyzed and Doped Silicon Nanowires for One-Pump-Down Fabrication of Radial Junction Solar Cells*. Nano Letters, 2012. **12**(8): p. 4153-4158.
6. Linwei, Y., et al., *Radial junction amorphous silicon solar cells on PECVD-grown silicon nanowires*. Nanotechnology, 2012. **23**(19): p. 194011.
7. Cho, J., et al., *Sn-catalyzed silicon nanowire solar cells with 4.9% efficiency grown on glass*. Progress in Photovoltaics: Research and Applications, 2012. **21**(1): p. 77-81.
8. Kelzenberg, M.D., et al., *Enhanced absorption and carrier collection in Si wire arrays for photovoltaic applications*. Nat Mater, 2010. **9**(3): p. 239-244.
9. Golap, K. and et al., *Silicon nanowire array/polymer hybrid solar cell incorporating carbon nanotubes*. Journal of Physics D: Applied Physics, 2009. **42**(11): p. 115104.
10. Kuo, C.Y. and C. Gau, *Arrangement of band structure for organic-inorganic photovoltaics embedded with silicon nanowire arrays grown on indium tin oxide glass*. Applied Physics Letters, 2009. **95**(5): p. 053302-3.
11. Garnett, E.C. and P. Yang, *Silicon Nanowire Radial p-n Junction Solar Cells*. Journal of the American Chemical Society, 2008. **130**(29): p. 9224-9225.
12. Monk, P.M.S. and C.M. Man, *Reductive ion insertion into thin-film indium tin oxide (ITO) in aqueous acidic solutions: the effect of leaching of indium from the ITO*. Journal of Materials Science: Materials in Electronics, 1999. **10**(2): p. 101-107.
13. Holmberg, V.C., K.A. Collier, and B.A. Korgel, *Real-Time Observation of Impurity Diffusion in Silicon Nanowires*. Nano Letters, 2011. **11**(9): p. 3803-3808.
14. Yu, L., et al., *Stability and evolution of low-surface-tension metal catalyzed growth of silicon nanowires*. Applied Physics Letters, 2011. **98**(12): p. 123113-3.
15. Hu, L. and G. Chen, *Analysis of Optical Absorption in Silicon Nanowire Arrays for Photovoltaic Applications*. Nano Letters, 2007. **7**(11): p. 3249-3252.

16. Huang, J.-S., et al., *Well-aligned single-crystalline silicon nanowire hybrid solar cells on glass*. Solar Energy Materials and Solar Cells, 2009. **93**(5): p. 621-624.
17. Dongaonkar, S., et al., *Universality of non-Ohmic shunt leakage in thin-film solar cells*. Journal of Applied Physics, 2010. **108**(12): p. 124509-10.
18. Yoo, S., B. Domercq, and B. Kippelen, *Intensity-dependent equivalent circuit parameters of organic solar cells based on pentacene and C₆₀*. Journal of Applied Physics, 2005. **97**(10): p. 103706-9.
19. Koster, L.J.A., et al., *Device model for the operation of polymer/fullerene bulk heterojunction solar cells*. Physical Review B, 2005. **72**(8): p. 085205.
20. Mandoc, M.M., et al., *Origin of the Reduced Fill Factor and Photocurrent in MDMO-PPV:PCNEPV All-Polymer Solar Cells*. Advanced Functional Materials, 2007. **17**(13): p. 2167-2173.
21. Kuik, M., et al., *Determination of the trap-assisted recombination strength in polymer light emitting diodes*. Applied Physics Letters, 2011. **98**(9): p. 093301-3.
22. Koster, L.J., *Light intensity dependence of open-circuit voltage of polymer:fullerene solar cells*. Appl. Phys. Lett., 2005. **86**(12): p. 123509.
23. Mandoc, M.M., et al., *Effect of traps on the performance of bulk heterojunction organic solar cells*. Applied Physics Letters, 2007. **91**(26): p. 263505-3.
24. McDowell, M.T., et al., *Novel Size and Surface Oxide Effects in Silicon Nanowires as Lithium Battery Anodes*. Nano Letters, 2011. **11**(9): p. 4018-4025.
25. Garnett, E.C., et al. *Silicon nanowire hybrid photovoltaics*. in *Photovoltaic Specialists Conference (PVSC), 2010 35th IEEE*. 2010.
26. Gowrishankar, V., et al., *Exciton harvesting, charge transfer, and charge-carrier transport in amorphous-silicon nanopillar/polymer hybrid solar cells*. Journal of Applied Physics, 2008. **103**(6): p. 064511-8.
27. Masanori Otobe, M.K.a.S.O., *Selective Etching of Hydrogenated Amorphous Silicon by Hydrogen Plasma*. Japanese Journal of Applied Physics, 1994. **33**: p. 4442-4445.
28. Liu, C.-Y., Z.C. Holman, and U.R. Kortshagen, *Optimization of Si NC/P3HT Hybrid Solar Cells*. Advanced Functional Materials, 2010. **20**(13): p. 2157-2164.
29. Pasquier, A.D., et al., *Photoinduced charge transfer between poly(3-hexylthiophene) and germanium nanowires*. Applied Physics Letters, 2007. **91**(18): p. 183501-3.
30. Jiang, X., et al., *Aluminum-doped zinc oxide films as transparent conductive electrode for organic light-emitting devices*. Applied Physics Letters, 2003. **83**(9): p. 1875-1877.

-
31. Dennler, G., M.C. Scharber, and C.J. Brabec, *Polymer-Fullerene Bulk-Heterojunction Solar Cells*. Advanced Materials, 2009. **21**(13): p. 1323-1338.
 32. Carlson, D.E. and C.R. Wronski, *Amorphous silicon solar cells*, in *Amorphous Semiconductors*, M. Brodsky, Editor 1985, Springer Berlin Heidelberg. p. 287-329.
 33. Koster, L.J., *Bimolecular recombination in polymer/fullerene bulk heterojunction solar cells*. Appl. Phys. Lett., 2006. **88**(5): p. 052104.
 34. Mandoc, M.M., *Charge transport in MDMO-PPV:PCNEPV all-polymer solar cells*. J. Appl. Phys., 2007. **101**(10): p. 104512.
 35. Mihailetschi, V.D., et al., *Charge Transport and Photocurrent Generation in Poly(3-hexylthiophene): Methanofullerene Bulk-Heterojunction Solar Cells*. Advanced Functional Materials, 2006. **16**(5): p. 699-708.
 36. Avasthi, S., et al., *Role of Majority and Minority Carrier Barriers Silicon/Organic Hybrid Heterojunction Solar Cells*. Advanced Materials, 2011. **23**(48): p. 5762-5766.
 37. He, L., et al., *High efficiency planar Si/organic heterojunction hybrid solar cells*. Applied Physics Letters, 2012. **100**(7): p. 073503-3.
 38. He, L., et al., *Highly efficient Si-nanorods/organic hybrid core-sheath heterojunction solar cells*. Applied Physics Letters, 2011. **99**(2): p. 021104-3.
 39. He, L., et al., *Si Nanowires Organic Semiconductor Hybrid Heterojunction Solar Cells Toward 10% Efficiency*. ACS Applied Materials & Interfaces, 2012. **4**(3): p. 1704-1708.
 40. Yuan, G., et al., *Understanding the Origin of the Low Performance of Chemically Grown Silicon Nanowires for Solar Energy Conversion*. Angewandte Chemie International Edition, 2011. **50**(10): p. 2334-2338.

Chapter 5

HYBRID HETEROJUNCTION BASED SOLAR CELLS

5.1	INTRODUCTION	144
5.2	HYBRID INTERFACE: P3HT AND SILICON MATERIALS	144
5.3	REALIZATION OF HYBRID SOLAR CELLS	148
5.4	DEVICE PERFORMANCES	150
5.4.1	DARK CURRENT-VOLTAGE CHARACTERISTIC	150
5.4.2	SOLAR CELL PERFORMANCE	153
5.5	CONCLUSION: CHALLENGES AND PERSPECTIVES	161
	<i>REFERENCE</i>	<i>163</i>

5.1 Introduction

This chapter tries to figure out hybrid solar cells based on hybrid interface between Bi-catalyzed SiNWs and P3HT. Potentially, a nano-structured hybrid solar cell based on the hybrid interface is one of candidates for the next-generation solar cells regard to the benefit from both types of materials and device design. However, reports on these types of hybrid solar cells suggest the achievement of high efficiency is still challenging. Bi-catalyzed SiNWs have n-type nature and the average interspacing between the nanowires around 20 nm. Based on these facts, it seems that they can be employed as an electron acceptor for excitons dissociation from P3HT. Band diagrams of P3HT, c-Si and a-Si:H are discussed to understand the exciton separation at these hybrid interfaces.

The solar cell device is realized based on a proposed device structure using grid electrode (Section 5.3). Basic working principle is also discussed. The diode performance under dark clearly demonstrates the n-type nature of Bi-catalyzed SiNWs again with the hybrid solar cells structure and the parameters are analyzed. Solar cell performances obtained from P3HT or P3HT:PCBM active layers are discussed. Then the analysis on the photocurrent is carried out to accurate comparison by excluding dark current density from total current density under illumination. The chapter is closed with the discussion on perspectives and further challenges.

5.2 Hybrid interface: P3HT and silicon materials

Electric devices based on the heterojunction of organic semiconductors with inorganic semiconductor were reported in early 1980. Forrest reported a contact barrier device by deposition of 3,4,9,10-perylenetetracarboxylic dianhydride (PTCDA) on p-type c-Si wafer [1]. It showed the potential of hybrid heterojunction for electrical uses. In 1984, McCaffrey reported the hybrid solar cells based on pyrene coated crystalline silicon with 4.53 % of efficiency [2]. Despite of the interest on it from 30 years ago, the devices

based on the hybrid heterojunction are not efficient compared to pure inorganic or organic based devices. In recent years, it is again drawing interest again for solar cell applications.

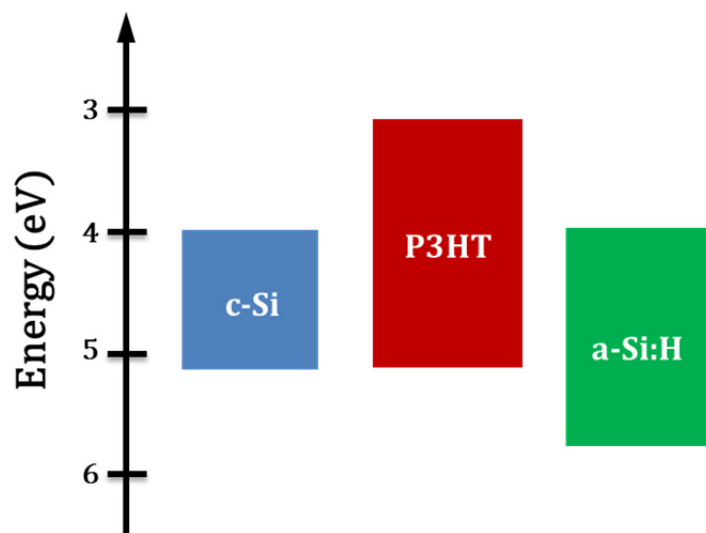


Figure 5.1 – Energy band diagrams of P3HT, crystalline silicon (c-Si) and hydrogenated amorphous silicon (a-Si:H)

Figure 5.1 illustrates band diagrams of c-Si, a-Si:H and P3HT at thermal equilibrium. P3HT, which is used as the main light absorbing material, shows higher LUMO level than conduction bands of silicon materials. On the other hand, HOMO level of P3HT is similar to the valence band of c-Si. It cannot be clearly stated due to the uncertainty of the HOMO level of P3HT (Section 1.3.2). P3HT has lower HOMO level than the valence band of a-Si:H. According to the band diagrams, excitons are probably dissociated at interfaces with silicon materials. In other word, electron of P3HT can be transferred toward silicon materials since both provide a sufficient band offset energy. Naturally, holes are conducted through P3HT. a-Si:H might be more stable than c-Si due to higher difference between HOMO of P3HT and valence band of a-Si:H. While c-Si has the advantage in electrical conductivity.

Solar cells based on silicon/P3HT junction were reported in literatures. First, the work on c-Si wafer/P3HT junction based solar cell was conducted by Avasthi et al [3]. Figure 5.2 shows solar cells structure and performances with various thickness of P3HT spin-coated on n-Si. Due to the thin P3HT and thick silicon wafer, n-Si performs the role of main absorber. However, it is sure that photo-generated holes are conducted through P3HT. P3HT brings V_{oc} improvement that means it effectively modifies the Schottky barrier at the interface compared to that without P3HT. On the other hands, J_{sc} is similar regardless of P3HT's thickness. It is attributed to close energy level of HOMO of P3HT with valence band of c-Si. Namely, negligible energy barrier is existed at n-Si/P3HT interface.

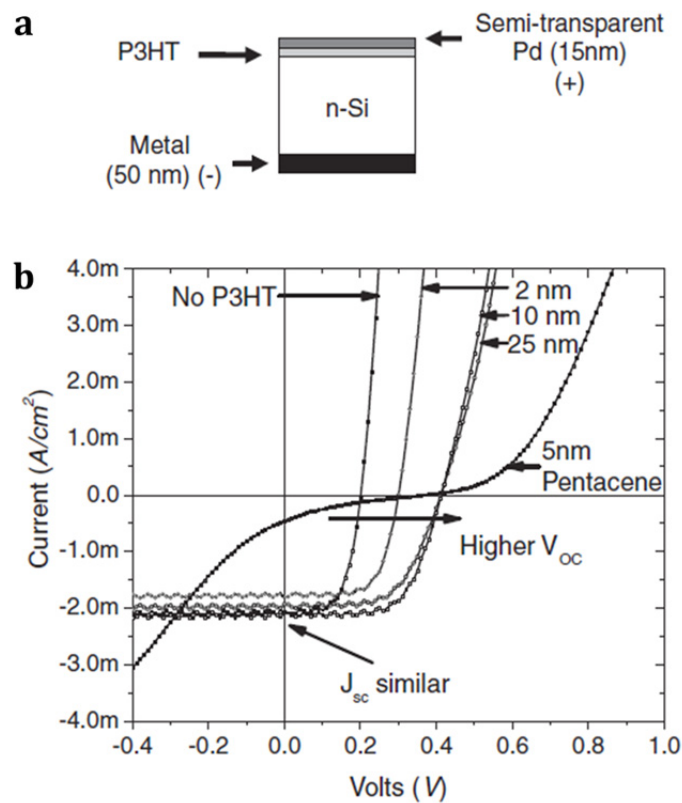


Figure 5.2 – Solar cell based on c-Si/P3HT junction. (a) Solar cell structure: P3HT is spin-coated on n-Si wafer, and then semi-transparent palladium is evaporated. (b) Solar cell performance with various thickness of P3HT. (Reprinted from Ref.[3])

Solar cell of a-Si:H/P3HT junction was investigated by our group. Figure 5.3 shows a solar cell structure and performance. P3HT is spin-coated on the 20 nm thick n-type a-Si:H. Here, P3HT is employed as the main absorber and the absorption of a-Si:H is not critical since it is thinner than P3HT. Before depositing P3HT, a-Si:H/ITO/glass substrate is dipped into hydrofluoric acid to remove native oxide which prohibits exciton dissociation [4]. The exciton generated in P3HT is probably separated in two different mechanisms. First, the electron can be transferred from LUMO of P3HT toward conduction band of a-Si:H while hole is in P3HT. Second, excitons can be also separated by the combination of energy transfer and hole back transfer.

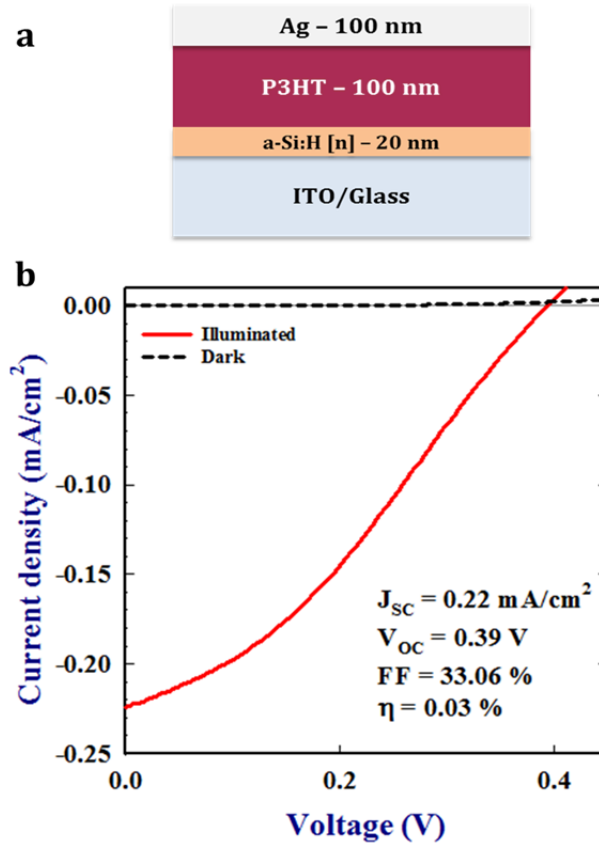


Figure 5.3 – Solar cell based on a-Si:H/P3HT junction. (a) Solar cell structure: n-type a-Si:H are deposited by conventional PECVD with 20 nm thick. P3HT is spin-coated on a-Si:H layer and then silver (Ag) electrode is deposited by thermal evaporation. (b) Solar cell performance.

Since P3HT has higher band-gap (2 eV) than a-Si:H (1.7 eV), energy can be transferred from P3HT to a-Si:H, namely, exciton goes to a-Si:H. And then, the holes are back transferred from valence band of a-Si:H to HOMO of P3HT. However, the hole transfer is limited process due to the localized states of a-Si:H at the interface (Section 1.2.2). From the report of Gowrishankar et al, the solar cell performance based on the interface is poor although most of excitons are harvested [4, 5]. Our result in Figure 5.3 (b) also shows poor performance with low J_{sc} and FF.

Both examples clearly show that exciton can be dissociated at silicon/P3HT interface. The charge transfer between silicon nanocrystals and P3HT was measured by light-induced electron spin resonance by Dietmueller et al [6]. The results agree with the exciton dissociation process of solar cells presented in last paragraph. Therefore, it is interesting to deal with hybrid solar cells based on Bi-catalyzed SiNWs and P3HT in terms of energy levels and structures. Nano-structures given by SiNWs can open a way to approach ideal nano-structured solar cells. In addition, Bi-catalyzed SiNWs grown by PECVD could considerably lower the fabrication cost than former solar cell fabrication techniques based on c-Si with keeping the high degrees of crystallinity [7].

5.3 Realization of hybrid solar cells

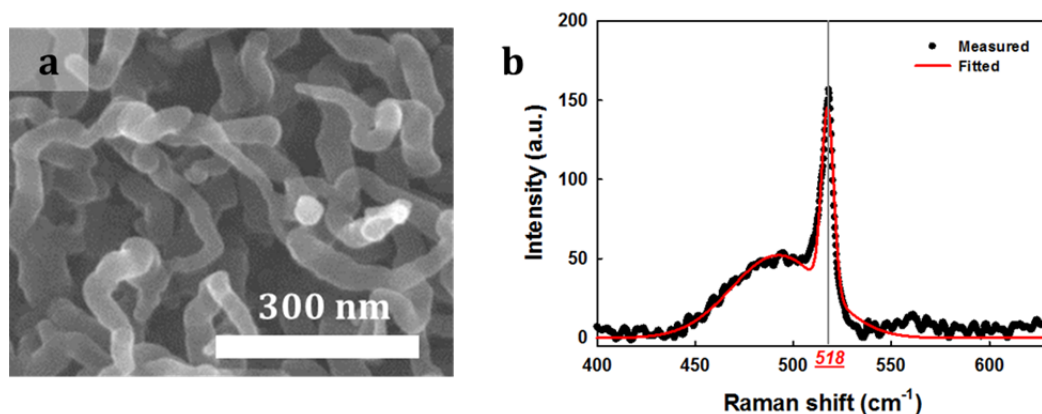


Figure 5.4 – Characteristics of Bi-catalyzed SiNWs. (a) SEM image: dense SiNWs are chosen for exciton dissociation and (b) Raman spectroscopy: crystalline silicon peak is observed with broad amorphous silicon peak.

To entirely benefit from Bi-catalyzed SiNWs/P3HT, the solar cell design is important. Before explaining the design, Bi-catalyzed SiNWs have to be reminded. Figure 5.4 shows the characteristics (nano-morphology and crystallinity) of Bi-catalyzed SiNWs used for the hybrid solar cell application. As mentioned in Section 2.6.2, denser Bi-catalyzed SiNWs were chosen for the hybrid solar cell application by considering the exciton diffusion length of P3HT. The mean interspacing is 20 nm. Figure 5.4 (b) illustrates the result of Raman spectroscopy of Bi-catalyzed SiNWs array. At 518 cm^{-1} , the sharp crystalline peak is observed. It means that the nanowires have good crystallinity. Broad spectrum with the peak at 480 cm^{-1} is observed as well. This peak corresponds to a-Si:H since the synthesis of SiNWs was carried out without hydrogen dilution to obtain high density.

Figure 5.5 describes the hybrid solar cell device structures. Detailed fabrication methods such as the SiNW growth and spin-coating are available in Chapter 2 and 3, respectively. The SiNWs are grown on aluminum doped zinc oxide (AZO), which is sputtered at $250\text{ }^{\circ}\text{C}$. It is used as the cathode for electrons collection. P3HT is spin-coated on the SiNWs array. The thickness of P3HT and length of nanowires are matched like as mentioned in Chapter 2.

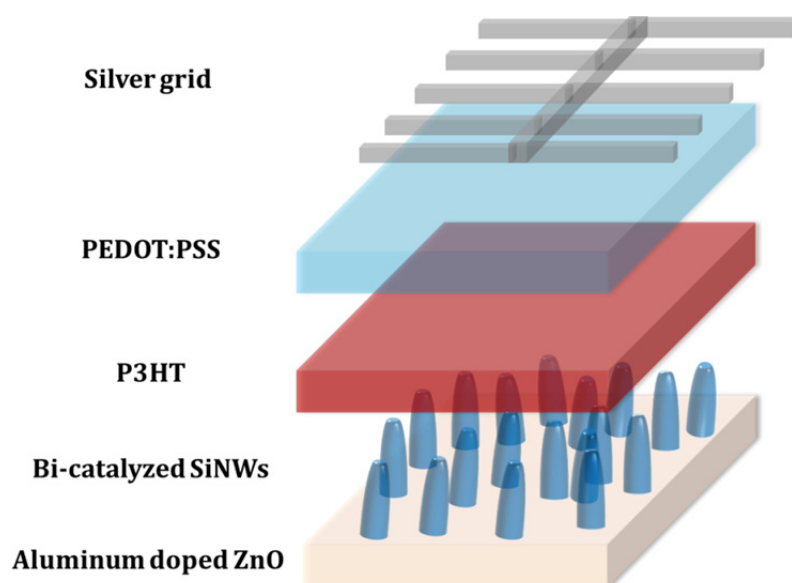


Figure 5.5 – Hybrid solar cell structures based on Bi-catalyzed SiNWs on aluminum doped zinc oxide and P3HT with grid silver electrode.

Subsequently, PEDOT:PSS is spin-coated on P3HT. To use grid electrode, the conductivity of PEDOT:PSS is improved by introducing 10 % of ethylene glycol (Section 1.3.3). However, water base PEDOT:PSS are not coated well on the P3HT film deposited from the solution based on 1,2-dichlorobenzene due to the great difference in surface tension. Surface tension of water and 1,2-dichlorobenzene is 72 and 37 dyne/cm, respectively. The surface tension of PEDOT:PSS is lowered by adding a surfactant called Triton X-100. It is soluble in water, nonconductive in solid and liquid. In addition, it has surface tension of 33 dyne/cm. Fabrication process is finished by evaporating grid patterned silver (Ag) electrode. The sample is illuminated from Ag grid to P3HT. Incident light mainly absorbed by P3HT due to high transparency of PEDOT:PSS. At SiNWs/P3HT interfaces, exciton can be separated. Free electrons and holes are collected thorough the SiNWs and P3HT, respectively.

5.4 Device performance

5.4.1 Dark current-voltage characteristic

Dark current density – voltage (J_D -V) characteristic of the hybrid solar cell is first explored before looking at solar cell performance. P3HT is a p-type organic semiconducting polymer, which can make up p-n junction with a n-type semiconductor material. Bi-catalyzed SiNWs are doped by the diffusion of Bi during the growth process [8, 9] and the n-type properties are proven by radial junction a-Si:H solar cells [10]. The hybrid heterojunction of Bi-catalyzed SiNWs/P3HT is expected to form the p-n junction which shows rectification characteristic in current-voltage curve. To minimize the effect of shunt current on J_D -V performance, length of SiNWs is matched with the thickness of P3HT which means the SiNWs are fully covered by P3HT.

Figure 5.6 shows the best performance of J_D -V curve of SiNWs/P3HT based solar cell. Measured curve shows nice diode behavior with four orders of magnitude in current density between -1 and 1 V. In reverse bias regime, the leakage current due to shunt resistance (R_{sh}) is observed. Extracted R_{sh} is the value of $2.7 \times 10^6 \Omega \cdot \text{cm}^2$ that is high enough. Meanwhile, in forward bias regime, J_D -V curve is consisted of the diode characteristic from 0.3 – 0.6 V, which is clearly shown as linear increase in semi-log plot of J_D -V and series resistance (R_s) limited regime over 0.7 V. Diode parameters are extracted by using the diode equation introduced in Section 1.4.5. The parameters are noted in Figure 5.6. Reverse saturation current, called J_0 , has sufficiently low value of $2.0 \times 10^{-6} \text{ mA/cm}^2$. Obtained diode ideality factor, namely n , is 1.7 which is comparable with that of organic bulk-heterojunction solar cells based on P3HT:PCBM blend in Chapter 4. Extracted series resistance (R_s) is $46 \Omega \cdot \text{cm}^2$.

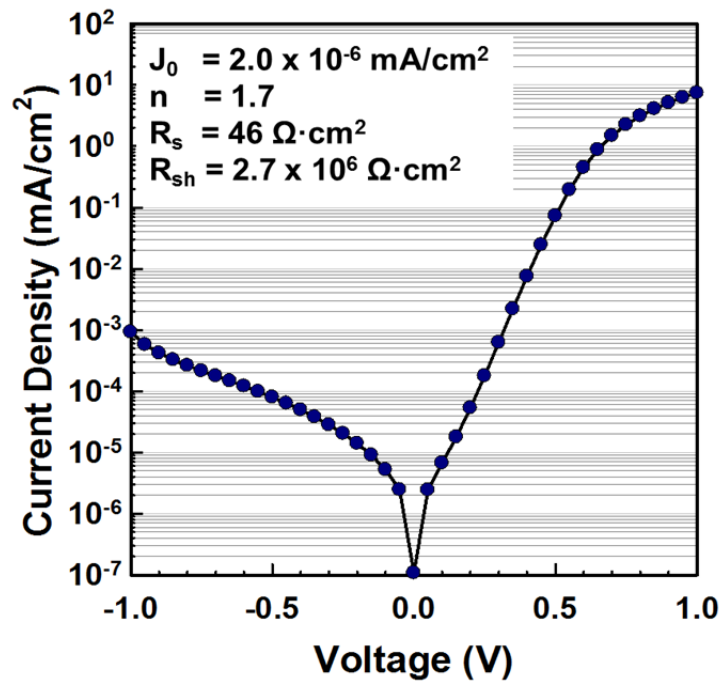


Figure 5.6 – Dark current density – voltage characteristics of the hybrid solar cell based on Bi-catalyzed SiNWs/P3HT interface. Diode parameters are summarized in the graph.

This J_D -V characteristic of the hybrid solar cell confirms again the n-type nature of Bi-doped SiNWs although it is difficult to extract exact doping concentration by a conventional method [10]. Rectifying junction is well formed which could be extended for other p-type organic semiconducting polymers. However, it should be noted that the diode performance can be easily affected by various reasons which can be caused during the fabrication. In addition, it is noted that large roughness due to nano-structured SiNWs could cause high leakage (shunt) current with combination with organic materials [11]. Figure 5.7 shows J_D -V curve which is affected by large shunt current and R_s . Thus, diode performance is limited. Namely, J_0 is only $2.2 \times 10^{-3} \text{ mA/cm}^2$ and diode ideality factor n has 3.4 that is double compared with that of Figure 5.6. This substantial leakage current also has an effect on solar cell performance.

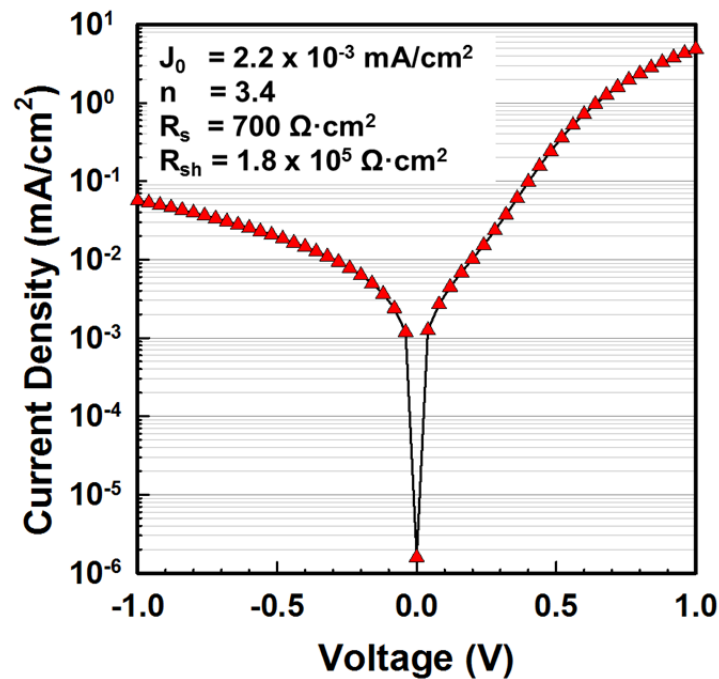


Figure 5.7 – Dark current density – voltage characteristics of the hybrid solar cell based on Bi-catalyzed SiNWs/P3HT interface. Diode parameters are summarized in the graph.

5.4.2 Solar cell performance

Solar cell performance was measured under AM 1.5 condition. Figure 5.8 shows the solar cell performance. The hybrid solar cell demonstrates very limited photovoltaic effect. Poor solar cell parameters are observed. J_{sc} and V_{oc} are only 0.14 mA/cm² and 0.1 V, respectively. Curve shape is not agreeable with an efficient solar cell. Due to the resistive effects, FF shows only 23 %. The solar cell performance is less efficient than that of organic bulk-heterojunction solar cell and c-Si based hybrid solar cells [3, 12-14].

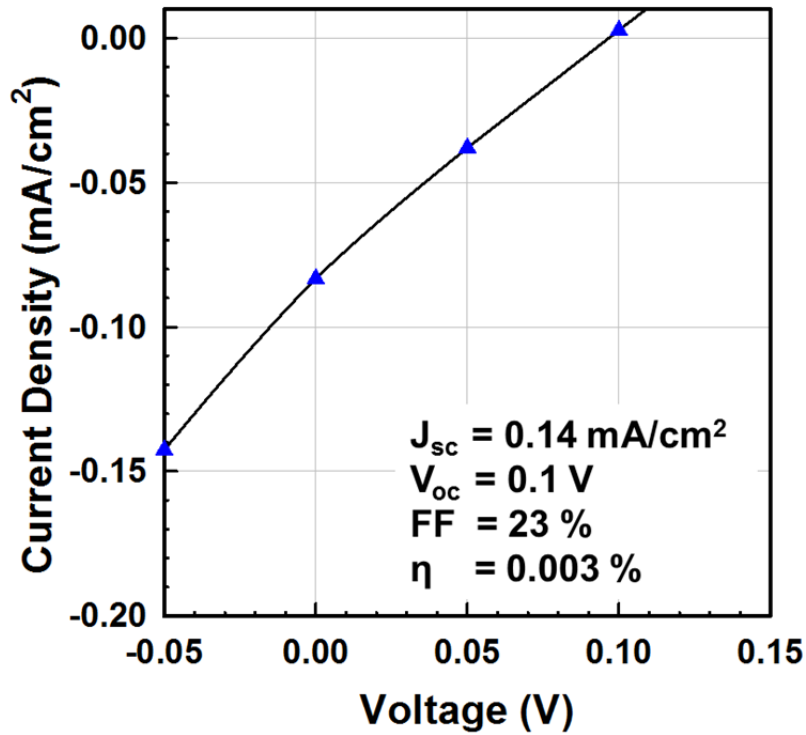


Figure 5.8 – Solar cell performance of the hybrid solar cell based on Bi-catalyzed SiNWs/P3HT interface. Solar cell parameters are summarized in the graph. Average length of Bi-catalyzed SiNWs and thickness of solar cell are 130 and 150 nm respectively.

The reports on solar cells based on the hybrid heterojunction showed also poor performance. Goncher et al. reported a hybrid solar cell based on Au-catalyzed SiNWs on n-type c-Si wafer and P3HT [15]. The solar cell parameters demonstrated poor performance comparable to our result of solar cell. J_{sc} , V_{oc} and FF are 0.03 mA/cm², 0.146 V and 26 %, respectively. It

showed $1.4 \times 10^{-3} \%$ of power conversion efficiency. They mainly ascribed the poor performance to the considerable leakage current. Davenas et al. reported a hybrid solar cells based on the active layer consisted of the blend of Au-catalyzed SiNWs and P3HT [16, 17]. The solar cell performance depends on the SiNWs concentration and the surface treatment of SiNWs. The exciton quenching efficiency showed the maximum with 10 wt% of SiNWs in P3HT. As produced SiNWs based solar cell has poorer performance than that of HF treated SiNWs. In this report, J_{sc} and V_{oc} are 1.42 mA/cm^2 and 0.45 V with FF of 34 % measured with the incident light intensity 20 mW/cm^2 . The efficiency of the solar cell was 1.14 % with the HF treated SiNWs. From both works, the performances of hybrid solar cells are sensitive to the leakage current and the surface state of nanowires.

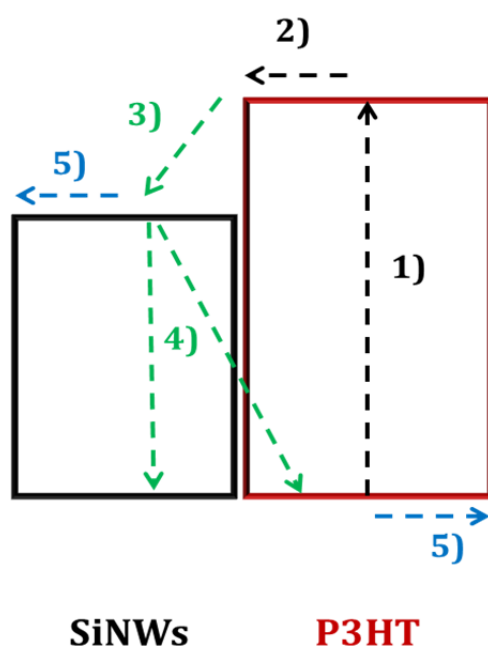


Figure 5.9 – Band diagram of SiNWs P3HT to explain photo-generated carrier generation. 1) Exciton generation by absorption of incident light. 2) Diffusion of exciton toward interface of SiNWs/P3HT. 3) Exciton dissociation (electron transfer from LUMO of P3HT to conduction band of SiNWs) 4) electron recombination 5) Transport of photo-generated carriers

To make a diagnosis for the poor solar cell performance, the band structures are reminded. Figure 5.9 illustrates the band structures of SiNWs and P3HT with assigned numbers to describe the generation of photo-carriers. Excitons are created in P3HT by absorbing incident light which has higher energy than the band-gap of P3HT (Process 1). Exciton, which is neutral, diffuses toward interfaces (Process 2). Exciton is separated at the interface by the energy offset between LUMO of P3HT and conduction band of SiNWs (Process 3). Thus, SiNWs and P3HT have electrons and holes, respectively. But some of electrons on SiNWs could be recombined by non-radiative decays (Process 4). Photo-generated electron and holes are conducted through conduction band of SiNWs and HOMO of P3HT, respectively (Process 5). It is believed that Process 1 and 2 don't cause problems since it is material properties of P3HT which are already well verified in many literatures [14, 18-22]. In a literature, The P3HT's exciton quenching by SiNWs was presented but it is not sure that all excitons turn into free carriers or the exciton lose its energy by non-radiative decay [16]. Potentially, problems could be occurred at Process 3, 4 and 5 due to SiNWs' surface states, similar energy level of valence band with HOMO of P3HT. The hole transport process through P3HT is not taken into count for the poor performance. Practically, it is not easy to quantitatively verify the problems. Instead, it is analyzed by investigating additional solar cell devices. For exploring the exciton separation in our hybrid solar cell, various concentration of PCBM is added to P3HT to ensure exciton dissociation in the blend. PCBM is classically used in organic bulk-heterojunction solar cells as electron acceptor for various organic semiconducting polymers.

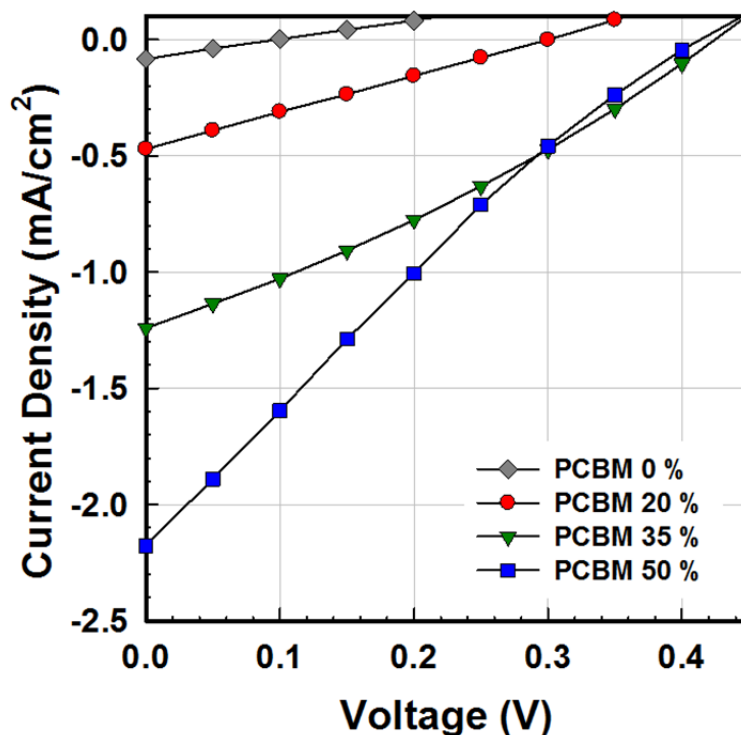


Figure 5.10 – Solar cell performance of the hybrid solar cell based on Bi-catalyzed SiNWs/P3HT interface; dependence of PCBM contents (%) in P3HT solution.

Figure 5.10 shows the solar cell performance depending on the PCBM contents in the P3HT:PCBM blend. First of all, the increase in J_{sc} is observed as PCBM content increases. J_{sc} was only 0.14 mA/cm^2 with PCBM 0 %. It becomes 0.47 mA/cm^2 with 20 % of PCBM concentration and it increases further with PCBM 50 % up to 2.2 mA/cm^2 . Considerable improvement of V_{oc} is also demonstrated. It is 0.3 V with 20 % of PCBM then it has the maximum value of 0.43 V with 35 % PCBM content. Compared to that without PCBM (0.1 V), it is largely improved. All three curves are linearly scale with voltage, suggesting that there are resistive effects (low R_{sh} , high R_s), thus, FF shows limited values ranged from 23 % to 30 %. The power conversion efficiency scales also with PCBM contents, namely, it shows 0.04, 0.16 and 0.20 % with 20, 35 and 50 % of PCBM in the blend. Hybrid solar cell demonstrates better performance with added PCBM into P3HT.

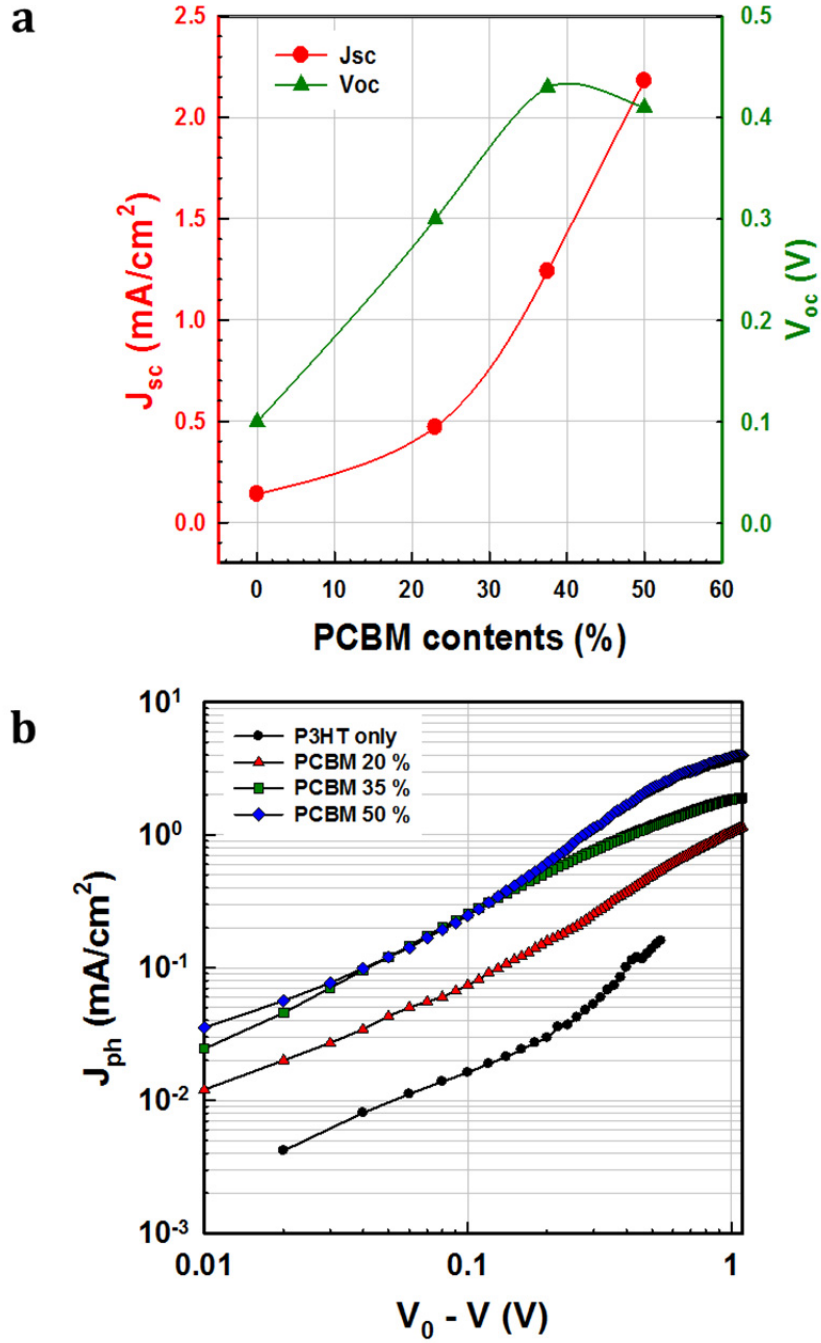


Figure 5.11 – (a) J_{sc} and V_{oc} of hybrid solar cells as a function of PCBM content (%) (b) Experimental photo-current extracted from the equation of $J_L - J_D = J_{ph}$ as a function of effective voltage, $V_0 - V$.

Figure 5.11 summarizes the trend of J_{sc} and V_{oc} variation as a function of PCBM contents and experimental photo-current extracted using a simple equation $J_L - J_D = J_{ph}$. As mentioned above, J_{sc} is substantially improved with PCBM addition. It scales like quadratic function (Figure 5.11 (a)) with PCBM contents. It means that photo-generated electrons and holes in the blend could be collected through SiNWs array/AZO and P3HT/PEDOT:PSS/Ag grid respectively. Therefore, the lower J_{sc} of solar cells without PCBM implies that the exciton dissociation process is not efficient at the SiNWs/P3HT interface. Thus, the added PCBM performs significant roles in increase of J_{sc} by activating the exciton dissociation.

In addition to J_{sc} , V_{oc} also shows great increases by PCBM. V_{oc} has a dependence on J_{ph}/J_0 . Figure 5.11 (b) shows experimental J_{ph} with various PCBM contents as a function of effective voltage, $V_0 - V$. V_0 is defined as a voltage where $J_D = J_L$ and V is applied voltage during the measurement. J_{ph} with only P3HT shows the worst performance. It might be not efficient for photo-current generation. The value is one order lower than others compared to the solar cells with PCBM addition. Under 0.1-0.2 V, where the diffusion is dominant, J_{ph} is improved with 20 % of PCBM but it saturated with 35 and 50 % of PCBM. It implies that the number of photo-generated carriers, which can be collected by the diffusion process, is limited even though there are excess photo-generated carriers. The difference is observed over 0.2 V of effective voltage where the drift process is predominant. The higher J_{ph} is observed with the higher concentration of PCBM. Exceed photo-generated carriers are collected with higher effective voltage. This trend is exactly same with J_{sc} variation with PCBM concentration. V_{oc} tends to increase with PCBM addition due to efficient photo-carrier generation. With 50 % of PCBM, V_{oc} is decrease a little since the J_0 of hybrid solar cell with 50 % concentration is higher than that of 35 % of PCBM.

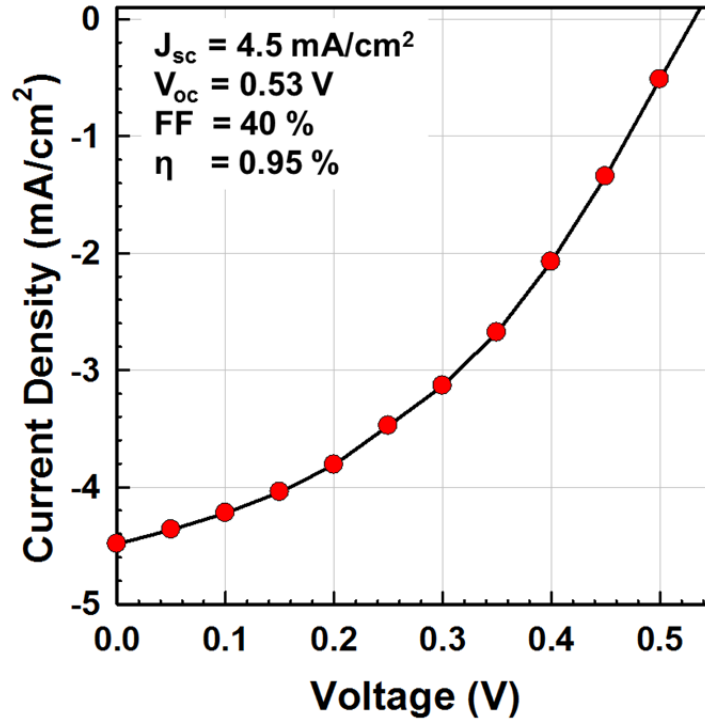


Figure 5.12 – Solar cell performance of planar solar cell without SiNWs. Solar cell parameters are summarized in the graph.

It seems that SiNWs has negative effect on the charge carrier collection compared to the planar solar cell without SiNWs. Figure 5.12 shows the solar cell performance of an inverted organic solar cell without SiNWs. Thus, the device has the structure; AZO/P3HT:PCBM/PEDOT:PSS/Ag grid. The solar cell curve shape is quite different compared to the solar cell with SiNWs in Figure 5.8 and Figure 5.10. The result comes from the better FF which is improved from 25 to 40 % although absolutely it is not efficient compared to other types of solar cells. It could be attributed to low resistance and smooth surface. Those factors contribute to reduce leakage current, thus, more photo-generated carrier can be collected. J_{sc} is 4.5 mA/cm² and V_{oc} is 0.53 V which is closer with reference value of P3HT:PCBM based organic bulk-heterojunction solar cell [14, 23, 24]. It demonstrates 0.95 % of efficiency.

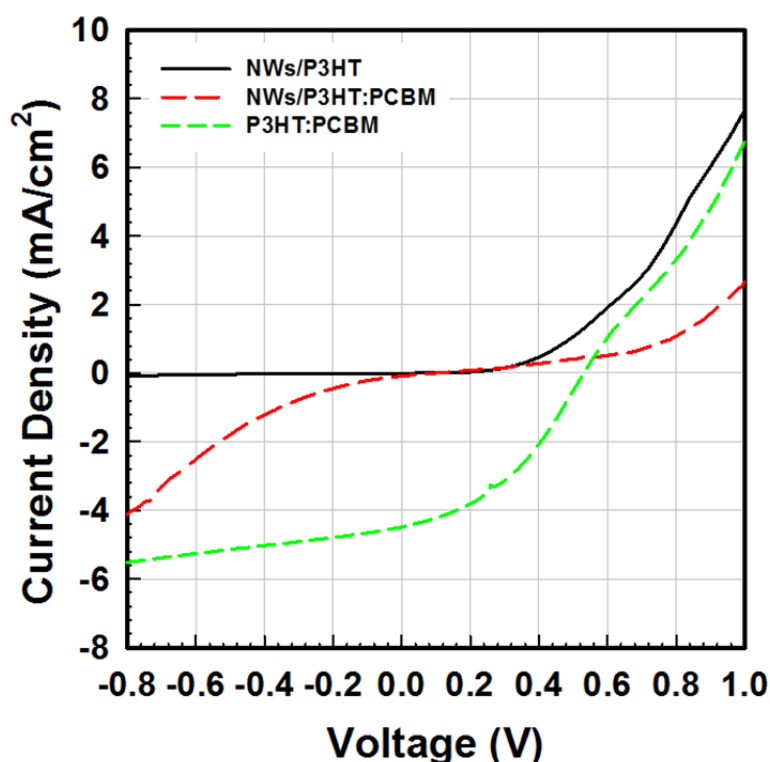


Figure 5.13 – Summary of solar cell performance of hybrid heterojunction based on SiNWs/P3HT, SiNW/P3HT:PCBM and organic inverted solar cells based on P3HT:PCBM.

Figure 5.13 shows the summary of solar cell performance of the SiNW/P3HT junction hybrid solar cells, the SiNW/P3HT:PCBM solar cell and the inverted organic solar cell. At a look, it is recognized that solar cells based on SiNWs shows worse performance than the inverted organic solar cell. We can observe that the SiNWs/P3HT junction produces seriously limited current in reverse bias regime. This is attributed to inefficient exciton separation at the interface. Whereas, SiNW/P3HT:PCBM produces more photo-generated carriers since PCBM helps to dissociate excitons of P3HT. It is believed that additional biasing is necessary for efficient carrier collection. The current density is increased with the negative voltage in reverse regime. But in forward bias regime, the SiNW/P3HT:PCBM solar cell shows lower current level than SiNWs/P3HT. This is due to HOMO level of PCBM (6.2 eV) is too low compared to the valence band of c-Si (5.12 eV). This might increase series resistance. It is reported that PCBM can act as hole blocking layer in solar cell structures [25].

5.5 Conclusion: challenges and perspectives

The use of the hybrid heterojunction in solar cell seems to be interesting since we can take advantages of both materials to achieve efficient solar cells with low fabrication cost. Typically, it is expected for inorganic materials to have high carrier mobility for efficient carrier collection, the nano-structure for large interfacial area and carrier collection pathway. Whereas, it is expected for organic materials that efficient light absorption with proper band gap for photo-carrier generation and solution processibility for room temperature fabrication instead of the vacuum process at high temperature. Nevertheless it is still challenging to achieve efficient hybrid solar cells in academia.

In this chapter, we investigated on the Bi-catalyzed SiNWs/P3HT based hybrid solar cells which have an ideal structure, that is, large interfacial area and efficient carrier collecting pathways. The Bi-catalyzed SiNWs are naturally doped by catalyst during the VLS growth. When the Bi-doped SiNWs forms a junction with P3HT, the device clearly demonstrated a diode characteristic which proves the n-type characteristic of SiNWs. Despite of good diode characteristic, the hybrid solar cell showed poor performance. Despite of many attempts to improve solar cell performances, the solar cell performance of the hybrid heterojunction is still discontented. The SiNWs/P3HT:PCBM based hybrid solar cells are fabricated for artificial exciton dissociation to investigate further on limiting factors. This is believed that exciton is not efficiently dissociated at SiNWs/P3HT interface from the results. Exciton may lose its energy before dissociation by non-radiative decay. Also, the SiNWs could not collect photo-generated carrier efficiently at 0 V. Namely, additional reverse bias results in large current density under illumination.

For efficient exciton dissociation, the surface state of SiNWs is one of important factor. It has strong effect on the interface recombination even for crystalline silicon based solar cells [12, 26-28]. Since chemically synthesized SiNWs have lower quality than c-Si, the surface state is more important.

Among variety methods to treat SiNWs surface, surface functionalization could propose a solution. Goh et al. reported a titanium oxide (TiO_2)/P3HT hybrid solar cell with the surface functionalization of TiO_2 [29]. Solar cell parameters are tunable according to the modification molecular. They control molecular interface between TiO_2 /P3HT. Especially, V_{oc} showed different values with functional molecules. We also investigated on the hybrid solar cell based on a-Si:H/P3HT junction with the structures drawn in Figure 5.3. V_{oc} increase about 0.2 V, which is substantial increase, is observed by the surface modification. As our Bi-catalyzed SiNWs/P3HT showed 0.1 V of V_{oc} , the surface functionalization could increase V_{oc} as the first step of efficiency improvement.

Introducing quantum dot or dyes on the SiNWs are also interesting method to improve interface characteristics. From the works of Zhang et al., the solar cell performance was further improved by introducing Platinum nanodots between nano-structured silicon and P3HT [12, 30]. Metal nanodots could tune electric field at the interface. Lastly, the correlation between catalyst thickness and solar cell performance should be considered. Bi-catalyzed SiNWs is a type of metal doped SiNWs. Thus, the electrical properties of SiNWs can be modified with the amount of catalyst metal. In that case, Bi catalyst is dopant and defect at the same time. Gunawan et al. reported Au-catalyzed SiNWs solar cell [31]. The effect of catalyst thickness on solar cell performance is investigated. The thicker catalyst results in large leakage current and V_{oc} decrease. J_{sc} and efficiency showed an optimum. Finding the optimum is main challenging since catalyst thickness variation changes not only electrical property but also nano-morphology of SiNWs.

Hybrid solar cell based on hybrid heterojunction is interesting topic although the demonstrated performance states the challenges since there is still the scope of efficiency improvement. Also, it is still necessary to understand the physics of hybrid interface. If we could overcome the barrier by employing the proposed potential solution, the hybrid solar cell will be an excellent alternative.

REFERENCE

1. Forrest, S.R., et al., *Organic-on-inorganic semiconductor contact barrier devices*. Applied Physics Letters, 1982. **41**(1): p. 90-93.
2. McCaffrey, R.R. and P.N. Prasad, *Organic-thin-film-coated solar cells: Energy transfer between surface pyrene molecules and the silicon semiconductor substrate*. Solar Cells, 1984. **11**(4): p. 401-409.
3. Avasthi, S., et al., *Role of Majority and Minority Carrier Barriers Silicon/Organic Hybrid Heterojunction Solar Cells*. Advanced Materials, 2011. **23**(48): p. 5762-5766.
4. Gowrishankar, V., et al., *Exciton harvesting, charge transfer, and charge-carrier transport in amorphous-silicon nanopillar/polymer hybrid solar cells*. Journal of Applied Physics, 2008. **103**(6): p. 064511-8.
5. Gowrishankar, V., et al., *Exciton splitting and carrier transport across the amorphous-silicon/polymer solar cell interface*. Applied Physics Letters, 2006. **89**(25): p. 252102-3.
6. Dietmueller, R., et al., *Light-induced charge transfer in hybrid composites of organic semiconductors and silicon nanocrystals*. Applied Physics Letters, 2009. **94**(11): p. 113301-3.
7. Lori Noice, G.G., Raj Solanki, *Progress on a photovoltaic cell design consisting of silicon nanowires and poly(3-hexylthiopenen)*. PSU McNair Scholars Online Journal, 2006. **2**(1): Article 28
8. Kumar, R.R., K.N. Rao, and A.R. Phani, *Bismuth catalyzed growth of silicon nanowires by electron beam evaporation*. Materials Letters, 2012. **82**: p. 163-166.
9. Holmberg, V.C., K.A. Collier, and B.A. Korgel, *Real-Time Observation of Impurity Diffusion in Silicon Nanowires*. Nano Letters, 2011. **11**(9): p. 3803-3808.
10. Yu, L., et al., *Bismuth-Catalyzed and Doped Silicon Nanowires for One-Pump-Down Fabrication of Radial Junction Solar Cells*. Nano Letters, 2012. **12**(8): p. 4153-4158.
11. Ki-Beom KIM, Y.-H.T., Yoon-Soo HAN, Kwang-Heum BAIK, Myung-Hee YOO, Moon-Ho LEE, *Relation between Surface Roughness of Indium Tin Oxide and Leakage Current of Organic Light-Emitting Diode*. Japanese Journal of Applied Physics, 2004. **42**.
12. Zhang, F.T., et al., *Air Stable, Efficient Hybrid Photovoltaic Devices Based on Poly(3-hexylthiophene) and Silicon Nanostructures*. Chemistry of Materials, 2011. **23**(8): p. 2084-2090.
13. Nolasco, J.C., et al., *Extraction of poly (3-hexylthiophene) (P3HT) properties from dark current voltage characteristics in a P3HT/n-crystalline-silicon solar cell*. Journal of Applied Physics, 2010. **107**(4): p. 044505-4.

-
14. Dang, M.T., L. Hirsch, and G. Wantz, *P3HT:PCBM, Best Seller in Polymer Photovoltaic Research*. Advanced Materials, 2011. **23**(31): p. 3597-3602.
 15. Gary Goncher and R. Solanki, *Semiconductor nanowire photovoltaics*. Proc. of SPIE, 2008. **7047**: p. 70470L.
 16. Davenas, J., et al., *Silicon nanowire/poly(3-hexylthiophene) hybrids for thin film solar cells*. Journal of Non-Crystalline Solids, 2012. **358**(17): p. 2534-2536.
 17. Davenas, J., et al., *Hybrid films based on silicon nanowires dispersed in a semiconducting polymer for thin film solar cells: Opportunities and new challenges*. Synthetic Metals, 2012. **161**(23-24): p. 2623-2627.
 18. Grzegorzcyk, W.J., et al., *Temperature-Independent Charge Carrier Photogeneration in P3HT-PCBM Blends with Different Morphology*. The Journal of Physical Chemistry C, 2010. **114**(11): p. 5182-5186.
 19. Nikitenko, V.R., H. Heil, and H. von Seggern, *Space-charge limited current in regioregular poly-3-hexyl-thiophene*. Journal of Applied Physics, 2003. **94**(4): p. 2480-2485.
 20. Zhokhavets, U., et al., *Relation between absorption and crystallinity of poly(3-hexylthiophene)/fullerene films for plastic solar cells*. Chemical Physics Letters, 2006. **418**(4-6): p. 347-350.
 21. Jin, H., et al., *Polymer-Electrode Interfacial Effect on Photovoltaic Performances in Poly(3-hexylthiophene):Phenyl-C61-butyric Acid Methyl Ester Based Solar Cells*. The Journal of Physical Chemistry C, 2009. **113**(38): p. 16807-16810.
 22. Kniepert, J., et al., *Photogeneration and Recombination in P3HT/PCBM Solar Cells Probed by Time-Delayed Collection Field Experiments*. The Journal of Physical Chemistry Letters, 2011. **2**(7): p. 700-705.
 23. Schafferhans, J., et al., *Oxygen doping of P3HT:PCBM blends: Influence on trap states, charge carrier mobility and solar cell performance*. Organic Electronics, 2010. **11**(10): p. 1693-1700.
 24. De Bettignies, R., et al., *Accelerated lifetime measurements of P3HT:PCBM solar cells*. Synthetic Metals, 2006. **156**(7-8): p. 510-513.
 25. Seo, J.H., et al., *High Efficiency Inorganic/Organic Hybrid Tandem Solar Cells*. Advanced Materials, 2012. **24**(33): p. 4523-4527.
 26. He, L., et al., *High efficiency planar Si/organic heterojunction hybrid solar cells*. Applied Physics Letters, 2012. **100**(7): p. 073503-3.
 27. Jeon, T., et al., *Effects of acid-treated silicon nanowires on hybrid solar cells performance*. Solar Energy Materials and Solar Cells, 2013. **117**: p. 632-637.
 28. Dan, Y., et al., *Dramatic Reduction of Surface Recombination by in Situ Surface Passivation of Silicon Nanowires*. Nano Letters, 2011. **11**(6): p. 2527-2532.

29. Goh, C., S.R. Scully, and M.D. McGehee, *Effects of molecular interface modification in hybrid organic-inorganic photovoltaic cells*. Journal of Applied Physics, 2007. **101**(11): p. 114503-12.
30. Golap, K. and et al., *Silicon nanowire array/polymer hybrid solar cell incorporating carbon nanotubes*. Journal of Physics D: Applied Physics, 2009. **42**(11): p. 115104.
31. Gunawan, O. and S. Guha, *Characteristics of vapor-liquid-solid grown silicon nanowire solar cells*. Solar Energy Materials and Solar Cells, 2009. **93**(8): p. 1388-1393.

Conclusion

Through this thesis, the hybrid solar cells drawing great attention as a 3rd generation of solar cells were explored. Especially, we have been investigated on the hybrid solar cells based on the PECVD grown SiNWs and P3HT as the principal light absorbing material. Initially, it aimed to overcome the shortage of organic materials such as low carrier mobility and limited device structure by taking advantages from the SiNWs. To realize the hybrid solar cells, it was necessary to grow the SiNWs with the proper morphology and to deposit P3HT by solution process on the SiNWs array, practically. We largely investigated on the realization of the hybrid solar cells to propose their potentials. Before the journey to the hybrid solar cells, the investigations on the SiNWs growth by PECVD technique and nano-morphology have been carried out using Sn or Bi as catalyst metals.

Sn-catalyzed SiNWs were already well studied by my colleagues for radial-junction a-Si:H solar cells. The SiNWs showed the straight and tapered appearance. In spite of the various experimental parameters we explored, the density of Sn-catalyzed SiNWs remained too low to effectively collect electrons from the P3HT. However, we still used the nanowires to enhance light trapping in our solar cells. Sn-catalyzed SiNWs were combined with P3HT:PCBM blend which is typical blend for organic solar cells for enhancing the light trapping in the organic active layer. Actually, the deposition of organic materials on a highly rough surface is quite challenging because organic materials are very sensitive to the surface roughness. It is surely a contradiction to deposit P3HT:PCBM on the Sn-catalyzed SiNWs showing needle-like morphology. It is shown that the hybrid solar cell performance is limited due to the surface roughness and the complex interfaces which have been overcome by introducing PEDOT:PSS between SiNWs and P3HT:PCBM layer. It makes the surface of the nanowires smooth and hinders the formation of complex interfaces by isolating P3HT:PCBM from the SiNWs array. Enhancement of light trapping is not observed although hybrid solar

cells with photovoltaic effect were achieved. By examining Sn-catalyzed SiNWs array, the two limiting factor of light-trapping were detected, that is, the residual catalyst and the co-deposition of a-Si:H around SiNWs. These problems were addressed by chemical and physical methods. 1) the residual catalysts are removed by HCl dipping process which results in the decreases in the shunt-current and parasitic absorption of metal droplets. In addition, the native oxide is etched by HF treatment. It contributes to lower series resistance and FF improvement. 2) a-Si:H layer is selectively etched by H₂ plasma just after growth process which selectively etch out a-Si:H. Thus, the resistive effect and parasitic absorption are greatly decreased without changing the nano-morphology of the SiNWs. Finally, the light-trapping enhancement has been discovered by EQE measurement.

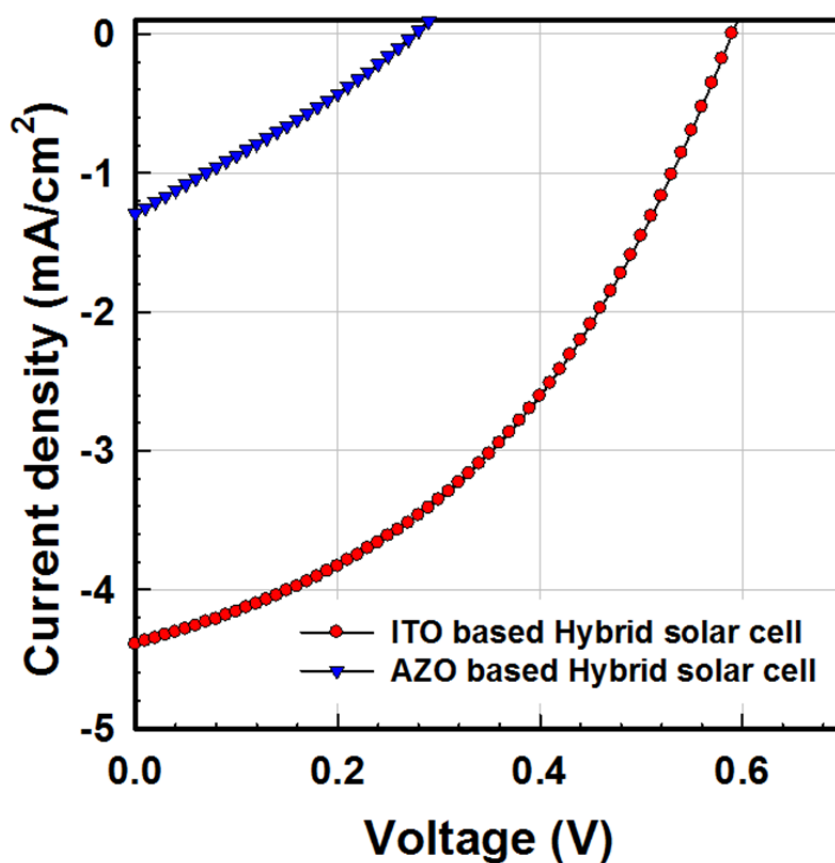
For Bi-catalyzed SiNWs, the parameter studies are performed to widely control the nano-morphology for the hybrid solar cells and the a-Si:H radial junction solar cells. From the winding and denser SiNWs to straight and less dense SiNWs were achieved. At the best, the SiNWs with 20 nm of an average interspacing obtained. Thanks to the sufficiently dense SiNWs array, it was applied to the hybrid solar cell as the electron acceptor of P3HT. Bi-catalyzed SiNWs are interesting due to its n-type nature obtained by catalyst doping during the growth process via VLS process without any doping gas. It was verified by P3HT (p-type)/Bi-catalyzed SiNWs (n-type) junction which demonstrated the rectifying action. Nevertheless, solar cell performance based on the hybrid interface was limited due to the inefficient exciton dissociation at the interface and the photo-generated carrier transportation. It might be necessary to functionalize the surface of SiNWs which is greatly related with the recombination and to control precisely the doping concentration. If the difficulties are surmounted, the hybrid solar cells can approach one more step toward the next-generation solar cells.

Appendix

A.1 TCO DEPENDENCE OF HYBRID SOLAR CELL PERFORMANCE	170
A.2 SINWS GROWTH CONDITIONS	171
A.2.1 SN-CATALYZED SiNWS: GROWTH TIME DEPENDENCE (SECTION 2.4.1)	171
A.2.2 SN-CATALYZED SiNWS: H ₂ DEPENDENCE (SECTION 2.4.2)	171
A.2.3 Bi-CATALYZED SiNWS: TEMPERATURE DEPENDENCE (SECTION 2.5.2)	172
A.2.4 Bi-CATALYZED SiNWS: RF POWER DEPENDENCE (SECTION 2.5.3)	172
A.2.5 Bi-CATALYZED SiNWS: GAS FLOW RATIO DEPENDENCE (SECTION 2.5.4)	172
A.3 ORGANIC THIN-FILM FORMATION	173

A.1 TCO dependence of hybrid solar cell performance

Hybrid solar cell performance is affected by the choice of TCOs. ITO and AZO are purchased and prepared by sputtering, respectively. Hybrid solar cells based on Sn-catalyzed SiNWs are fabricated on different substrates.



Hybrid solar cell based on	Jsc mA/cm^2	Voc V	FF %	PCE %
ITO	4.4	0.58	41	1.0
AZO	1.3	0.26	20	0.1

Figure A.1 – Hybrid solar cell performance with the structure of ITO or AZO/p-SiNWs/PEDOT:PSS/P3HT:PCBM/LiF/Al

Table A.1 – Summary of hybrid solar cell performance with the structure of ITO or AZO/p-SiNWs/PEDOT:PSS/P3HT:PCBM/LiF/Al

ITO clearly demonstrates higher solar cell performance and produces better solar cell parameters. This is mainly attributed to the work function difference between ITO (4.8 eV) and AZO. (4.2-4.5 eV).

A.2 SiNWs growth conditions

SiNWs are synthesized by PECVD technique. Detailed experimental conditions are noted in this section.

A.2.1 Sn-catalyzed SiNWs: Growth time dependence (Section 2.4.1)

PECVD Parameters	T _{sub} °C	T _{RF} °C	H ₂ sccm	SiH ₄ sccm	TMB sccm	Pressure mTorr	RF power Watt	Duration min
H ₂ plasma	350	200	100	-	-	380	5	3
SiH ₄ plasma	600	400	100	10	0.8	1000	2	<u>5, 10, 15</u>

Table A.2 – Experimental conditions of Sn-catalyzed SiNWs synthesis (Variable: SiH₄ plasma duration).

A.2.2 Sn-catalyzed SiNWs: H₂ dependence (Section 2.4.2)

PECVD Parameters	T _{sub} °C	T _{RF} °C	H ₂ sccm	SiH ₄ sccm	TMB sccm	Pressure mTorr	RF power Watt	Duration min
H ₂ plasma	350	200	100	-	-	380	5	<u>2, 4, 6, 8</u>
SiH ₄ plasma	600	400	100	10	0.8	1000	2	2

Table A.3 – Experimental conditions of Sn-catalyzed SiNWs synthesis (Variable: H₂ plasma duration).

A.2.3 Bi-catalyzed SiNWs: Temperature dependence (Section 2.5.2)

PECVD Parameters	T _{sub} °C	T _{RF} °C	H ₂ sccm	SiH ₄ sccm	Pressure mTorr	RF power Watt	Duration min
H ₂ plasma	350	200	100	-	600	5	10
SiH ₄ plasma	<u>450</u> , <u>500</u> , <u>550</u> , <u>600</u>	400	100	10	1000	20	4

Table A4 – Experimental conditions of Bi-catalyzed SiNWs synthesis (Variable: Substrate temperature of SiH₄ plasma).

A.2.4 Bi-catalyzed SiNWs: RF power dependence (Section 2.5.3)

PECVD Parameters	T _{sub} °C	T _{RF} °C	H ₂ sccm	SiH ₄ sccm	Pressure mTorr	RF power Watt	Duration min
H ₂ plasma	350	200	100	-	600	5	10
SiH ₄ plasma	550	400	100	10	1000	<u>20, 40, 60</u>	4

Table A.5 – Experimental conditions of Bi-catalyzed SiNWs synthesis (Variable: RF power of SiH₄ plasma).

A.2.5 Bi-catalyzed SiNWs: Gas flow ratio dependence (Section 2.5.4)

PECVD Parameters	T _{sub} °C	T _{RF} °C	H ₂ sccm	SiH ₄ sccm	Pressure mTorr	RF power Watt	Duration min
H ₂ plasma	350	200	100	-	600	5	10
SiH ₄ plasma	600	400	0 100 100 100	10 10 5 2	1000	20	4

Table A.6 – Experimental conditions of Bi-catalyzed SiNWs synthesis (Variable: Gas flow ratio of H₂/SiH₄).

A.3 Organic thin-film formation

In this thesis, organic materials are formed by spin-coating technique from the liquid phase of materials in which organic materials are dissolved in a solvent. Just after spin-coating, organic materials coated substrates are annealed on hot-plate to dry solvent in nitrogen atmosphere. Typical experimental conditions are summarized below.

	Spin-coating			Annealing	
	1 st step <i>rpm</i>	Interval <i>s</i>	2 nd step <i>rpm</i>	Temp. <i>°C</i>	Duration <i>min</i>
PEDOT:PSS	3500	5	4000	110	2
P3HT:PCBM or P3HT	500	5	1000	110	1

Table A.7 – Organic film formation conditions

Abstract

Solar cells are an exciting alternative energy technology due to the infinite energy source, the Sun. Many types of solar cells based on inorganic or organic materials are currently developed with the objective of higher efficiency and lower cost. In this context, this thesis suggests to study nano-structured hybrid solar cells based on silicon nanowires (SiNWs) and organic active materials to benefit advantages of both materials. SiNWs are grown by PECVD on transparent conducting oxide via Vapor-Liquid-Solid (VLS) mechanism with careful control of their nano-morphology. The organic materials made of polymers or blend polymers are then deposited by spin-coating on top of SiNWs. In these hybrid solar cells the SiNWs are used as light-trapping medium and/or electron acceptor material. For better solar cell performance, the optimization of SiNWs array is carried out by removing residual catalyst and etching parasitic hydrogenated amorphous silicon. Their effects on hybrid solar cells have been fully analyzed and discussed. Furthermore, the electron-acceptor properties of the nano-structured SiNWs have been estimated with Bismuth-doped n-type SiNWs. The results clearly reveal the potential of this type of hybrid solar cells, namely, 1) power conversion efficiency improvement by enhancing external quantum efficiency in longer wavelength regime and 2) variety uses of SiNWs by tuning their electrical property and morphology.

Key words: Hybrid Solar cell, Silicon Nanowires, Post-transition metal catalysts, VLS growth, Organic semiconductor

Résumé

Les cellules photovoltaïques proposent une solution au problème énergétique en raison de leur source inépuisable: le soleil. Plusieurs types de cellules, qu'elle soient inorganiques ou organiques, sont étudiées, avec comme objectif d'obtenir de hauts rendements pour de faibles coûts. Dans ce contexte, ce travail de thèse se propose d'étudier des cellules solaires hybrides nanostructurées à base de nanofils de silicium et de matériaux organiques afin de bénéficier des avantages de ces différents matériaux. La morphologie contrôlée de la croissance des nanofils de silicium par dépôt chimique en phase vapeur assisté par plasma (PECVD) via un procédé Vapeur-Liquide-Solide est présentée. Le mélange de matériaux organiques est ensuite déposé sur les nanofils de silicium par un procédé d'enduction par centrifugation. Dans ce type de cellules hybrides, les nanofils de silicium jouent le rôle de matériaux accepteurs ou aident à l'absorption de la lumière. Pour améliorer les performances de ces cellules, il est nécessaire d'optimiser la qualité du réseau de nanofils par une gravure chimique visant à éliminer les traces de catalyseur résiduelles ainsi que l'oxyde natif du silicium. Cet effet de la gravure a été largement étudié et discuté. De plus les propriétés d'accepteur d'électrons (type-n) des nanofils de silicium à base de catalyseurs de Bismuth ont été étudiées. Les résultats montrent clairement le potentiel de ce type de cellules, notamment 1) l'augmentation de la conversion de lumière par l'amélioration de l'efficacité du rendement quantique pour les grandes longueurs d'onde, 2) l'utilisation d'une grande variété de nanofils avec des morphologies et propriétés électriques finement contrôlées.

Mots clés: Cellules solaires hybrides, nanofils de silicium, croissance par catalyse métaux pauvres, procédé VLS, semi-conducteurs organiques